

# BERICHTE

aus dem MARUM und dem Fachbereich  
Geowissenschaften der Universität Bremen

No. 326

Bohrmann G,

Ahrlich F, Antoniou D, Behrendt N, Innocentini S, Coulibaly O,  
Eijsink A, Feddersen G, Gaide S, Kaul N, König T, Krahl J,  
Kürzinger V, Lenius S, Malnati J, Marschall L, Niederbockstruck B,  
Pormann S, Rau S, Römer M, Schillai S, Spiesecke U, Streuff K,  
Tseng Y, Vejzovic I, von Wahl T, Warnken N, Witzleb A

## FLUID-ROCK INTERACTION AT THE BACKSTOP TO THE MEDITERRANEAN RIDGE ACCRETIONARY COMPLEX SOUTH OF CRETE

R/V SONNE CRUISE REPORT SO278

EMDEN (GERMANY) – EMDEN (GERMANY)  
12.10.2020 – 01.12.2020

FRINGE



Berichte, MARUM – Zentrum für Marine Umweltwissenschaften, Fachbereich  
Geowissenschaften, Universität Bremen, No. 326, 208 pages, Bremen 2021

ISSN 2195-7894

# **Berichte aus dem MARUM und dem Fachbereich Geowissenschaften der Universität Bremen**

published by

## **MARUM – Center for Marine Environmental Sciences**

Leobener Strasse, 28359 Bremen, Germany

[www.marum.de](http://www.marum.de)

and

## **Fachbereich Geowissenschaften der Universität Bremen**

Klagenfurter Strasse, 28359 Bremen, Germany

[www.geo.uni-bremen.de](http://www.geo.uni-bremen.de)

The "Berichte aus dem MARUM und dem Fachbereich Geowissenschaften der Universität Bremen" appear at irregular intervals and serve for the publication of cruise, project and technical reports arising from the scientific work by members of the publishing institutions.

### **Citation:**

Bohrmann G, Ahrlich F, Antoniou D, Behrendt N, Innocentini S, Coulibaly O, Eijsink A, Feddersen G, Gaide S, Kaul N, König T, Krahl J, Kürzinger V, Lenius S, Malnati J, Marschall L, Niederbockstruck B, Pormann S, Rau S, Römer M, Schillai S, Spiesecke U, Streuff K, Tseng Y, Vejzovic I, von Wahl T, Warnken N, Witzleb A: Fluid-rock interaction at the backstop to the Mediterranean Ridge Accretionary Complex South of Crete, R/V SONNE Cruise Report SO278, 12 October – 01 December 2020, Emden (Germany) – Emden (Germany), FRINGE. Berichte, MARUM – Zentrum für Marine Umweltwissenschaften, Fachbereich Geowissenschaften, Universität Bremen, No. 326, 208 pages. Bremen, 2021. ISSN 2195-7894.

An electronic version of this report can be downloaded from:

<http://nbn-resolving.de/urn:nbn:de:gbv:46-MARUM9>

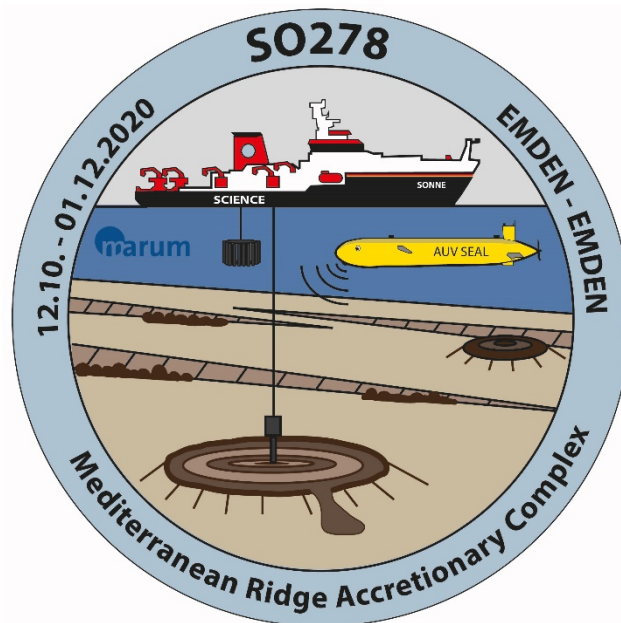
Please place requests for printed copies as well as editorial concerns with [reports@marum.de](mailto:reports@marum.de)

BERICHTE AUS DEM MARUM UND DEM FACHBEREICH GEOWISSENSCHAFTEN  
DER UNIVERSITÄT BREMEN

***Fluid-rock interaction at the backstop to the Mediterranean Ridge  
Accretionary Complex South of Crete***

R/V SONNE Cruise Report SO278

12 October – 01 December 2020  
Emden (Germany) – Emden (Germany)  
FRINGE



**AUTHORS**

Bohrmann G, Ahrlich F, Antoniou D, Behrendt N, Innocentini S,  
Coulibaly O, Eijsink A, Feddersen G, Gaide S, Kaul N, König T, Krahl J,  
Kürzinger V, Lenius S, Malnati J, Marschall L, Niederbockstruck B,  
Pormann S, Rau S, Römer M, Schillai S, Spiesecke U, Streuff K, Tseng Y,  
Vežovic I, von Wahl T, Warnken N, Witzleb A

Gerhard Bohrmann  
Universität Bremen, MARUM

## Table of Contents

1	Cruise Summary.....	1
1.1	Summary.....	1
1.2	Zusammenfassung.....	2
2	Participants.....	3
2.1	Principal Investigators.....	3
2.2	Scientific Party.....	3
2.3	Participating Institutions.....	4
3	Research Program.....	5
3.1	Description of the Work Area.....	5
3.2	Aims of the Cruise.....	9
4	Narrative of the Cruise.....	10
5	Preliminary Results.....	20
5.1	Seafloor Mapping by Multibeam.....	20
5.2	Parasound.....	24
5.3	Flare Imaging.....	28
5.4	Station Work with the AUV MARUM SEAL 5000.....	34
5.5	CTD Operations – Water Column Work.....	42
5.6	OFOS Deployments.....	45
5.7	Heat Flow Measurements.....	61
5.8	Sediment Sampling and Sedimentology.....	65
5.9	MSCL-Measurements of the Cores.....	80
5.10	Geotechnical Measurements.....	85
5.11	Pore Water Geochemistry.....	90
5.12	Gas Analysis of Sediment Cores.....	95
6	Station List SO278.....	102
7	Data and Sample Storage and Availability.....	107
8	Acknowledgements.....	107
9	References.....	107
10	Appendices.....	112
10.1	Gravity Cores: Strater Profiles and Core Photos.....	112
10.2	Minicorer/Multicorer Strater Profiles.....	184
10.3	Heat Flow Profiles.....	200
10.4	Geotechnical Measurements.....	204

# 1 Cruise Summary

## 1.1 Summary

The research cruise to the Eastern Mediterranean (GPF-18-2-40) originally planned on RV METEOR was relocated to RV SONNE (Fig. 1.2) due to the reduced number of scientists as part of the corona pandemic. The main objective of the Bremen Ocean Cluster expedition (DFG, EXC2077) was to investigate the interactions between the seabed and ocean water in Greek waters, whereby the plate tectonic constellation of a broad collision zone represents a special tectonic drive. A secondary goal was the sampling of the Sartori mud volcano, which is being processed in Italian waters as part of a separate DFG project and for which the GPF granted an additional permit for ship time (GPF 20-1\_054). The expedition began on 12 October in Emden/Germany and ended on 01 December 2020, in Emden. Investigations on mud volcanoes were carried out divided into 3 working areas (Fig. 1.1, the Sartori mud volcano in the Calabrian arc, the so-called Cobblestone Area, the Olimpi mud volcano field including the United Nation Ridge). With the MARUM AUV SEAL (Fig. 1.3) 11 dives were successfully carried out to create high-resolution detailed maps of certain seafloor structures. A total of 38 gravity cores (Fig. 1.4), 30 multicorers (Fig. 1.5) and 4 minicorers were used for sampling sediments and 6 CTD stations for sampling methane in the water column. Furthermore, 10 profiles were carried out with the heat flow lance and 5 observation profiles with the on-board OFOS. In four different provinces, 16 mud volcanoes were examined, 10 of which are characterized by pore waters that show a distinct freshening, while three mud volcanoes, Napoli, Heraklion and Gelendzhik, are characterized by very high salt concentrations. The salt accumulations in these structures are derived from the Messinian salt deposits in the subbed, from which salty brines arise through subrosion, which interact in various ways with the mud volcanoes. The study areas were selected based on preliminary surveys and morphological structures and increased backscatter patterns from multibeam mapping carried out over 3580 nautical miles in Italian and Greek waters.

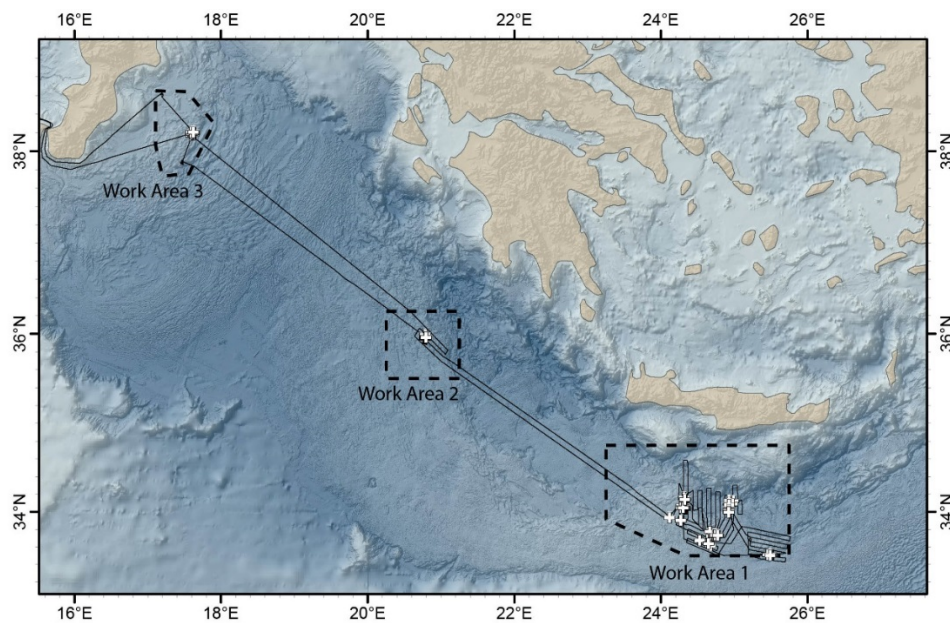


**Fig. 1.1:** Cruise track of RV SONNE SO278 in the eastern Mediterranean including three main areas of research (12 October – 01 December 2020, Emden – Emden). Work Area 1 includes the Olimpi mud volcano field and the United Nation Ridge; Work Area 2 represents the Cobblestone area and Work Area 3 in Italy includes the Sartori mud volcano.

## 1.2 Zusammenfassung

Die ursprünglich auf FS METEOR geplante Forschungsreise ins östliche Mittelmeer (GPF-18-2-40) wurde aufgrund der reduzierten Wissenschaftlerplätze im Rahmen der Corona-Pandemie-Maßnahmen auf FS SONNE (Fig. 1.2) verlegt. Hauptziel der Expedition des Bremer Ozeanclusters (DFG, EXC2077) waren Untersuchungen zu Wechselwirkungen zwischen Meeresboden und Ozeanwasser in griechischen Gewässern, wobei die plattentektonische Konstellation einer breiten Kollisionszone einen besonderen tektonischen Antrieb darstellt. Ein Nebenziel war die Beprobung des Sartori Schlammvulkans, der im Rahmen eines gesonderten DFG-Projektes in italienischen Gewässern bearbeitet wird und wozu der GPF eine zusätzliche Bewilligung von Schiffszeit (GPF 20-1\_054) erteilte. Die Expedition begann am 12. Oktober in Emden und endete am 01. Dezember 2020 in Emden. Aufgeteilt in 3 Arbeitsgebiete (Fig. 1.1, Sartori SV im Kalabrischen Bogen, Cobblestone Gebiet, Olimpi Schlammvulkanfeld mit dem United Nation Rücken) wurden Untersuchungen zu Schlammvulkanen durchgeführt. Mit dem MARUM AUV SEAL (Fig. 1.3) wurden erfolgreich 11 Tauchgänge durchgeführt zur Erstellung von hoch-auflösenden Detailkarten bestimmter Strukturen. Es wurden insgesamt 38 Schwerelotkerne (Fig. 1.4), 30 Multicorer (Fig. 1.5) und 4 Minicorer zur Beprobung von Sedimenten und 6 CTD-Stationen zur Beprobung von Methan in der Wassersäule eingesetzt. Weiterhin wurden 10 Profile mit der Wärmestromlanze und 5 Beobachtungsprofile mit dem bordeigenen OFOS durchgeführt. In vier verschiedenen Provinzen wurden 16 Schlammvulkane untersucht, von denen 10 Vulkane durch ausgesüßte Wässer charakterisiert sind, während drei Schlammvulkane, Napoli, Heraklion und Gelendzhik, durch sehr hohe Salzkonzentrationen gekennzeichnet sind. Die Salzanreicherungen in diesen Strukturen werden aus den messinischen Salzablagerungen im Untergrund abgeleitet, von denen durch Subrosion Salzlaugen entstehen, die in verschiedener Weise mit den Schlammvulkanen wechselwirken. Die Untersuchungsgebiete wurden anhand von Voruntersuchungen und von morphologischen Strukturen und erhöhten Backscattermustern der Multibeamkartierung ausgewählt, die über 3580 nautische Meilen in italienischen und griechischen Gewässern durchgeführt wurden.



**Fig. 1.2:** RV SONNE left the lock chamber to the Emden outer harbor.



**Fig. 1.3:** MARUM AUV SEAL recovery onboard RV SONNE during SO278.



**Fig. 1.4:** Gravity corer in RV SONNE's landing gear sampled by the scientists.

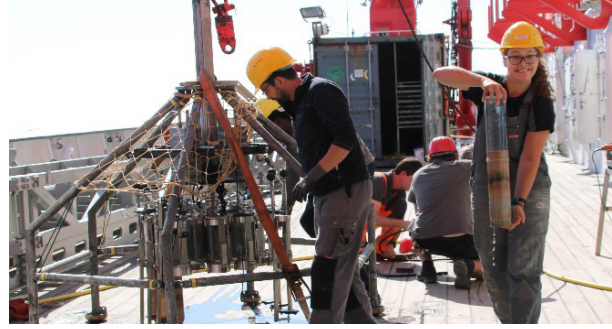


**Fig. 1.5:** Multicorer sampling on deck of the research vessel.

## 2 Participants

### 2.1 Principal Investigators

Name	Institution
Bohrmann, Gerhard, Prof.	MARUM
Kopf, Achim, Prof.	MARUM
Römer, Miriam, Dr.	MARUM

### 2.2 Scientific Party

Name	Discipline	Institution
Ahrlich, Frauke	AUV deployments	MARUM
Antoniou, Dimitra	Paleontology	OCEANUS
Behrendt, Nele	Sedimentology	MARUM
Bohrmann, Gerhard, Prof.	Marine Geology/Chief scientist	GeoB/MARUM
Innocentini, Simone	Marine geophysics	OGS
Coulibaly, Ousmane	Core technology	MARUM
Eijsink, Agathe	Sedimentology	MARUM
Feddersen, Greta	Sedimentology	GeoB/MARUM
Gaide, Stefanie	Hydro-acoustics	GeoB/MARUM
Kaul, Norbert, Dr.	Geophysics	GeoB
König, Tabea	Geochemistry	IfGB
Krahl, Julia	Sedimentology	IfGG
Kürzinger, Victoria	Geology	MARUM
Lenius, Sven	Geology	GeoB/MARUM
Malnati, Janice	Gas geochemistry	GeoB
Marschall, Lara	Hydro-acoustics	GeoB/MARUM
Niederbockstruck, Bryan	Geology	GeoB/MARUM
Pörrmann, Simon	Geochemistry	MARUM
Rau, Svenja	Geotechnics	MARUM

Römer, Miriam	Hydro-acoustics	GeoB/MARUM
Schillai, Sophia	AUV-technology	MARUM
Spiesecke, Ulli	AUV-technology	MARUM
Streff, Katharina, Dr.	Geology	GeoB
Tseng, Yiting	Oceanography	GeoB
Vejzovic, Ines	Hydro-acoustics	MARUM
Von Wahl, Till	AUV-technology	MARUM
Warnken, Niklas	Geophysics	GeoB
Witzleb, Antonia	Geochemistry	MARUM

### 2.3 Participating Institutions

- GeoB Fachbereich Geowissenschaften der Universität Bremen, Klagenfurter Straße, D-28359 Bremen, Germany, <https://www.geo.uni-bremen.de>
- IfGG Institut für Geographie und Geologie, Universität Greifswald, Germany, <https://geo.uni-greifswald.de>
- IfGB Institut für Geographie / FB 8, Universität Bremen, Universitätsboulevard 13 D 28359 Bremen, Germany, <https://www.geographie.uni-bremen.de>
- MARUM Zentrum für Marine Umweltwissenschaften, Universität Bremen, Leobener Straße, D-28359 Bremen, Germany, <http://www.marum.de>
- OCEANUS Marine Geology and Physical Oceanography Laboratory, University of Patras, 265 04 Patras, Greece, <http://www.upatras.gr/en/node/23>
- OGS Istituto Nazionale di Oceanografia e di Geofisica Sperimentale, Borgo Grotta Gigante 42/C - 34010 - Sgonico (TS), Italy, <https://www.inogs.it>



Fig. 2.1: Scientific crew onboard RV SONNE during cruise SO278.

### 3 Research Program

(G. Bohrmann)

#### 3.1 Description of the Work Area

Volatiles and fluids in subduction zones play major roles within the subduction factory. Fluids may move out of the overriding plate to the seafloor by diffusive flows or along structural conduits, or they may migrate to greater depths where they affect tectonic processes (e.g. Moore and Saffer, 2001). These fluids strongly affect the deformation style of the overriding plate. In addition, tectonic loading and mineral dehydration produce volatiles and fluids within the wedge. The resultant overpressure may have profound effects on faulting and earthquake mechanics through its influence on effective stress. Direct observations of overpressure in this setting are rare, as they require deep drilling. Submarine mud volcanoes are potential paths for migration of fluids from the underthrusting section through the accretionary prism to the seafloor. Therefore, studies of mud volcanoes hold promise in tracing the spatial distribution of overpressure within accretionary prisms.

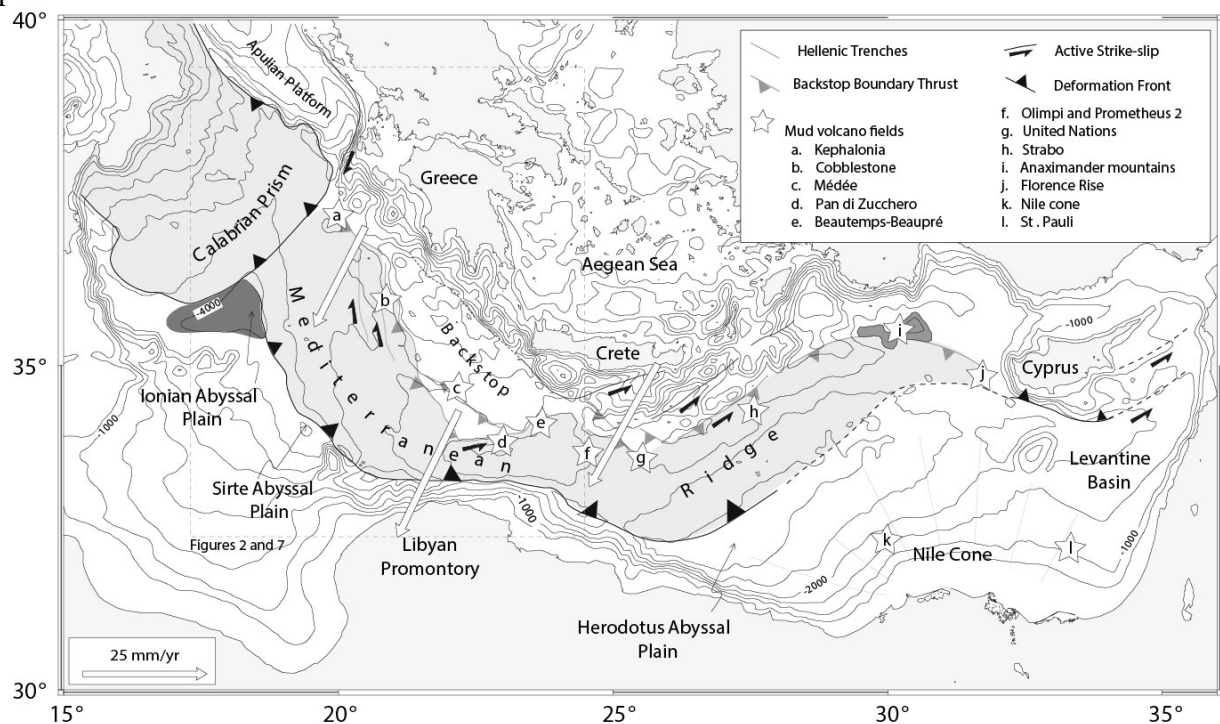


**Fig. 3.1:** Geological setting of the Eastern Mediterranean, showing the Mediterranean Ridge in contact with the Aegean backstop. Stars show specific mud volcano fields and their names used in the literature. Mud volcanoes of the Calabrian arc are not labeled (from Rabaute and Chamot-Rooke, 2007).

The eastern Mediterranean Sea is noted for its extensive field of mud volcanoes, which display many examples of various formations of mud volcanoes (e.g. Lykousis et al., 2009; Ceramicola et al., 2014; Mascle et al., 2014) and form a well-defined belt on the seafloor (Limonov et al., 1996). Mud volcanoes can be viewed as natural tectonic conduits that bring up deep materials to the seafloor and may be useful setting for exploring fluid migration processes (Kopf, 2002). Mud volcanoes are well known to occur on land (e.g. in Azerbaijan), where at least 1,000 MVs have been counted. The amount of submarine MVs is believed to be much larger and recent improvements in seafloor mapping led to the discovery of many MVs in all oceans. Specifically, in the Eastern Mediterranean Sea more than 500 MVs are known from several regions like the

Mediterranean Ridge, the Anaximander mountains and Florence rise, the Nile deep-sea fan area, and the Calabrian arc (Masclé et al., 2014). With the exception of the Nile deep sea fan, most of the mud volcanoes are related to the compressional regime of the plate boundaries between the African plate and Europe (Fig. 3.1). Studies of the cruise were concentrated on the Mediterranean Ridge south of Crete and the Calabrian arc west of Calabrian.

### The Mediterranean Ridge, tectonic elements and mud volcanoes

The main features of a N-S traverse of the Mediterranean Ridge and its backstop to the N are shown in Figure 3.2, from the North African passive margin, over a broad accretionary complex (ca. 100-120 km) and its backstop (ca. 80 km), across the forearc (Crete and adjacent islands), and the arc (e.g. Santorini), to the Aegean Sea back-arc basin. The MedRidge backstop domain is located 100-170 km behind the deformation front, and shows a northward increase in the thickness of the overriding forearc wedge/buttruss (4 - >7 km bsf). From MCS data, the intensity of deformation and compaction increase considerably at the transition from prism (ca. 100 km) to the Inner Ridge (ca. 150 km) behind the deformation front. Further north in the continental Cretan backstop, reverse, out-of-sequence thrusting is documented.

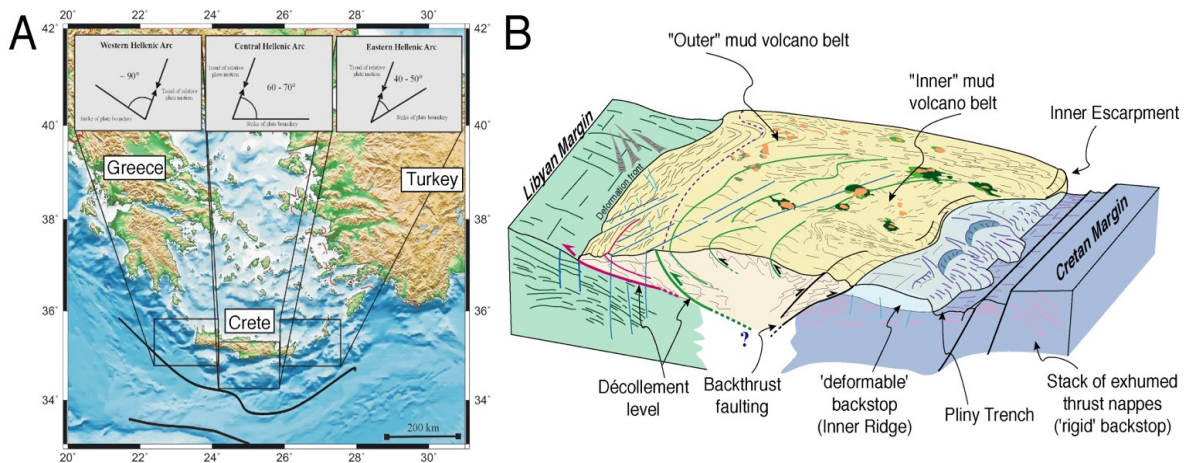


**Fig. 3.2:** a) Location map showing the Hellenic subduction zone (HSZ) in the Eastern Mediterranean, including plate convergence vector and stress regimes along strike (Robertson and Kopf, 1998). b) Schematic block diagram of the MedRidge bordered by the Lybian margin in the south (left) and the Cretan Margin in the north (right). Green and orange pie-shaped features illustrate the occurrence of mud volcanoes. Note deep-seated faults beneath the prism and backstop (Huguen et al., 2004).

The backstop of the MedRidge is located along the northern margin of a large accretionary prism created by Neogene-Recent subduction of oceanic crust of the African plate beneath the Eurasian active margin to the north (Fig. 3.2). In many accretionary complexes the imbricated wedge is backthrust over a backstop (e.g. Chile; Behrmann et al., 1992). The backthrusting is typically a response to the need to maintain a stable critical taper (Lallemand et al., 1994), and in the case of the MedRidge, this can clearly be related to collision of the more rigid backstop domain in the north with an accretionary wedge to the south (Fig. 3.2). In the Eastern Mediterranean, exhumed and uplifted Cretan continental rock initially acted as a backstop to accrete sediment. This initial wedge, the Inner Ridge, underwent compaction and was later overridden by the present accretionary prism (the MedRidge) as a result of incipient continental collision between Africa and Eurasia (Kopf et al., 2003). Hence, the Inner Ridge represents the transition from compacted accreted rock to rigid backstop material, allowing the study of incipient dewatering and diagenesis.

It is hence possible that the backstop with its deeply rooting faults as well as the landward MedRidge with the “inner belt“ MVs are very likely more significant pathways for expulsion of deep dehydration fluids than the decollement and toe of the accretionary prism (e.g. Kopf et al., 2001).

The Mediterranean Ridge is one of the areas where mud volcanism is most common globally (Masclé et al., 2014), with estimated dewatering rates exceeding that at the frontal toe of the prism. Together with the enigmatic fluid chemistry of such fluids (Deyhle and Kopf, 2001; Dählmann and De Lange, 2003), this attests a profound influence on geochemical cycling and fluid budgets in subduction zones. Over the last 10 years, the eastern branch of the Mediterranean Ridge has been heavily surveyed and sampled using side-scan sonar, seismics, submersible, coring, dredging, and in-situ fluids sampling, with a focus on several important mud fields: Olimpi, United Nations, Strabo, Anaximander, Florence Rise (see Fig. 3.1). The morphology of the mud volcanoes, their possible control by tectonic features and the mechanisms of extrusion were described (Huguen et al., 2004; Huguen et al., 2006). Extrusive activity has been shown to be episodic from ODP Leg 160 drilling (Emeis et al., 1996), and may be coupled to deep-seated processes (e.g. seismicity in the HSZ, release of brines from Messinian formations containing evaporites, etc.).

### **The Calabrian arc, tectonic framework and mud volcanoes**

The Calabrian Accretionary Prism (CAP) lies at the SE tip of the arcuate Apennine-Maghrebide subduction system, a product of rapid roll-back of a NW dipping oceanic slab over the last ca. 30 Ma (Neogene) to open back-arc basins in the western Mediterranean Sea (Malinverno and Ryan, 1986). Since ca. 10 Ma (late Miocene), slab retreat has driven the pulsed opening of back-arc basins in the Tyrrhenian Sea during migration of the accretionary system up to 380 km towards the Ionian domain (Faccenna et al., 2004). Consumption of the slab, and its fragmentation during episodes of tearing beneath bordering continental margins, has narrowed the subduction zone to a tongue of Ionian lithosphere confined between the Maltese and Apulian escarpments, descending NW into the mantle beneath the Aeolian volcanic arc (Faccenna et al., 2004). Roll-back of the subducting slab has slowed or ceased following a regional plate tectonic reorganization at ca. 0.8-0.5 Ma (Goes et al., 2004). Over the same time period, Calabria has undergone a rapid km-scale uplift, argued to be a response to mantle circulation around a slab window beneath the southern Apennines (Faccenna et al., 2011).

Above the subduction zone, the Calabrian accretionary prism is 300 km wide and extends almost 300 km from elevations of up to 1928 m in Calabria, to a frontal thrust in water depths of ca. 4000 m that intersects that of the Mediterranean Ridge. In the Ionian Sea, Rossi and Sartori (1981) showed the seaward-thinning accretionary prism, referred to as the ‘External Calabrian Arc’, to contain three main morpho-structural zones (Fig. 3.3 b), recognized in all subsequent work and corresponding to fore-arc basins and pre- and post-Messinian wedges (Praeg et al., 2009; Polonia et al., 2011). The inner fore-arc basins, up to 80 km wide, are underlain by strata up to 2 km thick that is inferred to include thin (<500 m) Messinian evaporites (Minelli and Faccenna, 2010). The pre-Messinian wedge to seaward, up to 100 km wide, is an area of irregular relief that corresponds to thrusts and back-thrusts; it is divided by the up to 750 m high Calabrian escarpment into an inner plateau and an outer area of higher gradient and relief (Ceramicola et al., 2014).

The post-Messinian wedge is up to 100 km wide and includes two main lobes (Fig. 3.3 b, d), the western with a décollement at the base of Messinian evaporites and the eastern cutting down into older strata (Polonia et al., 2011). Seismic reflection and refraction data across the external

wedge and its foreland indicate the down-going slab to comprise oceanic or highly-extended crust overlain by up to 4 km of pre-Messinian sedimentary strata, in turn overlain by thick Messinian evaporites. Seismic reflection profiles across the pre-Messinian wedge and fore-arc basins show that many seabed thrust structures record post-Messinian tectonic movements, expressed as offsets of the reflector marking the base of the Plio-Quaternary succession, the largest example being the Calabrian escarpment (Polonia et al., 2011). Mud volcanoes were first identified in the eastern Ionian Sea from cores of mud breccia from a structure on the western Mediterranean Ridge (Cita et al., 1978).

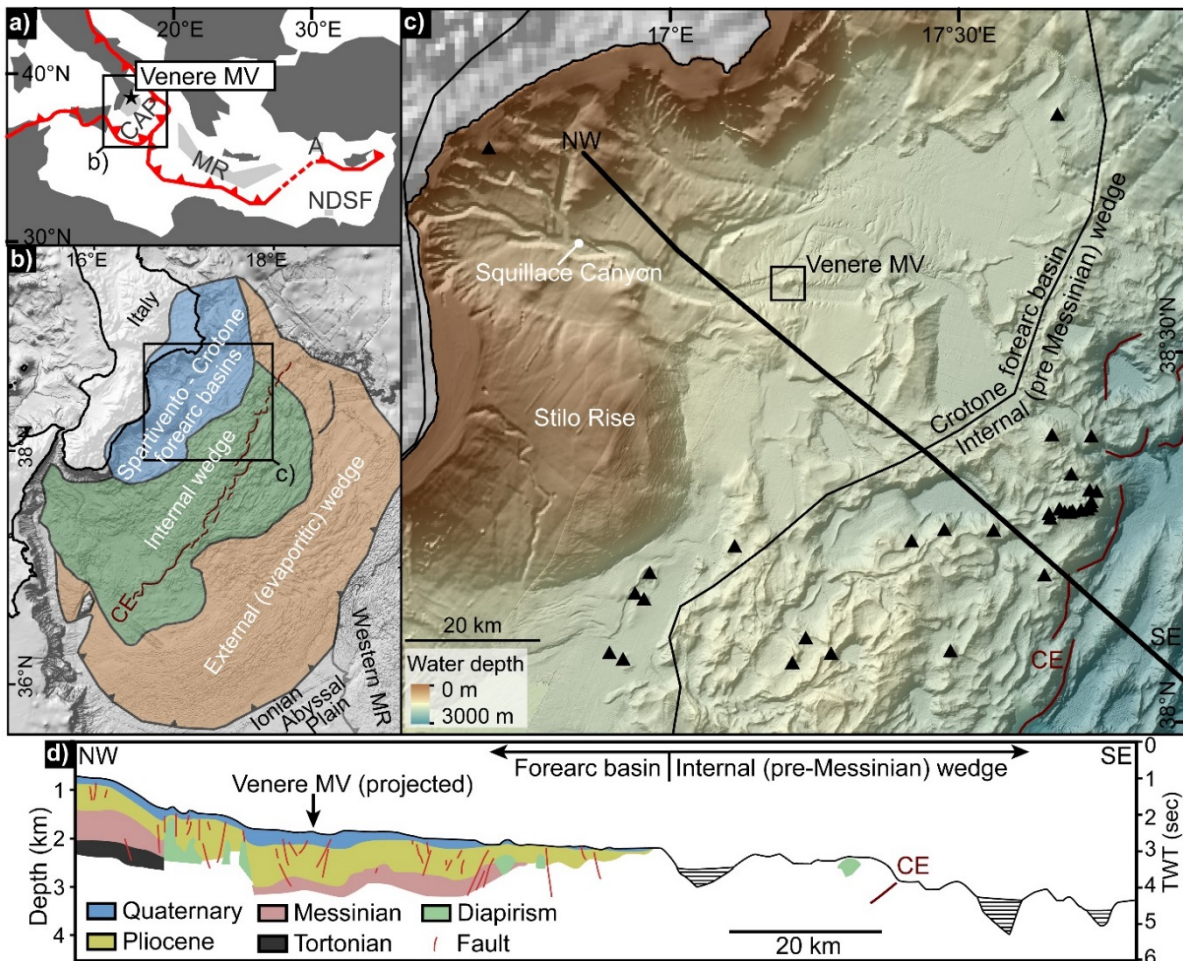


**Fig. 3.3:** Maps and geological cross section of the Calabrian arc. a): Location of Venere mud volcano (MV; star) in the Calabrian accretionary prism (CAP) relative to plate boundaries (red lines) and main MV provinces in the E Mediterranean Sea (MR = Mediterranean Ridge, A = Anaximander mountains, NDSF = Nile deep sea fan); b): Main morpho-structural zones of the CAP and boundaries; CE = Calabrian escarpment); c): Distribution of MVs (after Ceramicola et al., 2014) on the internal wedge and forearc basins (see b) for extent) including Venere MV; d) NE to SW profile across the Crotona basin showing the geological context of the study area (from Loher et al., 2018).

In contrast to the Mediterranean Ridge, until recently, little was known about mud volcanism at the CAP. In 1981, two cores containing ‘pebbly mudstones’ were recovered from a seismically unstratified body on the inner prism (subsequently identified as Sartori MV). The presence of MVs on the Calabrian accretionary prism was tentatively suggested from a few high backscatter patches observed on partial GLORIA sidescan coverage (Fusi and Kenyon, 1996). However, MVs were not proven until 2005, during a campaign of the RV OGS EXPLORA that acquired the first regional multibeam coverage of Italian waters SE of Calabria, along with cores of mud breccia

from two distinctive morphological features (Ceramicola et al., 2006), referred to as the Madonna dello Ionio MVs in the Spartivento fore-arc basin, and Pythagoras MV on the pre-Messinian wedge to seaward (Praeg et al., 2009). Recently, integration of multibeam morpho-bathymetry with backscatter data across the Calabrian accretionary prism has revealed at least 54 mud volcanoes across the fore-arc basins and pre-Messinian prism. Within the framework of several European projects, scientists from Italy, Germany, France and other countries collected over the last 10 years numerous multibeam and echosounder data from the inner and outer Calabrian arc (Gutscher et al., 2017). By combining multibeam bathymetry and backscatter imagery, integrated with sub-bottom profiles and locally proven from geological sampling, a total of 54 MVs have been identified in a sector of 35,600 km<sup>2</sup> within the Calabrian arc (Ceramicola et al., 2014). Sampling has been performed from only two MVs: the Madonna dello Ionio, and Pythagoras MV (Praeg et al., 2009). The role of the two MVs within the accretionary wedge of the Ionian Sea is rather unclear, although the presence of MVs is well known to be related to the collision zone.

### 3.2 Aims of the Cruise

The overall objectives of the proposed expedition aim to combine various disciplines to collect data on fluid flow, its geotechnical constraints (from cores and in situ measurements) and governing geochemical reactions, and PT effects to shed light on the “intermediate loop” in the subduction factory. The wider approach includes a data compilation of existing results from Hellenic subduction zone and Calabrian accretionary arc, the collection of new core and in situ data based on high-resolution micro-bathymetric maps, chemical and geotechnical analyses on the material to be recovered.

The key questions and testable hypotheses based on high-resolution mapping, sampling, in situ measurements and chemical analyses include:

- Can authigenic precipitates and/or free hydrocarbon gases provide evidence for active fluid flow or venting along fault outcrops and at the crest of the mud volcanoes?
- Are there inherited “deep” signatures, sulfate depletion or free hydrogen (i.e. the strongest electron donor) that indicate serpentinization and/or evidence for microbial activity or life at extreme depth?
- If the AUV maps enable us to identify different generations of mud flows or other evidence for episodic activity, may the youngest events be related to the 365 AD mega-earthquake?
- The permeability of surface and subsurface sediment, in particular in the shallow fault or on top of the mud dome, are sufficiently high to allow active venting.
- $\delta^{11}\text{B}$  signatures of the fluids found at the coring sites will be depleted relative to seawater because of deep-seated dehydration processes and other diagenetic reactions (see Kopf and Deyhle, 2002).
- Will other elements be mobilized, e.g. Li, Mg, Ba or K in the deep HSZ, as is indicated from the controlled hydrothermal deformation tests we carried out so far?
- Do heat flow measurements give evidence for deep-seated fluid flow, e.g. when measuring across the mud dome (see Grevemeyer et al., 2004 for comparison)?
- The aim for studies at Sartori mud volcano of the Calabrian arc are to enlarge our knowledge of the deeper accretionary prism, to understand the mud volcano evolution, and to understand the recent mud volcano activity.

## 4 Narrative of the Cruise

(G. Bohrmann)

On **Monday, 12 October 2020**, RV SONNE left its berth at the Südkai, Poller 16-20 in the Emden inland port, at 10:00 a.m. local time, to set out for the eastern Mediterranean, where marine geological studies are planned in Greece and Italy. The departure was preceded by 4 days of quarantine for all ship crew members and scientific participants, which were spent in single rooms in hotels in Leer without physical contact. Nevertheless, we stayed in contact via the internet and telephone and held a first video conference among the scientists. All participants were tested for the corona virus and after all tests were negative, the expedition was able to start. The crew and a vanguard of 3 scientists embarked on **Saturday, 10 October** on the SONNE, and the main group of scientists followed the day after. Our 6 containers with the scientific equipment had already been delivered from Bremen on **Friday, 9 October**, and had been loaded onto the ship at a place we had previously selected. After the arrival of the scientists on **Sunday morning, 11 October**, the containers were opened and most of the scientific equipment was distributed in the laboratories and on the working deck and tied down for the sea. After 4 days in the hotel almost all of us welcomed this physical work.

After a first night on the research ship in the port of Emden, it was time to cast off on **Monday, 12 October** at 10:00 a.m., and the SONNE moved away from the pier. After the SONNE had left the lock chamber, it followed the Ems estuary past the island of Borkum into the North Sea. On **Tuesday, 13 October**, the mandatory safety maneuver was carried out and that afternoon we started our daily series of lectures, which familiarize all scientists on board with the scientific topics of the voyage. The weather also played a role in the passage through the Biscay and got better and better on the journey along the Iberian Peninsula to the south. Consequently, we passed the Strait of Gibraltar into the Alboran Sea on **Saturday, 17 October** in glorious sunshine, and in the evening we were able to steam past the brightly lit METEOR at a distance of approximately 6 nautical miles.

In addition to setting up the equipment and laboratories, the transit route from Emden to the eastern Mediterranean was used to discuss the scientific program in order to be well prepared for the planned station work. The scientific crew counts 28 scientists, engineers, technicians and students from the universities of Bremen, Greifswald, Trieste and Athens. The expedition is part of the Bremen Cluster of Excellence "The Ocean Floor – Earth's Uncharted Interface" at MARUM. This region is characterized by the convergence of the Eurasian and African tectonic plates and has many characteristic elements of active fluid and mud flows. On the way to the destination south of Crete the border between Spain and Italy was crossed on **Monday, 19 October**. As it is said in the permission of the Italian authorities, recording of the hydro-acoustic systems started. On **Tuesday, 20 October**, the vessel passed Sardinia to the south on the way into the Tyrrhenian Sea. In the afternoon the vessel came through the Strait of Messina, the only up to 3 km wide strait between the Calabrian mainland and Sicily.

During the night the vessel reached the first working area in the Calabrian accretionary wedge, where the Sartori mud volcano (MV) is located. With a diameter of 1 km and a height of 45 m, the Sartori mud volcano is a striking feature that belongs to the inner Pre-Messinian accretionary wedge. The entire area of the mud volcano, including some mud flows that flowed over the rim into the neighboring basins, can be seen in the 12 kHz data of the ship's multibeam echo sounder due to increased backscatter. Moreover, a high-resolution bathymetric map acquired from an AUV

dive carried out during the METEOR expedition M112 shows this flat mud-pie structure in much greater detail. The 400 kHz multibeam data from the AUV also show two round chimneys, each 180 m in diameter, which serve as pathways for mud ascending from the subsurface, which is then extruded at the seafloor and distributed horizontally.

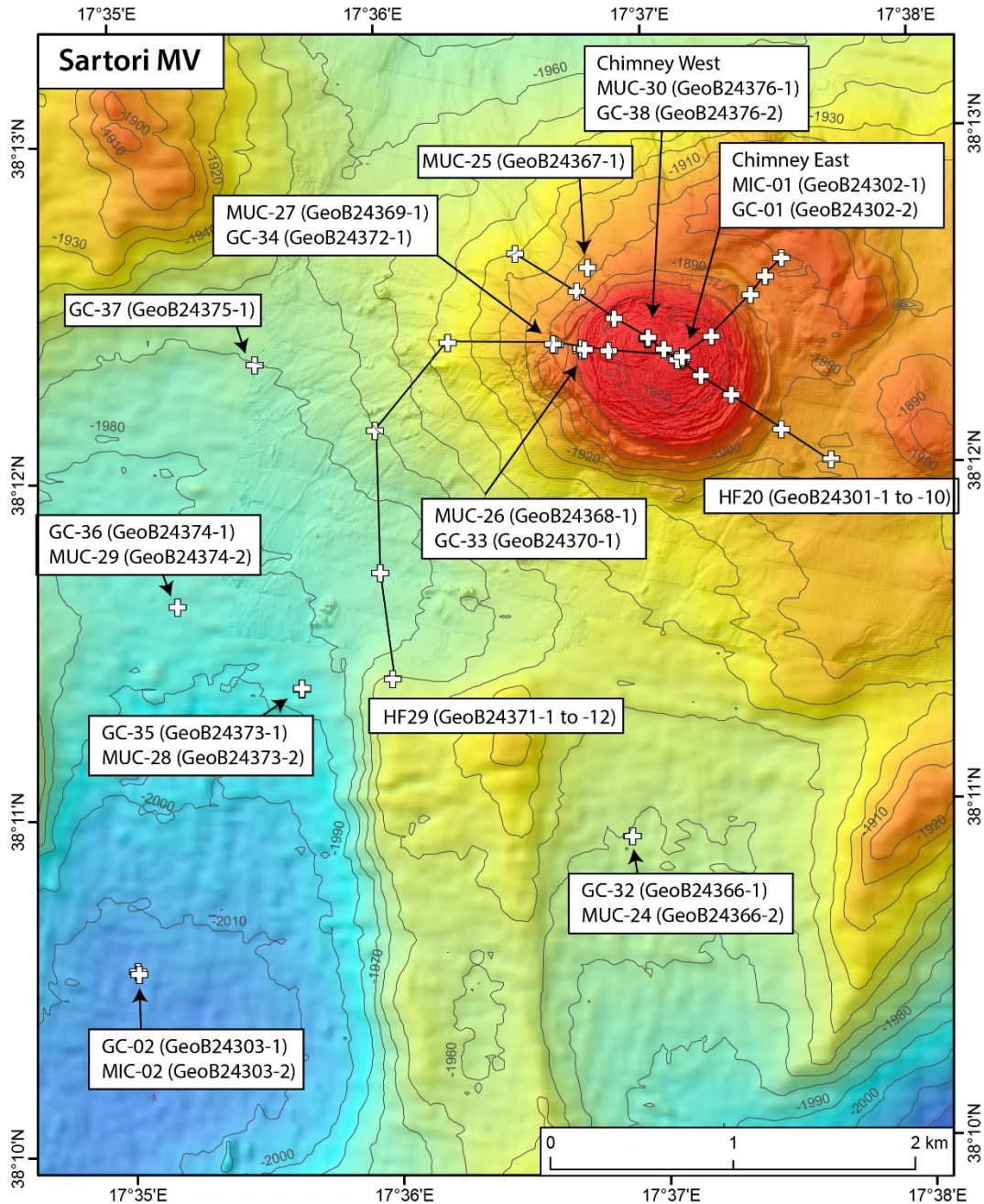


**Fig. 4.1:** Map of Sartori mud volcano of the Calabrian accretionary wedge with stations taken during SO278.

Station work started on the morning of **Wednesday, 21 October**, by taking heat flow measurements along a 10-point profile over the crater (Fig. 4.1) Using a temperature lance, a temperature-depth profile was measured at each point down to a sediment depth of 5 m. A very high heat flow could be measured in both chimneys, although the eastern chimney is characterized by a larger heat gradient and has therefore been active more recently. In the afternoon the AUV was tested for its upcoming dives and used the following night to acquire a grid of Parasound profiles over the mud volcano and its neighboring deep-sea regions. The aim was to map individual

mud flow deposits of the volcano in order to be able to assign them to individual eruption events using also the correlation with gravity cores. On **Thursday, 22 October** two gravity cores were collected and two minicores, which were subsequently processed (Fig. 4.1).

The first gravity core taken from the eastern, recently active chimney area of the Sartori mud volcano (Fig. 4.1) sampled over 2 m of mud breccia, showed a very fine-grained gray sediment with numerous clasts ranging from mm to several cm in size. The sediment had a high proportion of finely distributed gas bubbles, which, based on the dessert “mousse au chocolat”, was described by the sedimentologists as sediment with a “moussy” texture. Measurements of the gas showed mainly methane and, to a much lesser extent, ethane as the main components. Both gases, however, are already used up within the upper 20 cm due to the formation of H<sub>2</sub>S by microbial anaerobic methane oxidation. After great difficulties the geochemists eventually succeeded in extracting pore water samples with a volume of a few milliliters from the very porous mud, which are necessary to carry out important chemical analyses. In addition to the alkalinity the salt content of the samples was also determined, which decreased significantly from 39 ‰ (seawater concentration) near the seabed to 15.5 ‰ in the lower core section. The lower salinity in the deeper sediments is most likely caused by the release of relatively fresh water from mineral reactions, similar to the processes known from clay mineral transformation. Since the uppermost section of the core is influenced by seawater the conclusion was that the mud breccia emerged a long time ago, and seawater subsequently diffused into the upper core section.

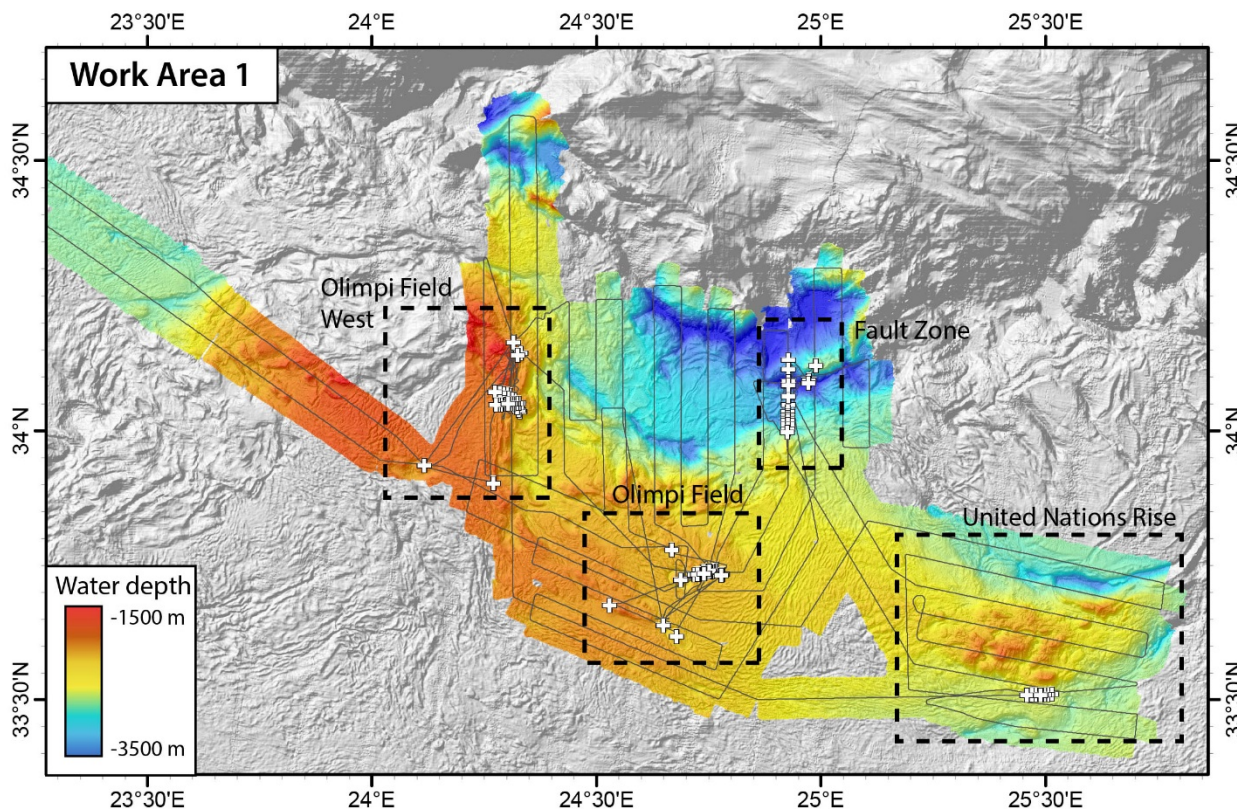


**Fig. 4.2:** Seafloor bathymetry of the Mediterranean Ridge south of Crete labeled work area 1. Four areas were visited during the SO278 cruise: The Olimpi Field, Olimpi West Field, Fault Zone and United Nations Rise.

A second sediment core was taken about 3 nautical miles southwest of the Sartori MV and yielded pelagic sediments of the past 40,000 years. The age stems from the correlation of a tephra

layer contained in the core with a dated tephra layer from other sediment cores of the area. On the evening of **22 October** the cruise continued to the next working area in Greece, where three hydro-acoustic profiles across the mud volcanoes Aros, Novorossiyks and Prometheus were gathered on **Friday, 23 October**. Unfortunately, the hydroacoustic systems did not detect any active gas emissions from these features, and as a result the vessel continued steaming to our main working area south of Crete (Fig. 4.2). Upon arrival on **Saturday, 24 October**, SONNE passed and surveyed numerous mud volcanoes from the Olimpi field (Fig. 4.3). Today, **25 October**, the MARUM AUV SEAL dove to the seabed for the first time and used its mutli-beam echo sounder to map in detail the Bergamo mud volcano (Fig. 4.3), whose activity will be further investigated in the upcoming days.

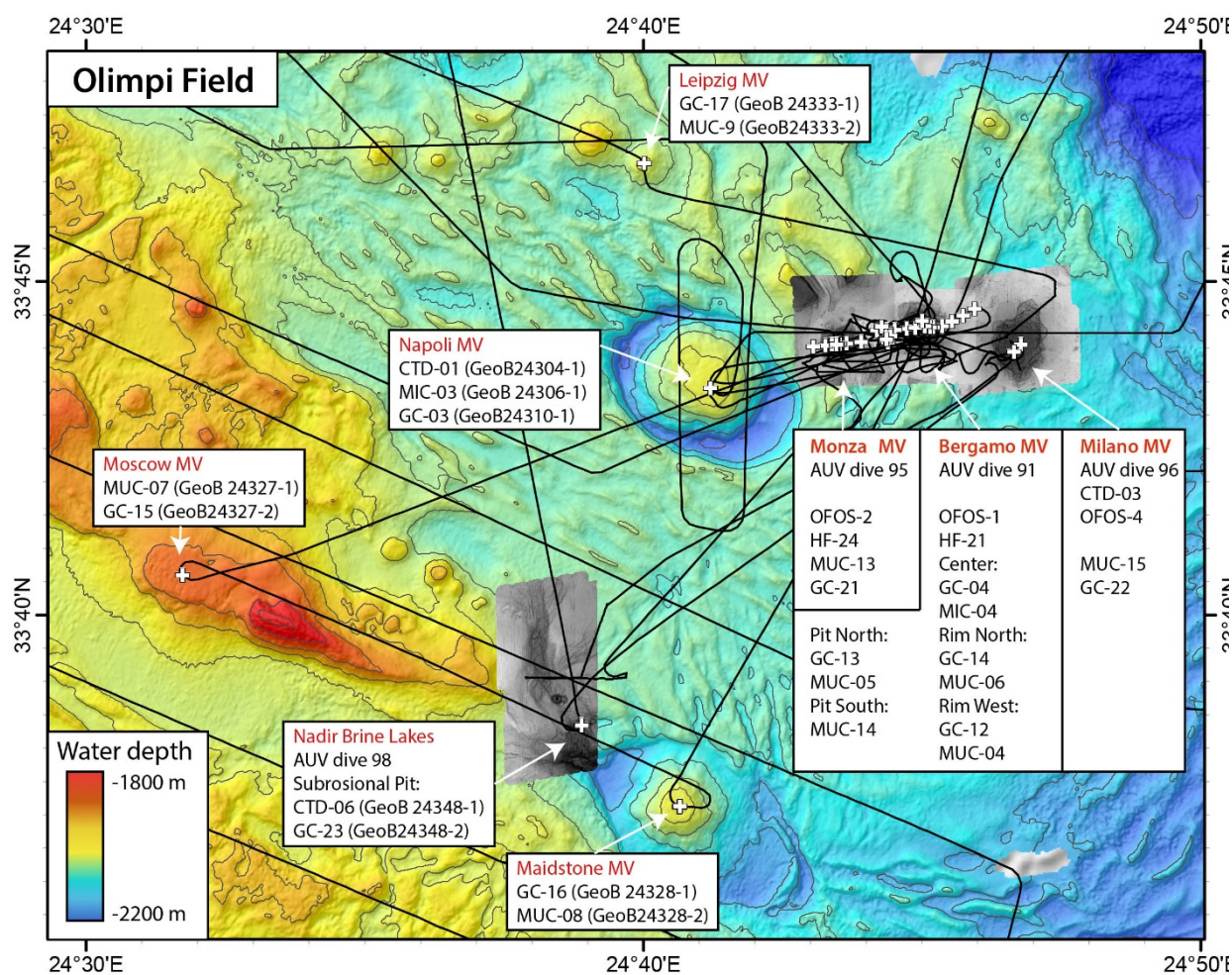


**Fig. 4.3:** Area of Olimpi Field with AUV-maps (b/w shading) and stations performed during SO278.

The first dive of the AUV (Autonomous Underwater Vehicle) SEAL 5000 on **Sunday, 25 October** was watched with excitement by everyone on board. The bathymetry group went to work immediately and converted the data into a high-resolution bathymetric map and a map of the backscatter values. All were amazed about the accuracy with which the morphological structures of the Bergamo mud volcano suddenly lay in front of the scientists and how they, of course, immediately aroused requests for sampling. First, however, an observation profile with the on-board video sled (OFOS) over the mud volcano (Fig. 4.3), which was carried out on **Monday, 26 October**, was supposed to clarify individual structures. The dive with the OFOS began on the

plateau-like central elevation of the mud volcano. Based on the flow structures two outflow areas are visible and according areas of high backscatter provide evidence for extensive eastward flow from the eastern, younger outflow area (several hundred meters). In the central area of the mud volcano typical mud breccias appeared with many clasts of solid rocks of various sizes in the OFOS video. Cracks in the mud caused by the movement of the mud flows often show gray colors, typical for reduced geochemical environments on their flanks, while the surface sediments are characterized by brownish colors common in oxygen-rich environments. Isolated tube worms and numerous shells of lucinid clams are evidence of chemosynthetic fauna that only occurs scattered about, and, hence, does not mark a center for fluid or gas outflow on the volcano.

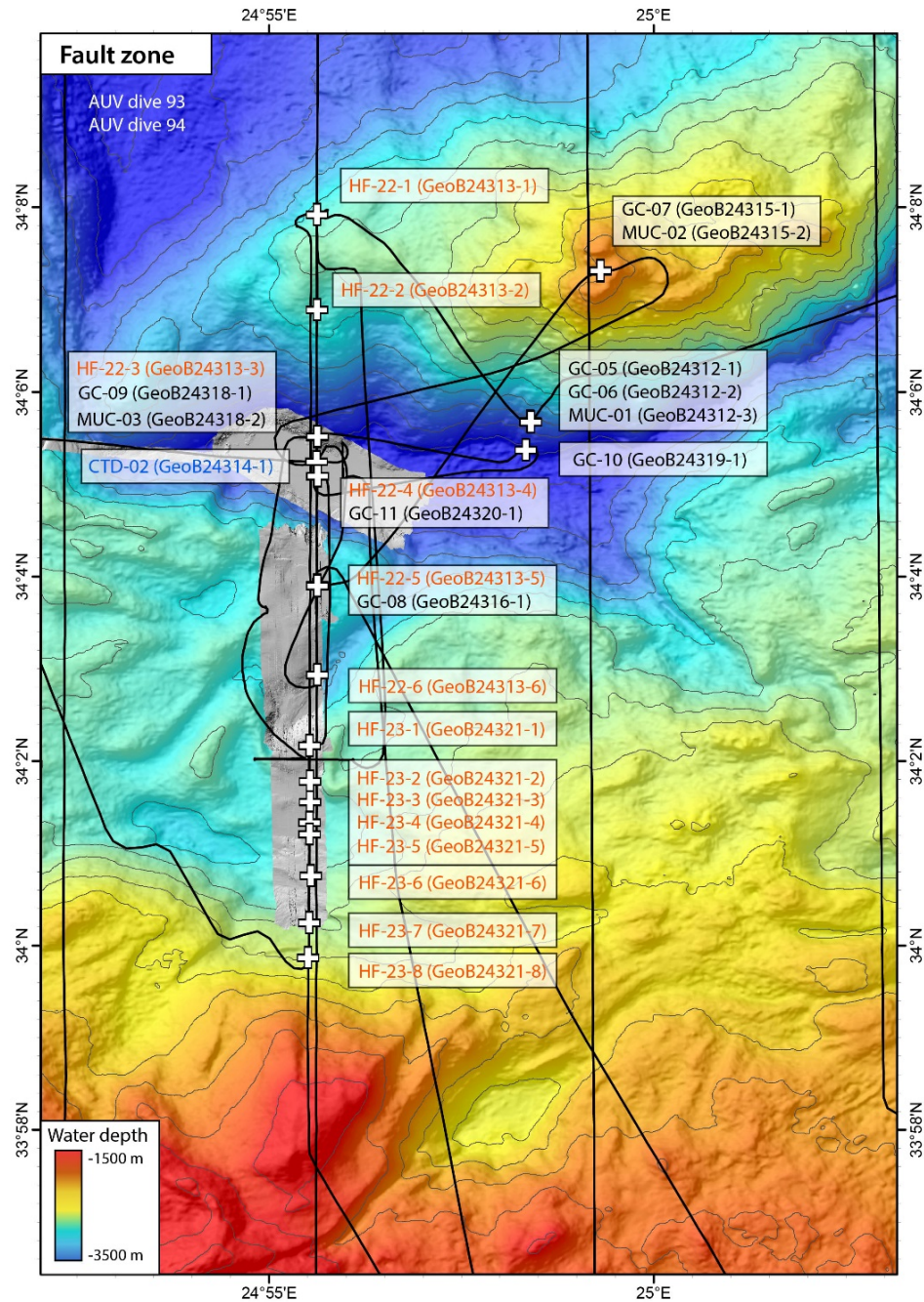


**Fig. 4.4:** Area north of Olimpi, where the continental backstop and the central Mediterranean Ridge meet each other.

Along the OFOS track, in a south-westerly direction, the western slope of the mud volcano went 80 m downhill, where several round craters with a diameter of 100-150 m and a depth of 20-40 m occurred, which appeared interesting not only because of their very low backscatter values. Extremely high backscatter values on the other hand exist around the edges of the craters and can be explained by the occurrence of strongly lithified sediments, while a selective carbonate precipitation seems to exist along traces of bioturbation. After the nightly mapping activity to the north, sediment cores were taken of the Bergamo and Napoli mud volcanoes (Fig. 4.3) on **Tuesday, 26 October**, from which primarily the pore water profiles were of interest. The Napoli mud volcano has increasing salt content with depth, which shows that the pore water is influenced by the Messinian salts occurring in the sediments below, while the pore water of the Bergamo mud volcano shows decreasing salinity to values of 10 ‰ in half a meter below seafloor, which indicates fluids from great depth.

Since **Wednesday, 28 October**, station work approximately 20 nautical miles north of the Olimpi mud volcanic field was carried out in the so-called zone of the Inner Ridge (Fig. 4.4). The Inner Ridge is laying between the actual accretionary wedge of the collision zone between Africa and Europe and the backstop of the continental margin of Crete in the north. Since Wednesday we have also carried out 2 AUV measurements and 2 heat flow profiles at specifically selected locations, and have taken 6 gravity cores and 4 multicores (Fig. 4.4). From Wednesday evening, the wind increased for the first time to Beaufort wind strengths of 6 and gusts of up to 7, with a swell from west to northwest causing waves up to 3.5 m high. As a result, an AUV dive was postponed and mapping of the region of the United Nations Rise (Fig. 4.5) became the program in the night from **Thursday, 29 October** to Friday with the ship's hydro-acoustic systems instead. On Reformation day, **Saturday, 31 October**, a profile measurement of a section along the Inner Ridge was carried out during the night with the heat flow probe, after several core stations were completed during the day. This morning, the AUV dove to a depth of 3,500 m for mapping and will only return to the ship with its measurement data shortly before it gets dark.

During the past week mud volcanoes of the Olimpi mud volcano field and the United Nations Rise were intensively investigated. In principle, mud volcanoes transport a mixture of clay, rock fragments or clasts, water and gas. Due to its low density, the mixture is not stable in deeper sediment layers. The lithostatic pressure of the overlying sediment causes the mud to rise to the surface of the earth or to the seafloor along weak areas, e.g. tectonic faults, where it forms cone-like structures, which look similar to magmatic volcanoes. Mud volcanoes are particularly common on the Mediterranean Ridge south of Crete, where the compressive stress field of the converging tectonic plates in particular promotes the rising of mud and the formation of mud volcanoes. For the Bremen Ocean Floor Cluster, the exchange of fluids and gases from the mud volcanoes with the seawater, which will be investigated with our samples, is of particular importance. The small-scale distribution plays an important role in sampling, because the exchange of fluids and gases is very different in the chimney area of a mud volcano compared to older mud flow deposits or on sediments at the edge of the volcano. Therefore, the high-resolution bathymetric maps of the AUV surveys form an essential basis for very targeted sampling, which has only been possible since AUV mapping became technologically feasible. The advantage of targeted sampling with a high spatial resolution, which is conducted using the ship's own underwater navigation, was especially evident this week, because the pore waters from the

sediment cores show very large deviations from the salinity of the seawater (39 ‰), with brines with a concentration of 200 ‰ and freshened formation waters with a concentration of 10 ‰.

The AUV was used on **Monday, 02 November** to map the Monza mud volcano (Fig. 4.3) and on **Wednesday, 04 November** on the Milano mud volcano. This mapping work was carried out during the night, with the device going into the water in the evening when it was still bright and coming out the next morning shortly after sunrise at 6:30 a.m. During the day mainly sediment core sampling and multicorer / minicorer stations were carried out for surface sediment sampling on the Bergamo, Moscow, Maidstone, Milano and Leipzig mud volcanoes (Fig. 4.3). The diverse names of the mud volcanoes show that international teams discovered mud volcanoes here as early as the 1990s and helped to shape the term “marine mud volcanism”. The Monza mud volcano was measured on **Tuesday, 03 November** with a heat flow profile and on **Wednesday, 04 November** with an OFOS observation profile of the seafloor. In this operation, the AUV map again proved itself in a great way because it allowed very targeted navigation of the OFOS. Numerous cold seeps were discovered with their typical chemosynthetic living organisms, such as tube worms, lucinid clams and bacterial mats. Even small backscatter anomalies of 5-10 m in diameter were confirmed as seep regions, so that we can apply the findings to the entire map of the mud volcano.

**Thursday, 05 November** was a special day as it was the 25th day at sea and thus marked the middle of the 50-day expedition. The time was used on the transit to the United Nations Rise for a longer mapping survey (Fig. 4.5). Although several mud volcanoes have been described from the United Nations Rise, it was decided to map the Dublin mud volcano in more detail, on the grounds of its high backscatter values in the swath mapping. Since an atmospheric low (1012 hPa) south of Cyprus slowly shifted its center south-south-west and gave a strong northerly wind current with isolated showers and a sea with swells up to 2.5 m high on Friday and Saturday, unfortunately, an AUV dive was possible neither on **Friday, 06 November**, nor on Saturday. So, after an interesting OFOS sled profile on the ground and after a sampling with the gravity corer and multicorer, the eastern work area was left and the vessel steamed back west to the Olimpi field. During a survey it was also possible to hydro-acoustically detect an escape of free gas on the sea floor in 1800 m water depth for the first time of this cruise, with gas bubbles rising to 400 m above the seafloor.

One of the objects of investigation in the western Olimpi field on the seabed was the Nice mud volcano, whose central mud outlet area we mapped with the AUV during the night from **Sunday, 8**, to **Monday, 9 November**. While most of the mud volcanoes investigated so far have more dome-like structures, the Nice mud volcano forms a flat elevation. Its mud flow deposits appear to be significantly more water-bearing and have flown in all directions from the central ascent channel. The AUV map also showed that the youngest mud flows mainly flowed towards the south, which prompted us to expand the map with an additional AUV dive carried out in the night from **Friday, 13**, to **Saturday, 14 November**. It was MARUM AUV SEAL's 100th dive (Fig. 4.6). Like in other cases, the detailed bathymetry acquired with the AUV allowed to pursue the scientific goals with further, more targeted sampling. On the Nice mud volcano, for instance, measurements of two heat flow profiles could be assigned to distinct mud flow units stacked on top of each other. Moreover, the acoustically detected and further examined gas plume located at a fault zone to the north of the Nice mud volcano was selected for sampling. The water samples that were collected at this location on **Monday, 9 November**, as part of a CTD station, showed up to 90 times higher methane levels directly above the seafloor and up to 150 m above it. An AUV

survey on **Thursday, 12 November**, was able to specify several gas seeps that were close together. Finally, an observation profile with the OFOS on Friday, 13 November, showed how the corresponding sources with chemosynthetic living organisms and authigenic carbonates are built up on the seafloor.

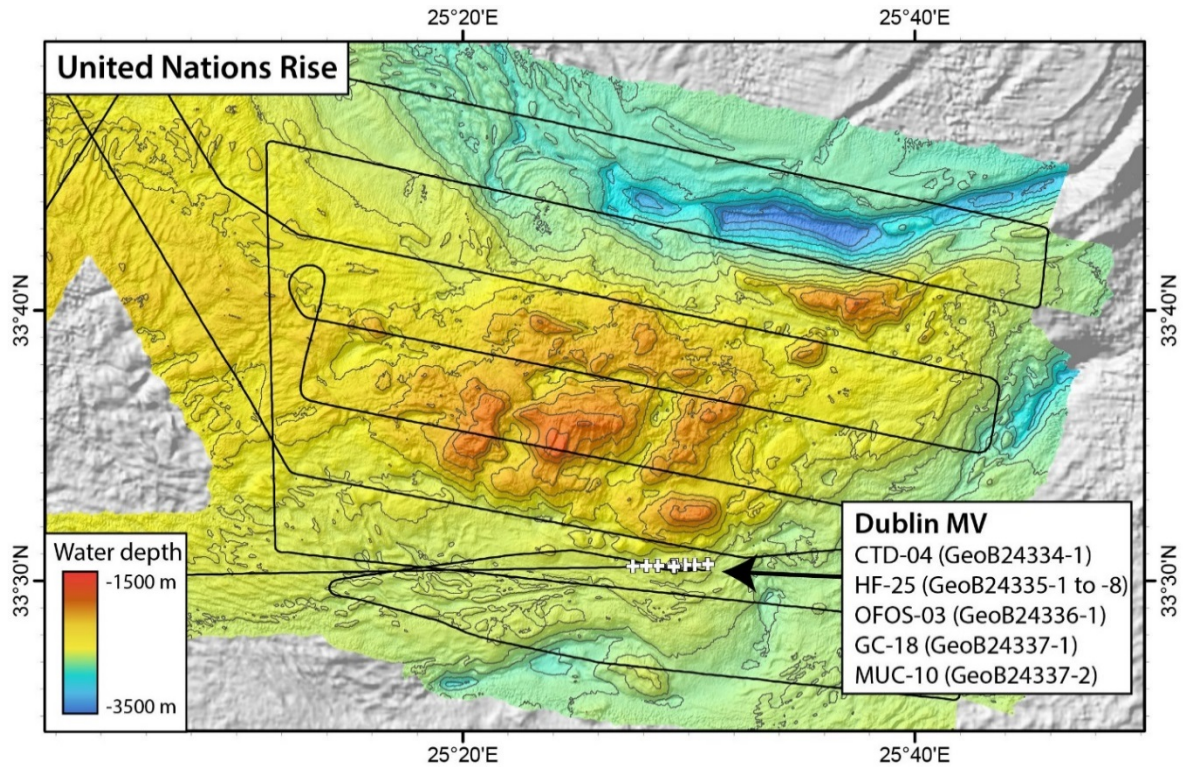


**Fig. 4.5:** Track lines of multibeam mapping and stations located to the Dublin mud volcano.

Another highlight of the week were the findings of circular depressions on the seafloor with a diameter of 50 - 400 m, which are reminiscent of sinkholes and which were observed in various places on the AUV maps. Although their origin is unclear, their genesis seems to be related to the subsidence of the Messinian salts in the subsurface. Many indications were found that they were once filled with brine. Such a pit was examined, still filled with brine, on **Wednesday, 11 November**, with a gravity corer equipped with temperature sensors (Fig. 4.3). The brine was characterized by a clearly defined halocline, below which the salt content jumped to 270 ‰ in the gravity corer and the temperature rose from 13.8°C to a constant value of 14.5°C. With increasing depth, a second sharp transition was measured to likely brine-rich waters, that caused a further temperature increase of more than 1°C. The initial methane and H<sub>2</sub>S concentrations were correspondingly high, hence the scientists carried out the analyses of this gas-rich sediment core with great caution, working in fresh air on the open deck as far as possible. Further sediment samples were taken this week on the Nice, Milano, Monza, Gelendzhik and Heraklion mud volcanoes, the processing of which often kept the scientists busy until late at night.

After the vessel left the work area south of Crete to the northwest on **Saturday evening, 14 November**, a smaller work area was reached southwest of the Peloponnese on **Sunday, 15 November**, after 20 hours of steaming. This area, located on the western Mediterranean Ridge, is also very close to the border between the accretionary wedge and the tectonic backstop and is officially referred to as the “cobblestone region” due to its morphological phenomena. Here an area of approx. 1500 km<sup>2</sup> previously was mapped with the ship's own multibeam echo-sounder on

the transit to the main working area more than 3 weeks ago. The resulting backscatter map enabled the scientists to assign values of high backscatter to known mud volcanoes from the area. One mud volcano with particularly high backscatter intensity was noticed, which, according to the literature known to us, was unnamed and had never been properly investigated. As the high backscatter seemed to indicate that it could be one of the recently active mud volcanoes, we wanted to conduct more measurements at this location. An AUV dive started by carrying from **Sunday evening, 15 November**, to Monday morning (Fig. 4.7). On **Monday, 16 November**, while waiting for the AUV data to become available, we sampled the central area of the mud volcano and a neighboring mud volcano with a gravity corer and a multicorer, with sampling locations based on the ship-acquired data. In the afternoon we were then able to use the newly acquired AUV map to plan a transect with heat flow measurements for the following night (Fig. 4.7). From the map it also became clear that the previous coring stations had not been ideal, and had missed the crater area by several meters. On **Tuesday, 17 November**, we therefore took some more gravity and multicores, using the AUV data for crater-targeted location selection. This whole process showed once again how important AUV maps are for scientifically precise sampling. During the afternoon meeting the scientists discussed the positive results and also chose the name “Helios mud volcano” for the mud volcano, which will be used in future scientific publications (Fig. 4.7).

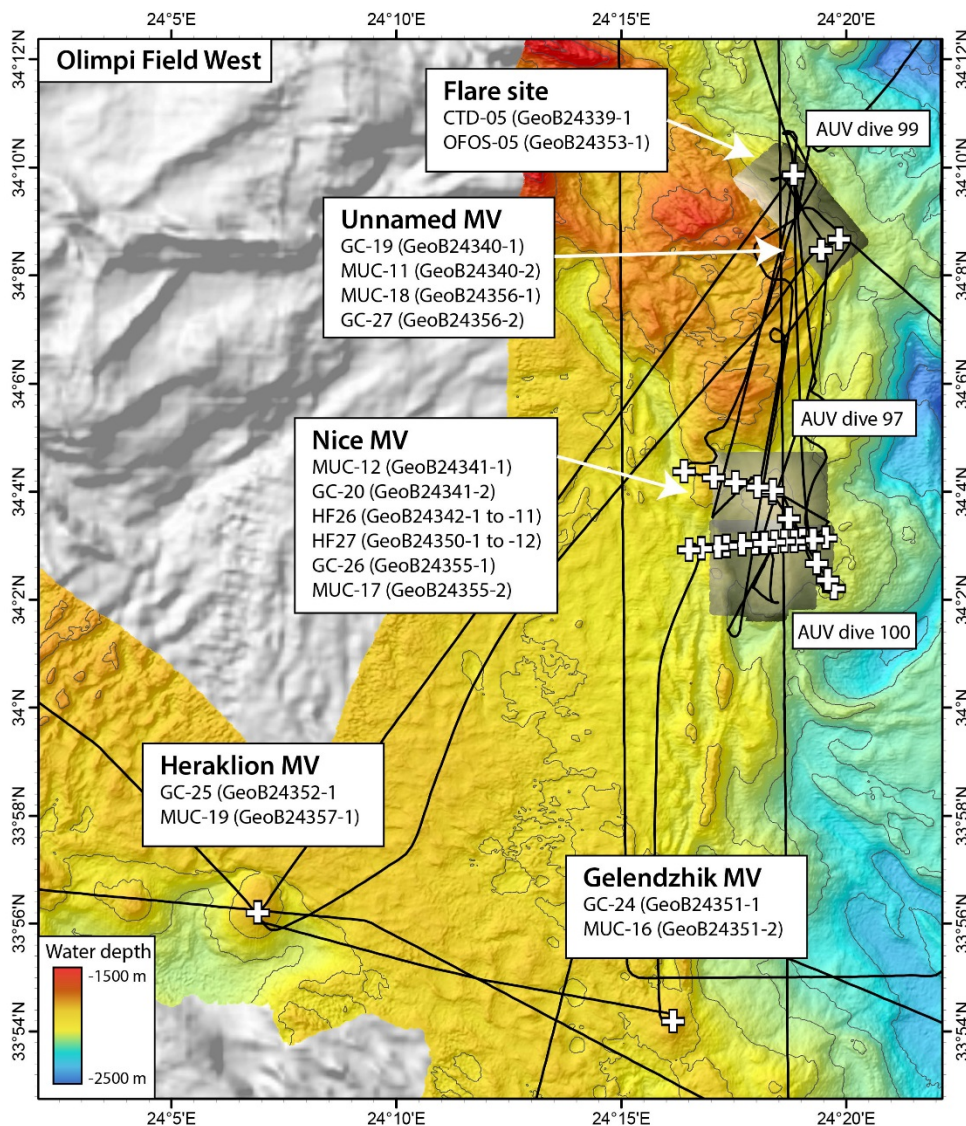


**Fig. 4.6:** Western part of the Olimpi mud volcano field with Nice and Gelendzhik mud volcanoes and sample and observation stations of SO278.

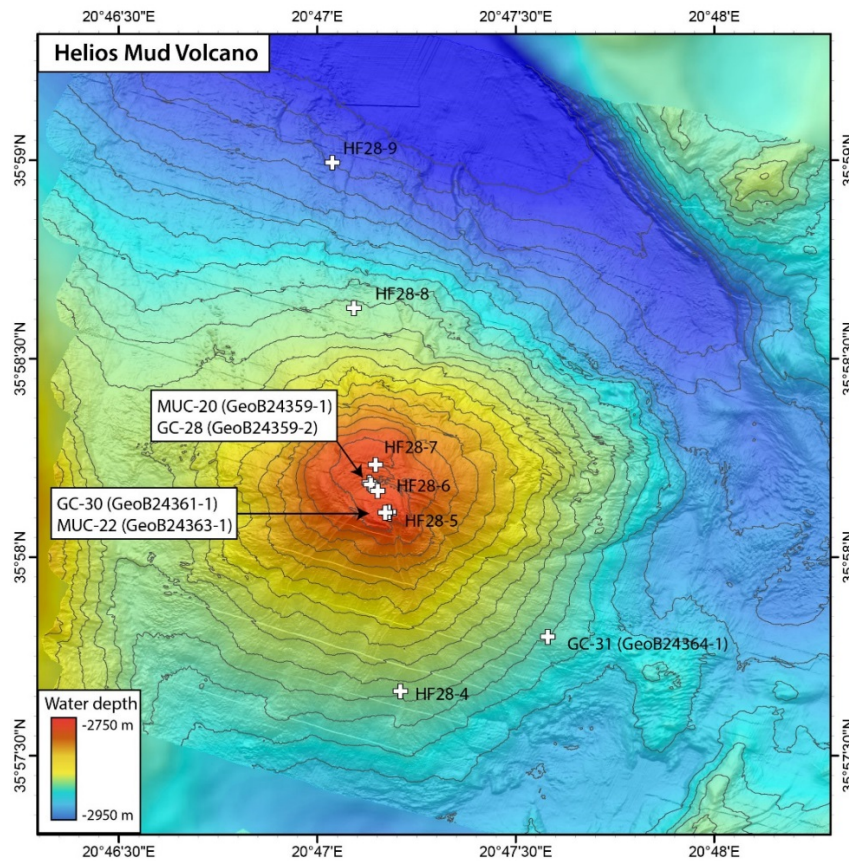


**Fig. 4.7:** AUV map from the newly named Helios mud volcano. Stations taken during SO278 were indicated.

As the pore water investigations have shown, the fluids of the Helios mud volcano have a significantly lower salinity than the seawater. On Tuesday afternoon the Cobblestone area was left and we started another transit to the Calabrian arc in Italy. There, the sampling began with gravity and multicorers in the vicinity of the Sartori mud volcano on the afternoon of **Wednesday, 18 November** (Fig. 4.1). When selecting the stations for sampling mud flow deposits of different ages, an AUV backscatter map was used which was acquired during a previous cruise, and chose sampling sites based on different backscatter intensities. This succeeded quite well, as both, hemipelagic sediments with sapropel layers and individual volcanic ash with mud flow breccias, were cored.

The age determination of the mud flow deposits will be carried out in the Bremen laboratories in the future, using radiocarbon dating (mainly  $^{14}\text{C}$ ) of carbonate grains and tephra layers in sediments which are above and below the mud flow deposits. In addition to the thus obtained sediment ages, the distribution of the magnetic susceptibility, which were already measured on board with the multisensor core logger, will be used to correlate stratigraphic horizons. The multisensor core logger is also used to measure the electrical conductivity of the sediments, which gives information on lithological parameters. On the afternoon of **Thursday, 19 November**, the station work of the cruise was stopped and carried out a short survey profile over the Venere mud volcano, with the focus on mapping previously observed flares in the water column. 6 years ago, this mud volcano was the most active, showing gas emissions of variable intensity at 5 locations on the edge of the caldera and in the center. This time, 4 of the 5 locations were active and showed acoustic anomalies in the water column. On **Friday, 20 November** the ship was already on the way back to Germany, where the vessel arrived on **Monday, 30 November** in the harbor of Emden and the scientists disembarked on **Tuesday, 01 December 2020**.

## 5 Preliminary Results

### 5.1 Seafloor Mapping by Multibeam

(M. Römer, S. Gaide, K. Streuff, I. Vejzovic, L. Marschall, V. Kürzinger, S. Innocentini)

#### Introduction

The main purpose of most of the surveys was mapping for bathymetry and searching for gas flares in the water column, often both in combination. Therefore, both hydroacoustic systems available on RV SONNE a) the multibeam KONGSBERG EM 122 and b) the parametric sub-bottom profiler ATLAS PARASOUND P70 were operating almost continuously. In addition, the split-beam echosounder SIMRAD EK60 has been used only during two surveys for specific flare imaging that could be used for gas emission quantification purposes.

Recording started with entering the Italian EEZ on 19 October 2020 and ended with leaving the Italian EEZ almost at the same position on 21 November 2020 (Table 5.1.1). A total of more than 70 GB of raw data (.all and .wcd) were acquired and 3577 miles surveyed.

**Table 5.1.1:** Overview of the data recording during SO278. Eight surveys were defined covering the transit, and the three work areas.

Survey	Area	Start	End	Duration (days)	Miles	Storage MBES Raw (GB)	Storage Parasound ASD (GB)	Storage EK60 (GB)
1	EEZ Italy	19/10/2020 07:11	21/10/2020 03:55	1.86	507	1.40	10.4 (PHF), 10.4 (SHF), 6.0 (SLF)	2.03
2	Work Area 3 (Italy)	21/10/2020 03:55	22/10/2020 17:50	1.58	54	7.87	4.3 (PHF), 4.3 (SHF), 2.5 (SLF)	
3	Work Area 2 (Cobblestone)	22/10/2020 17:50	24/10/2020 10:00	1.67	346	7.34	12.6 (PHF), 12.6 (SHF), 6.9 (SLF)	
4	Work Area 1 (South of Crete)	24/10/2020 10:00	15/11/2020 00:29	21.60	1408	39.30	119 (PHF), 119 (SHF), 64.0 (SLF)	
5	Work Area 2 (Cobblestone)	15/11/2020 00:29	17/11/2020 22:22	2.91	517	4.37	19.4 (PHF), 19.4 (SHF), 10.4 (SLF)	
6	Work Area 3 (Italy)	17/11/2020 22:22	19/11/2020 21:30	1.96	80	3.86	16.6 (PHF), 16.6 (SHF), 9.0 (SLF)	
7	Work Area 3 (Italy)	19/11/2020 21:30	20/11/2020 00:03	0.11	17	0.37	1.0 (PHF), 1.0 (SHF), 0.6 (SLF)	0.09
8	EEZ Italy	20/11/2020 00:03	21/11/2020 19:00	1.79	517	6.07	14.5 (PHF), 14.5 (SHF), 7.8 (SLF)	
<b>Total</b>		<b>19/10/2020 07:11</b>	<b>21/11/2020 19:00</b>	<b>33.49</b>	<b>3577</b>	<b>70.58</b>		<b>504</b>
								<b>2.12</b>

#### Description of the methods

During cruise SO278 seafloor maps have been primarily acquired by the multibeam echosounder (MBES) KONGSBERG EM122 installed onboard RV SONNE. Since the depths of the research area were more than 1500 meters the shallow & midwater MBES EM710 was not used. The EM122 is a deep-sea system operating with 12 kHz, at RV SONNE a configuration of 1 by 2 degrees is implemented, swath angle of up to 150 degrees and a maximum coverage of 6 times the water depth can be reached.

The EM122 multibeam sonar system was running during the whole cruise, except AUV deployment times. The weather and sea state was mostly cooperative. During surveys the ping mode was manually set by the operators according the depth range to improve the water column resolution. The maximum swath angle was set to 130 degrees (65° to both sides) to improve data quality by reducing the amount of noisy data at the outer beams and increase the ping rate. Dual swath mode could not be used during the whole cruise due to technical issues. Between the surveys, CTDs were carried out and used to calculate Sound Velocity Profiles (SVP) that were inserted in the acquisition software Seafloor Information System (SIS). The Surface Sound Velocity (SSV) was measured by the C-Keel sensor and worked flawlessly during the entire cruise. The logging of the data was set to generate a new file every 30 minutes with the water column in a separate file. The filter settings used were “Spike Filter Strength” as WEAK, “Range Gate” as SMALL, “Phase Ramp” as NORMAL, “Penetration Filter Strength” as MEDIUM. “Slope” filter

was activated, and Roll, Pitch and Yaw corrections were not active during the whole cruise. During the surveys, the EM122 failed a few times (acquisition software and/or processing unit) and had to be restarted but was otherwise operated in a stable fashion during the whole cruise.

### Technical problems

Already during the several days lasting transit to the Mediterranean, it turned out that the multibeam system EM122 had severe problems, which have been focused for the onboard working WTD. It has been detected that one of the pre-amplifier units had a general failure. In order to allow data acquisition using the system, this pre-amplifier unit has been turned off and the resolution had to be reduced to  $RX=2^\circ$ . The system worked from then on, however, we figured out that dual swath mode can also not be used as half of the swath would have gaps every second ping. The data recorded the first days of the cruise revealed therefore relatively bad quality. Although from this modification on the system worked stable and produced better bathymetric data, the water column was continuously noisy, especially in the central sectors, which clearly limited the possibility to detect water column anomalies.

### Sound velocity profiles (SVP)

Seventeen sound velocity profiles (SVP) were measured during cruise SO278 (Fig. 5.1.1). The results are essential for an accurate localization of bathymetric data. Six SVPs were calculated from CTD measurements using the software SBE Data Processing Version 7.26.1.8. Ten SVPs were extracted from the AUV deployments during the cruise. Finally, one SVP has been measured by the ships-owned sound velocity probe attached to the minicorer (Station 02-1). The measured SVPs had been applied to the Kongsberg's acquisition software SIS in order to correct multibeam echo sounder data.

The SVPs showed only slight differences in the uppermost 800 m water depth. The sound speed in waters deeper 800 m is very consistent in all work areas.

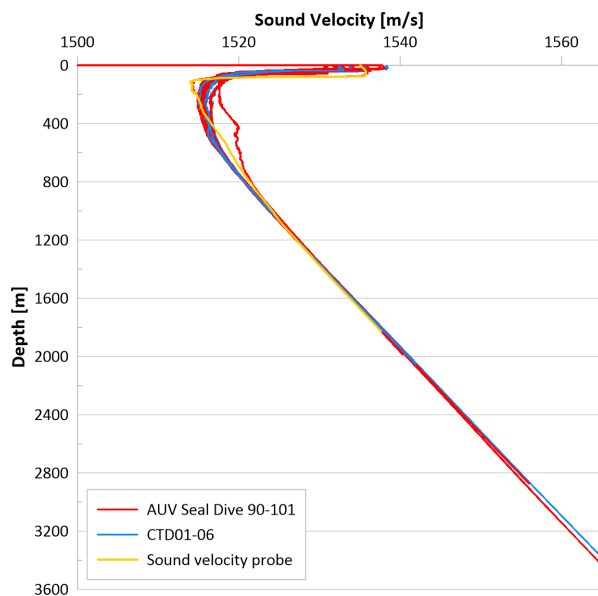


**Fig. 5.1.1:** Sound velocity profiles measured during SO278.

### Data processing

All data from SO278 was post-processed during this cruise using the open source software MB-System version 5.7.7 (Caress and Chayes, 1995). Sound velocity profiles (SVPs) were periodically

measured and inserted into the acquisition software (SIS from Kongsberg). Amplitude (backscatter) and sidescan (time series) values were corrected based on a function of grazing angle with respect to the seafloor (slope). The resulting maps are presented by Figures 5.1.2 to 5.1.6.

Generally, processing of multibeam data requires different processing steps: the check of navigation and attitude data, the application of tidal corrections, the calculation of water depth and position of the footprint of the beams by raytracing through the water-column taking into account the sound velocity profile, and data cleaning by removing artefacts and erroneous data points:

- converting the data to editable MB-format,
- applying correct SVP if needed,
- applying tide correction,
- manual editing of the dataset,
- correcting amplitude (aka backscatter) and sidescan (time series) values based on a function of grazing angle with respect to the seafloor (slope),
- applying the changes to the raw files, creating processed files,
- grid the data, using netCDF (GMT) file format.

ESRI ArcGIS vers. 10.4.1 was used to create maps and a sustainable spatial data management of the data obtained during the cruise.

### Preliminary results

Despite the technical limitations, especially in the beginning of the cruise, the resulting bathymetric grids revealed high quality seafloor data with a final resolution of 25 m grid cell size. All data has been processed und final edited until returning to harbor.

Besides the bathymetric information, also the backscatter has been calculated and grids are available for the three work areas.

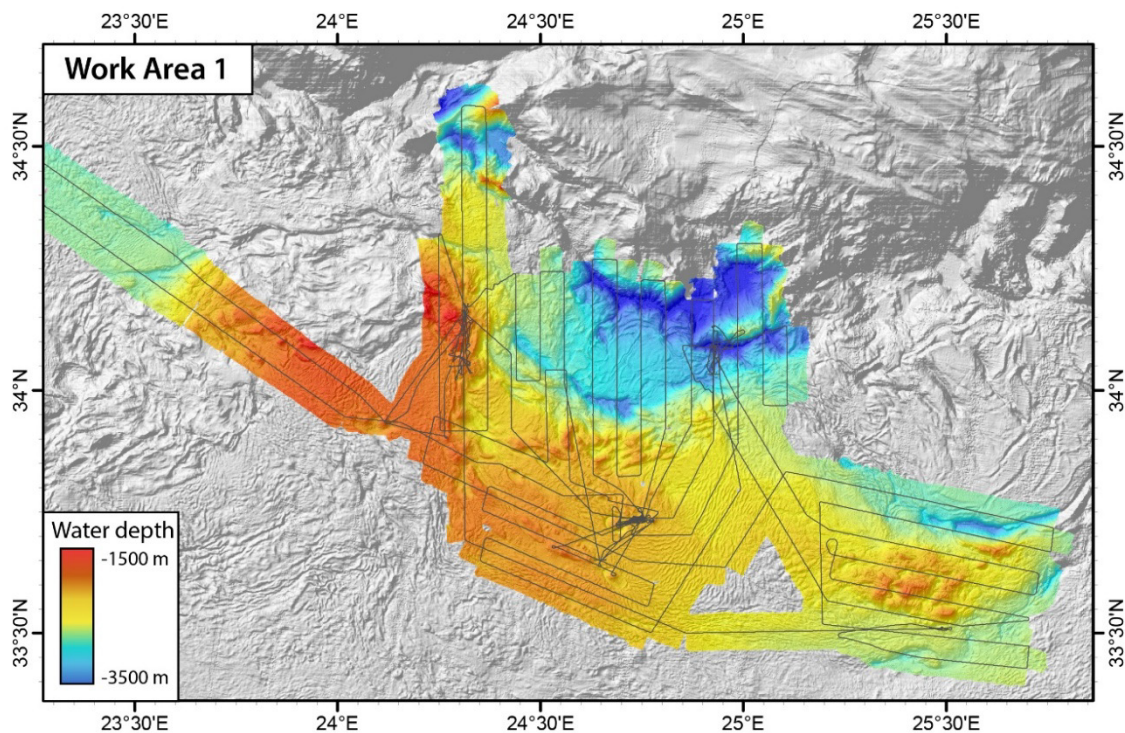


**Fig. 5.1.2:** Bathymetry grid processed and calculated in a resolution of 25 m cell size in the main work area 1 in the Greece EEZ south of Crete.

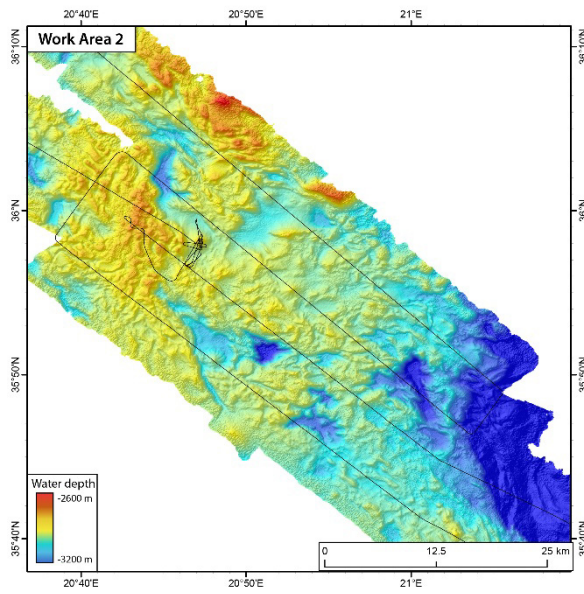


**Fig. 5.1.3:** Finally edited bathymetry grid of work area 2, called the Cobblestone area, located in the Greece EEZ.

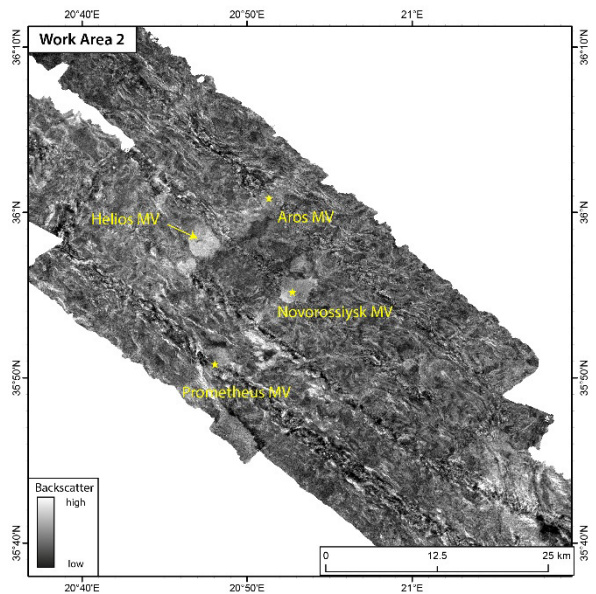


**Fig. 5.1.4:** Finally edited backscatter grid of work area 2, showing clearly the most prominent mud volcanoes as areas of high backscatter signals.

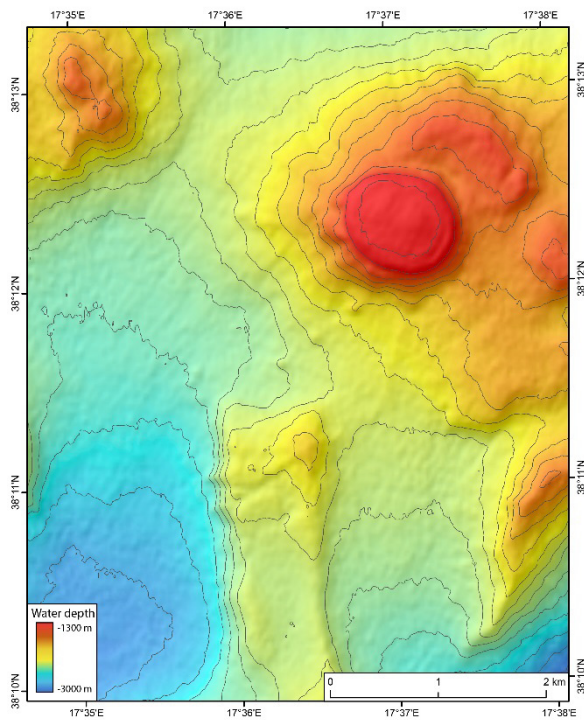


**Fig. 5.1.5:** Bathymetry grid processed and calculated in a resolution of 25 m cell size in the Italian work area 3, which concentrated on the Sartori mud volcano.

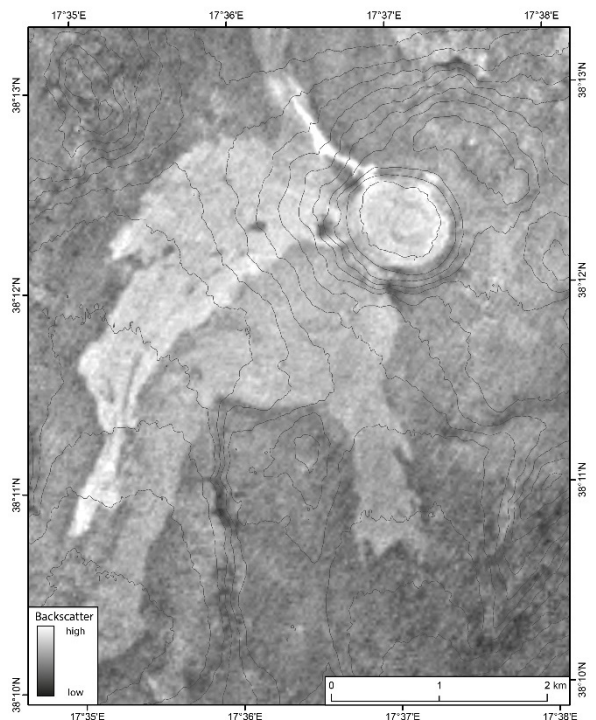


**Fig. 5.1.6:** Backscatter grid illustrating clearly different mud flow generations around the Sartori mud volcano.

## 5.2 Parasound

(K. Streuff, M. Römer, S. Gaide, I. Vejzovic, L. Marschall, V. Kürzinger, S. Innocentini)

### Introduction

Sediment echo sounders are used to gather information about the upper ~100 m of the seafloor. Like all echo sounders they use the principle of acoustic wave propagation to identify differences in material properties, such as density and sound velocity, through which lithological changes can be identified in the sediment column. RV SONNE is equipped with an ATLAS Parasound sediment echo sounder, which, compared to conventional echo sounders, offers an improved lateral and vertical resolution of sedimentary structures within the subsurface. The latter is due to the so-called parametric effect, the interaction between two simultaneously emitted sound waves of finite amplitude, which is caused through the non-linear relationship between density and pressure changes in the water column. Furthermore, when operated at a frequency of 4 kHz, the Parasound echo sounder has an opening angle of 4° compared to 20° for conventional echo sounders. As a result, the instrument interpolates across a footprint of only 7% of the water depth, which is a mere 20% of the area conventional echo sounders integrate over. Accordingly, the imaged data are more accurate and of better quality than those of other sediment echo sounders.

### Description of the methods

The software interfaces ATLAS Parastore and ATLAS Hydromap Control Center were used to control the settings of the Parasound. During cruise SO278, the Parasound echo sounder was mainly used with two different frequency signals in order to be able to resolve flares as an indication for gas bubbles in the water column (Primary High Frequency, 18-20 kHz) as well as sedimentary characteristics in the sub-bottom (Secondary Low Frequency, 22-24 kHz). In order to achieve satisfactory quality for both types of data, the echo sounder was generally set to operate in Single Pulse mode; however, on a few occasions priority was given to the imaging of the sub-seafloor sediments, and the sounder was set to operate in Quasi-Equidistant Transmission mode, which yields slightly better results. This was specifically the case around the Sartori mud volcano, where Single Pulse data were already available from previous cruises and we could use the opportunity to acquire some higher-resolution sub-bottom profiler data. Using ATLAS Parastore, the data, while being recorded, were displayed in two separate echogram windows, where settings could be modified both for the display of the PHF and for the SLF signals. The window length was usually kept at 200 m for both and the water depth adjusted when appropriate. Although not used during the cruise, the ATLAS Parastore was also set to store SHF (Secondary High Frequency) raw data.

During cruise SO278, a total of 504 GB of Parasound raw data were recorded (see Table 5.1.1). Data storage occurred as raw .asd files, which can be replayed should need be, and both, pre-processed .ps3 and .sgy files. Due to their superior quality, however, only the .ps3 files were used; they were converted into UTM-corrected amplitude .sgy files with the help of the software tool PS32SGY. The resulting output files were then imported into SMT The Kingdom Suite v. 2017 for visualisation and on-the-fly interpretation. An overview of the surveys imported into SMT The Kingdom Suite is given in Figure 5.2.1a.

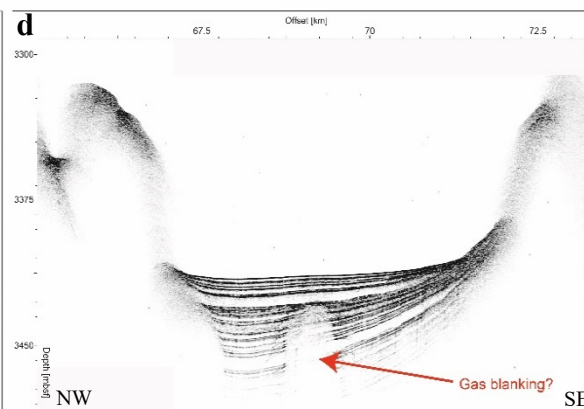
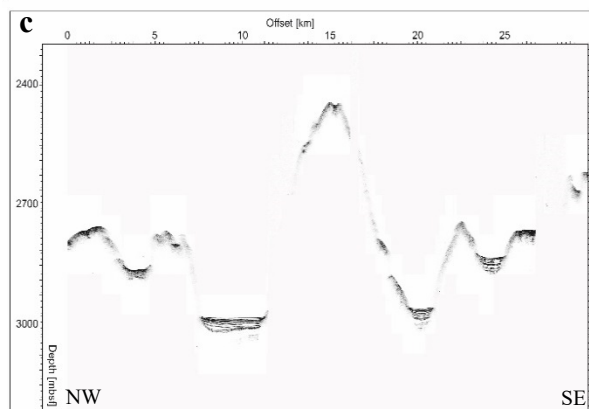
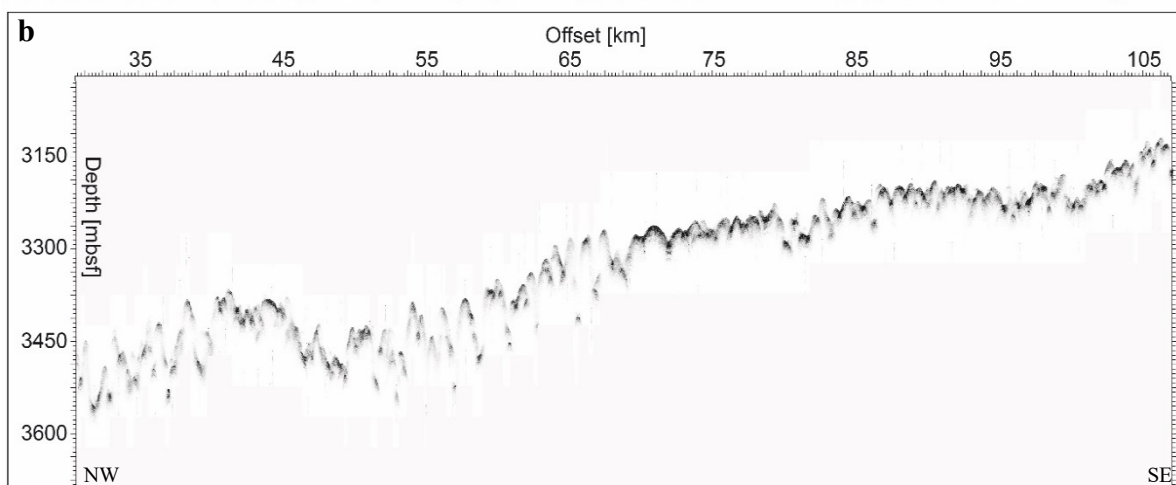
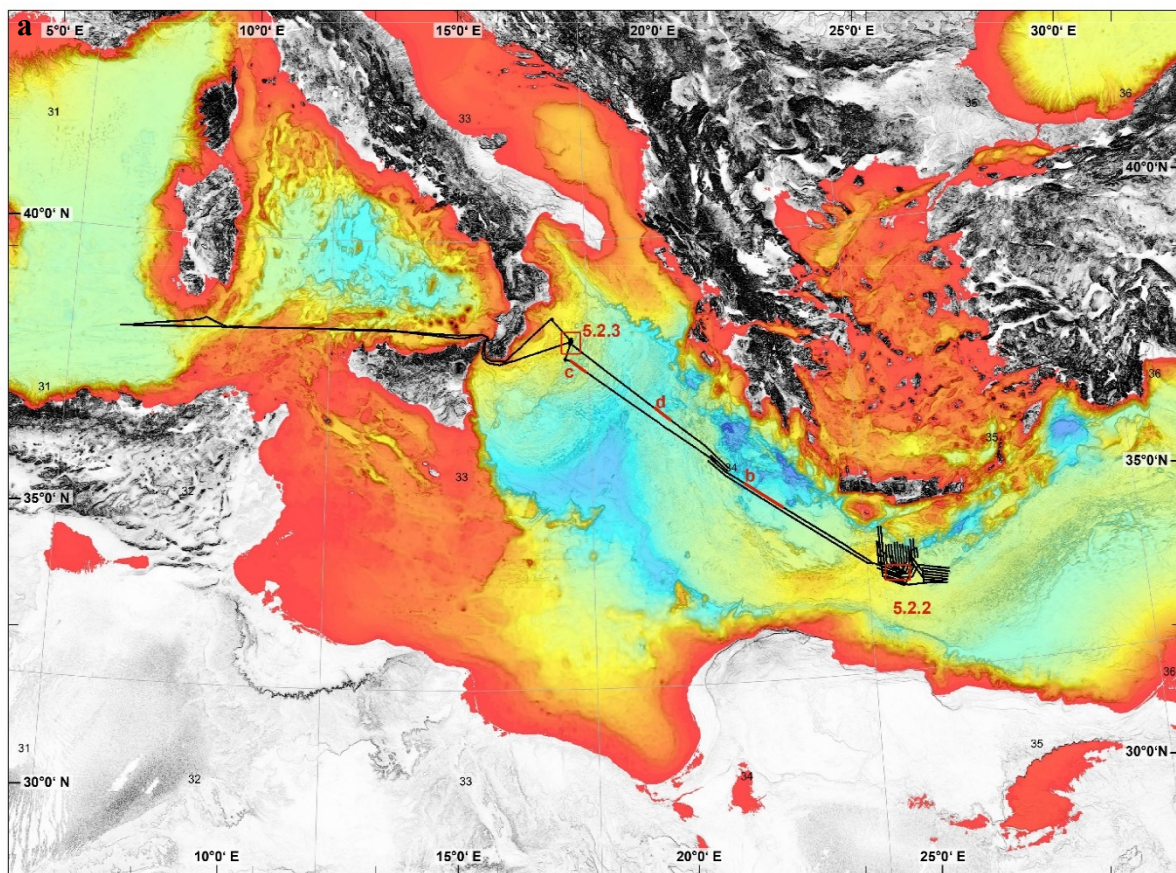


**Fig. 5.2.1:** a) Overview of the Mediterranean Sea with all Parasound lines that were loaded into SMT The Kingdom Suite. Red lines show the Parasound excerpts displayed in subfigures b), c), and d). Red boxes show locations of subsequent figures. b) Excerpt of a Parasound line from the transit between the Sartori MV and the Cobblestone area, displaying the hummocky seafloor given by compression ridges related to the fault zones. c) Example of the Parasound signal over bathymetric highs and in basins. Nicely layered thicker sediment packages can be observed in the basins, while the bathymetric highs are acoustically impenetrable and likely consist of bedrock. d) Example of one of the very few locations where signal blanking was observed in the Parasound data. This could be related to salt tectonism, the presence of gas, or it could be a buried bedrock high.

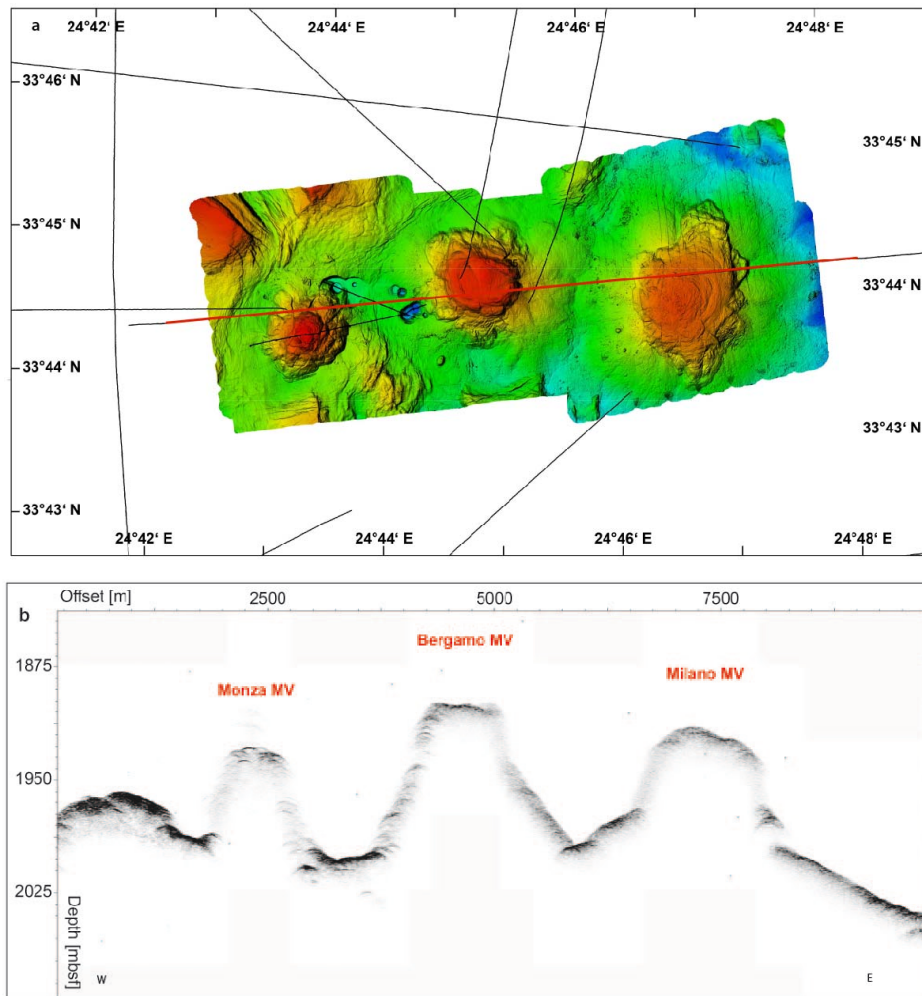


**Fig. 5.2.2:** a) Assembled AUV map of the Monza, Bergamo and Milano mud volcanoes (from East to West) and the Parasound lines recovered during the cruise. The red line indicates the line displayed in subfigure b). b) Parasound profile across the three mud volcanoes. The distinct morphological structure is clearly visible.

### Preliminary results

The seafloor of the research areas as well as the areas crossed during transits was characterized by a generally rough appearance with strong side reflections and many reflection hyperbolae. Moreover, the Mediterranean seafloor largely consists of a hard, acoustically impenetrable material interpreted to be bedrock. The Parasound signal therefore often has a somewhat distorted appearance and it was often difficult to identify individual sediment layers with increasing depth. Particularly close to the major fault zones, numerous small compression ridges give the seafloor a very hummocky appearance and are clearly visible in the Parasound data (Fig. 5.2.1b). Sediment

cover of the bedrock seemed to be relatively thin on bathymetric highs (max. 15 m); in basins, however, nicely layered sediments of up to ~70 m thickness had accumulated (Fig. 5.2.1c), a process which was likely facilitated by downslope gravitational processes.

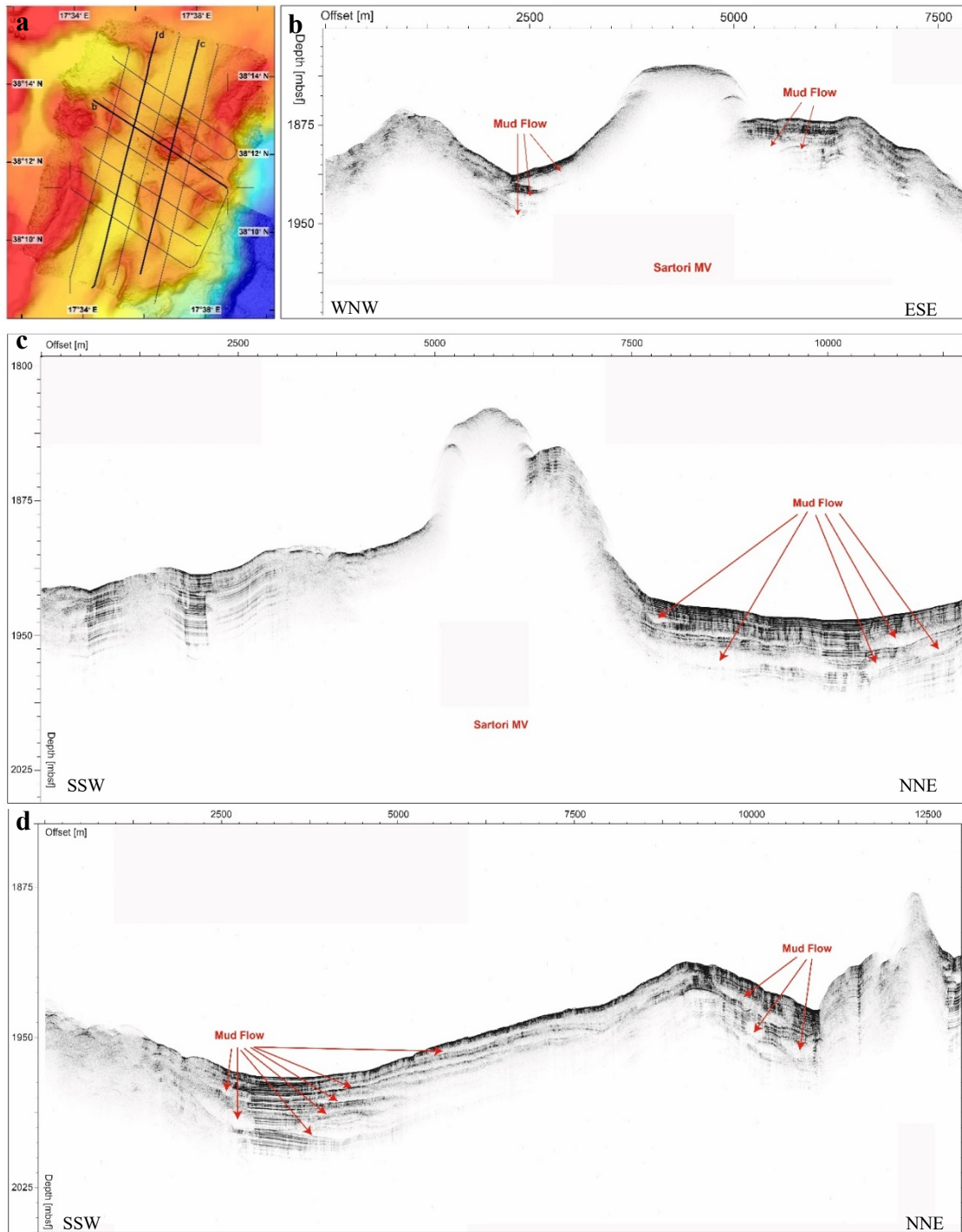


**Fig. 5.2.3:** a) Overview of the Parasound grid collected from the Sartori mud volcano. Bathymetry is partly AUV-based bathymetry acquired during a previous cruise, combined with ship bathymetry gathered during this cruise and a background of GEBCO data. Bold lines show selected Parasound profiles displayed in the subfigures. b) Cross-line from WNW to ESE, recovered from across the center of the mud volcano. Some slumps and mud flows as well as the morphology of the MV are clearly visible. c) Parasound line across the center of the MV from SSW to NNE. d) Parasound line parallel to the MV showing several generations of mud flows.

The mud volcanoes investigated were usually characterized by a distinct morphological signature with numerous strong side reflections and low signal penetration, which made it impossible to resolve the centers of the mud volcanoes in terms of sedimentary structure (Fig. 5.2.2). Nevertheless, the Parasound nicely shows their central structure, i.e. whether the mud volcano is flat-topped or cone-shaped in its center (Fig. 5.2.2). The areas around the mud volcanoes, specifically those around the Sartori mud volcano, where we acquired an extensive grid of Parasound lines (Fig. 5.2.3), consist of layered sediments intercalated with a large amount of acoustically transparent, downslope-thinning wedges (Fig. 5.2.3), which are interpreted to be mud flows of several generations, being extruded from the mud volcanoes during active times. Given the large number of mud volcanoes in the Mediterranean Sea and the ubiquitous fault structures, as well as the previous documentation of numerous flares from the areas, it is surprising that the Parasound does not indicate notable amounts of gas in the sediments and that no definitive acoustic blanking occurs. Only in a few selected locations is the Parasound signal “blanked” from depth (Fig. 5.2.1d), but it is unclear whether this is due to local salt tectonism, the occurrence of gas, or just the presence of some sediment-buried bedrock highs. Nevertheless, the apparent absence of gas could be a consequence of the sparse distribution of thicker sediment packages and, accordingly, fewer locations where the Parasound could actually penetrate into the subsurface. A further possibility is that any gas that used to be present in the subseafloor has been released into the water column and can therefore no longer be detected in the sediments. The fact, that evidence for gas emitted at the seafloor was not found frequently during this cruise (see also chapter 5.3) could corroborate this hypothesis; however, given that likely extremely large quantities of gas would have had to escape the sediments, we consider this possibility rather unlikely.

### 5.3 Flare Imaging

(M. Römer, S. Gaide, K. Streuff, I. Vejzovic, L. Marschall, V. Kürzinger, S. Innocentini)

#### Introduction

A major aim of the cruise was to investigate sites of gas bubble emissions both from mud volcanoes and fault zones. Mapping and imaging of the water column was achieved with four different techniques: a) ship-based multibeam (Kongsberg EM122), b) ship-based single-beam (Parasound) echosounders c) split-beam SIMRAD EK60, and d) AUV-mounted multibeam (Kongsberg EM2040). The water column and bathymetry data were analyzed for hydroacoustic evidence of bubble emissions (flares) of which the origins could be picked and pin-pointed on the seafloor.

For reliable flare observations a reduced ship speed of 6-8 kn is necessary. During SO278 the survey speed was mostly 8 knots, with exceptions for Sartori MV and Cetus MV which were mapped with 6 kn and the final survey at Venere MV has been conducted with only 4 knots.

#### Description of the methods and preliminary results

##### *Multibeam Flare Imaging with Kongsberg EM122*

The ship-based multibeam system EM122 MBES images and stores water column data for each ping of the swath. Compared to the single-beam Parasound the coverage is much larger and a 3D-visualisation of gas flares can be achieved. The bathymetry and water column data were recorded

in separate files (.all files for the bathymetry, .wcd files for the water column data) to avoid overly large files. In Fledermaus Midwater (© QPS) the relevant .wcd files were opened and converted into .gwc files using the “Convert Sonar Data” function. Through the use of the “geo-picking” tool of Fledermaus Midwater (© QPS) flares can be picked in the water column for each individual ping and the coordinates exported and saved as .xyz files. In a next step a pseudo-3D visualisation of the flares can be attempted. Therefore, all the exported .xyz files are merged into a single .txt file containing all the picked points. In the Fledermaus software these points were then imported and consequently displayed as small spheres hovering above the bathymetry. By extrapolation of the flares onto the seafloor in Fledermaus Midwater (© QPS) or by draping the flares onto the bathymetry in Fledermaus, source points of the flares on the seafloor can be precisely defined.

### Flare Site

During SO278, only one flare has been detected in the water column data of the EM122. It cannot be excluded that flares were not visible due to the technical problems the system had during the entire cruise. Most of the mud volcanoes were passed in its central part, which was generally the noisiest area of the swath and flares might not have been recognizable. Also, surveys were not designed for full water column coverage but planned for bathymetric mapping, which means that not the entire work areas were checked for the presence of flares.

However, the flare detected was clearly recognized as produced by gas bubble emission and has been verified by passing centrally in the Parasound PHF signal. The flare rose about 400 m into the water column (Fig. 5.3.1) and was slightly deflected towards SSE. The area was named “Flare Site” and has been investigated by OFOS and sampled with the CTD. An AUV dive was also surveying this area and provided further details about the gas emissions.

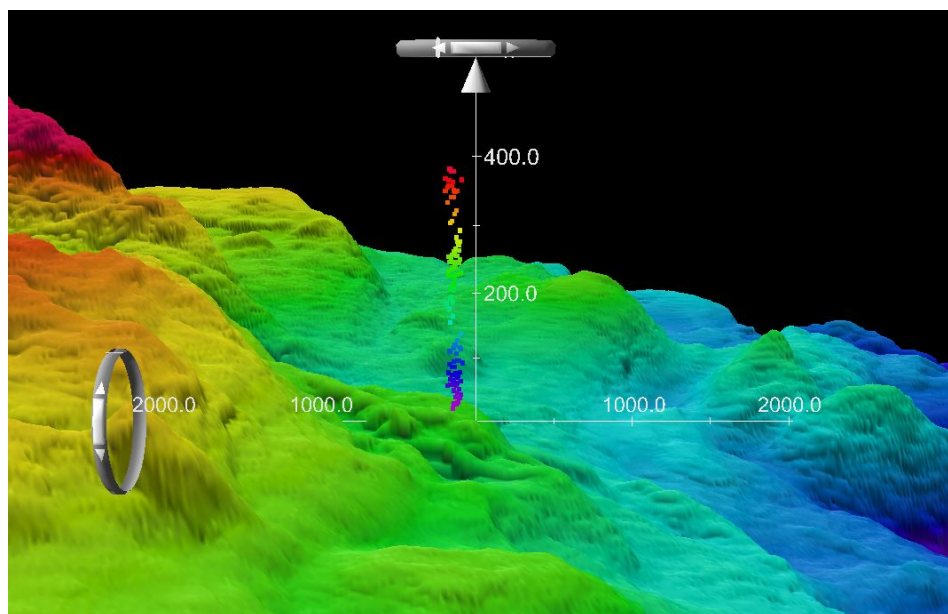


**Fig. 5.3.1:** Flare extracted from the multibeam water column data plotted above the ship based bathymetry.

### Flares at Venere MV

A circular designed survey (“Schneckensurvey”) has been repeated that was surveyed several times during RV METEOR cruise M112 in 2014. The purpose was to see whether flares detected during this former cruise around and at this mud volcano would still show gas emission activity

or not. However, as all flares were passed in its central part and our water column swath view was strongly limited especially in its central sectors, the flares could not be recognized in this system. Nevertheless, the Parasound echogram did reveal the activity of 4 out of 5 known flare sites.

#### Nadir brine lakes

AUV water column data revealed the presence of flares in the area of the Nadir Brine Lakes. Although special attention was paid while passing these sites with the vessel as well, no flares were recorded in both running ship-based systems (multibeam and Parasound). The reason could be the size of the released bubbles. If bubbles are very small and released from >2000 m water depth, the systems operating with a frequency of 12 – 20 kHz are not capable of distinguishing these from background noise (Fig. 5.3.2).

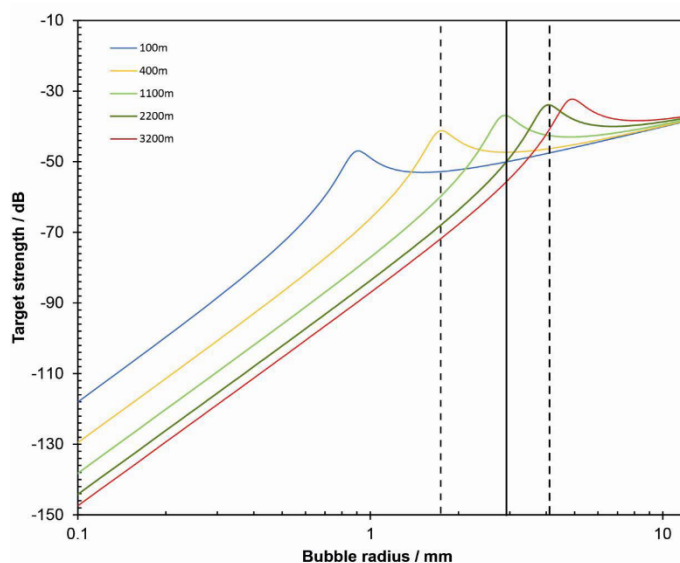


**Fig. 5.3.2:** Relation between bubble size and target strength depending on water depth for the 12 kHz multibeam system. Bubbles released in <2000 m water depth should have a radius larger 2 mm to be clearly visualized in the echogram.

#### Single-beam Flare Imaging with Parasound

In the past, the 19 kHz signal (PHF) of the ATLAS Parasound has proven to be an efficient tool for the detection of flare activity. With a footprint of ~7% of the water column, the ATLAS Parasound imaged flares, which were crossed in the central beam of the echosounder. The system was running in single pulse mode for this purpose during most of the cruise (see also chapter 5.2).

During gravity coring the ATLAS Parasound kept recording in order to observe the potential bubble release, which would have been caused by the penetration into gas rich layers or gas hydrate. Unfortunately, this effect was never observed throughout SO278.

Flares imaged in PHF echograms were only retrieved from the “Flare site” (Fig. 5.3.3) and at Venere MV (Fig. 5.3.4). The “Flare Site” has been mapped subsequently with the AUV revealing at least 9 gas bubble emission sites sourcing in an area of only 30 m. Such a high resolution cannot be achieved with the Parasound system, as the footprint does not allow distinguishing bubble streams in such a small area. But in contrast to the AUV derived data, the height of the flare as well as its deflection while rising through the water column can be described. The flare was about 400 m high and deflected in SSE direction (Fig. 5.3.3). The flare at Venere MV was imaged while running the “Schneckensurvey”. Unfortunately, the track was sometimes not exactly followed and already a deviance of few tens of meters resulted in missing the flare in the PHF echogram. Flare 4, south of Venere MV, has been nevertheless imaged, not in its most central part, but became

visible (Fig. 5.3.4). Three further passed flares were also found to be active using the EK60 echosounder, however not exactly enough to become visible in the PHF echogram.

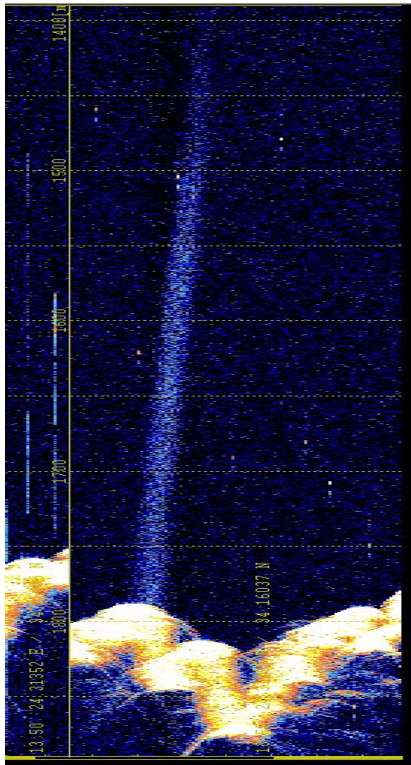


**Fig. 5.3.3:** Hydroacoustic evidence for gas bubbles in the water column at the “Flare Site” as seen in the ATLAS Parasound. The flare has been passed at its central part and is visible from the seafloor in about 1800 m to 1400 m water depth illustrating rising gas bubbles over at least 400 m height.

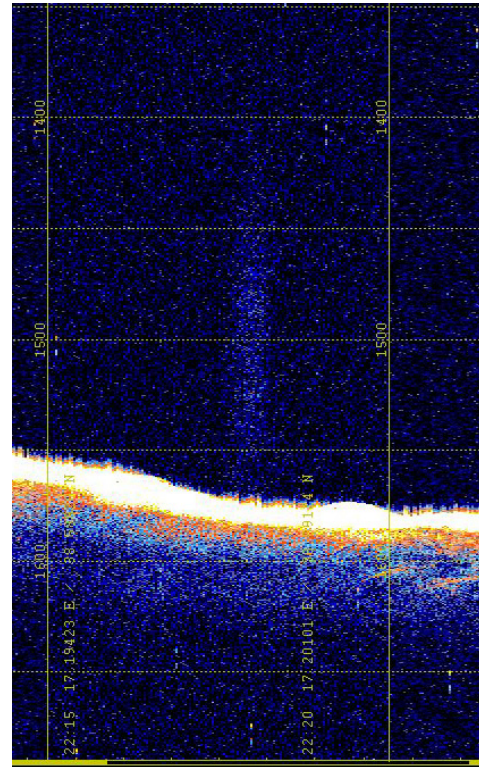


**Fig. 5.3.4:** Flare recorded at Venere MV. The flare has been passed few tens of meters south of its source at the seafloor limiting its appearance in the single beam echosounder. However, flare height is at least 150 m.

#### *Split-beam Flare Imaging with EK60*

The split-beam echosounder EK60 has not been used continuously. It was pinging and recording during survey 1 (transit through the Italian EEZ until our first work area) for testing purposes, whereas two frequencies (18 and 38 kHz) were working. The purpose of using the system was not the detection of gas emissions but allowing to quantify gas emission after its detection. It is also not optimal to use in water depths >2000 m. Therefore, it was not possible to image the flare at the “Flare Site” as only the 38 kHz was available at this time and the water depth too deep. However, the frequency was useful when running the “Schneckensurvey” at Venere MV, during which 4 of the 5 known flares could be proven to be still actively releasing gas bubbles. Flares 4, 5, 2, and 3 were imaged with the EK60, whereas Flare 1 was clearly inactive even though we passed it a second time before leaving the area to prove that the ship was not only slightly aside the track. Only Flare 4 was passed relatively exactly in its center, so that a flare of about 150 to 200 m height could be imaged (Fig. 5.3.5). Flares 5, 2, and 3 were seen only with less intensity close to the seafloor not forming linear features. The latter flare, however, has never been very high also when passing it several times centrally during M112.

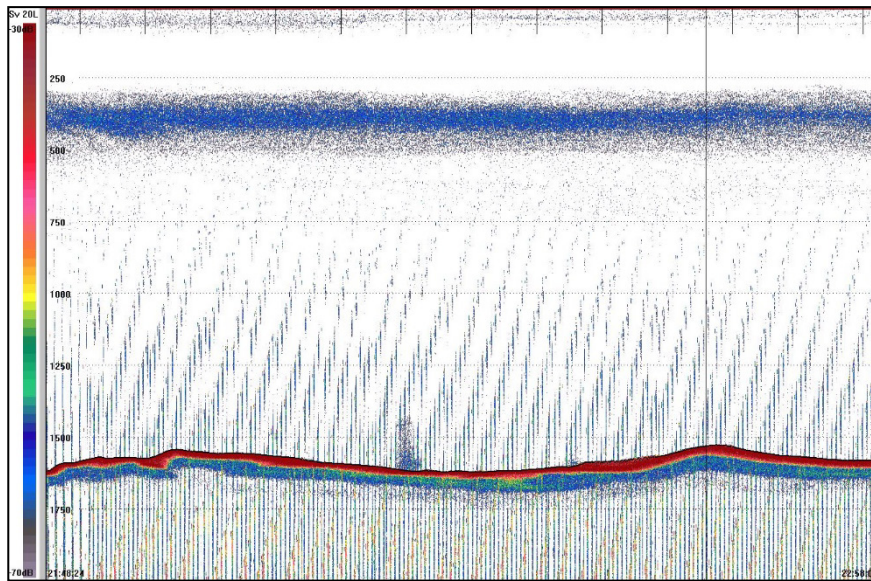


**Fig. 5.3.5:** Screenshot of the EK60 Echogramm using the 38 kHz frequency while running the “Schneckensurvey” around and at Venere MV in the Italian work area. Flare 4 was the most clearly visible flare, which could be proven to still actively release gas bubbles.

#### *AUV-based Flare Imaging with EM2040*

The multibeam data recorded with the AUV-mounted MBES Kongsberg EM2040 (400 kHz) could be used to detect and locate gas flares with a high accuracy. Ten AUV dives were conducted during SO278, which resulted in the coverage of several mud volcanoes, fault zones, brine pools, and the “Flare Site”. Similar to the ship-based multibeam water column data, the .wcd files were opened in Fledermaus Midwater, converted to .gwc and replayed either swath by swath or in the stacked view, allowing the detection of flares. Water column recording was carried out during all AUV dives. The flares were manually picked in the water column and the points exported from Fledermaus Midwater. In Fledermaus these points could then be displayed in 3D and the source points on the seafloor could be estimated. Due to navigation corrections, the positions need to be shifted according to the bathymetric data after post-processing.

#### **Results from AUV Dive 98 at the Nadir brine lakes**

Flares were not expected to be detected in this area, as ship-based echosounder records did not indicate any gas emission activity. Therefore, we had been very surprised to find even several flares in the water column records of this AUV dive. The flares are relatively weak and do often not reach the height of the AUV, which supports the hypothesis that gas bubbles are very small and dissolve rapidly. And this would explain that they are not visible in the ship-based echograms.

Flares are concentrated at two clearly visible subrosional pits, one of it should be the Nadir brine lakes, the other a probably so far unknown brine lake. Subsequent sampling with CTD and GC has proven the existence of a brine lake in this latter pit and elevated methane concentrations supports the presence of methane escape through bubbles at this site. The sampling was focused on the center of the pit, where flares were seen to be sourced (Figs. 5.3.6 and 5.3.7) reaching the height of the AUV (~ 80 m). One more flare was found spatially unrelated to a subrosional pit (Fig. 5.3.8), however, high-backscatter patches in this area could indicate a seep environment (Fig. 5.3.9).

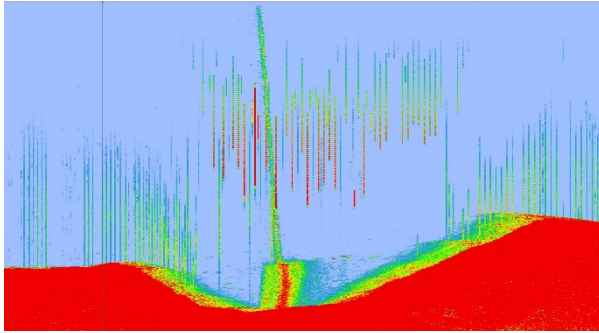


**Fig. 5.3.6:** Stacked view of the water column data retrieved from AUV dive 98 passing a subsional pit with active gas escape. The flare in its center is strongly amplified within the brine filling up the pit.

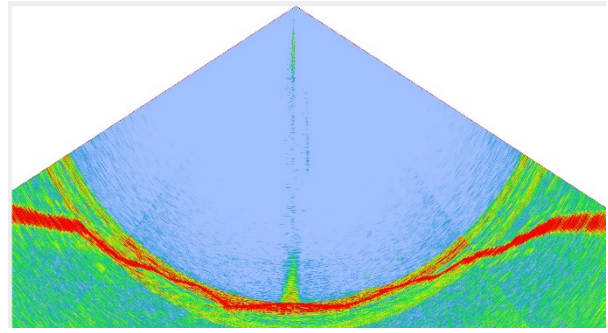


**Fig. 5.3.7:** Swath view of the flare located in the central part of the brine pool. The flare reaches the AUV, however is not very strong in intensity.

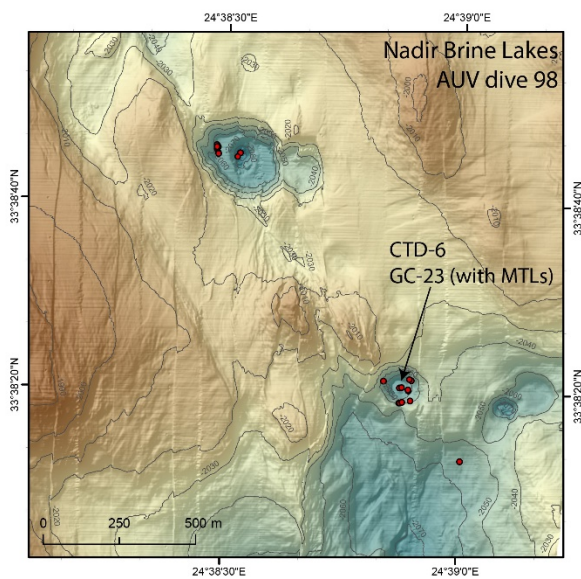


**Fig. 5.3.8:** Bathymetric map of the Nadir Brine Lake area with flare locations (red points) concentrated in and around the subsional pits.

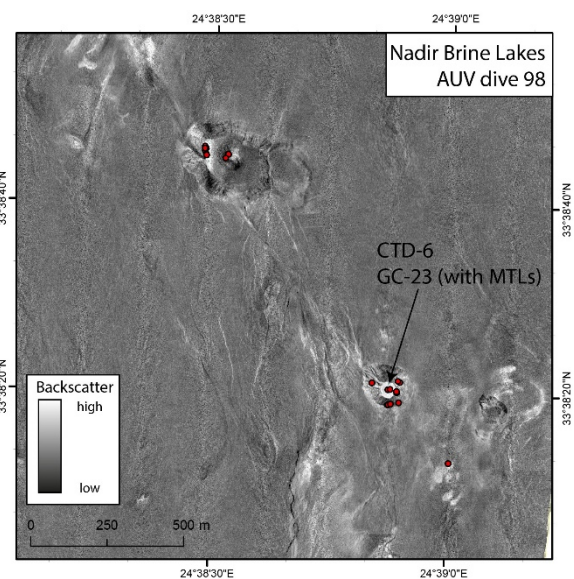


**Fig. 5.3.9:** Backscatter map of the Nadir Brine Lake area illustrating high backscatter at the flare locations.

### Results from AUV Dive 99 at the Flare Site

The flare at this site has been already been detected with the multibeam system and proven with the Parasound system subsequently. The AUV dive was therefore dedicated to cover this area and allow more detailed analysis using the high-resolution data. This was done successfully, the area of the Flare Site was entirely covered and the water column recorded. The site is relatively unsuspecting for active seepage and it is not related to mud volcanism. The seep area is located on a flank of a ridge directed NW-SE in about 1850 m water depth (Fig. 5.3.10). The backscatter map does not indicate pronounced anomalies, in contrast, the entire surrounding is very heterogeneous in terms of backscatter values. The water column data revealed the presence of at least 9 distinguishable gas bubble streams, sourcing closely together in a linear arrangement of about 30 m length. The flare appearance is much more intense compared to the flares imaged during AUV dive 98 at the Nadir brine lakes (Fig 5.3.11).

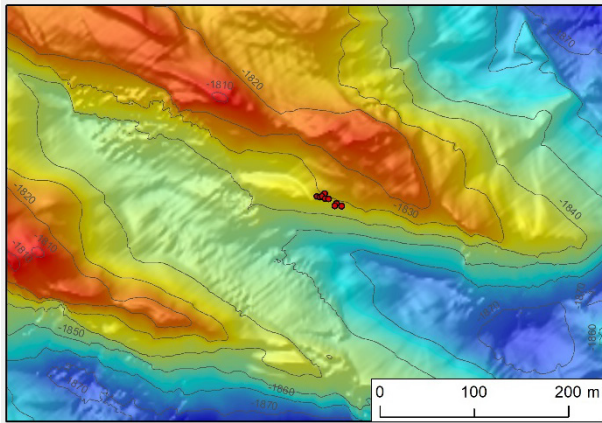


**Fig. 5.3.10:** Preliminary bathymetric map of the area at the Flare Site and the flare source points (red dots).

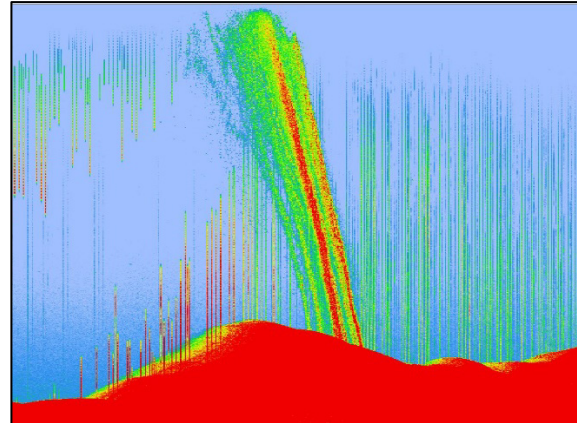


**Fig. 5.3.11:** Stacked view of the water column data retrieved from AUV dive 99 showing several intense flares rising up to the AUV flight height of 80 m above seafloor.

## 5.4 Station Work with the Autonomous Underwater Vehicle (AUV) MARUM SEAL 5000

(U. Spiesecke, F. Ahrlich, S. Schillai, T. von Wahl)

### Introduction

In the year 2006 the MARUM ordered a deep diving autonomous underwater vehicle (AUV), designed as a modular sensor carrier platform for autonomous underwater applications. The company “International Submarine Engineering“ (I.S.E.) built this AUV in Canada. In June 2007 the AUV “SEAL” was delivered to MARUM and tested afterwards on the French vessel RV SUROIT (June 2007) and the German RV POSEIDON (November 2007) in the Mediterranean Sea. Since then, the AUV is in operational mode and was used 13 times on field cruises on-board research vessels (RV SONNE, RV METEOR, RV M.S.MERIAN, RV POSEIDON, RV SUROIT, RV OR5) and 2 times in Lake studies (Lake Constance, Lake Neuchatel). This RV SONNE cruise SO278 is the 18th field cruise of MARUM SEAL.

### SEAL vehicle – basics

The MARUM SEAL is No. 5 of the Explorer-AUV series from the company I.S.E. The AUV is nearly 5.75 m long, with 0.73 m in diameter and a weight of 1.35 tons. The AUV consists of a modular atmospheric pressure hull, designed from 2 hull segments and a front and aft dome. Inside the pressure hull, the vehicle control computer (VCC), the payload control computer (PCC), 8 lithium batteries and spare room for additional “dry” payload electronics are located. Actually, the inertial navigation system PHINS and the Kongsberg multibeam-processor are located as dry payload here. The tail and the front section are flooded wet bays and made out of GRP. In the tail section the motor, beacons for USBL, RF-radio, flashlight, IRIDIUM antenna and DGPS antenna are located. In the newly designed aluminum front section the Seabird SBE 49 CTD, the Sercel MATS 200 acoustic modem, the DVL (300 kHz), Kongsberg Pencil beam (675 kHz), the recently implemented Kongsberg EM2040 (200, 300, 400 kHz), the PAROSCIENTIFIC pressure-sensor and the BENTHOS dual frequency (100/400 kHz) side scan sonar are located.

Actually, the SEAL AUV has a capacity of approx. 15,4 KWh of battery power installed, which enables the AUV for approx. 70 km mission-track lengths. Although the max. track length on bottom is a bit shorter than with the formerly installed Reson 7125, the outcome in surveyed area increased significantly with the new multibeam, as the AUV is flying with greater altitude resulting in a larger beam width and an increased line spacing for the survey. Now the AUV is able to survey an area of approx. 10 km<sup>2</sup> in one dive with an even better data quality than with the Reson.

For security aspects, several hard- and software mechanisms are installed on the AUV to minimize the risk of malfunction, damage and total loss. More basic features are dealing with fault response tables, up to an emergency drop weight, either released by the user or completely independent by the AUV itself.

MARUM puts special emphasis on an open architecture in hard- and software design of the AUV, in order to be flexible in vehicle operations as well as in repair and maintenance. Therefore, the VCC is based to a large extent on industrial electronic components and compact-PCI industrial boards and only very rare proprietary hardware boards have been implemented. The software is completely built QNX 4.25 – a licensed UNIX derivate, that is to a large extent open for user modifications. The payload PC is built on comparable hardware components, but running either with Windows and/or Linux.

On the support vessel, the counterpart to the VCC is located on the surface control computer (SCC). It is designed as an Intel based standard PC, also running with same QNX OS and a Graphic User Interface (GUI) to control and command the MARUM SEAL AUV. Direct communication with the AUV is established via an Ethernet-LAN, either by hard-wired 100 mb LAN cable plugged to the AUV on deck, or by the Ethernet-RF-LAN modem – once the vehicle is launched. The typical range of the RF-link is around 1 – 2 km distance between the ship and the vehicle. Within this range the user has all options to operate the AUV in Pilot-Mode, e.g. to maneuver the AUV on water or change vehicle settings.

Once the AUV is submerged, all communication links are shut down automatically and the AUV is in mission-mode, means it is working based on specific user-defined missions. Despite being in mission-mode it is necessary to communicate with the AUV when it is under water, i.e. asking for actual position, depth and status. To achieve this, onboard the support vessel an acoustic underwater modem with dunking transducer has to be installed (SERCEL MATS modem) communicating with the counterpart on the AUV, on request. Due to limited acoustic bandwidth only rare data sets are available.

### **Mission-mode**

The AUV - as dedicated autonomous vehicle - has to be programmed before operated under water. As mentioned, only at the surface a real-time control by the pilot is possible - once it dives, it will lose any real-time communication and therefore must be in a defined mission-mode. Initialized correctly, fault prevention mechanisms take action in the case that the AUV maneuvers into a dangerous scene.

Simplified, an AUV mission is a set of targets; clearly defined by its longitude, latitude, and a given depth/altitude that the vehicle should reach/keep at a given speed in a distinct time. The AUV needs to be in a definite 3-dimensional underwater space to know exactly its own position over mission time in order to actively navigate on this. To achieve this basic scenario, the AUV is working with best position updates possible, e.g. DGPS position at the surface. Once it dives, it

takes the actual position as starting point of navigation, looks for its own heading and the actual speed and calculates its on-going position change based on the last actual position, e.g. method known as dead reckoning. To achieve highest precision in navigation, a combination of Motion Reference Unit (MRU) and Inertial Navigation System (INS) is installed on the MARUM SEAL AUV – the PHINS inertial unit made by IXSEA. Briefly, the MRU is measuring any acceleration of the vehicle in all 3 axis (x,y,z). The INS is built on 3 fibre-optic gyros (x,y,z) and gives a very precise/stable heading, pitch and roll information, based on rotation-changes compared to the axis. Even on long duration missions, the position calculated by the AUV will be very accurate based on that technique. Once the AUV is close to the seabed, the DVL delivers accurate navigational data on the vehicle's motion relative to the seafloor.

### **Mission planning**

In principle and very briefly, the VCC of the AUV accepts a simple list of waypoints as targets for the actual mission (the list has to be in a specific syntax). In order to arrange it more efficient and convenient a graphical planning tool is used for this mission planning. The MIMOSA (© Ifremer) mission-planning tool is a software package specially designed to operate underwater vehicles (AUVs, ROVs, Glider). The main goal of this software is to plan the current mission, observe the AUV once it is underwater and to visualize gathered data from several data sources and vehicles. MIMOSA is mainly built on 2 software sources, an ArcView 9.1 based Graphical Information System (© ESRI ArcGIS) and a professional Navigation Charting Software (© Chersoft UK). In order to plan a mission, the user has to work on geo-referenced charts with a given projection (UTM); either GIS-maps, raster-charts or S-57 commercial electronic navigational charts (ENCs). These basic charts could be easily complemented with user specified GIS projects and with already gathered data, e.g. multibeam data, or different points of interest. Once installed in MIMOSA, the user can create AUV missions by drawing the specific mission by mouse or by using the implemented set of tools (MIMOSA planning mode). Missions created in that way are completely editable, movable to other geographical locations and exportable to other formats. In order to be interpretable by the MARUM SEAL AUV, the created mission will be translated into the I.S.E. specific syntax; a set of targets, waypoints, depth information and timer will be created and written into an export path. From here the mission file can be uploaded via the SCC (support vessel) onto the VCC (AUVs control PC). From here on the AUV has its mission and is capable to dive, based on a valid mission plan.

### **Mission observing/tracking**

The MIMOSA planning tool is also used for supervision, in order to monitor the vehicle at sea surface and under water (MIMOSA observation mode). The MIMOSA software is client based, that means one dedicated server is used for planning, while the others are in slave/client mode, referring to the actual mission. Therefore, position data strings (UDP broadcast data) from the support ship (i.e. RV SONNE's position and heading) are being sent to the local network and fed into the MIMOSA software. The same protocol is active for the AUV position data, e.g. DGPS signal once it is at surface. During the dive the AUV can be tracked automatically via ship-borne ultra-short baseline systems (USBL), e.g. IXSEA GAPS or POSIDONIA, using the on-board AUV installed USBL transponder beacon. In addition to that the vehicles own calculated (VCC) position

can be displayed also. This position is supplied by transmitted data strings from the MATS underwater acoustic modem, which is only sent by the AUV on user request.

To summarize, the following navigational data is displayed in tracking mode:

- - position of support vessel (lon/lat and heading)
- - either DGPS of AUV during surface track, or
- - USBL position (GAPS or POSIDONIA)
- - and MATS position (underwater acoustic on request)

### **Operational aspects**

MARUM SEAL was used at least 18 times on field cruises so far. Thus, different research vessels have served as a base and on each of them the handling of the AUV is slightly different. Generally, the A-frame is supposed to be the best position to launch and recover the AUV, because the tendency to hit the ship is minimized compared to a sideward operation, based on experiences. On RV SONNE the AUV was successfully launched and recovered with the A-Frame at the stern.

In principle, the AUV can be operated out of the lab, just with a simple laptop. On this cruise the AUV operations were run out of a 20' operation/workshop van, located on the main deck, midships. Not only the file-server and several displays, but also a printer, a workbench, tools and different spares are installed in this container. In addition to the control van a transport van was used that comes with all the bigger spares, tools and the AUV itself.

The SERCEL MATS acoustic transducer was installed in the moon pool. For USBL positioning, the hull-mounted POSIDONIA system was used.

Prior to every launch of the AUV, the PHINS INS (on-board the AUV) needs to be calibrated. In order to do so, the INS is reset and the support vessel must hold its position for at least 5 minutes. After that initial phase (INS coarse align), the ship needs to sail a course with quasi rectangular heading alterations – either a square-like course, 3 minutes @ 3-5 knots each line (INS fine align) or a stair-like course. At the end of that calibration procedure, the PHINS is in a so called “normal mode”, which means it has its highest position quality.

### **Station work on RV SONNE**

During SO278 cruise we had 11 dives plus 1 check+trim dive in the beginning, all of them without serious technical problems on the AUV. In total, 615 km of track lines have been surveyed at bottom. Most of the surveys were conducted with a line spacing of 200 m at an altitude of 80 m above seafloor. Beam width is then approx. 235 m and frequency chosen was 400 kHz. Water column data was recorded in order to find potential gas flares.

All multibeam data shown here are raw and unprocessed data. Details of the AUV data are listed in the station list (chapter 6).

#### *Dive No. 90*

Launch was at 13:00 UTC on 21 October 2020 near Sartori mud volcano south of Italy. Wind was approx. 10 m/s. This dive to a depth of 350 m was necessary in order to adapt the vehicle for the higher density of the seawater and hence higher buoyancy of the AUV on this cruise and to check all relevant systems on board the AUV and ship. AUV was back on deck at 16:00 UTC.

*Dive No. 91 (GeoB24305-1)*  
 Launch was at 05:00 UTC on 25 October 2020 south of Crete. Wind was approx. 13 m/s. This dive at Hellenic arc was nearly completed before it had to be aborted because dusk was approaching. Track length on bottom was 40 km at a spacing of only 130 m at this first dive. Recovery was at 16:00 UTC.

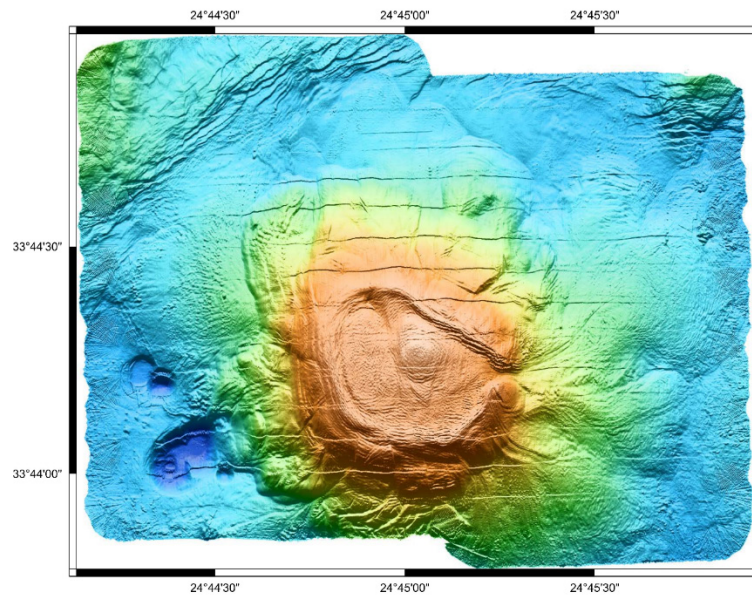


**Fig. 5.4.1:** Dive 91 mapped the main part of Bergamo mud volcano within the Olimpi mud volcano field.

*Dive No. 92 (GeoB24309-1)*

Launch was at 04:30 UTC on 27 October 2020 at winds of 7 m/s south of Crete in the Hellenic arc area at Bergamo mud volcano. Track length was 55,3 km on bottom at 2000 m water depth. This dive was shortened to avoid a recovery in the dark. At 16:00 UTC the AUV was back on deck and an error in the Kongsberg Processing Unit was discovered that hindered the hdd to record multibeam data.

*Dive No. 93 (GeoB24317-1)*

Launch was at 15:30 UTC on 30 October 2020 at winds of 11 m/s in a fault area south of Crete. The AUV followed 8 km long tracks in 3000 m depth with a spacing of 160 m at 80 m altitude. The dive was supposed to be 65 km long but an unknown obstacle forced the AUV to abort the mission after approx. 50 km. Recovery was at 06:00 UTC the next day.

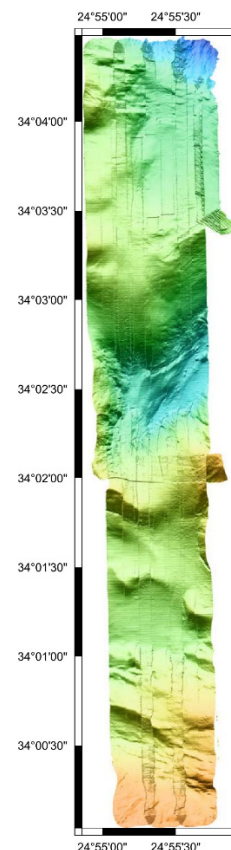


**Fig. 5.4.2:** Dive 93 mapped a transect covering the transition between Inner and Outer Ridge.

*Dive No. 94 (GeoB24322-1)*

Launch was at 04:30 UTC on 1 November 2020 at winds of 5 m/s also in a fault area south of Crete. Line spacing was 160 m in a depth of 3000 m at a total length of 53 km. After approx. 50 km the mission was aborted so as to recover before darkness at 16:00 UTC.

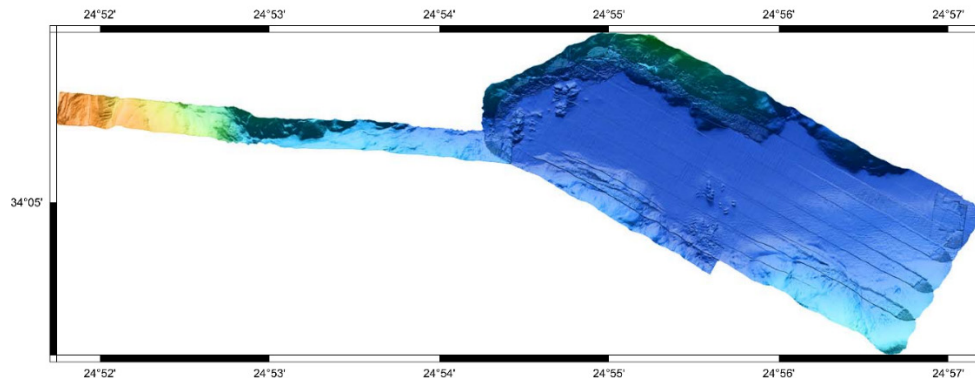


**Fig. 5.4.3:** Dive 94 mapped a basin related to a major fault zone south of Crete

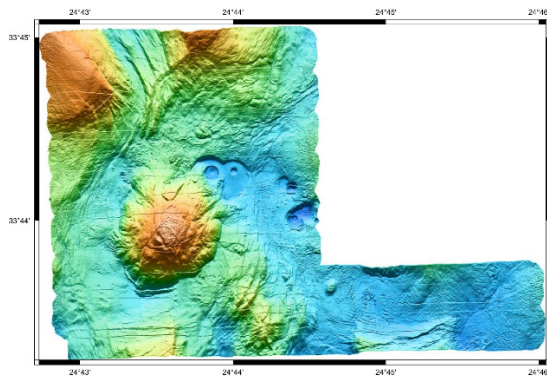


**Fig. 5.4.4:** AUV Dive 95 covered the Monza mud volcano of the Olimpi mud volcano field.

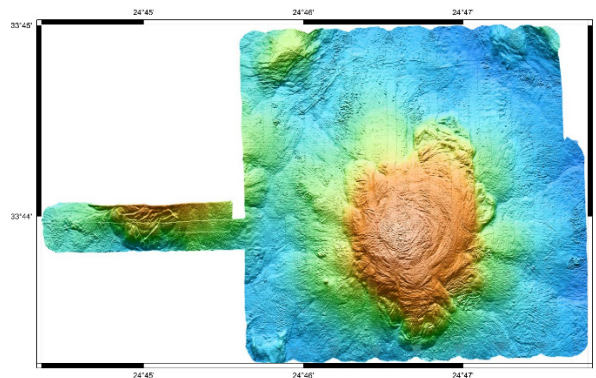


**Fig. 5.4.5:** Monza mud volcano was mapped during Dive 96 within the Olimpi field.

*Dive No. 95 (GeoB24325-1)*

Launch was at 15:30 UTC on 02 November 2020 at winds of 5 m/s at the Monza mud volcano. The survey was conducted at a depth of 2000 m with a spacing of 200 m and a total length of 60 km on bottom. The dive was completed and the vehicle recovered at 05:00 UTC the next day. Dive 91 complements the upper corner.

*Dive No. 96 (GeoB24332-1)*

Launch was at 15:30 UTC on 4 November 2020 at winds of 9 m/s at the Milano mud volcano. The survey with a spacing of 200 m and a length of 62 km on bottom was completed. The AUV was recovered at 05:00 UTC the next day. Together with dive 91 and dive 95 the bathymetry shows 3 adjacent volcanoes.

*Dive No. 97 (GeoB24338-1)*

Launch was at 15:00 UTC on 08 November 2020 at winds of 8 m/s. Target was the Nice mud volcano at a depth of 1900 m. The survey with a total length on bottom of 64 km was successfully completed and the vehicle recovered at 05:00 UTC the next day.

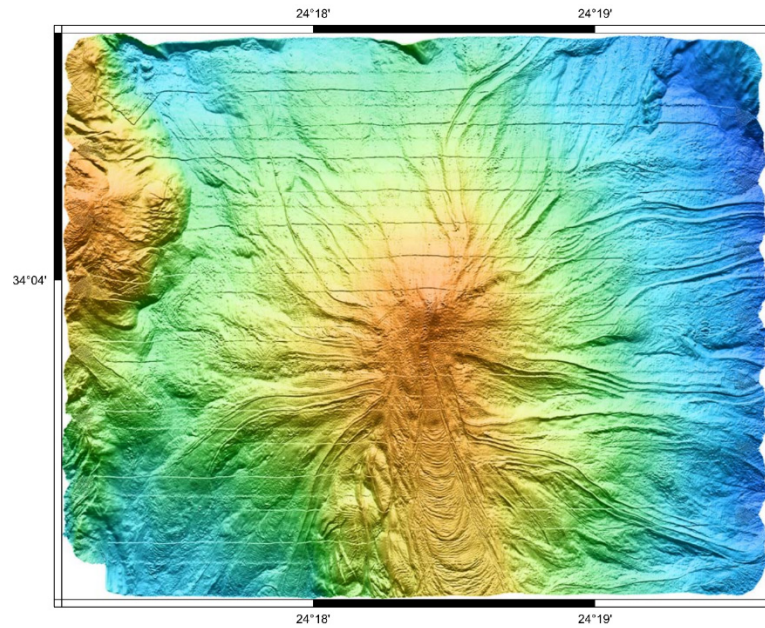


**Fig. 5.4.6:** Main area of Nice mud volcano mapped during Dive 97

*Dive No. 98 (GeoB24345-1)*

Launch was postponed to 15:00 UTC on 10 November 2020 due to bad weather in the early morning. Target was Nadir brine and the survey length on bottom was 70 km. When the dive was completed, the AUV was recovered at 06:00 UTC the next day.

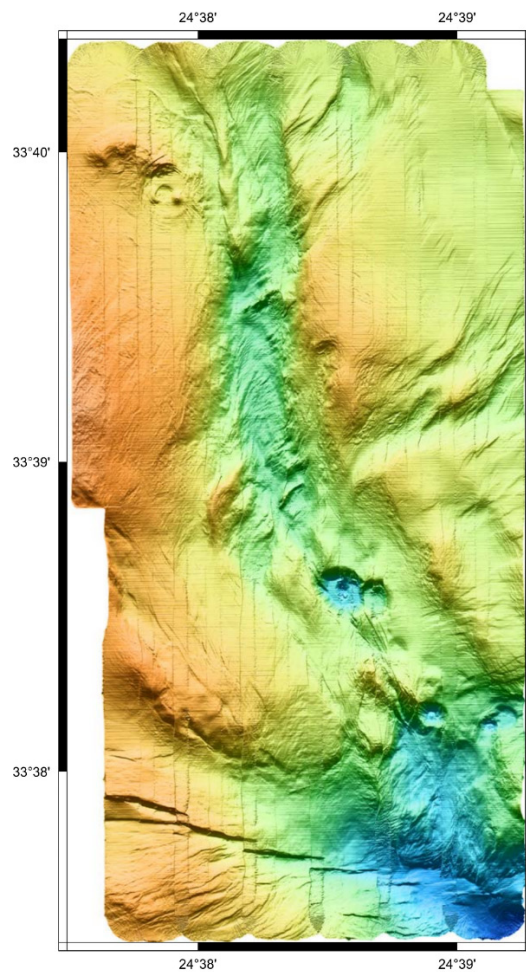


**Fig. 5.4.7:** AUV Dive 98 mapped a fault zone related to Nadir brine lake.

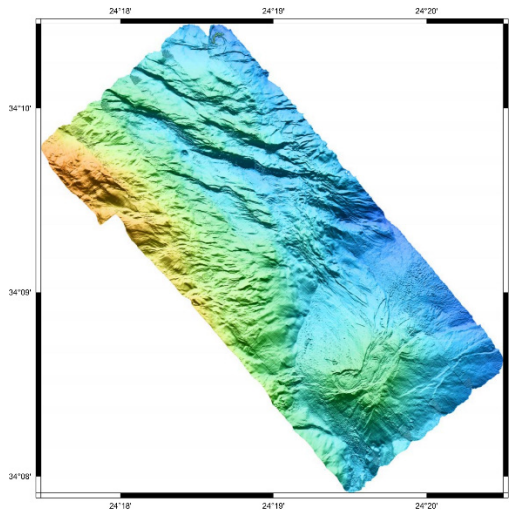


**Fig. 5.4.8:** AUV Dive 99 mapped the location of a distinct gas flare related to a fault zone and covered an unnamed mud volcano.

*Dive No. 99 (GeoB24349-1)*

Launch was at 05:00 UTC on 12 November 2020 at the Nice mud volcano with a flare as prominent target. Mission depth was 1900 m. Since 2 of the 24 battery cells were erratic, the dive was aborted automatically after approx. 50 km. The AUV was recovered at 17:00 UTC.

*Dive No. 101 (GeoB24358-1)*

Launch was at 16:10 UTC on 15 November 2020 at winds of 6 m/s at a site called “Cobblestone field”. Track length in total was 68,5 km at a depth of 2900 m and 80 m altitude. When the dive was successfully completed, the vehicle was recovered at 06:50 UTC the next day.

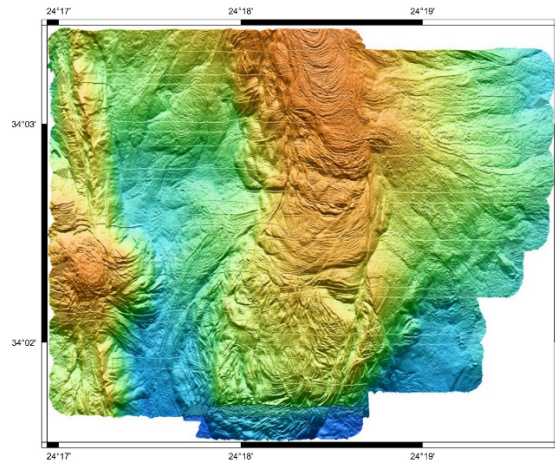


**Fig. 5.4.9:** Dive 100 mapped the southern extent of Nice mud volcano.

*Dive No. 100 (GeoB24354-1)*

Launch was at 19:20 UTC on 13 November 2020 at winds of 5 m/s at the Nice mud volcano. The total survey length of 70 km on bottom could nearly be completed before it was cancelled due to a low battery. The vehicle was on deck at 09:30 UTC next day. The bathymetry recorded and shown below is the southern complement to dive 97.

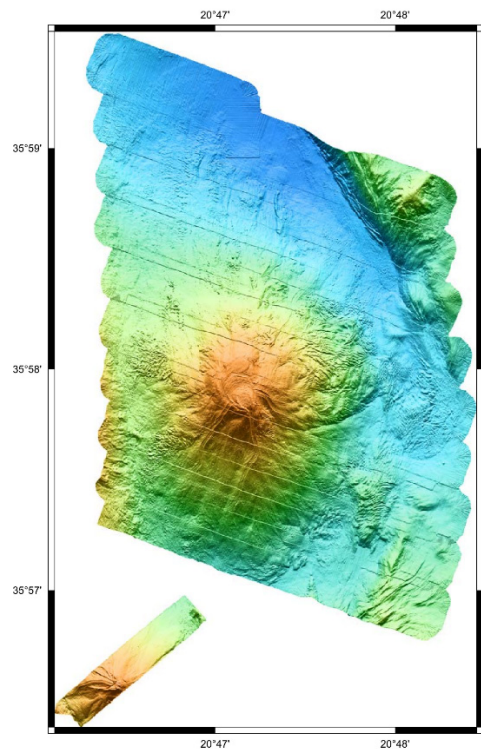


**Fig. 5.4.10:** Dive 101 mapped the Helios mud volcano related to the Cobblestone area.

## 5.5 CTD Operations - Water Column Work

(V. Kürzinger, Y. Tseng, J. Malnati, G. Feddersen)

### Introduction

Methane does not only occur in the atmosphere, but is also a small component of our oceans. There it can be generated in different ways: it is either generated in the water column or originates from fluid seepage from sediments at the seafloor. The latter was of particular relevance for this cruise, because the activity of the mud volcanoes in the working area was investigated.

In total, six CTDs were deployed. Oceanographic data as well as water samples were collected at the Olimpi mud volcano field (flare position, Milano MV, Napoli MV), United Nations Rise (Dublin MV), in the fault zone at the northern part of the Mediterranean Ridge and at the site of a subsurface brine pit close to the Nadir brine lake (Fig. 5.5.1).

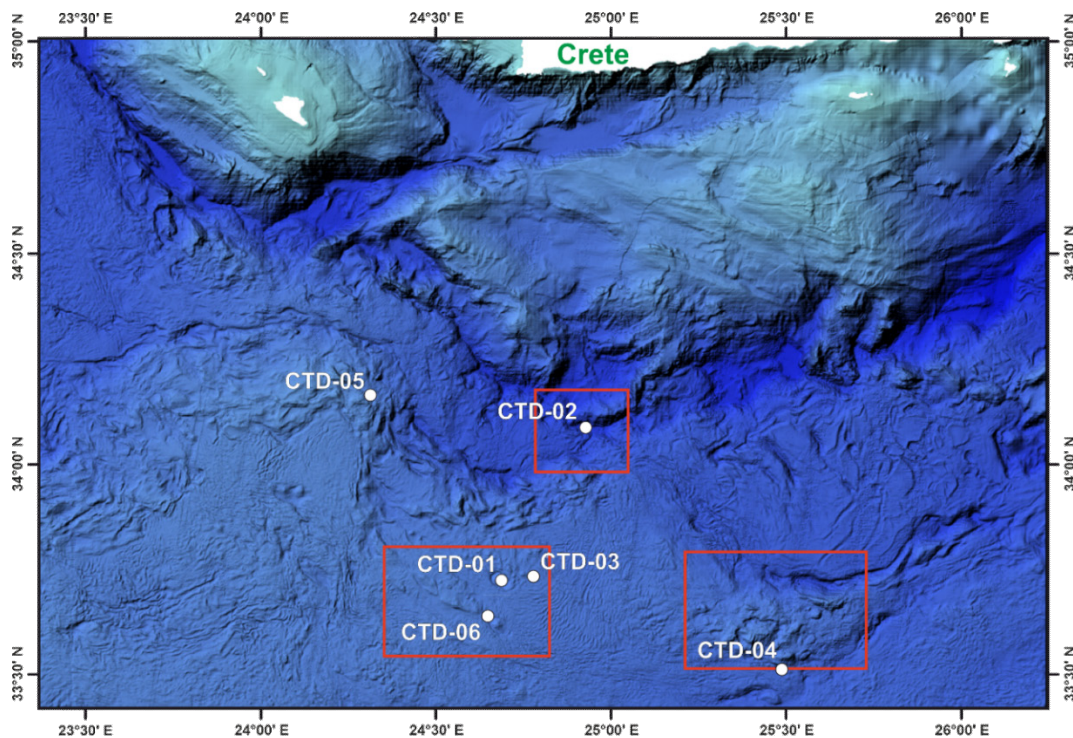


Fig. 5.5.1: CTD station map of the Central Mediterranean Ridge.

The first CTD (CTD-01) was deployed on top of Napoli MV (Fig. 5.5.1), followed by CTD-02 at the deepest point of the fault zone in the northern part of the Mediterranean Ridge, where we detected an anomaly during heat flow measurements. We also took water samples from Milano MV (CTD-03) and Dublin MV (CTD-04) as these are said to be the most active mud volcanoes in the Olimpi field and the United Nations Rise (Fig. 5.5.1). One of the most interesting sites was a spot at a small fault in the NNW of Olimpi field. There, during a hydroacoustic survey, a gas emission (flare) was detected with Parasound, so water samples were taken at this location (CTD-05) to measure the probable increased methane concentrations. The last CTD station (CTD-06) was realized at a new discovered location near the Nadir brine lake (Fig. 5.5.1). During a previous AUV dive, a weak gas emission was detected in the middle of an interesting structure, interpreted as a subsurface (brine) pit that we wanted to sample in terms of elevated methane concentration and salinity.

## Description of the methods

Water samples were taken at all CTD stations named above. The ships-owned Seabird CTD was used which comprises conductivity, temperature and depth/pressure sensors. Furthermore, a SBE 43 oxygen sensor and a turbidity sensor are mounted to the CTD as well as a Wetlab fluorometer. Water samples were taken from the entire water column by using 24 Niskin bottles. The water itself was sampled from up to 1 m above the seafloor to near-surface water.

For the analyses of methane concentrations in the water column, water was sampled from the Niskin bottles by two 140 ml syringes. Directly after recovery of the system on deck, the syringes (outfitted with a gas tight valve) were flushed and each filled with 100 ml of the respective seawater sample to avoid any air bubbles. In the remaining 40 ml, a methane-free air headspace (so called “Zero Air”) was generated. These syringes then were vigorously shaken for at least 1.5 minutes to allow the equilibration between the water sample and the headspace air.

Afterwards, methane concentrations in the headspace air were measured with a Greenhouse Gas Analyzer (GGA). To avoid the risk of water injection into the GGA, the 2 x 40 ml headspace gas of both syringes was transferred in a dry 140 ml syringe and injected into the GGA using a Luer-Lock adapter. This was followed by the injection of 60 ml "Zero Air", which is needed to provide the required gas volume of 140 ml in the GGA measuring cell.

During this cruise, methane concentrations from in total 144 water samples were determined.

## Preliminary results

During SO278, six CTDs were deployed to collect oceanographic data as well as water samples from different locations. The results of potential temperature, salinity and oxygen concentration in the water column are shown in Figures 5.5.2 and 5.5.3. The surface water extends from sea surface to about 50 m water depth with temperatures ranging from 22.1 to 24.6°C and relatively low salinities. A salinity maximum (39.18 to 39.22) marks the subsurface water with temperatures decreasing to 16.5°C located in a water depth of roughly 100 m.

At all CTD sites, the trend of the potential water temperature follows the same pattern and differs only slightly in the upper 700 m (Fig. 5.5.2). On the other hand, a bigger difference can be seen in the oxygen content of the waters and their salinity.

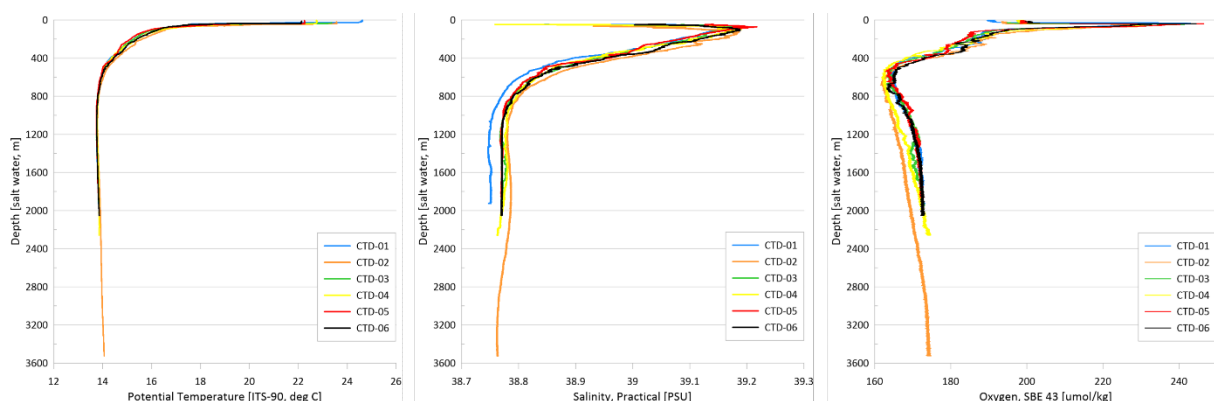


**Fig. 5.5.2:** CTD generated depth profiles of potential temperature, salinity and oxygen.

The data from CTD station 06 (Fig. 5.5.3) represent a special feature because during this deployment the surface of the assumed brine was touched and thus the presence of a brine pit was confirmed. The temperature at the surface of this submarine lake increases by ca. 0.5°C. In contrast

to the salinity, which increases drastically (up to 214.1 ‰), the oxygen content decreases to about  $-2960 \mu\text{mol/kg}$ .

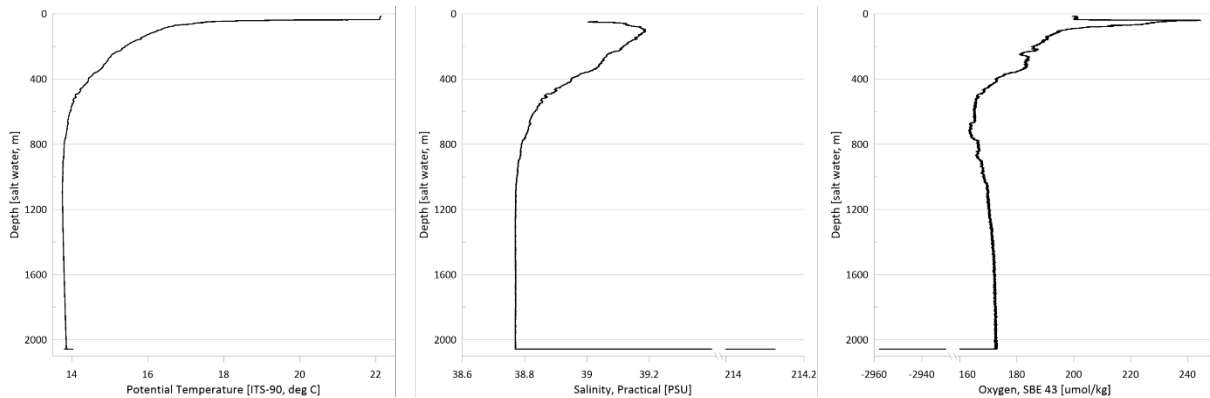


**Fig. 5.5.3:** Oceanographic data from CTD-06: depth profiles of potential temperature, salinity and oxygen.

The results of the concentrations of dissolved methane in the water column (measured on board of the vessel) are shown below (Fig. 5.5.4). Close to the seafloor, methane concentrations increase at all sites except station CTD-02. However, only near gas emission sites the methane concentrations are distinctly higher than the background. The highest concentrations were measured at the flare position (CTD-05) with values up to  $470 \text{ nmol/L}$ . At this site, we did not hit the exact flare position at the seafloor, but cross through it during the upcast.

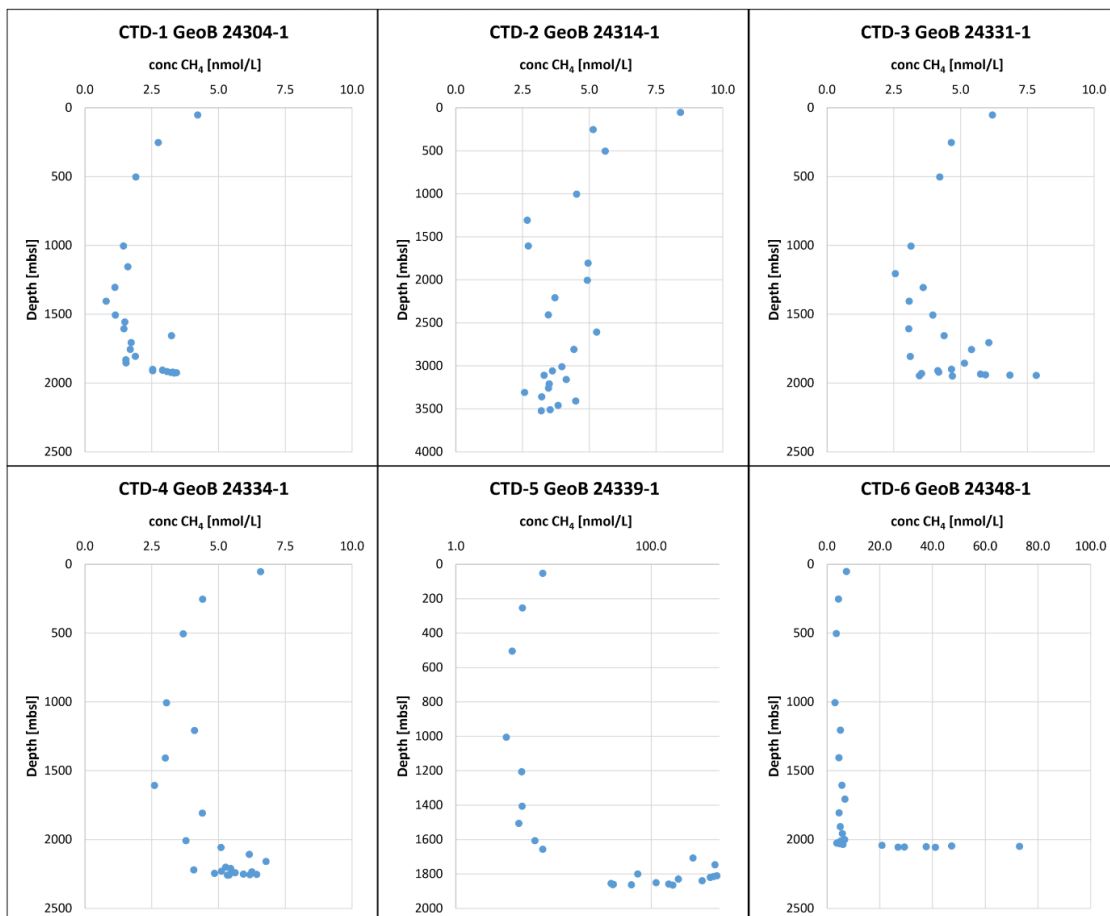


**Fig. 5.5.4.** Methane concentrations from all CTD stations throughout the entire water column.

## 5.6 OFOS Deployments

(M. Römer, G. Bohrmann, K. Streuff, Y. Tseng, S. Gaide, I. Vejzovic)

### Introduction

Images from the deep seafloor have been collected by remotely operated vehicles, by submersibles, by autonomous vehicles, by deployed cameras connected to cabled observatories or towed camera sleds. RV SONNE which was in operation from 1978 to 2014 for scientific work has a long tradition back in the past for operation ground truthing the seafloor by using TV-sleds. Since the ship was the first vessel of German's research fleet which operated fiber optic tethered platforms the developments of such tools were prototype systems which stimulated the developments of similar ground truthing systems at other marine science institutions in Germany and elsewhere. We are therefore very happy that onboard the new RV SONNE a new TV-sled called OFOS (Ocean Floor Observation System) is available since 2018. This modern system operated with the fiber optic cable has state of the art digital video and still cameras of high resolution, which allow features of millimeter size to be resolved on images of the seabed.

During RV SONNE cruise SO278 we used the TV-sled for ground truthing mud volcanoes, seep sites and subsurface pits within the area of the Mediterranean Ridge. The deployments of the OFOS most often used high resolution AUV bathymetry maps as well as backscatter maps as a primary information to investigate interesting features at the seafloor. Drastic changes on the seafloor e.g. by the appearances of chemosynthesis community and authigenic carbonate could be easily identified by visual surveillance of the OFOS. High resolution still frame-camera pictures and videos in combination with positioning instrument provided very detailed variations on the types and spatial differences of biogeochemical processes induced by the gas and saline water migration to the seafloor.

### Instrument description

The Ocean Floor Observation System OFOS (Figs. 5.6.1 and 5.6.2) is a visual towed seafloor survey instrument on RV SONNE.

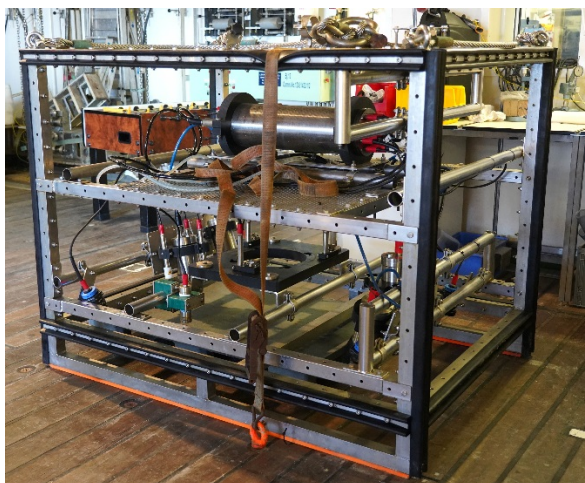


**Fig. 5.6.1:** The Ocean Floor Observation System (OFOS) of RV SONNE.

It is a camera system with high resolution still frame-camera (Panasonic Lumix DMS-LX2) and a HD video camera (Micro SeaCam 2002) connected to surface vessel by fiber optic cable (Rochester, 18.2 mm). Position of the unit is by a USBL (IXSEA). Light is supplied by four LEDs (Deep Sea Power & Light Multi Sea-Lite). The power supply unit is capable to supply

continuous light for video camera, as well as extra strobe light (Benthos M383) for still frame-camera. Three laser pointers (Micro-Sea-Laser) arranged to provide a scale measure, with a distance of 15 cm between two points. Other details as shown in the OFOS specification (Table 5.6.1).

**Table 5.6.1:** OFOS specifications provided by the WTD of RV SONNE.

<b>Fibre-Optic, LWL-Datatransfer</b>	LWL Downlink
	LWL Uplink
<b>Cable</b>	Manufacturer: Rochester
	18,2 mm Diameter
<b>Power for Underwater-Frame</b>	1000 V/ 1A/max. 1050 W
<b>Telemetrie</b>	Manufacturer: RTB
<b>Videocamera black/white</b>	Manufacturer: Deep Sea Power & Light
	Sensor: ½ inch CCD
	Focus: 60 mm to infinity
	Power: 10-36 V
<b>Videocamera color</b>	Manufacturer: Deep Sea Power & Light
	Sensor: ½ inch type IT CCD with complementary mosaic filter
	Angle in water: 81 deg (D) x 64 deg (H) x 47 deg (V)
	Power: 10-40 V
<b>Light</b>	Manufacturer: Deep Sea Power & Light
	Ballast with 2 Lighthouse 200W each
<b>4 x floodlight</b>	Manufacturer: Deep Sea Power & Light
	Power: 24V/ 150 W
<b>Photosystem</b>	Manufacturer: Panasonic
	Sensor: 1/1,65" CCD
	700 fotos (4 GB SD-Card)
	Operating depth: 6000 meter
<b>Strobelight</b>	Manufacturer: Benthos
	Double-strobe, 2 flash-heads
	Switching power 300 Ws, 400 Ws and 600 Ws
<b>3 x Laserpointer</b>	Manufacturer: Deep Sea Power & Light
	Power 7.5 V – 16 VDC/47 mA
<b>Altimeter</b>	Manufacturer: Benthos
	Range 0-99,9 meter or 0-9,99 m
	Operating frequency: 100 kHz
<b>CTD</b>	Manufacturer: Seabird
	Sensores: p, t, c
	Power: internal battery or external 15 VDC
<b>Nav. –System</b>	Manufacturer: IXSEA
	Power: internal battery or external VDC
<b>Interface</b>	Manufacturer: RTB
<b>Kompass</b>	Manufacturer: RTB
	Accuracy: 2° RMS
<b>Roll and Pitch</b>	Manufacturer: Mark II (part of the telemetry)

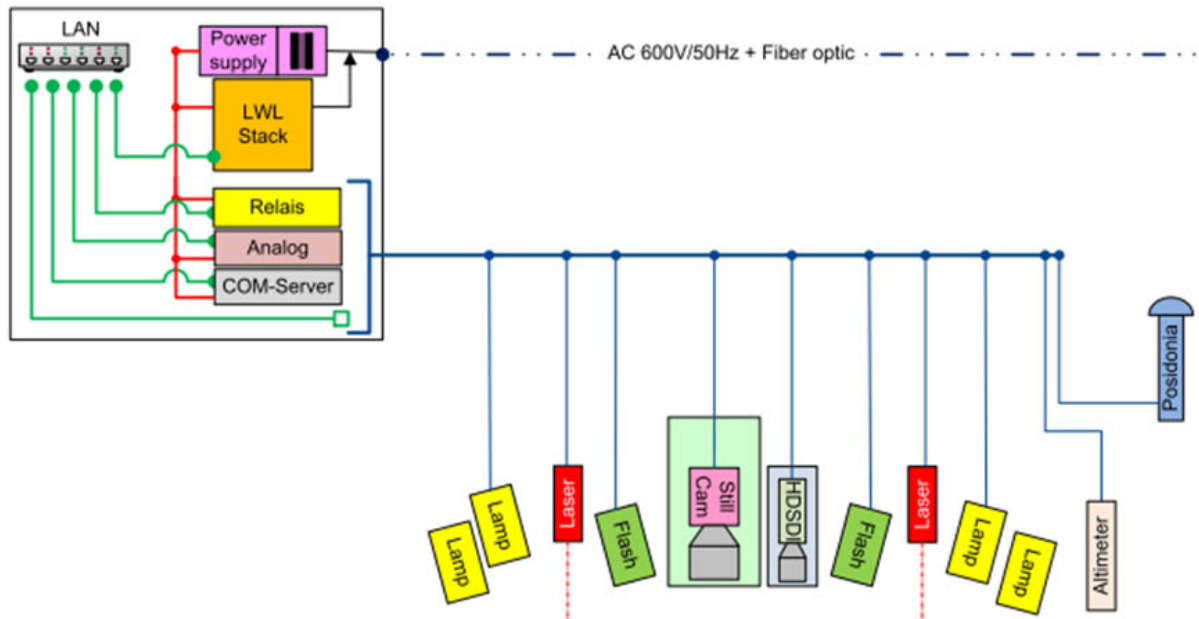


Fig. 5.6.2: Schematic diagram of the OFOS.

## OFOS Deployments

### OFOS-01 Deployment (Station SO278-07-1, GeoB24307-1)

Area:	Bergamo mud volcano
Date:	Monday, 26 October 2020
Start bottom (UTC):	12:39
End bottom (UTC):	16:16
Bottom time:	03:37
Start bottom (Lat, Long, Depth):	33°44.367'N, 24°45.134'E, 1929 m
End bottom (Lat, Long, Depth):	33°44.390'N, 24°44.352'E, 2028 m
Responsible Scientist:	Gerhard Bohrmann

**Goal of the dive:** Exploration of the Bergamo mud volcano to compare features of the AUV map with seafloor observations.

**Key results:** Mud breccia deposits were confirmed to cover the plateau-like area of the mud volcano. Scattered tube worms and lucinid clam shells are indicators for fluid seepage, which seems not very active during recent times. High backscatter rims of circular depressions are related most probably to carbonate precipitation in an unknown strata-bound level. Very low backscatter areas west of the mud volcano are characterized by a smooth seafloor, showing large traces of bioturbation.

### Description along the track:

During OFOS deployment 01 the Bergamo mud volcano was explored from its central part to its southwestern flank and the rim area, where pockmarks are well seen in the AUV maps (Fig. 5.6.3). The mud volcano is a flat-top medium-sized mud volcano 80 m high and around 1,500 m in diameter. The flat plateau of the mud volcano measures around 600 m in diameter and has at its

eastern rim a distinct overflow structure through which mud flow deposits clearly have been flown down and form large lobes at the flank of the mud volcano. Typical structures of down flow mud breccia in the bathymetry are accompanied by high backscatter pattern. After downloading the OFOS through the water column, we reached bottom sight at 12:31 UTC and recognized many clasts of various sizes and colors at the seafloor (Fig. 5.6.4). Small sized clasts seem to accumulate in grooves, which occur often in parallel pattern. We landed close to the eastern wrinkled bulge of the plateau and moved slowly in southwestern direction over the plateau.

At around 13:00 UTC we reached the area of the estimated center of the eastern outflow region. The seafloor contained much less clasts and fissures in the mud which often showed grey colors of a reduced sediment environment (Fig. 5.6.5). Further along the track the occurrence of clasts increased again and at around 13:15 UTC we moved into the western outflow region of the mud plateau, without no obvious change in the density of clast occurrence. However, indicators for fluid venting became more frequent. Individual tube worms and shell detritus of lucinid clams were recognized as well as small pieces of yellowish seep carbonates with clam shells involved were observed in this part of the plateau. Following the track the OFOS was towed downwards the southwestern flank of the mud volcano. Less clasts are to be seen in this area and seafloor contained many small circular traces of bioturbation. In elongated depressions darker grains are sometimes accumulated. Upon closer inspection, the grains turned out to be pteropod shells.

Around 14:23 UTC we reached an area where the seafloor appeared more lithified with many traces of bioturbation, which we attributed to the high backscatter area of the AUV map around the circular depressions southwest of the mud volcano. Shortly before 14:28 a several cm thick lithified bank of probably carbonate in origin was observed on top of a scarp. Evaluation by a more detailed view turns out that bioturbation traces are strongly precipitated. The track followed the slope of the southeastern side of two circular 25 m deep and around 200 m in diameter depressions without surveying the bottom of the depressions.

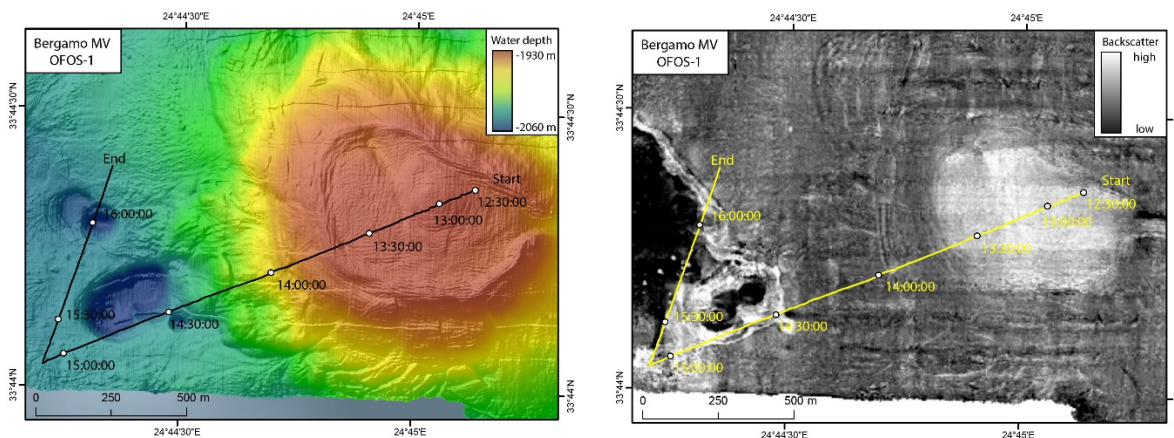


**Fig.5.6.3:** Seafloor track during the OFOS deployment 01 covering Bergamo mud volcano. Detailed bathymetry (left) and backscatter map (right) measured by EM 2040 during AUV Dive 91 and plotted as raw data.

At 14:51 UTC we crossed again the rim of the depression and found a precipitated seafloor on its shoulder. At 15:10 UTC we changed our direction on the seafloor to NNE and surveyed the very low backscatter area on the map (Fig. 5.6.3). This part of the seafloor until the next depression was characterized by flat sediment surface with 4-6 cm broad burrow traces which have been widely distributed (Fig. 5.6.7). Dead sea urchins lying around indicate that the burrow traces were

produced most probably by these animals. Following the track we moved with OFOS into another depression 25 m deep and 100 m in diameter. When we climbed up the northeastern rim of the depression, we found again the distinct carbonate precipitation following burrow traces (Fig. 5.6.6). At 16:16 UTC we left the bottom, which was the end of the dive.



**Fig. 5.6.4:** Mud flow deposits with clasts of various sizes and composition. Clusters of white rock debris are striking.



**Fig. 5.6.5:** Small-scale scarps are visible in mud breccia deposits of the center of the mud volcano.



**Fig. 5.6.6:** A strange pattern of a strata-bound solid rock formation is likely caused by carbonate precipitation of bioturbation structures at the rim of the pockmarks.



**Fig. 5.6.7:** Flat seafloor with distinct traces probably caused by sea urchins in the center of the pockmarks.

### OFOS-02 Deployment (Station SO278-30-1, GeoB24330-1)

Area:	Monza mud volcano
Date:	Tuesday, 4 November 2020
Start bottom (UTC):	04:10
End bottom (UTC):	11:40
Bottom time:	07:30
Start bottom (Lat, Long, Depth):	33°44.105'N, 24°43.364'E, 1939 m
End bottom (Lat, Long, Depth):	33°44.123'N, 24°44.404'E, 2058 m
Responsible Scientist:	Miriam Römer

**Goal of the dive:** Exploration of Monza mud volcano: investigation of high-backscatter areas visible in the AUV map, the peak and potential former outflow area, as well as a probably former brine pool.

**Key results:** The high-backscatter areas visible in the AUV map has been proven to represent seep areas with authigenic carbonates, and chemosynthetic living organisms. However, activity seems

to have decreased as only few living tubeworms have been documented. The peak of the mud volcano showed mud breccia mixed with broken authigenic carbonate rocks, tubeworms, shells and a whitish material outcropping, which we interpret as gypsum deposits. In contrast, soft sediments colonized by sea urchins have been seen within the supposed brine pool area surrounded by a precipitate outcropping at its rim and shown up as high backscatter in the AUV map.

### Description along the track:

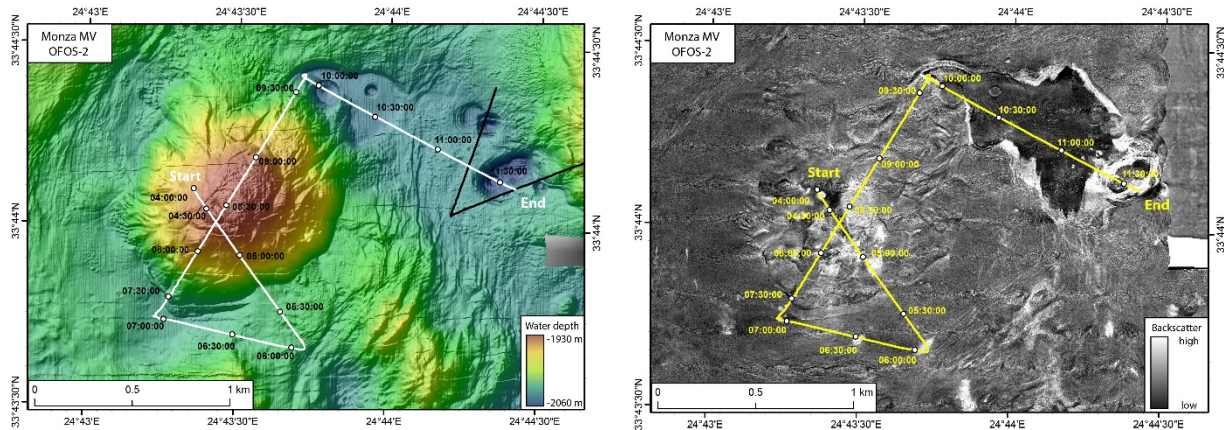


**Fig. 5.6.8:** Seafloor track during the OFOS deployment 02 covering Monza mud volcano. Detailed bathymetry (left) and backscatter map (right) measured by EM 2040 during AUV Dive 95 and plotted as raw data.

The OFOS dive focusing on Monza mud volcano was planned for 4 November 2020 and lasted about 7:30 hours at the seafloor. A prior acquired AUV dive revealed a high-resolution map (grid cell size >2 m) that has been used to plan and navigate the OFOS deployment (Fig. 5.6.8). Start of the dive has been chosen at the flank of the mud volcano, northwest of the peak. A pronounced subcircular and distinct high backscatter patch became visible in the AUV backscatter map, which we planned to investigate about what it is caused by. Bottom view started at 04:10 UTC a few tens of meters NW of this high-backscatter patch and the first impressions showed soft sediments at the seafloor with some cm-large clasts in different colors, bioturbation signs and pteropod remains. By reaching the high-backscatter patch, a typical seep structure was observed, clearly causing the anomalous backscatter signal. Precipitates, most possibly authigenic carbonate precipitates, cover the seafloor, partly broken and piled up (Fig. 5.6.9), some areas with whitish bacterial mats at its rims. Darkish grey, reduced sediments become visible in cracks of the carbonate plate and at its rims, which are covered by white filamentous microbial mats (Fig. 5.6.9). Tubeworms are abundant, appearing individually or in small groups, many of them alive. White small clam shells (probably Lucinid clams) are also numerous in the entire area (Fig. 5.6.9). Crabs were documented as well (Fig. 5.6.9). The seep area is about 30 m in diameter.

Along the flank of the mud volcano down to the foot in the SE, the backscatter signature shows a mixture of areas with low to intermediate and high backscatter and revealed accordingly alternating mud breccia covered by soft sediments and seep influenced regions. However, seeps at this flank appear older and not active anymore. Soft sediments occurred in the surrounding of the mud volcano. Three more high-backscatter patches in the surrounding of the mud volcano however revealed further seep structures, again characterized by precipitates, reduced sediments, microbial mats, tubeworms, and clam shells (Fig. 5.6.10).

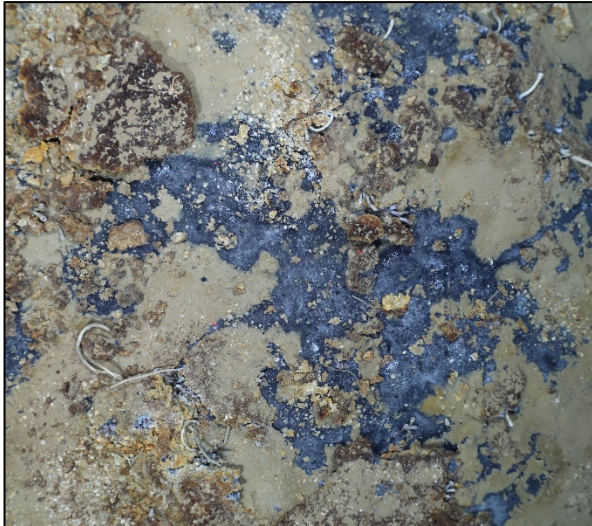


**Fig. 5.6.9:** Picture of an active seep site at the flank of the mud volcano characterized by authigenic carbonate precipitate, reduced sediments and bacterial mats, living tubeworms, clam shells and crabs.



**Fig. 5.6.10:** Seep influenced area at the surrounding of Monza MV with brownish colored sediments, abundant clam shells, tubeworms, bacterial mats at the reduced sediments and the exposed authigenic carbonate precipitate.



**Fig. 5.6.11:** Peak of the mud volcano close to the site where a heat flow measurement was taken (grey mud in the lower right part of the picture shows fresh mud probably fallen of the lance).



**Fig. 5.6.12:** The peak of the mud volcano shows a mixture of mud breccia, seep remains (tubeworms, shells, broken pieces of precipitate) and some whitish material interpreted as gypsum deposits.

At around 07:30 UTC, the OFOS was towed again above the mud volcano from the southwest to the northeast. This side of the flank did not show suspicious backscatter signals and was mostly covered by soft sediments with pteropods and small clasts. The mud breccia showed gravitationally produced blocky cracks along steeper parts of the flank. At the peak, we found fresh appearing grey mud at the position of the heat flow locations, which has most probably fallen off from the lance during heaving (Fig. 5.6.11). The sediments here and also along the northwestern plateau area of the peak are characterized by a mixture of mud breccia, seep remnant like dead tubeworms, clam shells and precipitate pieces (Fig. 5.6.12). In addition, a white appearing outcropping material could be observed in the central part of the peak, which we suspect to be at the surface eroding gypsum deposits (Fig. 5.6.12).

The last part of the dive was the investigation of the depressions northeast of Monza MV. At 09:30 UTC, the rim of the large suspected former brine pool was reached, characterized by high backscatter in the AUV map, which could be proven to be caused by platy outcropping hard material (Fig. 5.6.13). We do not know what this material is made of, however we hypothesize that it has been precipitated along the former brine level. At about 10:05 UTC the deepest part of the closest depression has been reached. Very soft appearing sediments were seen at the flank and bottom of the depression. At its deepest part, a (probably whale) bone was found which was colonized by microbes and tiny worms (Fig. 5.7.14). Small little tubes of unknown organisms were colonizing the surrounding at the bottom of the depression.



**Fig. 5.6.13:** Rim of the suspected former brine pool. Platy precipitates have been formed and produce a very high backscatter signal in the AUV map.

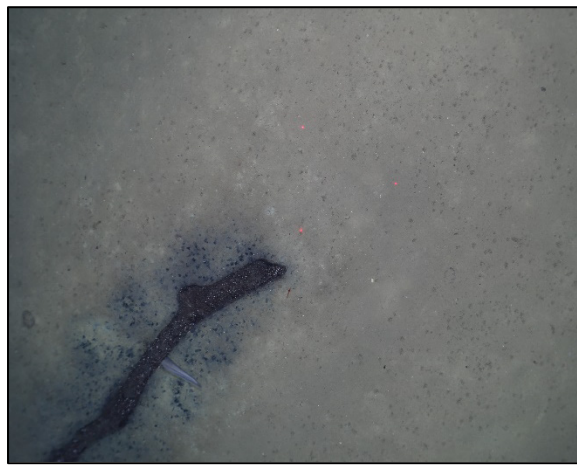


**Fig. 5.6.14:** The bottom of the depression showed soft sediments, colonized by unknown organisms, visible as small protruding tubes. A (whale) bone was documented.

The more shallower part of the former brine pool with a very flat surface was all covered by soft sediments heavily colonized and bioturbated by sea urchins. At about 11:15 UTC the rim of the deepest depression was reached, again showing platy precipitates explaining the high backscatter. Tubeworms, white shells and broken parts of precipitates were found along the flank into the depression, possibly sliding downslope from the rims. At the deepest part at the bottom of the depression, the soft sediments show varying colors from light grey to very dark grey, illustrating different areas of reduced sediments. The seafloor is heavily colonized by some unknown organisms only visibly as small tubes protruding the surface. Several crabs were documented and small white clam shells.

### **OFOS-03 Deployment (Station SO278-36-1, GeoB24336-1)**

Area:	Dublin mud volcano
Date:	Saturday, 07 November 2020
Start bottom (UTC):	06:03
End bottom (UTC):	10:35
Bottom time:	04:32
Start bottom (Lat, Long, Depth):	33°30.612'N, 25°30.259'E, 2353 m
End bottom (Lat, Long, Depth):	33°30.706'N, 25°29.376'E, 2291 m
Responsible Scientist:	Katharina Streuff

**Goal of the dive:** Exploration of the Dublin mud volcano (MV) to understand its structure and to look for potential evidence of methane seeps and recent activity.

**Key results:** The Dublin mud volcano is characterized by large areas of what appears to be hemipelagic mud with abundant traces of bioturbation and variable amounts of clasts. These sediments occurred where backscatter data were reasonably high. In contrast to other mud volcanoes already investigated, mud breccia was only observed in a few places. Instead, the assumed center of the mud volcano showed variably extensive outcrops and fragments of a dark grey rock, which we interpret to be manganese-crust sandstones, but which may also be of magmatic origin. Only two dead tubeworms were observed, indicating that fluid seepage may have occurred in the area some time ago.

### Description along the track:

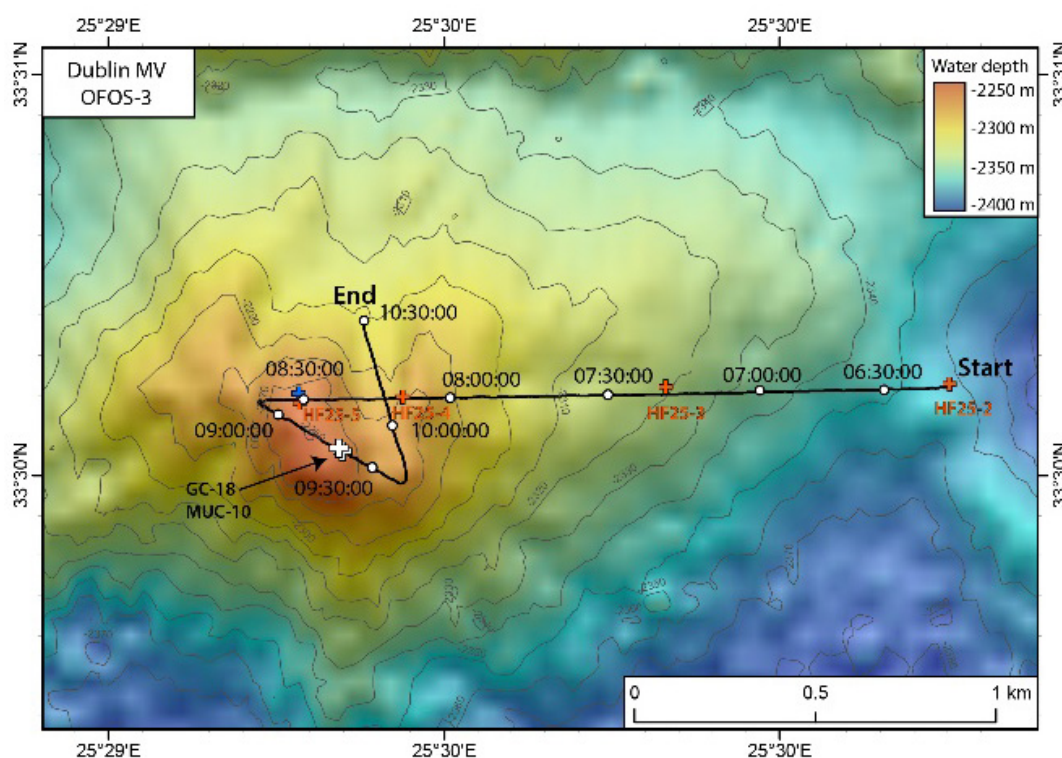


**Fig. 5.6.15:** Overview Map of the Dublin mud volcano, the OFOS track, as well as the heat flow stations (red crosses). A CTD station is indicated by the blue cross.

During its third deployment the OFOS first followed the heat flow profile (stations 035-2 to 035-5), which had been conducted the previous night, east to west across the eastern flank and the assumed top of the Dublin mud volcano, before diving in a southeasterly direction for 400 m, followed by another 400 m in a northwesterly direction (Fig. 5.6.15). The latter two parts were added to gain a better understanding of the composition of the presumed central part of the MV. Unfortunately, bad weather had prevented the acquisition of a high-resolution bathymetric map with the AUV. Navigation was instead based on the bathymetry data collected with the EM122 multibeam echosounder mounted on the ship, and gridded to a resolution of only 75 m. It was therefore difficult to pinpoint characteristic features of the MV, such as the precise location of the central chimney and its rims. The mud volcano is characterized by generally high backscatter with

little variation between the flanks and its top. In terms of fauna, shrimp were ubiquitous, as well as pteropods, the latter often accumulating in already existent bioturbation grooves (Fig. 5.6.18). Argonauta were observed in some places. A few fish (mostly red tails) and a jelly fish were also observed. Tubeworms as well as chemosynthetic mussels, commonly associated with mud volcanoes due to their use of the byproduct of anaerobic methane oxidation,  $H_2S$ , were lacking throughout the entire area, apart from two dead tubeworms which probably indicate that fluid seepage was present at some point in the past.

The OFOS was released into the water at 04:57 UTC and reached the seafloor at 06:03 UTC, slightly east of the point where the second heat flow measurement had been taken the night before (035-2, Fig. 5.6.15). The seafloor was characterized by relatively smooth, light brown to beige mud with large amounts of pteropods and occasional clasts. Bioturbation by sea urchins and some smaller mussels or worms were commonly observed (Fig. 5.6.16). At the location of the heat flow station, the imprint of the heat flow lance and the impressions the attached wire had left on the seafloor were clearly visible (Fig. 5.6.17). A red tail fish had nestled into the small crater left by the instrument. The seafloor sediment stayed relatively similar along the OFOS track, although at 06:25 UTC we saw the first fragments of a dark gray to black rock, that occurred more and more commonly as the dive progressed, and that often appeared to be outcropping at the seafloor. It is not clear what this rock is; but it mostly looks like bedrock, partially with a manganese crust, that may have been extruded from the mud volcano. We did not see any imprints at heat flow station 035-3, but saw impressions of the cable and the lance at Station 035-4 around 08:08 UTC. Immediately after this, the OFOS followed a downhill slope into what we assumed was a sort of caldera structure; indeed, a small crater can be observed in the instrument's depth profile. Lithologies changed to muds with a higher number of clasts and rock fragments downslope (Fig. 5.6.18), but the inner part of the "caldera" was once again characterized by the smooth, clast-poor, pteropod-rich and bioturbated sediments. On the subsequent slope uphill, large (>50 cm) "outcropping" rock and rock fragments were observed together with common clasts and pteropods. Muds with frequent smaller clasts occurred beyond this slope on a sort of plateau, and remained the main lithology until around 08:33 UTC (Fig. 5.6.19), at which point clast abundance was substantially reduced, with very few big to medium-sized clasts scattered about.

The ship, and with it the OFOS, turned in a south-easterly direction at 08:44 UTC, diving over a small basin with largely smooth, bioturbated sediments with scattered rock fragments and "outcrops", the latter particularly concentrated on the slopes. Here, the clast frequency increased again and remained high across the subsequent plateau (Fig. 5.6.20). From around 09:07 UTC the seafloor changed to a rougher appearance with large areas of the outcropping bedrock (Fig. 5.6.21), many small clasts and high amounts of pteropods. The outcrops were sparser after 09:13 UTC, from where clast-rich mud breccia prevailed. Clasts disappeared at around 09:32 UTC and the smooth seafloor dominated until we changed direction again at around 09:37 UTC. After that the seafloor stayed smooth with very few clasts, apart from a few scattered outcrop areas, until the OFOS started its ascent through the water column at 10:36 UTC.



**Fig. 5.6.16:** Seafloor with pteropod-filled bioturbation trace (OFOS Dive 03).



**Fig. 5.6.17:** Imprint of heat flow lance and red tail fish (OFOS Dive 03).



**Fig. 5.6.18:** Seafloor at a downhill slope with apparently outcropping rock and clasts



**Fig. 5.6.19:** Seafloor with frequent small and big clasts, mud breccia (OFOS Dive 03).



**Fig. 5.6.20:** Seafloor with high clast abundance and some outcropping rock (OFOS Dive 03).

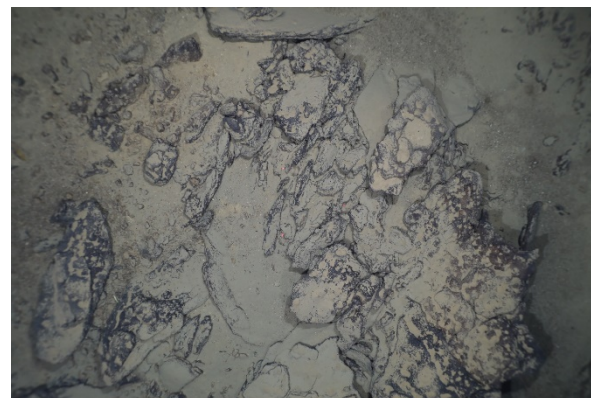


**Fig. 5.6.21:** Large areas of outcropping unknown rock (OFOS Dive 03).

#### **OFOS-04 Deployment (Station SO278-47-1, GeoB24347-1)**

Area: Milano mud volcano  
 Date: Monday, 11 November 2020  
 Start bottom (UTC): 11:28  
 End bottom (UTC): 15:50  
 Bottom time: 03:42  
 Start bottom (Lat, Long, Depth): 33°43.673'N, 24°46.758'E, 1974 m

End bottom (Lat, Long, Depth): 33°43.769'N, 24°46.166'E, 2014 m

Responsible Scientist: Yiting Tseng

**Goal of the dive:** The objective of the fourth OFOS dive was to find out the seafloor morphology on the top of Milano MV and its surrounding area. A previous study from Huguen et al. (2005) had reported the active area consisted of thin carbonated crusts, covered by bacterial mats and chemosynthetic communities, tubeworms and bivalve shells (Fig. 5.6.22). Also, from the latest acquired AUV map, a better understanding of the surrounding area showing two interesting structures at the southwestern MV (Fig. 5.6.22), one is a protruding structure and second is the following low backscatter anomaly. Additionally, the previous ODP drilling site (970D) was designed in the track line in order to observe the transition of the anthropogenic turbation on the seafloor.

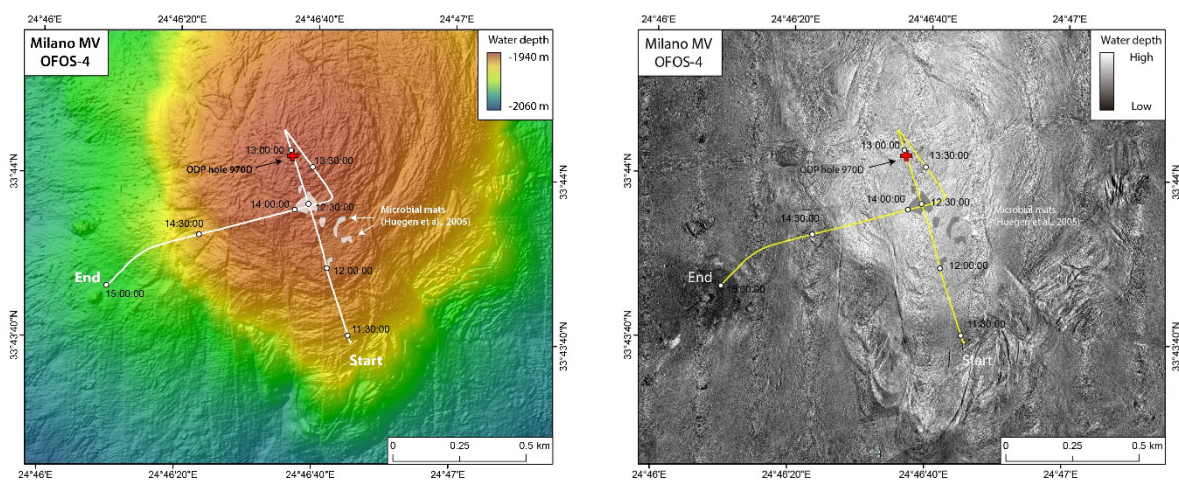


**Fig. 5.6.22:** Track line of OFOS-04. Detailed bathymetry (left) and backscatter map (right). Red cross: ODP bore hole 970d; White blocks: bacterial mats reported by Huguen et al., 2005.

### Description along the track:

We deployed the OFOS south east of Milano MV and traversed with 0.3 knots along the mud flow structure approaching the recorded bacterial mats, and the most active area, after crossing the most active area we moved towards the ODP drilling location. After we reached the reported ODP bore hole site, we extended along the same track to the edge of the previously recorded active area and then made a turn in order to re-enter the major bacterial mats area. Afterward we traversed to the west of the MV in order to reach the target area of a protruding structure following with low backscatter. However, before we reached the next target, we lost the HD video camera signal hence we ended the survey.

**Key results:** Along the mud flow structures, deposition of pteropod can be observed along the low-lying area (Fig. 5.6.25). We could not find the bacterial mats on the mud flow of the previously recorded sites. However, increasing small clasts patches with the mixture of shells could be observed as we followed along the mud flow (Fig. 5.6.24). The previous recorded most active area currently shows the similar extent of thin carbonate crust and reduced sediment spots (Fig. 5.6.25). Wide extent of shell patches can be observed. The yellow-brown colored sediment patches were reported as yellow bacterial mats. The yellow brown sediment patches were observed covering the thin carbonate crust in this OFOS deployment; however, it is not confirmed as bacterial mats. At

the same area, reduced sediment patches were observed accompanied with white discoloring rim (Fig. 5.6.27). Tubeworms could also be observed in this area, however only a few of living tubeworms were found (Fig. 5.6.26). Although we had passed the ODP 970d drilled site, the bore hole was not observed. Tectonic scarps were observed within a short distance to the active area (Fig. 5.6.28). The re-entering of the active area is showing the similar variation of sediment color, carbonate crusts and the increasing number of shell patches and tubeworms. As we left the active area, the seafloor shows the transition from the dense shell patches to mixture of small clasts to the pteropod.



**Fig. 5.6.23:** Pteropod along the low-lying area.



**Fig. 5.6.24:** Mixture of clasts and shells.



**Fig. 5.6.25:** Living and dead tubeworms and the area covered by mixture of dense shell patches and clasts.



**Fig. 5.6.26:** Thin carbonate crusts covered by yellow-brown patches with reduced sediments under-lying.



**Fig. 5.6.27:** Reduced sediment and dis-coloring observed in the northwestern domain of the active zone.



**Fig. 5.6.28:** Tectonic scarp observed in the northwestern domain of the active zone.

### OFOS-05 Deployment (Station SO278-53-1, GeoB24353-1)

Area:	Flare Site	
Date:	Friday, 13 November 2020	
Start bottom (UTC):	12:39	
End bottom (UTC):	17:03	
Bottom time:	04:24	
Start bottom (Lat, Long, Depth):	34° 09.87738' N	24° 18.82541' E, 1847 m
End bottom (Lat, Long, Depth):	34° 09.76004' N	24° 18.36878' E, 1861 m
Responsible Scientist:	Miriam Römer	

**Goal of the dive:** Find and document the seep area at which the flares detected hydroacoustically originate and investigate the brine pool visible in the high-resolution AUV map acquired prior to the OFOS deployment.

**Key results:** During the first part of the OFOS deployment, the seep area has been crossed several times. Seep indicators were found, e.g. tubeworms (some still living), shells, precipitates, however, uprising bubbles could not be proven visually. The second part of the dive was dedicated to find and explore the brine pool. The area was found immediately and crossed several times. Although the brine pool is not filled by brine anymore, a highly heterogeneous seep environment could be documented.

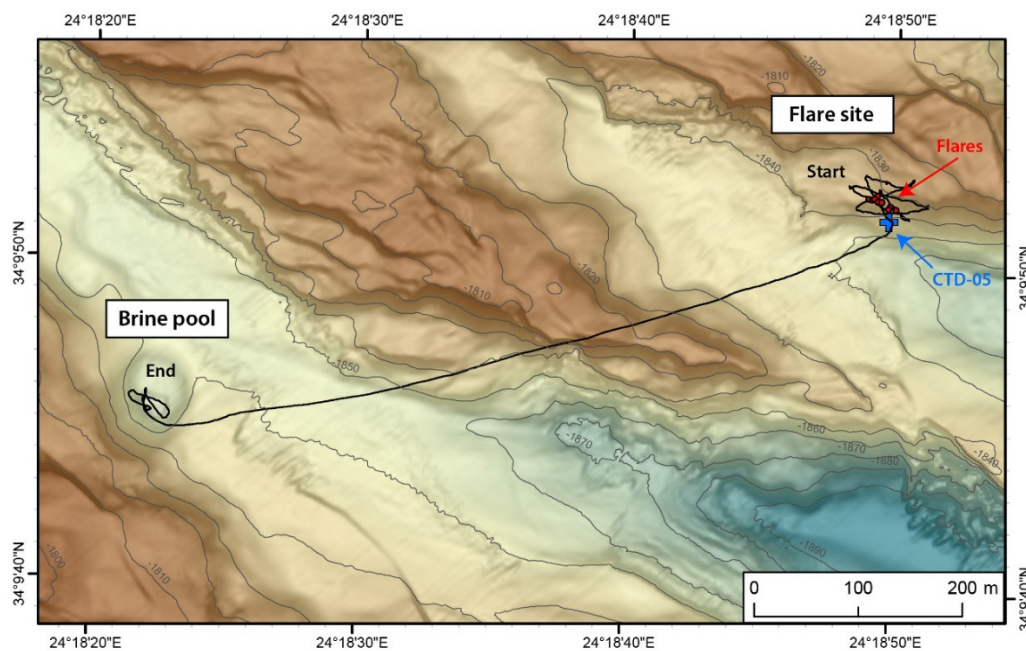


**Fig. 5.6.29:** Seafloor track during the OFOS-05 deployment starting at the Flare Site in the east and ending at the brine pool investigated in the west. The navigation based on the mapping data acquired during AUV Dive 99.

#### Description along the track:

The major aim of the OFOS-05 deployment was to detect and visually document the area in which flares have been found hydroacoustically (Flare Site, Fig. 5.6.29). A flare has been first seen in ship-based multibeam records and proven with Parasound after passing the site in its central part. The subsequent AUV Dive 99 has finally provided more details of the Flare Site (Fig. 5.6.30) and shown that about 9 individual gas bubble streams occur in an area of about 30 m length. However,

exact geographic positioning was difficult due to rectification of the AUV multibeam records and had to be estimated based on ship-based records. The start of our search was only few meters north of the estimated position of these gas bubble emissions at a flank of a NW-SE directed ridge in about 1840 m water depth. Several transects were mapped in a star-like pattern and about 70-80 m transect lengths to cover as much of the area as possible without missing the most interesting areas. This search and documentation of the flare site took about 2.25 hours, from 13:45 UTC to 15:00 UTC.

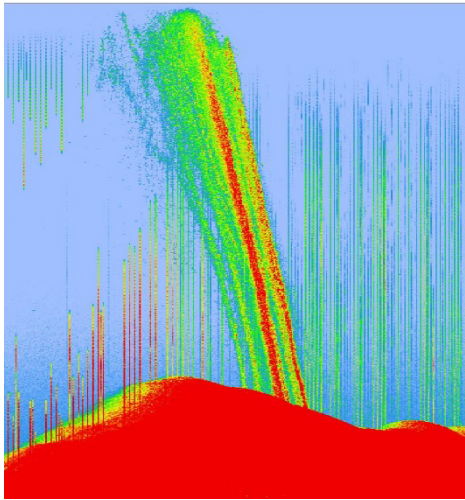


**Fig. 5.6.30:** Flares visualized from the multibeam water column data recorded during AUV Dive 99.

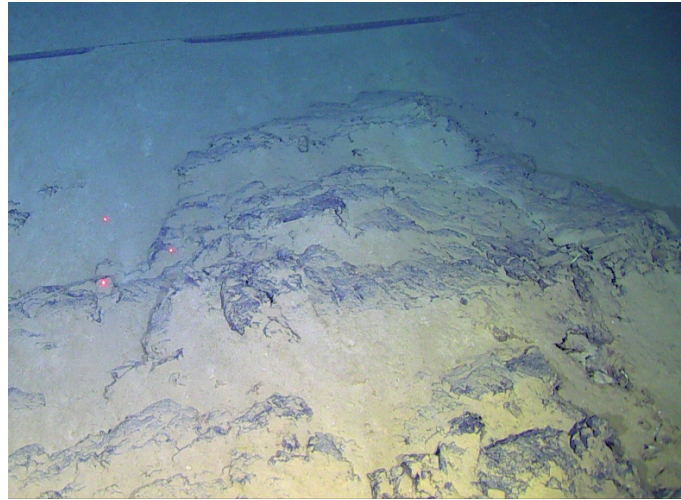


**Fig. 5.6.31:** Seafloor image from the seep area detected. Living tubeworms settle along a crack in the outcropping bedrock.

Gas bubble emissions could not be observed. However, numerous indications for seepage in the close surrounding were detected, of which living tubeworms have been the strongest indication for recent methane escape. The only living tubeworms were seen settling along a crack in outcropping bedrock material (Fig. 5.6.31). Remains of dead tubeworms have been found in the entire area, most of them probably transported from a higher level at the ridge. Although some seem to be in situ position nestling at holes in the sediment. Numerous tubes were found individually occurring, but in some places, also accumulations were observed (Fig. 5.6.32). A small whitish patch could be made of microbial mat, which has been detected in a more darkish appearing area (Fig. 5.6.33).



**Fig. 5.6.32:** Area of dense tubeworm remains, white shells and possibly precipitate crumble (yellowish).

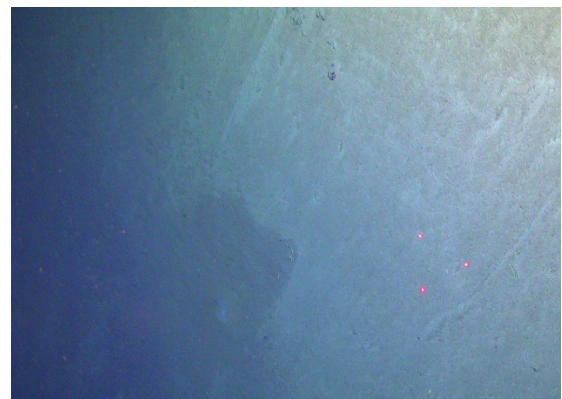


**Fig. 5.6.33:** A darkish appearing area with a small whitish patch, possible made of microbial mat.

At 15:00 UTC the southern end of the estimated seep area was reached, which is the position of CTD-05 revealing elevated methane concentrations, especially high in 20 to 150 m above seafloor. As flares were deflected to the SSE, it appeared the CTD-05 deployment was positioned few tens of meters south of the seafloor source of bubble streams. Any sign of seafloor seepage has been visible at this site, confirming this assumption.

A transit of about 730 m to 256° with increased tow speed of 0.5 knots followed this first part of the dive. The aim for the second part of the OFOS-05 deployment was to detect and investigate the erosional pit visible in the AUV Dive 99 bathymetric map, which was interpreted to be a brine pool (Fig. 5.6.29). It was unclear if the pit is still filled by a brine lake or already empty. The transit to that area did not show any signs of seepage. A ridge of about 30 m in height was passed. Soft sediments with bioturbation signatures and pteropod remains have been most abundant, as well as bedrock outcrops. After about one hour the brine pool area was reached.

The pit has a diameter of about 80 m and is less than 10 m in total depth. A smaller inner depression of only about 15 m in diameter and just 2-4 m in depth became visible in the AUV map. This central depression is also characterized by high backscatter. The OFOS was maneuvered nicely into the most central part of this pit in the area of high backscatter and the transition between soft sediments to shell accumulations and dense rock clasts has been observed (Fig. 5.6.34). The clasts are most probably the cause for the high backscatter. No brine lake has been found. The inner depression has been surveyed for the last hour of the dive and it was possible to cross the depression three times. Besides the dense rocks in the inner part, a flourishing seep community has been observed. Some areas show highly reduced sediments covered by microbial mats (Fig. 5.6.35). Between the rock clasts, lots of still living tubeworms were seen (Fig. 5.6.34) as well as crabs.

Unfortunately, this OFOS dive could not be conducted using the still camera (due to technical issues). However, the video camera has been recorded and can be used to produce mosaics of this pit.



**Fig. 5.6.34:** Large and dense rock clast in the central part of the pit investigated. Not a brine lake has been found, but a flourishing seep environment with living tubeworms, crabs and shells.



**Fig. 5.6.35:** Some part of the pit I covered by smaller, whitish clasts. Darkish reduced sediments and covering white microbial mats document the ongoing seep activity in this pit.

## 5.7 Heat Flow Measurements

(N. Kaul, N. Warnken)

During cruise SO278 we used the 6 m long Giant Heat Flow Probe (GHF) from GEOMAR, Kiel. The heat probe is designed for operation in a pogo-style mode up to 6000 m water depth. Due to the 5.25 m operation-length of its temperature sensor string, the influence of gas or gashydrate beneath the AOM transition zone can be observed.

The heat probe (Fig. 5.7.1) is constructed in the classical “violin bow” design (Hyndman et al., 1979; Hartmann and Villinger, 2002, Villinger et al., 2010), with 22 thermistors distributed over an active length of 5.25 m in 0.25 m intervals mounted inside an oil filled hydraulic tube (O.D. 14 mm) which is attached to the strength member (O.D. 130 mm). The sensor tube also contains a heater wire for the generation of high energy heat pulses, typically of 1100 J/m. This enables in-situ thermal conductivity measurements according to the pulsed needle probe method (Lister, 1979).



**Fig. 5.7.1:** Recovery of the heat probe, using the deep sea wire and the crane (Photo: Yiting Tseng).

The data acquisition unit including power supply (Sea & Sun, Trappenkamp, Germany) is housed in a single titanium pressure case (110 mm O.D. x 300 mm) and mounted inside the probe's weight stand. A second pressure case houses the battery pack for heat pulses. For heat flow stations during this cruise, data acquisition unit #212 was used. The signal of the temperature sensors is measured with a resolution of 20-bit at a sample rate of 1 sec, resulting in a final temperature resolution of better than 1 mK at ambient seafloor temperatures. A calibrated PT-100 seawater sensor allows for calibration of the sensor string with reference to the deep water. Inclination and acceleration of the probe is measured to monitor the penetration. We used the 18 mm coring wire and operated in autonomous mode with internal data storage and automated heat pulse trigger at all times.

Winch speed for penetration of the heat probe is 1.0 m/s at all sites. Time to equilibrate to in situ temperatures is assumed to be 7 minutes; time for heat pulse decay observation takes another 8 minutes. A USBL (IXSea Posidonia) pinger, mounted to the coring wire 50 meters above the instrument allowed to monitor the position of the heat probe at depth on all sites. As the water depth rarely exceeds 2000 m this works reliable. Figure. 5.7.2 shows two examples of heat flow measurements made during SO278.

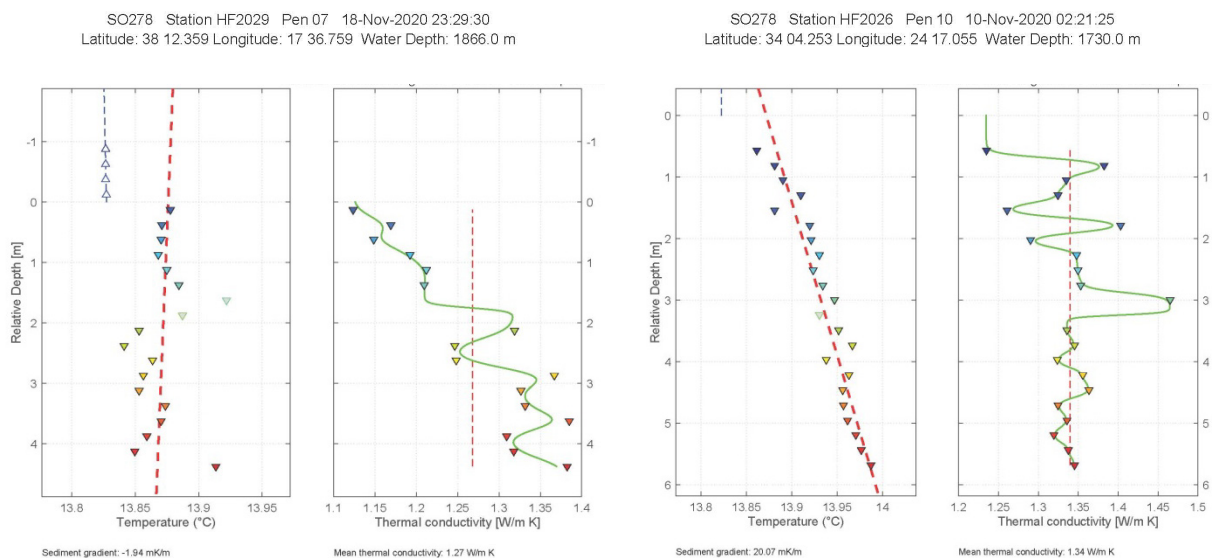


**Fig. 5.7.2:** Temperature gradient ( $dT/dz$ ) and thermal conductivity ( $k$ ) results of two representative sites. a) is located on Sartori MV, Calabrian arc, b) near Nice MV, Olimpi mud volcano field. Penetration depths of 4 m and more are abundant;  $k$ -values above 1.25 W/m K are common.

### Temperature measurements at a brine pool

At site GeoB24348 (HF2040 in Table 5.7.1) a gravity corer (GC 23), equipped with 6 autonomous temperature loggers (MTLs) was lowered into a structure, inferred as submarine brine pool. Temperature measurements are intended to detect a temperature anomaly in and underneath this water mass. The GC was lowered at a speed of 0.3 m/s to account for the assumed soft seafloor. First, the boundary between seawater and brine was met, indicated by a temperature jump of  $+0.49^{\circ}\text{C}$ , then after 66 seconds or 19.8 m the seafloor was reached. The temperature increase is almost instantly by  $+1.13^{\circ}\text{C}$ . Thus upper and lower boundary of the brine pool appear as remarkable temperature boundaries, pointing to an additional heat source to maintain these steep temperature gradients.

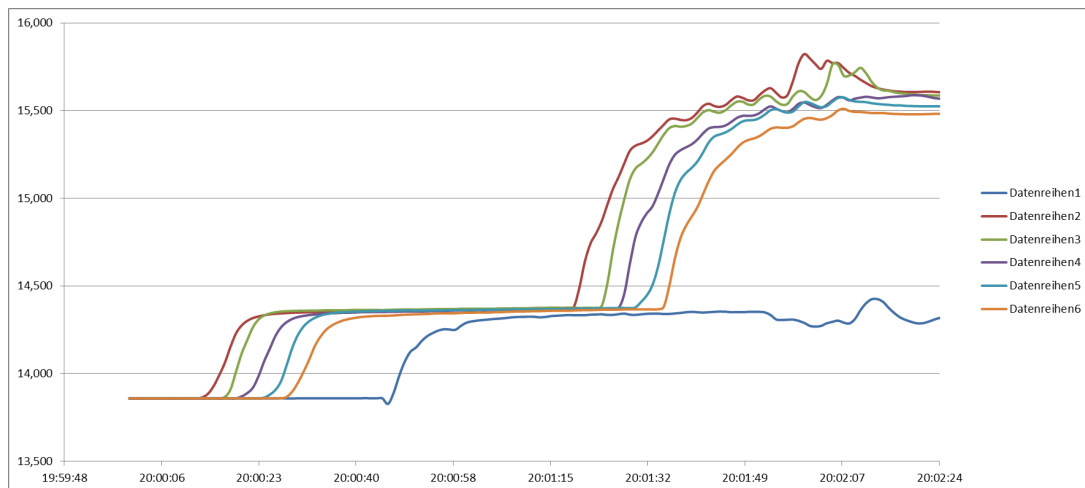


**Fig. 5.7.3:** Temperature-time graph of all six MTLs on GC23. The red line (left most) corresponds to the logger at the tip, the blue line (right most) to that, mounted above the head of the GC. The lag between loggers relates to their distances (0.89 m) @ 0.3 m/s. First temperature jump: top of brine, second jump: top of sediments.

### Preliminary results

In total, a number of 100 positions were tested on 10 stations. At 3 sites we failed to penetrate the ground, resulting in a success rate of 97%. All of the sites are located in or near mud volcanoes of varying activity. Thus many temperature-depth profiles include signs of non-steady-state processes. These processes can include gas emissions, gas hydrate dissolution or mud flows. As a result these measurements do not represent the geothermal heat flow but processes connected to the activity of mud volcanoes. In many cases the resulting calculated vertical temperature gradient is negative pointing to an unbalanced temperature field.

The highest temperature gradients can be found on the eastern chimney of Sartori MV (0.37 – 0.45°C/m) of the Calabrian accretionary wedge while all other measurements within or near the MV exhibit low gradients (Fig. 5.7.4). The second most active MV is the Nice MV of the Western Olimpi field. Here we find 0.26°C/m, a value which could not be observed on any other MV of the Hellenic MV fields.

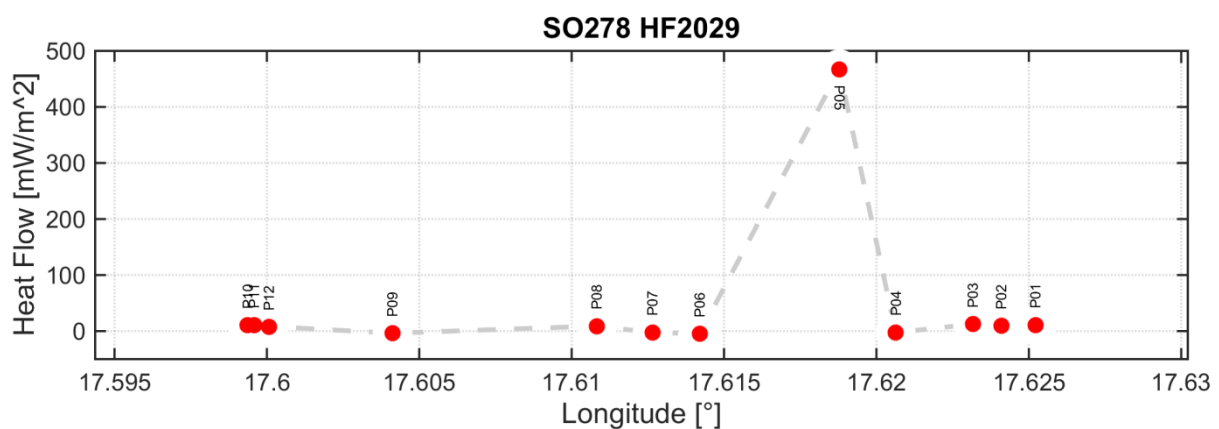


**Fig. 5.7.4:** Heat flow profile from W to E across Sartori MV, Calabrian arc. Sites P04 - P06 are located on top of the MV, P07 – P12 are up to 2 km away. The difference in activity between the chimney and the surrounding is obvious. All other HF values are about 10 mW/m<sup>2</sup>.

**Table 5.7.1:** Temperature gradients and thermal conductivities of all sites.

ID	Latitude		Longitude		Temp. Grad. [mK/m]	Mean TC [W/Km]
	DD	MM.MMM (N)	DDD	MM.MMM (E)		
HF2020P01	38	12.037	17	37.686	7.0	1.20
HF2020P02	38	12.128	17	37.504	6.6	1.20
HF2020P03	38	12.234	17	37.316	-2.9	1.20
HF2020P04	38	12.296	17	37.191	66.5	1.20
HF2020P05	38	12.343	17	37.118	367.8	1.20
HF2020P06	38	12.378	17	37.052	89.5	1.20
HF2020P07	38	12.411	17	36.988	139.9	1.20
HF2020P08	38	12.472	17	36.870	-15.4	1.20
HF2020P09	38	12.554	17	36.728	6.9	1.20
HF2020P10	38	12.674	17	36.507	8.5	1.20
HF2021P01	33	44.592	24	45.945	10.7	1.39
HF2021P02	33	44.485	24	45.741	NaN	1.20
HF2021P03	33	44.403	24	45.541	0.3	1.20
HF2021P04	33	44.331	24	45.362	13.4	1.43
HF2021P05	33	44.316	24	45.201	-7.3	1.20
HF2021P06	33	44.315	24	45.144	5.6	1.78
HF2021P07	33	44.315	24	45.054	91.0	1.44
HF2021P08	33	44.308	24	44.866	8.0	1.20
HF2021P09	33	44.289	24	44.723	NaN	1.20
HF2021P10	33	44.272	24	44.504	10.6	1.20
HF2021P11	33	44.273	24	44.363	23.3	1.47
HF2021P12	33	44.270	24	44.188	42.5	1.42
HF2021P13	33	44.088	24	44.388	19.7	1.20
HF2022P01	34	07.915	24	55.619	13.2	1.27
HF2022P02	34	06.883	24	55.620	19.2	1.20
HF2022P03	34	05.510	24	55.618	60.5	1.16
HF2022P04	34	05.080	24	55.625	32.1	1.15
HF2022P05	34	03.903	24	55.619	23.7	1.18
HF2022P06	34	02.932	24	55.625	21.4	1.20
HF2023P01	34	02.169	24	55.520	11.1	1.24
HF2023P02	34	01.782	24	55.528	11.0	1.20
HF2023P03	34	01.557	24	55.534	14.0	1.20
HF2023P04	34	01.333	24	55.525	19.1	1.16
HF2023P05	34	01.207	24	55.525	16.6	1.20
HF2023P06	34	00.757	24	55.539	12.9	1.20
HF2023P08	33	59.866	24	55.504	20.3	1.32
HF2024P01	33	44.177	24	44.436	20.5	1.20
HF2024P02	33	44.143	24	44.353	26.2	1.20
HF2024P03	33	44.100	24	43.904	18.3	1.20
HF2024P05	33	44.067	24	43.515	-6.0	1.20
HF2024P06	33	44.061	24	43.471	4.8	1.39
HF2024P08	33	44.052	24	43.380	8.3	1.30
HF2024P09	33	44.040	24	43.267	10.7	1.30
HF2024P10	33	44.022	24	43.037	20.0	1.30
HF2025P01	33	30.625	25	30.834	21.9	1.19
HF2025P02	33	30.613	25	30.254	18.4	1.20
HF2025P03	33	30.611	25	29.831	3.6	1.20
HF2025P04	33	30.597	25	29.430	2.9	1.44
HF2025P07	33	30.571	25	28.112	26.4	1.20
HF2025P08	33	30.559	25	27.516	27.4	1.20
HF2026P01	34	02.205	24	19.731	2.8	1.29
HF2026P02	34	02.363	24	19.597	33.2	1.20
HF2026P03	34	02.668	24	19.351	1.8	1.20
HF2026P04	34	03.107	24	19.024	17.6	1.20
HF2026P05	34	03.496	24	18.721	-13.9	1.20
HF2026P06	34	03.965	24	18.356	182.3	1.41
HF2026P07	34	04.019	24	18.367	259.2	1.20
HF2026P08	34	04.085	24	18.033	68.0	1.20

HF2026P09	34	04.168	24	17.534	28.5	1.41
HF2026P10	34	04.253	24	17.055	20.1	1.34
HF2026P11	34	04.369	24	16.395	14.8	1.20
HF2027P01	34	03.141	24	19.547	7.8	1.50
HF2027P04	34	03.080	24	18.629	-5.8	1.41
HF2027P05	34	03.059	24	18.410	1.8	1.40
HF2027P06	34	03.040	24	18.167	.0	1.40
HF2027P07	34	03.032	24	17.977	-13.6	1.40
HF2027P08	34	03.016	24	17.681	11.7	1.38
HF2027P09	34	02.986	24	17.335	-12.1	1.40
HF2027P10	34	02.966	24	17.141	2.7	1.28
HF2027P11	34	02.940	24	16.741	19.7	1.20
HF2027P12	34	02.921	24	16.512	30.2	1.12
HF2028P01	35	56.616	20	46.394	NaN	0.90
HF2028P02	35	56.920	20	46.848	11.2	0.90
HF2028P03	35	57.282	20	47.248	10.7	1.33
HF2028P04	35	57.660	20	47.208	-12.2	1.20
HF2028P05	35	58.113	20	47.182	101.1	1.34
HF2028P06	35	58.165	20	47.150	23.4	1.30
HF2028P07	35	58.231	20	47.146	-18.7	1.44
HF2028P08	35	58.627	20	47.092	-51.6	1.40
HF2028P09	35	58.991	20	47.037	-0.7	1.40
HF2028P10	35	59.459	20	46.981	3.7	1.40
HF2029P01	38	12.612	17	37.513	9.0	1.20
HF2029P02	38	12.562	17	37.446	7.8	1.20
HF2029P03	38	12.504	17	37.390	10.7	1.15
HF2029P04	38	12.386	17	37.238	-1.9	1.29
HF2029P05	38	12.331	17	37.127	447.2	1.05
HF2029P06	38	12.353	17	36.852	-4.0	1.20
HF2029P07	38	12.359	17	36.759	-1.9	1.27
HF2029P08	38	12.374	17	36.649	7.0	1.33
HF2029P09	38	12.390	17	36.247	3.4	1.26
HF2029P10	38	12.135	17	35.962	8.0	1.25
HF2029P11	38	11.716	17	35.975	9.5	1.15
HF2029P12	38	11.410	17	36.004	6.6	1.12
HF2040P01	33	38.347	24	38.882	17.8	1.20

## 5.8 Sediment Sampling and Sedimentology

(N. Behrendt, A. Eijsink, B. Niederbockstruck, O. Coulibaly, D. Antoniou, J. Krahl, G. Feddersen, S. Rau)

### Introduction

During expedition SO278 with RV SONNE gravity cores (GC), minicores (MIC) and multicores (MUC) were taken in order to investigate mud breccia of different mud volcanoes, stratigraphic sequences and fault zone material between the Mediterranean Ridge (MedRidge) accretionary complex and the Inner Ridge/Cretan margin. Overall, we sampled 16 mud volcanoes (MVs) in 5 different areas: 1) the Calabrian arc (Sartori MV); 2) the Olimpi mud volcanic field (Bergamo MV, Napoli MV, Monza MV, Moscow MV, Maidstone MV, Leipzig MV, Milano MV, unnamed MV); 3) the western Olimpi mud volcanic field (Nice MV, Gelendzhik MV, Heraklion MV and an unnamed MV); 4) the United Nation Rise (Dublin MV) and 5) the Cobblestone area (Helios MV and an unnamed MV). These mud volcanoes were sampled to investigate their activity and recent evolution.

A first indication of the activity of a mud volcano is given by the amount of hemipelagic sediment overlaying the mud breccia. Based on the sedimentation rate, which is between 2.2 to 4.3 cm/kyr (Mercione et al., 2000) in the eastern Mediterranean and 2 to 3 cm/kyr (Cita et al., 1996) in the region of the MedRidge, the last activity of the mud volcanoes can be estimated. For this, especially cores taken at the active center are important. Cores taken on the flanks of the mud volcanoes will give information about successive mud flows, if multiple are found in one core, as well as the relative timing of individual mud flows. When present, marker horizons, such as tephra layers (Keller et al., 1978, Narcisi et al., 1999) and sapropels (DeLange, 2008; Mercione et al., 2000) can provide more detailed timing of the activity.

The Sartori mud volcano within the Calabrian arc has been investigated in the past by expedition M112 with RV METEOR in 2014 (Bohrmann et al., 2015) and expedition POS499 with RV POSEIDON in 2016 (Bohrmann et al., 2016). The current expedition aimed to reveal the structure and evolution of the mud volcano and individual mud flows in more detail. Therefore, the Sartori mud volcano was cored both at the active center and compared with several gravity cores in the surroundings.

The sampling of the mud volcanoes at the MedRidge was mainly meant to compare their geochemical (pore water and interstitial gas) compositions. Therefore, at these mud volcanoes we targeted the region of the latest outflow. This was done either by using detailed AUV maps (bathymetry and backscatter images) or by bathymetric data obtained by swath sonar bathymetry from the RV SONNE. In this case, a low amount of hemipelagic sediments overlying the mud breccia confirms the core was taken at an active chimney. Several mud volcanoes within the Olimpi and Cobblestone mud volcanic fields have been successfully sampled. When possible, the sampling strategy was based on AUV maps, which allowed precise sampling within the region where the latest outflow occurred. This was done for Milano MV, Bergamo MV, Monza MV, Helios MV, Gelendzhik MV and Nice MV. The locations of latest outflow on other MVs were determined by using swath sonar bathymetry in combination with backscatter imaging. The high amount of successfully cored mud volcanoes gives a comprehensive picture of the mud volcanoes at the different positions and allows for further analyses of the differences and similarities between individual mud volcanoes as well as between the different mud volcanic fields.

The fault zones between the MedRidge, the Inner deformation front and the Inner Ridge of the Cretan margin have been targeted during the POS410 expedition with RV POSEIDON in 2011 (Kopf et al., 2012a, 2012b). Some sites where mud breccias were found during those previous cruises have been revisited, to locate these possible mud outflow sites with more targeted coring based on the more detailed maps that could be made by the swath sonar bathymetry system present on board of the RV SONNE and the AUV.

## **Description of the methods**

### *Gravity Corer (GC)*

During SO278 a gravity corer from the MARUM – Center for Marine Environmental Science, Bremen, was deployed 38 times. The barrel has a weight of ca. 1.5 t. Depending on the area of investigation, the gravity corer was equipped with a pipe length of either 5.75 m for sediments expected to contain mostly mud breccia or 8.75 m to retrieve longer records with hemipelagic sediments. After the liner was inserted into the pipe, a core catcher was mounted to hold the sediment back during the heaving process.

The gravity corer was deployed into the water with a deep-sea winch via the RV SONNE's cradle system (Fig. 5.8.1). To have an accurate position of the gravity corer a pinger was mounted 50 m above the device of the wire.

The device then was lowered with a speed of 1.0 m/s to a depth of 100 m above the seafloor. This position was held for 1 minute to reduce oscillating and rotating movements of the system. After that the shorter gravity corer (5.75 m) was lowered with a speed of 0.6 m/s and the longer one (8.75 m) with 1.0 m/s until it hit the seafloor. For deeper penetration, the device remained in the sediment for 1 minute until it was heaved with 0.2 m/s out of seafloor.



**Fig. 5.8.1:** Deployment of the gravity corer via the RV SONNE's cradle system (©Sven Lenius).

When the device left the seafloor it was heaved with 1.3 m/s to the sea surface where it got placed back into the cradle system.

#### *(TV-)Multicorer (MUC) and Minicorer (MIC)*

In order to retrieve non-disturbed surface sediment samples a multicorer got deployed on 30 stations equipped with 6 tubes and an additional weight of 320 kg on the top. The tubes have a length of 61 cm and an inner diameter of 9.4 cm. Three of them contained a vertical row of small holes with a spacing of 5 cm to allow fast pore water analyses along the sediment tube. These holes are taped before every deployment (Fig. ).

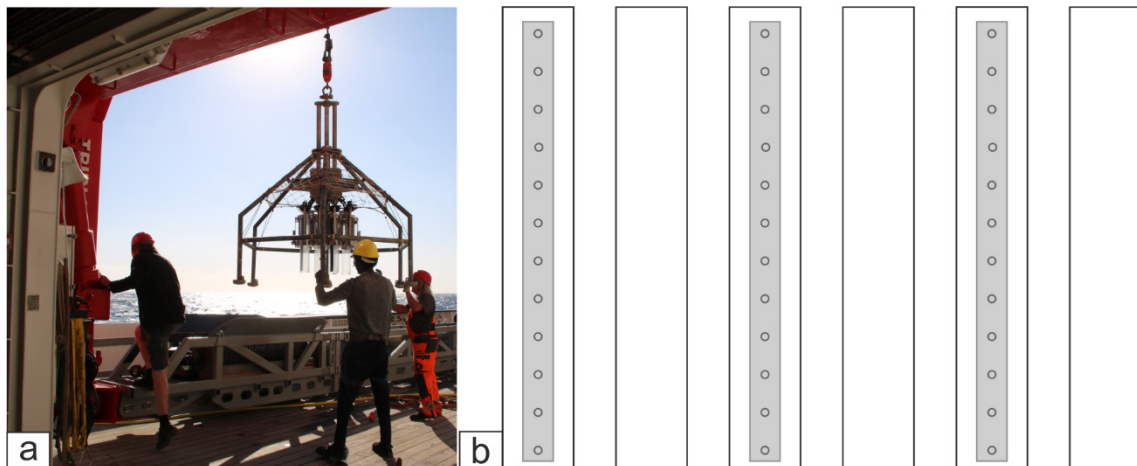


**Fig. 5.8.2:** a) shows the deploying of the multicorer attached to a deep-sea winch (©Julia Krahl). b) schematic sketch of the tubes. Half of them were prepared with holes every 5 cm in order to allow pore water analyses.

The multicorer was deployed directly into the water by the deep-sea winch. As for the gravity corer, a pinger was mounted after 50 m above the device to get the exact position of the sample at the seafloor. The multicorer was lowered with a speed of 0.7 m/s to a depth of 100 m above the seafloor. The position was held for 1 minute to reduce oscillating and rotating movements of the

system. The multicorer was lowered with 0.3 m/s until it reached the seafloor. For successful penetration, the device remained in the sediment for 1.5 minutes until it was heaved with 0.3 m/s out of the sediment. Then the multicorer was heaved back to sea surface with 1.0 m/s.

In addition to the multicorer we also used a minicorer on 4 stations to retrieve non-disturbed surface sediment samples. The minicorer was equipped with 4 tubes with a length of 61 cm and an inner diameter of 5.6 cm. Similar to the multicorer, half of the tubes were prepared for pore water analyses. The process of lowering and heaving followed the same principles as for the gravity corer and the multicorer, with as main difference that it was lowered and heaved at a lower velocity (Tab. 5.8.1). The minicorer (MIC) was deployed at the beginning of the expedition, but after four deployments it was decided to replace the MIC by the faster multicorer (MUC).

**Table 5.8.1:** Rope speed during different steps of retrieving sediment with the devices used on board during SO278.

	lowered to 100 m above the seafloor [m/s]	penetrate the seafloor [m/s]	heaved out of the seafloor [m/s]	heaved to sea surface [m/s]
Gravity Corer (5.75m)	1.0	0.6	0.2	1.3
Gravity Corer (8.75m)	1.0	1.0	0.2	1.3
Multicorer	0.7	0.3	0.3	1.0
Minicorer	0.5	0.3	0.3	0.7

From each deployment, two multicores were used for gas chemistry and pore water geochemistry, one was used for sediment description and one was immediately frozen at -20°C. Before the multicore was frozen, a part of the overstanding water column was removed. After the multicores were completely frozen, the line was removed as well as the redundant water column and they were refrozen wrapped in plastic foil. This was done for all MUCs, except for MUC-14, where we preserved the water column because it showed tubeworms within the water column. The MICs obtained during this expedition were handled similar as the MUCs.

### *Sediment description*

When the gravity core was on deck, the core catcher was removed from the liner and when significant amounts of sediment were present, these were either described or preserved. Then, starting from the bottom, the gravity core liners were cut into sections of 1 m length. Headspace and porosity samples have been taken directly from working half each of bottom segment. The sections were closed with caps and tape on both ends and labeled according the GeoB-standard scheme. Then first, their magnetic susceptibility and electrical conductivity were measured by the Multi-Sensor-Core-Logger (see Chapter 5.9). From several cores which contained undisturbed mud breccia, as confirmed by the MSCL data, some whole round samples were taken for further geotechnical analysis at MARUM – Center for Marine Sciences in Bremen. Overall, whole round samples have been taken from 11 gravity cores. Each mud volcano and fault zone, where mud breccia was assumed, 10-20 cm material was taken at the top or bottom of one segment. Some geotechnical methods (e.g. oedometer tests) require undisturbed material. Due to the significance of the water content in these tests, whole round samples have been preserved in the liners and will also be stored at 4°C in the core repository at MARUM – Center for Marine Sciences. The core liners were split sideways using two vibration saws and the cored sediment was cut with a fishing line into working and archive half. After splitting the cores, samples for gas chemistry (see Chapter 5.12) and pore water geochemistry (see Chapter 5.11) were taken from the working half. The archive halves were scanned with a line scanner and afterwards described from a sedimentological

viewpoint. Archive and working half were separately stored in D-tubes and stored at 4°C, as were the whole round samples.

Sediment description was done on the archive halves. The color and the grain size of the sediment were visually described according to the Munsell's color chart nomenclature and Wentworth's (1922) classification using a hand-lens. HCl-testing was done on some clasts, aiding the distinguishing between gypsum and calcite. When describing the clasts present in mud breccias, we distinguished between clay/mud/silt clasts and mudstone/claystone/siltstone by their grade of lithification. Mudstone clasts are lithified, while clay/mud clasts can be compacted but are not lithified. All information, including sedimentary structures have been noted. Additionally, smear slides of dominant lithologies were prepared and have been studied under an optical microscope equipped with plane and crossed polarized light. The examination of very fine grain size particles gives the opportunity to have a more detailed overview of the lithology of the sediment. During this expedition, 288 smear slides were prepared, of which 276 were examined. The preparation of the smear slides was completed according to the directions of International Ocean Discovery Program (IODP). The study of the smear slides and the recognition of the minerals and fossils was based on Marsaglia et al. (2013), Marsaglia et al. (2015) and Rothwell (1989).

The mini- and multicores were described in a similar manner. They had to be pushed out of their respective liners, during which they were compressed. The top part was often too incoherent to stay stable outside of the liner. Their lengths were therefore measured both before and after removing them from the liner, to estimate the right depths for layer boundaries.

For each core two pages are compiled in the appendix: one describing the stratigraphy of the core, with a basic sedimentary description of different layers (e.g. sapropel or tephra layer), including an overview of the samples that were taken at certain depths (smear slides, pore water samples and CH<sub>4</sub>) and measurements that were performed (shear strength, electric conductivity and magnetic susceptibility).

#### *Sediment core imaging (Line Scanner)*

To capture the visual appearance of the freshly split gravity cores, the archive core sections are optical documented directly after splitting in high quality onboard. For this, we used the SmartCIS 1600 LS line scanning system of the MARUM GeoB Core Repository. As a standard resolution for imaging, 500 dpi was selected, and the camera aperture was fixed at f/8 (MARUM webpage to GeoB smartCIS 1600 Line Scanner). To achieve optimal exposure of the sediment surface and to reduce potential shadow effects of rough surfaces two light sources for scanning were used. A white calibration of the system was done with the help of a standardized white tile every day. The automatic application of an IT8.7/2-target referenced ICC-profile ensured the absolute color reproduction of the line scan images. The section images are directly saved into the database system ExpeditionDIS as jpeg files. In addition, a tab-delimited text file with red, green, blue and lightness (%) values as well as red/blue ratios in 1 mm down-core resolution for each section is output.

During the cruise, we took cores with different sedimentological appearances, which had to be prepared for the line scanner in different ways. The very fine grained hemipelagic core sections with high water contents were freshly scraped with a spatula to ensure both a smooth surface without blurred boundaries of the layers and to capture the ephemeral nature of sedimentary

features as some features oxidize within minutes. Coarser layers like turbidites and ash layers were omitted. The surface of the core sections, which contain different kinds of mud breccia of the mud volcanoes were not smoothed. This was important to show the internal structure present in mud breccia better in the photos, for example vugs and bubble structures due to gas emission or small clasts. Big clay or stone clasts, which seemed to be interesting, were cleaned and repositioned in the archive half, before the line scan was taken. Especially the moussy structure of some mud volcanoes and also of the subsrosional pit next to the Nadir brine hole is easily recognizable in the obtained photos. Compilations of all sections for each core can be found in the appendix).

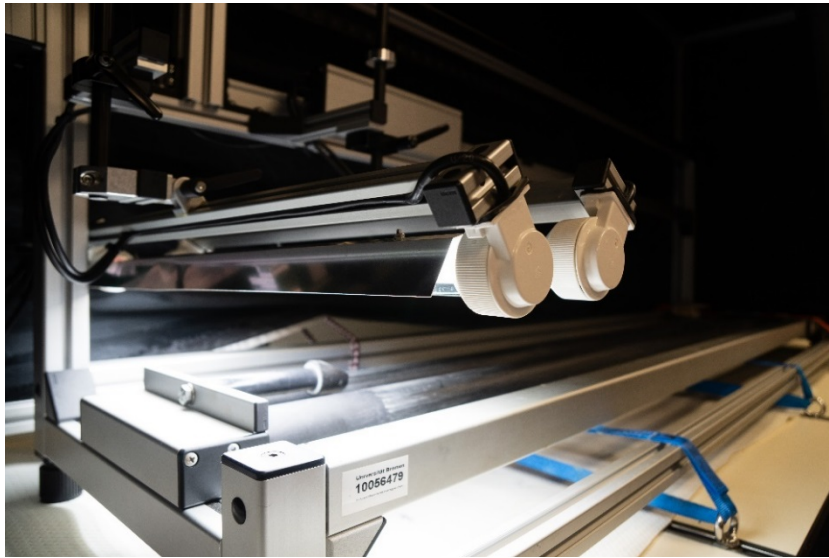


**Fig. 5.8.3:** SmartCIS 1600 LS line scanning system of the MARUM GeoB Core Repository on board of RV SONNE during expedition SO278 (©Heike Dugge).

Multicores and minicores were photographed by a camera and not by the line scanner, after they were cut lengthwise with a knife. The surfaces are more uneven, and lighting was not optimized, because of which colors might vary from the pictures.

### Preliminary results – sediment description

The gravity corer was overall deployed 38 times and 36 gravity cores were successfully recovered from the research areas. Table 5.8.2 provides an overview of the gravity cores, their length, location, as well as the corresponding MIC # or MUC # if one was taken at the same locality.

**Table 5.8.2:** Gravity cores sampled during SO278 expedition: GC # and GeoB # in compared with the length of the recovered gravity cores [cm], the water depth [m], the location and the corresponding MUC/MIC.

GC #	GeoB #	Recovery [cm]	Water depth [m]	Location	Corresponding MUC/MIC
GC-01	24302-02	205	1856	Sartori MV	MIC-01 / MUC-23
GC-02	24303-01	488	2006	Sartori MV	MIC-02
GC-03	24310-01	280	1933	Napoli MV	MIC-03
GC-04	24311-01	356	1930	Bergamo MV	MIC-04
GC-05	24312-01	20	3346	Fault Zone	-
GC-06	24312-02	61	3320	Fault Zone	-
GC-07	24315-01	393	2501	Fault Zone	MUC-02
GC-08	24316-01	480	3105	Fault Zone	-

GC-09	24318-01	482	3530	Fault Zone	MUC-03
GC-10	24319-01	-	3521	Fault Zone	-
GC-11	24320-02	519	3521	Fault Zone	-
GC-12	24323-01	318	1934	Bergamo MV	MUC-04
GC-13	24324-02	445	2038	West of Bergamo MV	MUC-05
GC-14	24326-01	238	1937	Bergamo NE plateau	MUC-06
GC-15	24327-02	219	1824	Moscow MV	MUC-07
GC-16	24328-01	185	1934	Maidstone MV	MUC-08
GC-17	24333-01	26	1933	Leipzig MV	MUC-09
GC-18	24337-01	183	2269	Dublin MV	MUC-10
GC-19	24340-01	124	1813	Unnamed MV	MUC-11
GC-20	24341-02	282	1737	Nice MV	MUC-12
GC-21	24343-01	318	1921	Monza MV	MUC-13
GC-22	24346-02	274	1956	Milano MV	MUC-15
GC-23	24348-02	537	2081	Subrosinal brine	MUC-14
GC-24	24351-01	284	1709	Gelendzhik MV	MUC-16
GC-25	24352-01	272	1714	Heraklion MV	MUC-19
GC-26	24355-01	78	1819	Nice MV	MUC-17
GC-27	24356-02	268	1812	Unnamed MV	MUC-18
GC-28	24359-02	251	2753	Helios MV	MUC-20
GC-29	24360-01	25	2762	Unnamed MV II	MUC-21
GC-30	24361-01	247	2751	Helios MV	MUC-22
GC-31	24363-02	198	2867	Helios MV	-
GC-32	24365-01	574	1967	South of Sartori MV	MUC-24
GC-33	24370-01	324	1887	Mud flow rim of Sartori MV	MUC-26
GC-34	24372-01	-	1888		MUC-27
GC-35	24373-01	564	1981	SW of Sartori MV	MUC-28
GC-36	24374-01	443	1977	SW of Sartori MV	-
GC-37	24375-01	464	1976	SW of Sartori MV	MUC
GC-38	24376-01	254	1858	2 <sup>nd</sup> chimney Sartori	MUC-30

In addition, 4 minicores (MICs) and 30 multicores (MUCs) have been taken from the research areas. These were deployed as supplement to the gravity corer to assure an accurate sampling of the hemipelagic layer, which is commonly disturbed when using the gravity corer. An overview of the MICs and MUCs can be found in Table 5.8.3. Because the MICs and MUCs were sampled in addition to the gravity cores, they will be discussed together in the following sections.

**Table 5.8.3:** MUCs/MICs sampled during SO278 expedition: MIC/MUC # and GeoB # in compared with the length of the recovered MIC/MUC [cm] and the water depth [cm].

MUC/MIC	GeoB #	Recovery [cm]	Water depth [m]	Location
MIC-01	24302-01	-	1856	Sartori MV
MIC-02	24303-02	15	2006	Sartori MV
MIC-03	24306-01	13	1932	Napoli MV
MIC-04	24311-02	23	1930	Bergamo MV
MUC-01	24312-03	30	3354	Fault Zone
MUC-02	24315-02	31	2501	Fault Zone
MUC-03	24318-02	38	3532	Fault Zone

MUC-04	24323-02	27	2041	Bergamo MV plateau
MUC-05	24324-01	59	2041	West of Bergamo
MUC -06	24326-02	32	1936	Bergamo NE plateau
MUC -07	24327-01	36	1824	Moscow MV
MUC -08	24328-02	32	1933	Maidstone MV
MUC -09	24333-02	34	1936	Leipzig MV
MUC -10	24337-02	24	2265	Dublin MV
MUC -11	24340-02	32	1812	Unnamed MV I
MUC -12	24341-01	28	1721	Nice MV
MUC -13	24343-02	27	1926	Monza MV
MUC -14	24344-01	55	2077	Brine hole
MUC -15	24346-01	32	1947	Milano MV
MUC -16	24351-02	43	1696	Gelendzhik MV
MUC -17	24355-02	32	1811	Nice MV
MUC-18	24356-01	-	1803	Unnamed MV
MUC-19	24357-01	30	1722	Heraklion MV
MUC-20	24359-01	34	2754	Unnamed MV I
MUC-21	24360-02	29	2758	Unnamed MV II
MUC-22	24363-01	33	2753	Unnamed MV I
MUC-23	24365-01	38	1856	Sartori MV
MUC-24	24366-02	23	1950	South of Sartori MV
MUC-25	24367-01	36	1894	Mud flow Sartori MV
MUC-26	24368-01	21	1865	Mud flow rim
MUC-27	24369-01	-	1888	Outflow west Sartori
MUC-28	24373-02	24	1980	SW of Sartori MV
MUC-29	24374-02	27	1976	SW of Sartori MV
MUC-30	24376-01	34	1858	2 <sup>nd</sup> chimney Sartori

### *Calabrian arc*

In the Calabrian arc, the Sartori MV has been the main target and was investigated in detail at the beginning and in the end of the expedition. In total, the gravity corer was deployed nine times at the Sartori MV and surroundings, whereby the deployment failed once, and the corer remained empty. Additionally, the hemipelagic top of the sequence was sampled by 2 MICs and 8 MUCs.

Both chimneys of the Sartori MV have been sampled (GC-01/MIC-2 and GC-38/MUC-30) and showed both a thin hemipelagic layer (MUC-23: 5 cm) on top of the moussy greenish-gray mud breccia. Both gravity cores showed larger siltstone clasts (up to 9 cm) and some clay clasts.

Three gravity cores (GC-32, GC-36 and GC-37) recovered mud breccia flows overlain and underlain by hemipelagic sediment (Fig. 5.8.4). The mud breccia flows in this case had a thickness of 133 cm, 178 cm and 134 cm. All three cores showed a small (4 cm) layer of mud breccia with smaller clasts and similar color to the upper hemipelagic material on top of the mud flows. The color transition here might be due to reducing conditions of the mud breccia material. These cores are ideal for investigating the time of the mud flows, as the hemipelagic sediments as well as the event layers that are present can be dated.

Two cores showed the boundary of hemipelagic sediment to mud breccia, but do not penetrate the mud flow (Fig. 5.8.4). GC-33 was sampled from a mud flow at the rim of the Sartori MV and showed mud breccia overlain by 65 cm hemipelagic sediment. The hemipelagic sediment includes

a tephra layer and a sapropel in the first two sections of the core. In GC-35, which was sampled southwest of Sartori MV, 464 cm hemipelagic sediment are on top of the underlying mud breccia. Only Core GC-02 which was taken further away from Sartori MV, showed hemipelagic sediment throughout the whole core (Fig. 5.8.4)

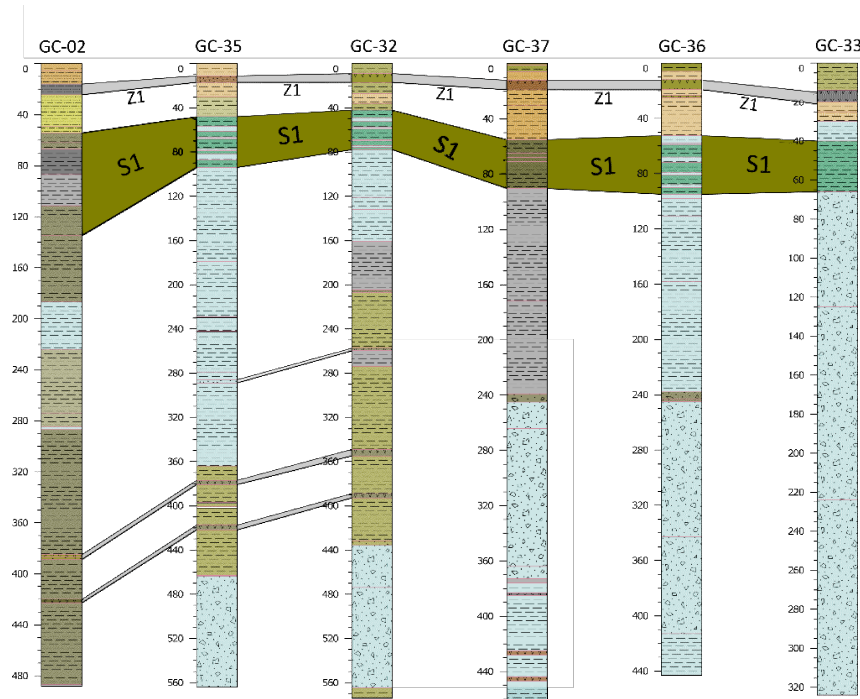


**Fig. 5.8.4:** Stratigraphic profiles of the gravity cores taken in the surroundings of the Sartori MV. Event layers as the distinct tephra layer Z1 and sapropel S1 can be correlated: tephra layers (correlated in gray) and sapropel (correlated in green). Further descriptions of the stratigraphic profiles can be found in the appendix.

Due to the occurrence of tephra layers and sapropels in most of the cores obtained from the Sartori MV and surroundings, a correlation of the stratigraphic profiles can be done. The tephra layer Z1, which has been dated of 45.7 ka cal. BP by Ar/Ar (Tomlinson et al., 2015) and sapropel S1, which was deposited between 10.4 – 5.7 ka cal. BP (Mercone et al., 2000) or 10.8 – 6.1 ka cal. BP (De Lange et al., 2008) could be recognized within all the gravity cores taken in the surroundings of the mud volcano (Fig. 5.8.4). The marker bed sapropel S1 was interrupted by nine turbidite beds during deposition (Polonia et al., 2015), which explains the distinctive color transition within the sapropel beds. We can also attempt to correlate the underlying ash layers with the aid of their magnetic susceptibility signature, but without more detailed analyses these should be viewed as preliminary correlations. Based on this, we can attempt to order the mud flow events, in which case GC-33 would be the youngest mud flow we cored, since it is directly overlain by the sapropel. GC-37 and/or GC-36 would be the before last mud flows, since they occur above the second tephra layer, although this is missing in GC-36 and therefore dating of the hemipelagic sediment is required. The mud breccias in GC-35 and GC-32 are likely to be the oldest we cored, since they occur below the lowest tephra layers we found.

#### *Olimpi mud volcanic field*

The gravity core from Napoli MV (GC-03) showed a greenish grey mud breccia with H<sub>2</sub>S smell and gas bubbles and gas expansion cracks in the lower sections. A hemipelagic cover of 11.5 cm

on top of the mud breccia could be determined by the corresponding MIC (MIC-03). In comparison to the Napoli MV, the Milano MV had a higher abundance of smaller clasts and gas bubbles as well as cracks through gas extension within the whole core. A hemipelagic cover was assumed by brownish material with a high-water content at the rim of the core and a hemipelagic coverage of 2 cm was confirmed afterwards by the corresponding MUC (MUC-15).

The Bergamo MV has been sampled by three gravity cores directly on the plateau (see Fig. 4.3). The latest outflow (GC-04) was sampled, as well as a location where the obtained heat flow profile showed an interesting anomaly (GC-12). Additionally, a core from the northeast (GC-14), where the backscatter was also significantly high, was sampled. GC-04 showed dark greenish-gray mud breccia with light H<sub>2</sub>S smell and many gas bubbles, some mud clasts up to 5 cm without a hemipelagic coverage while the other two cores had a hemipelagic cover of a few centimeters (MUC-04 and MUC-06, both with a hemipelagic cover of 3 cm) on top of the mud breccia, a stronger H<sub>2</sub>S smell and gaps through gas expansion.

The Monza MV is located between the Bergamo and Napoli MV and is rather small in comparison. The obtained gravity core (GC-21) showed a relatively dry dark greenish-gray mud breccia with different mud clasts, gas expansion gaps in the lower part of the core and inclined darker and lighter layers within the first segment. The gravity core showed no signs of a hemipelagic coverage, whereas the corresponding MUC (MUC-13) showed 4 cm of hemipelagic sediment overlaying the mud breccia.

Unfortunately, the gravity core taken at the Leipzig MV (GC-17) was relatively short (26 cm) and showed hemipelagic sediment throughout. The corresponding MUC (MUC-09) in comparison was a success and showed 27 cm hemipelagic sediment underlain by 7 cm of gray clay with very low water content and smaller (few mm) dark clay clasts, which might represent the top of the mud breccia.

At the Moscow MV, it was possible to distinguish five different mud flows (GC-15). They showed different colors (Fig. 5.8.5), water content and size of occurring gas bubbles and clasts. A striking feature is the higher water content of the second mud flow within the first section of the core. In contrast to the gravity core, which showed no hemipelagic coverage due to disturbance through coring, the corresponding MUC (MUC-07) showed a hemipelagic coverage of 15 cm. The hemipelagic cover showed some thin ( $\ll$  1 mm) worms and consisted of soupy clay with foraminifera, bivalves and pteropod fragments. On top of the MUC different clasts have been observed, including a small gypsum clast.

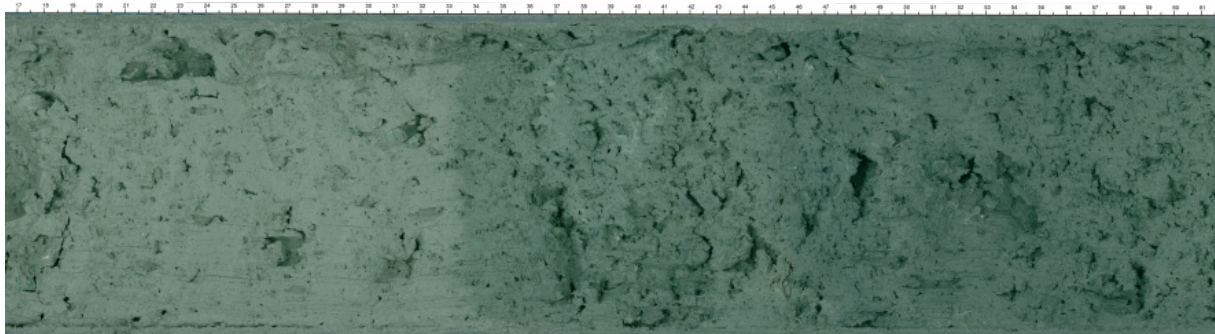


**Fig. 5.8.5:** Close-up of section 2 from the Moscow MV (GC-15) (left: 35.5 to 80.5 cmbsf). Two different mud breccia flows with a distinctive boundary: distinguished by their color and texture as well as their water content.

The gravity core obtained at the Maidstone MV (GC-16), which is located similar to the Moscow MV in the south of the Olimpi mud volcanic field, showed dark bluish-gray mud breccia with H<sub>2</sub>S smell, small gas holes in the second section, and small vugs due to escaping gas, different clay clasts and a large (~ 5 cm in diameter) subangular sandstone clast. The corresponding MUC (MUC-08) showed 7 cm of hemipelagic sediment – which again, showed the thin (<< 1 mm) worms, which here could also be observed within the water column.

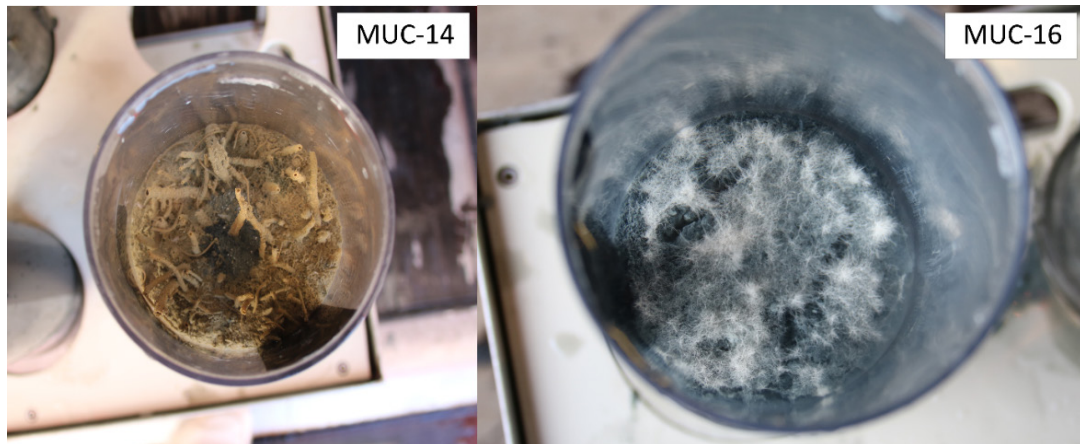


**Fig. 5.8.6:** Left: tubeworms on the surface of MUC-14 (subrosional pit) and in the right: microbial mat on the surface of MUC-16 (Gelendzhik MV).

Apart from mud volcanoes, two subrosional pits have been investigated within the Olimpi mud volcanic field. A subrosional pit located between in the west of Bergamo MV was investigated by a gravity core (GC-13) and a corresponding MUC (MUC-05). The gravity core consisted mainly of a structureless dark grey mud, which was overlain by a thin hemipelagic layer (~ 7 cm) and underlain by ~ 100 cm mud breccia. The MUC showed only a hemipelagic layer of 5 cm and a conspicuous light gray mud layer with sharp boundaries to the upper and lower sections between 21 and 28 cmbsf. In close proximity to the Nadir brine lakes, which are located between the Moscow and Maidstone MVs, a gravity core (GC-23) was taken from a subrosional pit with an overall length of 537 cm. The sediment core was compiled mainly of dark moussy clay and some silt particles with a high-water content, which decreased downcore. Due to a very strong H<sub>2</sub>S smell of the whole core, the sections were opened and described on the next day, after degassing of the sediment.

#### *West of Olimpi mud volcanic field*

In the western Olimpi mud volcanic field, three mud volcanoes have been sampled: the already known Gelendzhik and Nice mud volcanoes as well as a smaller unnamed mud volcano in close proximity to the Nice MV.

The Nice MV has been sampled by two gravity cores (GC-20 and GC-26). The 282 cm long GC-20 showed greenish-gray mud breccia with some mudstones and different smaller clay clasts. The mud breccia showed gas bubbles of different sizes (up to 3 cm) and 6 cm foam had to be added on top due to collapse of gas extension gaps within the section. A small gypsum clast amongst other clasts has been observed within the core catcher material. A hemipelagic layer of 5 cm was confirmed by the corresponding MUC (MUC-12). The second gravity core was significantly shorter (78 cm), seemed to be more compacted and showed a hemipelagic layer of 9 cm. Between 9-16 cmbsf a transition layer to the mud breccia, similar to those observed in the

Calabrian arc, was observed. The corresponding MUC (MUC-17) showed 17 cm of hemipelagic sediment with an inclined surface and inclined boundary to the underlying mud breccia.

Two gravity cores (GC-19 and GC-27) and corresponding MUCs (MUC-11 and MUC-18) have been taken from a small unnamed mud volcano in close proximity to the Nice MV (Fig. 4.6). The first attempt was based only on swath sonar bathymetry and brought back a 124 cm long gravity core which consisted mainly of hemipelagic sediment. Mud breccia was found within 113 to 124 cmbsf. A successfully taken 268 cm long gravity core taken on the most recent outflow point based on AUV data consisted mainly of moussy mud breccia with a few larger clasts. The MUC on this station failed - probably due to a hard carbonate crust on top of the mud breccia, which was visible in the gravity core. Apart from that, dead tubeworms were observed on top of the sediment.

At the Gelendzhik MV, we recovered a 284 cm long gravity core compiled of greenish-gray mud breccia with a very low water content. The whole core showed angular to subangular clay clasts (mm – 1 cm) as well as gas bubbles and holes. Some larger mudstones (up to 5 cm) and sandstones (up to 7 cm) as well as clay clasts (up to 8 cm) have been observed in this core. No hemipelagic coverage could be observed in the gravity core or the corresponding MUC (MUC-16). On top of the MUC whitish microbial mats and gas cracks on the surface have been observed (Fig. 5.8.5). Underneath the microbial mat a thin, darker layer – probably reduced material, was observed. Overall, the upper 28 cm of the MUC showed very soupy mud material followed by moussy mud breccia with mm-sized clasts, gas expansion cracks (up to 1 cm) and also one of the MUCs actively degassed on board.

The Heraklion MV was sampled by one gravity core (GC-25) and corresponding MUC (MUC-19), which both showed mud breccia throughout the whole core. The moussy mud breccia showed some larger clasts, a decreasing H<sub>2</sub>S smell downcore and a slightly higher water content in the lowest section. A bacterial mat on top of the mud breccia could be observed within the MUC.

#### *MedRidge/Inner Ridge and Cretan margin fault zones*

Overall, the gravity corer was deployed seven times at the fault zones between the MedRidge/Inner Ridge and the Cretan margin.

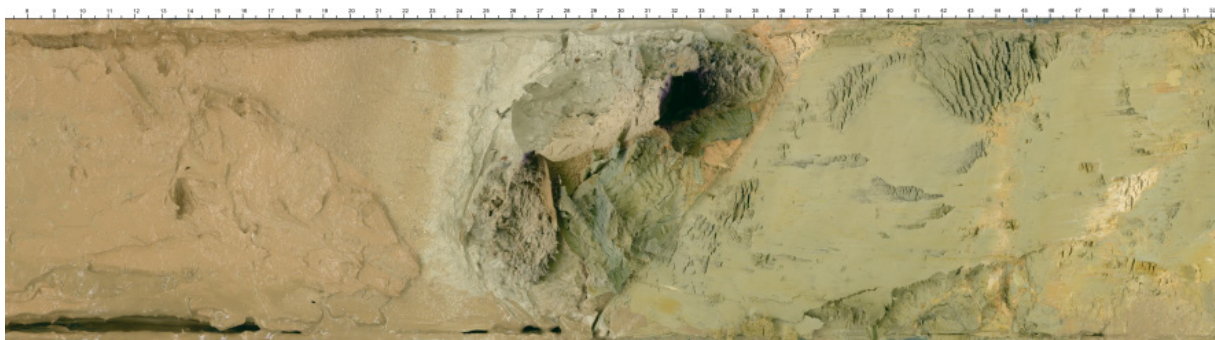


**Fig. 5.8.7:** Close up of section 1 from GC-06 (left: 7 to 52.5 cmbsf). The top of the segment shows hemipelagic material while the lower part might represent fault gouge material.

Fault zones at the boundary between the MedRidge accretionary complex and the Inner Deformation front as well as between the Inner Deformation front and the Inner Ridge/Cretan margin were one of the main target areas during POSEIDON cruise POS410 and POS429 in 2011 and 2012 (Kopf et al., 2012a, 2012b). A station, where the POSEIDON cruise sampled material similar to mud breccia from mud volcanoes of the Olimpi mud volcanic field, has been revisited. Unfortunately, the first deployment of the gravity corer (GC-05) contained only fragments of

carbonate crusts. The crust must have been too hard to let the gravity corer penetrate into the sediment. The second attempt (GC-06) at the same position recovered 61 cm sediment material. GC-06 showed mainly yellowish-brown clay with a highly compacted and dry layer in the middle of the core. Based on the brownish color, the MSCL data and the lack of a moussy structure and clear clasts, we do not interpret this as a mud breccia. It might represent a slump or similar mass wasting event or possibly a fault gouge (Fig. 5.8.7).

A third attempt to sample material in this region was deployed at a deeper depth and failed. Only the outside of the gravity corer showed some specific sediment material (greyish mud) which reminded of mud breccia from mud volcanoes. Above the fault zone a topographic high with conspicuous backscatter has been sampled (GC-07) in order to resolve if the 2011/2012 sampled mud breccia might be related to a mud volcano above the escarpment caused by the fault zone, of which material could have flowed down. The recovered gravity core (GC-07) showed only a sequence of hemipelagic sediment, therefore this high backscatter zone is not a mud volcano, which means the question where the mud breccia sampled during the POSEIDON cruises came from remains unresolved.



**Fig. 5.8.8:** Close up of section 5 from GC-11 (374 to 419 cmbsf).

Further westward three additional gravity cores have been sampled at locations where heat flow measurements were done before. Two cores were sampled within the fault zone between the Inner Ridge/Cretan margin and the Inner Deformation Front (GC-09 and GC-11) and one on top of the Inner Deformation Front (GC-08). GC-08 represents hemipelagic sediment throughout the whole core while GC-09 and GC-11 show over 200 cm greenish-grey clay material additionally to a hemipelagic sequence. They both also show slump structures (Figs. 5.8.8. and 5.8.9) within the second section and GC-11 shows material similar to mud breccia between 375 and 415 cmbsf (Fig. 5.8.8), although also here the brownish color as well as different MSCL signatures set them apart from the mud breccias sampled in mud volcanoes.

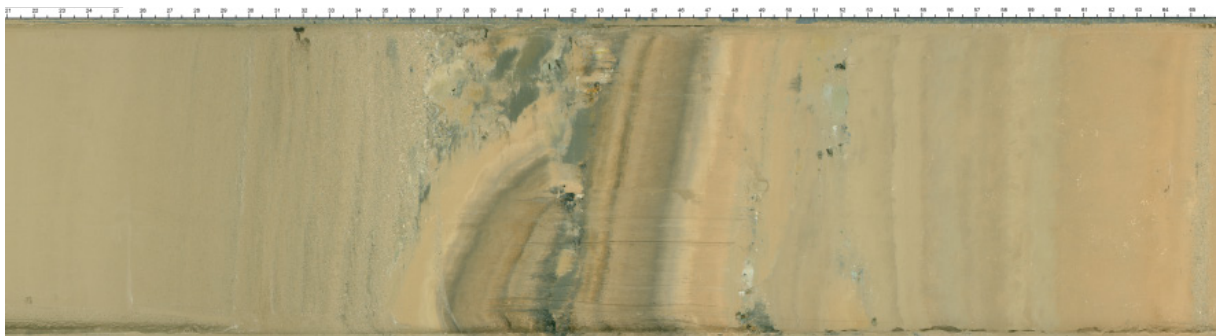


**Fig. 5.8.9:** Close up of section 2 from GC-11 (57 to 102 cmbsf). Slump structure within the fault zone between the Inner Deformation Front and the Inner Ridge/Cretan margin.

### *United Nations Rise*

One gravity core and a corresponding multicore was taken from the prominent Dublin MV within the United Nations Rise. The gravity core (GC-18) showed a highly compacted and stiff mud breccia with an exceptionally low water content. The mud breccia within the gravity core was overlain by 16 cm hemipelagic sediment. The corresponding MUC (MUC-10) showed only 3 cm of hemipelagic sediment on top of the mud breccia.

The uneven recovery in the liners of the MUC suggests a rather rough topography on the Dublin MV. Despite the small distance between the liners, they showed a major difference in their recovered depth. One side of the MUC showed three liners with 24 cm recovery, from which the top 3 cm were identified as hemipelagic sediment. The other side of the liners showed a larger hemipelagic layer with a huge amount of pteropods, which could not be found within the other three liners. This difference is probably related to the rough topography in that region – pteropods and sediments were probably trapped in a local depression, which has been sampled by only one side of the multicorer.

### *Cobblestone area*

Within the Cobblestone area two mud volcanoes were sampled, Helios MV and the second unnamed mud volcano (unnamed MV 2).

The Helios MV was investigated by three gravity cores (GC-28, GC-30, and GC-31) which were supplemented by two MUCs (MUC-20 and MUC-22). Only one gravity core (GC-31) showed a hemipelagic layer on top of the recovered mud breccia. GC-28 and GC-30 showed no hemipelagic cover, which might be disturbed through coring. At least for GC-28 a thin hemipelagic cover of 4 cm, which might be disturbed through coring as well, was confirmed by the corresponding MUC-20.

The gravity core taken at the unnamed MV 2 (GC-29) had a length of 25 cm, whereby the lowest 4 cm consisted of greyish-brown mud breccia with a low water content and some clasts (mm to cm). The outside of the gravity corer was covered in stiff mud breccia with many different clasts visible. The corresponding MUC (MUC-21) was 29 cm long and showed dark greenish-gray mud breccia from 25 to 29 cmbsf.

### *Smear slide analysis*

Based on the studied smear slides of both gravity cores and multicores from different study areas, we were able to distinguish three main groups of lithologies that are present. Most cores contain layers from multiple lithological groups, due to for example event layers or because they are partly comprised of mud breccia. However, we have made a rough classification of which lithological groups occur in which locations. Table 5.8.4 gives a selection of a few cores that are representative for each of the groups

**Table 5.8.4:** Selection of smear slides from different gravity cores (GC) and multicores (MUC) assigned to three main groups of lithology.

Group I	GC-01, -02, -03, -04, -06, -07, -08, -09, -10, -13, -14, -15, -16, -18, -19, -20, -21, -22, -24, -25, -26, -27, -28, -30, -38; MUC-01, -02, -05, -06, -07, -08, -09, -10, -11, -12, -16, -19, -20, -21, -23
Group II	MUC-05 and MUC-14; GC-23
Group III	GC-32; 33, 35, 36, MUC-29; GC-07 and 08; -17

The first group (I) refers to the lithology most commonly found, both in the hemipelagic sediments and in the mud volcanoes deposits. They are characterized by microcrystalline matrix with bigger clasts of feldspar, quartz and carbonate minerals, biotite, organic matter, and opaque minerals which may be metal oxides, sulfides, or organic matter. A wide variety of fossils is present in this group, of which coccoliths and discoasters are dominant. The foraminifera that are present are mostly planktonic. Other common secondary components in this group are diatoms and siliceous sponge spicules. This composition was present in all the smear slides of mud breccia samples with different percentages of siliceous and carbonate clasts as well as in the organic components (Fig. 5.8.10). Lithologically, it can be described as mud with calcareous or biogenic ooze, sometimes complemented by the occurrence of metal minerals and/or organic matter.

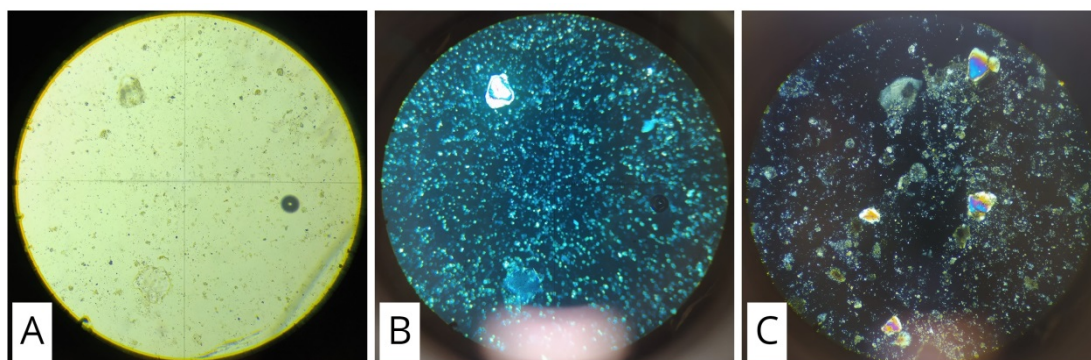


**Fig. 5.8.10:** Parallel (A) and crossed (B,C) light photography of smear slides from mud breccia samples. Image A and B are from Helios MV (GC-30) and image C is from Bergamo MV (GC-12). The percentages of siliceous or carbonate clasts and of the organic components vary.

The second group (II) refers to a biosiliceous ooze with clay. This lithology is present in the subrosional pit, located near the Nadir brine lakes between the Moscow MV and Maidstone MV (GC-23). The dominant fossils found within this group are diatoms, radiolarians, and silicoflagellates, whereas foraminifera are present in lower percentages. Some layers of this core (GC-23) are enriched in organic matter or metal oxides or sulfides are present. Siliceous or calcareous clasts are present in lower percentages (Fig. 5.8.11). Similar layers can be found in some layers of cores taken from SW of Sartori MV (GC-33 and GC-36).

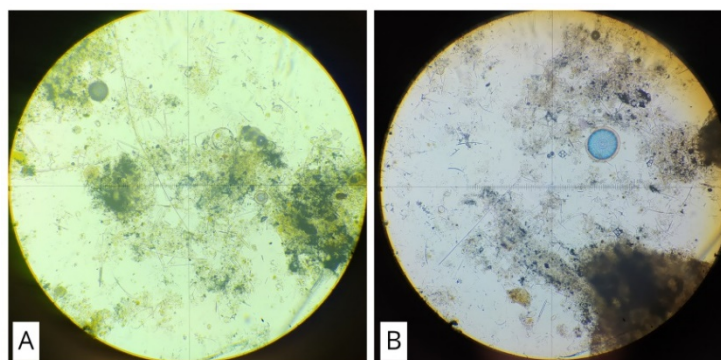


**Fig. 5.8.11:** (A, B) Microphotographs using plane polarized light from smear slides of samples taken from the brine hole (MUC-14). Diatoms, silicoflagellates, radiolarians and organic matter are the dominant crystalloclasts of this slide.

The third (III) group consists of redeposition-/event layers (i.e., sand layers accompanied with foraminiferal ooze, volcanic ash layers, clear evidences for mass movement deposits or sapropel

layers). Ash layers and turbidite layers (Fig. 5.8.11) were identified in several of the cores in the surroundings of the Sartori MV as well as in the cores taken from the fault zones north of the Olimpi field. Some smear slides with both, ash layer and turbidite were recognized (GC-35; Fig. 5.8.12).

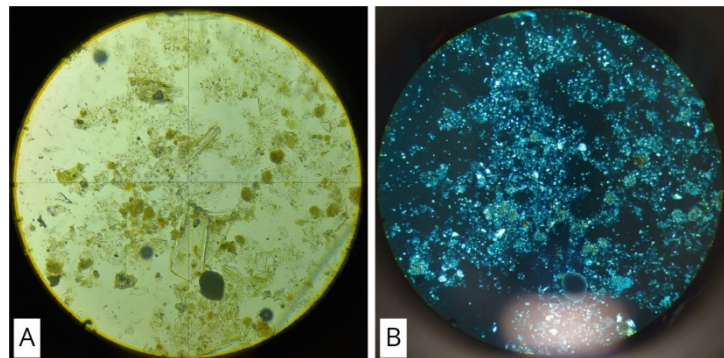


**Fig. 5.8.12:** Microphotographs using plane (A) and crossed (B) polarized light from tephra-turbidite samples from the southwest of Sartori MV (GC-35). Glass crystals, clay minerals, carbonate minerals, quartz and feldspar are easily recognizable among the microcrystalline matrix.

Finally, in the cores from the surroundings of Sartori MV (GC-02, -32, -33, -35, -36, -37) and the fault zone north of the Olimpi field (GC-07), we found sapropel layers. They show higher percentages of organic matter and opaque minerals which could be metal oxides, sulfides or organic matter and abundant foraminiferal assemblages in comparison to other smear slides.

## 5.9 MSCL-Measurements of the Cores

(S. Lenius; Ch. Hilgenfeldt, not onboard)

### Introduction

The sediment series recovered during FS SONNE research cruise SO278 by gravity corer were subjected to routine laboratory geophysical studies: shipboard measurements on the segmented cores were made using a Multi-Sensor Core Logging System (MSCLS) (Fig. 5.9.1) that was developed at MARUM (Center for Marine Environmental Sciences, University of Bremen) in 2018.

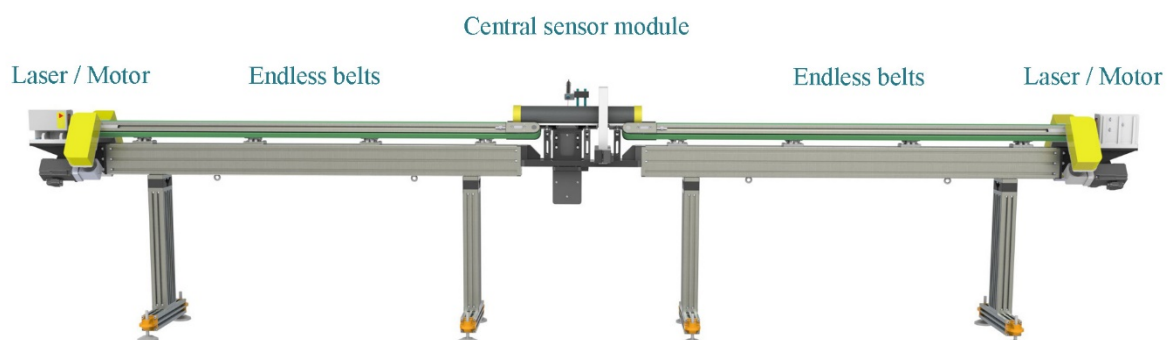


**Fig. 5.9.1:** CAD drawing of the Multi-Sensor Core Logging System (MSCLS) consisting of two-sided (endless) conveyor belts, the central sensor module, the drive motors and the laser distance sensors.

The MSCLS measurements routinely comprise two basic physical parameters:

- electrical resistivity  $R_s$  or conductivity  $\sigma$ ,
- magnetic volume susceptibility  $\kappa$

These properties are closely related to the lithology and grain size of the sediments. Electrical resistivity and magnetic volume susceptibility yield medium-resolution core logs available prior to most other detailed investigations. Individual core sections are moved along the static sensors on a horizontal conveyor belt. The latter consists of an endless tooth belt system which is able to transport the core sections with almost no slippage, thus ensuring an accurate horizontal positioning of the objects to be measured. Two laser distance meter measure in real time the distance to the respective edges of the core section and guarantee for a positioning accuracy and determination of section length of better than 0.1 mm.

Since only a single core section is measured at a time, it is possible to horizontally traverse the section forward and backward along the conveyor belt. Any number of background measurements (without a core section within the sensitive volumes of the sensors) during a measuring cycle can be conducted in order to determine any eventual sensor drift. Therefore, sediment cores were usually measured shortly after their recovery.

## Description of the methods

### *Magnetic Volume Susceptibility*

Magnetic volume susceptibility  $\kappa$  is defined by the equations

$$B = \mu_0 * \mu_r * H = \mu_0 * (1 + \kappa) * H = \mu_0 * H + \mu_0 * \kappa * H = B_0 + M$$

with magnetic induction  $B$ , absolute and relative permeabilities  $\mu_0$  and  $\mu_r$ , magnetizing field  $H$ , magnetic volume susceptibility  $\kappa$  and volume magnetization  $M$ . It can be inferred from the third term,  $\kappa$  is a dimensionless physical quantity. It represents the amount to which a material is magnetized by an external magnetic field.

Measurements on gravity cores were made on whole-round core sections using a MS2C loop sensor (Bartington Instruments Ltd., UK) with a diameter of 140 mm (S/N 827). The functional principle of the susceptibility meter is an oscillator circuit that produces a weak (approx. 80 A/m RMS) non-saturating alternating magnetic field with a frequency of 565 Hz.

For marine sediments the magnetic susceptibility may vary, between an absolute minimum value of around  $-15 \cdot 10^{-6}$  SI units (diamagnetic value of pure carbonate or silicate) to a maximum of some  $10.000 \cdot 10^{-6}$  SI for basaltic debris rich in (titano-) magnetite. In most cases  $\kappa$  is primarily determined by the ferrimagnetic mineral content, while paramagnetic matrix components such as clays are of minor importance. High magnetic susceptibilities indicate high terrigenous or low carbonate deposition. Low values of magnetic susceptibility can also result from post-depositional reduction of oxic iron minerals. In absence of pervasive diagenesis, magnetic susceptibility can serve for a correlation of sedimentary sequences deposited under similar conditions.

Due to its size, the sensor integrates the response signal over a core interval of about 5-8 cm. Consequently, sharp susceptibility changes in the sediment column appear smoothed in the  $\kappa$  log.

### *Electrical Resistivity*

Electrical resistivity is a measure of how strongly a material opposes the flow of electric current and is the reciprocal of electrical conductivity. It was measured by means of a non-contact resistivity (NCR) sensor (Version 02.2016) by Geotek Ltd. (UK).

A low resistivity indicates a material that readily allows the movement of electrical charge. The SI unit of electrical resistivity is the Ohm-meter and the SI unit of electrical conductivity is Siemens per meter. The electrical sediment resistivity  $R_s$  was determined using an external inductive sensor. A non-contact infrared thermometer is used to measure the temperature at exactly the spot where contemporaneously electrical resistivity is determined. For the necessary NCR calibration, we daily measured a set of saline solutions at concentrations of 0.35 - 1.75 - 3.5 - 8.75 - 17.5 - 35 g/l. The respective voltage readings minus the zero level of the sensor are automatically saved to the control software and applied to the voltage data from the core section.

The NCR sensor uses a transmitter coil to induce a high-frequent magnetic field in the sediment which in turn generates an electrical current in the sediment that is inversely proportional to the resistivity. A receiver coil measures the very small magnetic field regenerated by the electrical current in the sediment. These readings are compared with those from a second identical coil operating in air. This difference technique provides the required accuracy and stability. Electrical resistivities between 0.21 and 15.48 Ohm-m (at 20°C) can be measured with a spatial resolution along the core of approximately 2 cm.

The temperature of the object to be measured, which was used to calculate the specific resistance, was recorded using a non-contact Omega OS151 infrared thermometer. In its simplest construction, an infrared thermometer consists of a lens that focuses the infrared energy on a detector. This energy is then converted into an electrical signal (4 - 20 mA) which has also been digitized with 16 bits. This ensures an accuracy of  $\pm 1\%$  of the measured value, or a repeatability of 0.5 % of the measured value.

### *Parameter-Setup*

The following parameters were usually applied for physical properties measurements during SO278:

<b><i>General settings</i></b>	
Distance between core section and sensors for sensor initialization	40 (50) cm
Number of drift measurements	2 (3)
Sampling interval for all sensors	1 cm
Motor velocity	150 mm/s
Motor acceleration / deceleration	100 mm/s <sup>2</sup>
Thickness of end caps	2 mm
<b><i>Magnetic susceptibility</i></b>	
Integration time	3500 ms
Leader distance	14 cm
<b><i>Electrical conductivity</i></b>	
Integration time	3.500 ms (16-Bit, 100 S/s)
Leader distance	14 cm
<b><i>Temperature</i></b>	
Integration time	3.500 ms (16-Bit, 100 S/s)

### **Preliminary shipboard results**

During expedition SO278, both physical properties, magnetic susceptibility and electrical conductivity of 35 gravity cores, were measured. The full core sections with diameter of 12.1 cm had lengths between 17 and 101 cm, which brings a total core length of 106.95 m.

The electrical conductivities of all cores reach from 0.1 to 6.68 S/m with an average value of 2.26 S/m. In Figure 5.9.2 it is nice to see, that the conductivities can be divided into three parts, which are the low, medium and high conductive sediments. All of the low conductive sediments consist exclusively of mud breccia with a low amount of pore water. The areas with nearly zero conductivity are gas expansions that occur from the pressure decrease when the gravity corer came up after coring on the seafloor.

The range of the medium conductive sediments reaches from 1.5 to 4.0 S/m. The sediments of this area are mostly hemipelagic with different layers and grain sizes. Only Gravity Core 24 (GC 24) / GeoB24351-01 does not correspond to the other sediments, as it is a mud breccia with low water content. It is also the only core of medium conductive sediments that has gas expansion and so a negative peak 166 cm depth. GeoB24316-01 has an area from 332 cm on where it suddenly increases to a value way higher than its neighbors. It is an area with very fine, darkish gray to black material bedded into the hemipelagic sediments.

The high conductive sediments take place in values between 4.0 and 6.7 S/m. Only four of 35 measurements had such high values (highest GeoB24324-02, 6.68 S/m at 324.9 cm depth). GeoB24310-01 has two negative peaks at 221 and 240 cm which are two gas expansions, but the decrease of GeoB24324-02 at 392 cm is a change in lithology where the sediments change from dark gray clay to a mud breccia. Really exciting is the occurrence of GC 25 / GeoB24352-01 in the high conductive area because it is the only mud breccia with higher conductivity than 3 S/m.

As different to the electrical conductivities, the **magnetic volume susceptibility** does not form such nice trends that can be separated from each other. However, it is possible to correlate the curves of the hemipelagic sediments, to get horizons of the same layers. The tephra layer at 14 to 21 cm depth is visible in all plots of magnetic susceptibility of the researched area around Sartori mud volcano. The sapropel in the upper part of the cores appears as a very low susceptibility matter even less than the mud breccias which always have values between  $100 \cdot 10^{-6}$  and  $150 \cdot 10^{-6}$  SI. GC 02, GC 35 and GC 32 (GeoB24303-01, GeoB24373-01, GeoB24366-01) also provide another very strong peak at depths of 350-390 cm.

The maximum value of all magnetic volume susceptibility measurements is  $4183.39 \cdot 10^{-6}$  SI in gravity core GeoB24315-02 but sadly it is not a sedimentary value. Due to hard sediment the pipe of the gravity corer bent so it had to be cut off. The iron splinter that fell into the core caused the high peak at 21 cm. Beside this the highest value in GeoB24316-01 has a magnetic susceptibility of  $1247.1 \cdot 10^{-6}$  SI recovered from the fault zone in the north of the Olimpi field. Such a high value speaks for a ferrimagnetic material content like iron rich minerals in a volcanic ash. Without the wrong measurement the average of all magnetic volume susceptibility measurements is  $162.85 \cdot 10^{-6}$  SI.

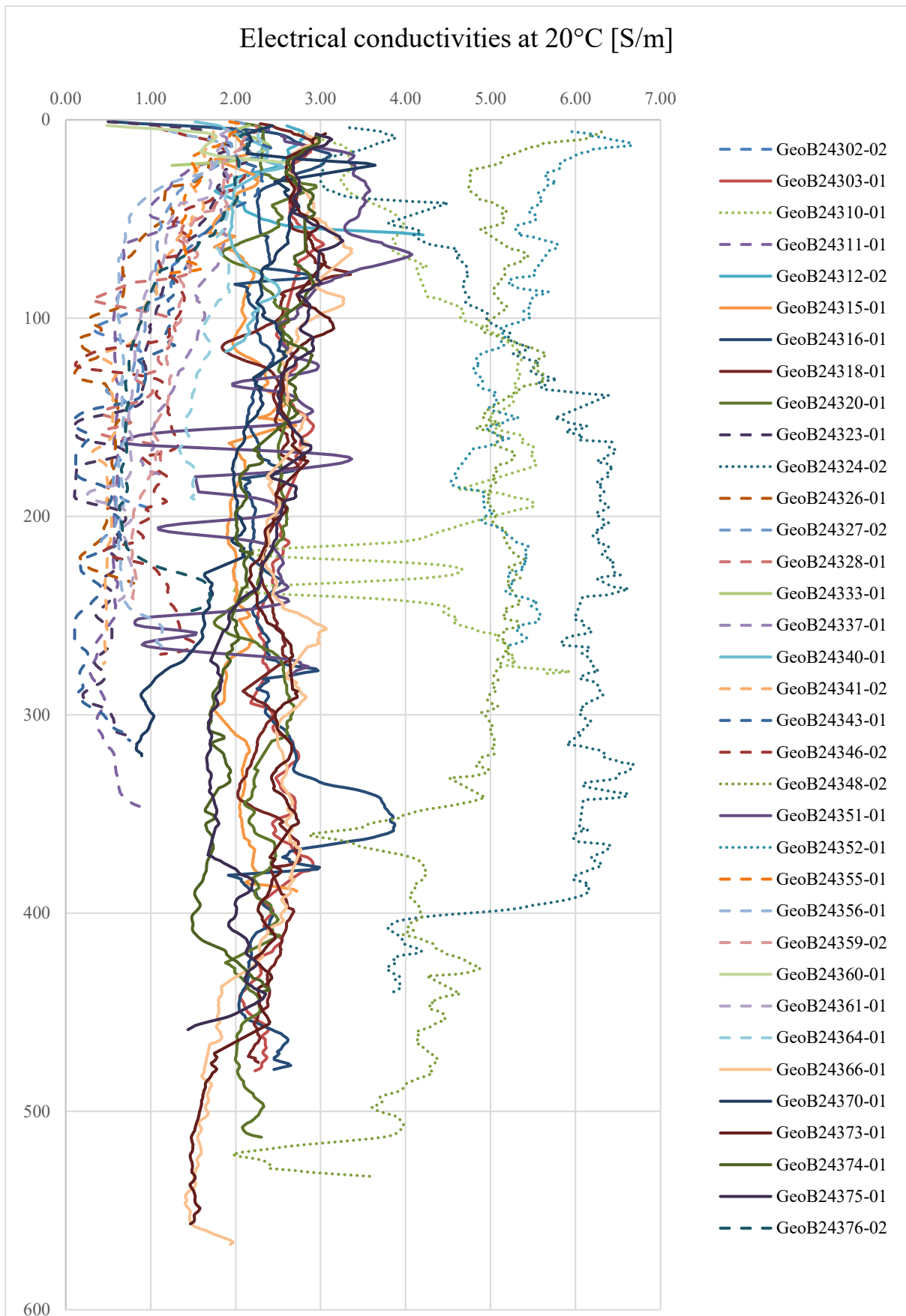


**Fig. 5.9.2:** Electrical conductivities of all cores measured at 20°C. It is nice to see that there are three types of conductive sediments. The low conductive sediments are really stiff and dry mud breccias, the medium conductive sediments are hemipelagic sediments with different layers and the high conductive sediments are such clay rich sediments with a lot of pore water or water with high salinity.

## 5.10 Geotechnical Measurements

(S. Rau)

### Introduction

During expedition SO278 geotechnical measurements in form of falling cone penetration tests and vane shear tests were carried out on the working half of 32 gravity cores from each working area. The overall goal was to define the unconsolidated-undrained shear strength of the sediments to have a better understanding of the origin and compaction of the material. Since the undrained shear strength depends mainly on the water content of the sediment the measurements need to be carried out as soon as possible on undisturbed material after splitting the core (Blum, 1997).

### Description of the methods

The maximum shear strength of sediments from 32 gravity cores has been determined on board after splitting the core and extraction of pore water samples by fall cone and vane shear tests (Fig. 5.10.1). No measurements were taken from six gravity cores because of little to no recovery of material (GC-05, -10, -17, -29, -34) or because of the very high water content in the sediments from the subrosional pit (GC-23).

While the vane shear measurements give more accurate data, the fall cone penetration test is less time consuming and more measurements can be carried out in a shorter amount of time. Both methods should give similar results. On this expedition an average of four fall cone tests and one vane shear test were carried out per section depending on the section length and the number of changes in lithology. The measurements were carried out at sites with undisturbed material with as little clasts as possible and an even sediment surface.

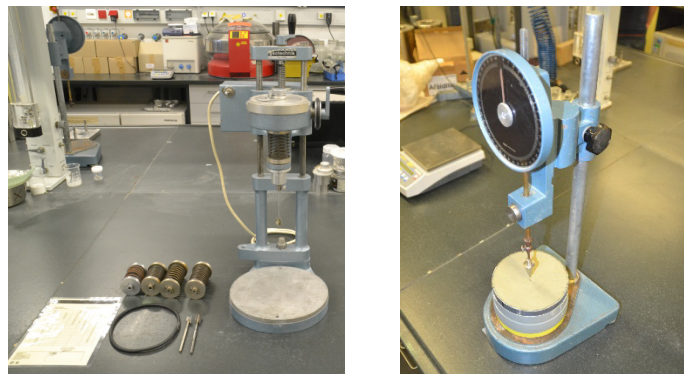


Fig. 5.10.1: left) Vane shear, right) Fall cone.

### Cone penetrometer

The undrained shear strength of the cored sediments was determined according to British Standards Institutions (BS1377, 1975, <https://doi.org/10.3403/00078016U>). A Wykeham-Farrance fall cone penetrometer WF 21600 was used for a first-order estimate of the sediment stiffness. At the beginning of the measurement the metal cone was brought to a point exactly on the sediment surface (Wood, 1985) and then released in form of a free fall into the sediment. The distance of the cone prior and after the penetration of the material was measured by a manual displacement transducer with a precision of 0.01 mm. The penetration depth can then be translated into sediment strength (Hansbo, 1957).

The undrained shear strength can be calculated using the equation  $s_u = (k \cdot m \cdot g) / d^2$  with the gravity  $g$ , the penetration depth  $d$  [mm], the mass of the cone  $m$  and the cone factor  $k$  via the “cone factor” after Wood (1985) in dependence of the cone geometry. In our case is  $k = 0.85$  for a 30° cone.

### Vane shear testing

In addition, a vane shear apparatus by GSC ATLANTIC was used for information about sediment stiffness and undrained shear strength. A four-bladed vane ( $L = 12.5$  mm,  $h = 6.25$  mm,  $d = 12.5$  mm) was inserted completely into the undisturbed sediment of the working half and rotated at a constant rate of  $10^\circ/\text{min}$ .

A calibrated spring transmits the rotation to the vane so a torque is applied to the sediment. A set of four calibrated springs with different spring constants is used depending on the sediment stiffness. By measuring the rotation angle the applied torque can be calculated using a calibration line for each spring. The vane constant  $K$  is a function of the vane size and geometry and was used during the measurements with  $K = \pi * d^2 * (h/2) + \pi * (d^2/6)$ . The undrained shear strength depends on the torque  $T$  and the vane constant  $K$  and can be calculated by the equation  $s_u = T/K$ .

### Preliminary results

Overall, the shear strength was obtained for gravity cores of six different study areas: 1) Olimpi MVF (GC-03, -04 -12, -13, -14, -15, -16, -21, -22), 2) West Olimpi field (GC-19, -20, -24, -25, -26, -27), 3) United Nations Rise (GC-18) and 4) the Cobblestone area (GC-28, -30, -31), 5) the fault zone at the inner deformation front (GC-06, -07, -08, -09, -11). and 6) the Calabrian arc south of Italy (GC-01, -02, -32, -33, -35, -36, -37, -38).

### Olimpi field

In the Olimpi field six mud volcanoes have been sampled. The sediments of two cores from the Bergamo MV (GC-04, -13) show a very low shear strength ( $<10$  kPa) that slightly decreases within a depth of 3.80 mbsf (Fig. 5.10.2a). Smaller peaks of up to 20 kPa are most likely related to the presence of stronger mud or rock clasts. Moscow MV (GC-15) shows an increase in shear strength up to  $\sim 20$  kPa in a depth of 2.40 mbsf and a decrease in shear strength from there to  $<5$  kPa in a depth of 2.20 mbsf. This can most likely be related to different mud flows. The sediment of two cores taken on the Bergamo MV plateau (GC-12, -14), at a certain distance from the active chimney shows a slightly higher shear strength, which increases with depth from  $<5$  kPa up to  $\sim 40$  kPa in a depth of 3.0 mbsf. The outstanding peak ( $>120$  kPa) observed in GC-14 can also be related to a hard rock clast (Fig. 5.10.2b).

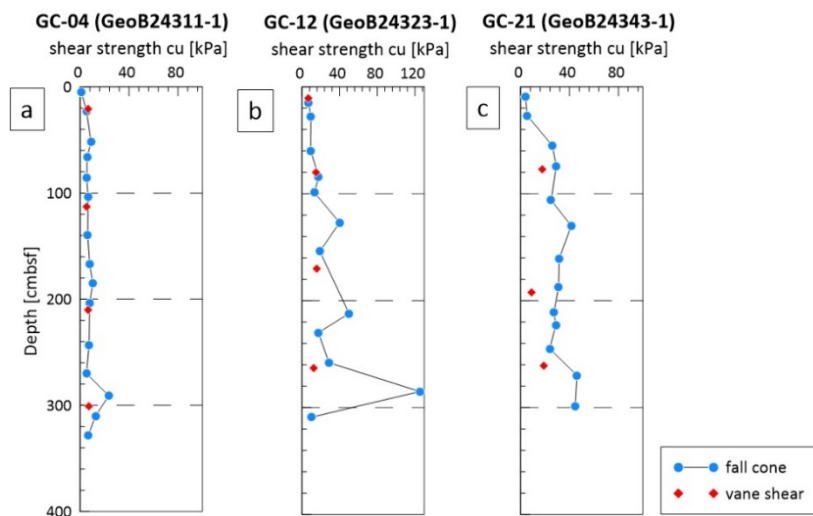


**Fig. 5.10.2:** Shear strength of sediments retrieved from the Olimpi field. a: Bergamo MV (GC-04), b: Bergamo plateau (GC-12), c: Monza MV (GC-21).

The shear strength of the mud breccias observed at the Napoli MV (GC-03), Monza MV (GC-21), Milano MV (GC-22) and Maidstone MV (GC-16) increases with depth (<5 kPa to ~30 kPa) up to a depth of 3.0 mbsf (Fig. 5.10.2c). Local high strength values (up to <40 kPa) can be related to mud clasts found in the mud breccias.

No shear strength was determined for the gravity core taken at Leipzig MV (GC-17) due to a very short core (26 cm recovery).

#### *West Olimpi field*

Along the fault zone in the west of the Olimpi field 4 mud volcanoes were sampled. The Nice MV (GC-20, -26) and the Gelendzhik MV (GC-24) show similar shear strength data: the shear strength of the mud breccia with a medium to low water content increases with depth between <10 kPa at the top to values between 20-50 kPa towards a depth of 3.0 mbsf (Fig. 5.10.3a). Some outstanding peaks (>100 kPa) are most likely related to the presence of mud or rock clasts. The sediment taken from the Heraklion MV (GC-25) and the unnamed MV (GC-19, -27) shows a much higher water content. Therefore, the measured shear strength of the unnamed MV does not exceed 10 kPa in a depth of 2.60 mbsf at the center with a decrease in shear strength with depth (Fig. 5.10.3b) and 20 kPa in a depth of 1.10 mbsf at the flank. The sediment from the center of the Heraklion MV is moussy and shows outstanding low shear strength (<5 kPa) at a depth of 2.60 mbsf.

**Fig. 5.10.3:** Shear strength of sediments retrieved from in the west of the Olimpi field. a: Nice MV (GC-20), b: unnamed MV (GC-27).

#### *Fault zone*

The sediment in GC-09 showed a very typical increase in shear strength with depth (<2 kPa up to ~20 kPa) in a depth of 4.80 mbsf (Fig. 5.10.4a). Also, GC-08 showed an increase in the shear strength data with depth, but up to ~150 kPa in a depth of 4.80 mbsf. The sediment in GC-07 shows a less typical distribution of the measured shear strength with higher values at the upper half (0-2.10 mbsf) of the core at <20 kPa and lower values at the lower half of the core (2.10-3.80 mbsf) at <10 kPa (Fig. 5.10.4b). In GC-06 only 60 cm of sediment were recovered. The shear strength of the hemipelagic sediment does not exceed 5 kPa. The peak in shear strength (~50 kPa) at 0.40 mbsf can be related to a coarser layer within the soft clay sediment.

The shear strength in GC-11 shows an increase with depth from <5 kPa in the first 0.3 mbsf up to 25 kPa at depth 5.20 mbsf (Fig. 5.10.4c). The peak in shear strength at 3.86 mbsf (116 kPa) can be related to rock clasts in the mud breccia from 3.80–4.20 mbsf.

There was little to no sediment recovery in GC-05 and -10 and no measurements were done.

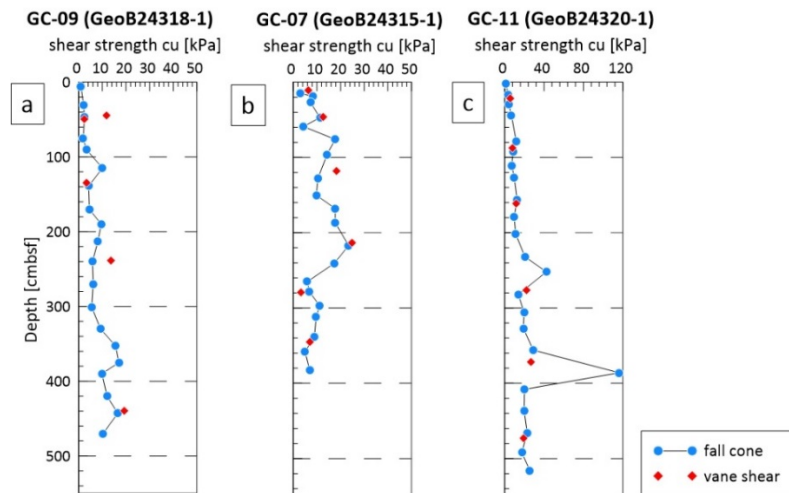


**Fig. 5.10.4:** Shear strength of sediments retrieved from the fault zone (GC-09, -07, -11).

#### Cobblestone area

The Helios MV shows very low shear strength data in the upper few centimeters of sediment of <10 kPa due to a high water content. As the water content decreases with depth the measured shear strength of the sediment increases up to 30–40 kPa in a depth of 2.40 mbsf (Fig. 5.10.5a). Some outstanding peaks in shear strength (>200 kPa) are most likely related to an increased occurrence of larger and stronger mud or rock clasts such as mud or siltstone in the lower half of the mud breccias.

Due to a recovery of only 25 cm of hemipelagic sediment in GC-29 from the unnamed MV 2 and no geotechnical measurements were executed.

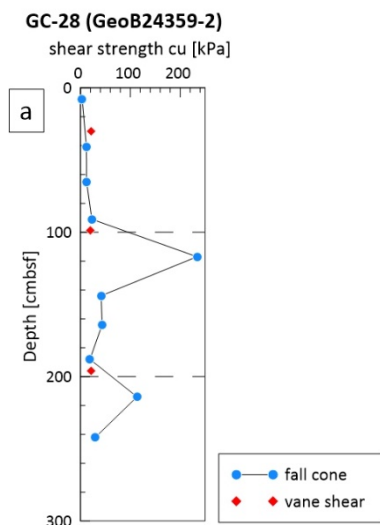


**Fig. 5.10.5:** Shear strength of sediments retrieved from the Helios MV (GC-28) in the Cobblestone area.

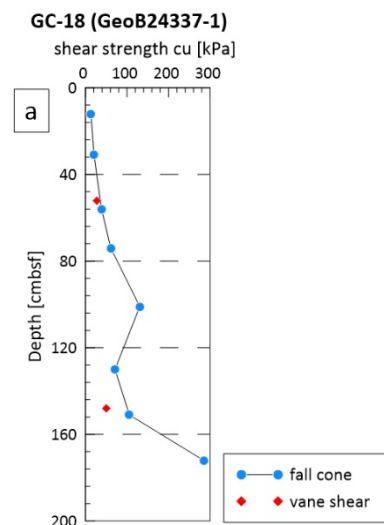


**Fig. 5.10.6:** Shear strength of sediments retrieved from the Dublin MV (GC-18) at the United Nation Rise.

### United Nation Rise

Generally, the mud breccia recovered from the Dublin MV shows generally higher shear strength values: the shear strength reaches values of up to 280 kPa at a depth of 1.80 mbsf (Fig. 5.10.6a).

### Calabrian arc

All investigated gravity cores within the Calabrian arc are either directly related to the Sartori MV or the surroundings of the Sartori MV. The moussy mud breccia found within the two chimneys of the Sartori MV (GC-01, -38) show similar low shear strength values which rarely exceed 8 kPa in a depth of 2.10 mbsf (Fig. 5.10.7a). The cores taken at the rim, in the south and southwest of the Sartori MV show hemipelagic sediment sequences of varying thicknesses. GC-33, at the rim of the central mudflow, where hemipelagic sediments are overlying a mud flow, show a general increase in shear strength (Fig. 5.10.7b), which fits the observed decreased water content with depth. While the shear strength of the vane shear measurements does not exceed 23 kPa in a depth of 3.0 mbsf, the fall cone measurements reach values up to 72 kPa. This difference can be explained due to the presence of stronger mud or rock clasts such as clay or siltstone right under the sediment surface, which can have an impact on the penetration depth of the fall cone. In the cores GC-32, -35, -36 and -37, the thicker hemipelagic sediments shows a low shear strength up to a depth of 4.0 mbsf up to 10 kPa. The buried mud breccia shows a slightly higher shear strength of up to 20 kPa obtained by the vane shear measurements (Fig. 5.10.7c). The shear strength data obtained by the fall cone test show much higher values up to 60 kPa in depth < 5.0 mbsf, which might be explained by many small clasts at underneath the sediment surface. The shear strength of the mud breccia in GC-37 does not exceed 15 kPa throughout the whole core.

GC-02 consists only of hemipelagic sediment and reaches a slightly higher shear strength of ~20 kPa with depth (Fig. 5.10.7d). An outstanding peak in shear strength (>90 kPa) was measured in a tephra layer, which consists of coarser and therefore stronger material.

There was no recovery within GC-34.

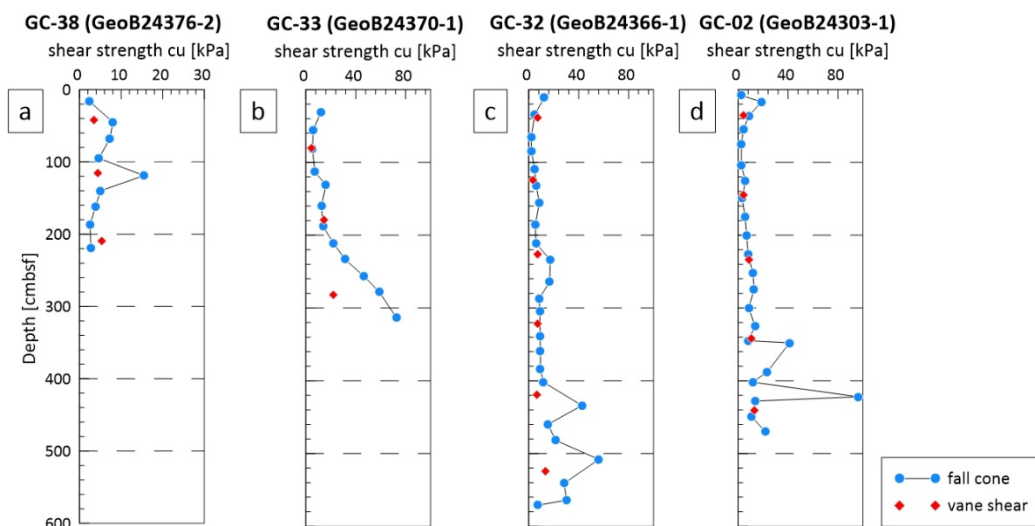


**Fig. 5.10.7:** Shear strength of sediments retrieved from the Sartori MV (GC-38, -33, -32, -02) at the Calabrian arc.

## 5.11 Pore Water Geochemistry

(S. Porrmann, A. Witzleb, T. König)

### Introduction

The main objective of the pore water geochemistry on the cruise was to investigate the differences of the pore water composition in several mud volcanoes of the Hellenic and the Calabrian arc. The pore water data shows not only the activity of mud volcanoes but can also contain information about the source region of fluids passing through. For mud volcanoes, different to majority of marine sediments, advection is the dominant transport process. In the working area this advection is caused by the subduction of the African Plate and the following compression and deformation of buried deposits that lead to an upward movement of fluids. Pore water geochemistry is a suitable method to investigate those fluids in terms of quantity and composition.

In addition, pore water profiles could reveal different processes in the sediment, for instance changes in microbiological reactions or gas hydrate formation.

### Description of the methods

Pore water samples were taken from 31 gravity cores (GCs), 23 multicores (MUCs) and 3 minicores (MICs). In total 1028 samples were obtained during the cruise.

For the pore water extraction on MICs and MUCs, multiple liners were modified beforehand with holes of 5 cm distance to each other, starting at 2.5 cm. For suspension of the devices these holes were closed with tape. For sampling, the liner with most material, least disturbed sediment and cleanest sediment surface was chosen and immediately brought to the 4°C cooling lab. The remaining bottom water in the liner was removed and sampled through a filter.

Rhizons were inserted in the predrilled holes and allowed to extract the pore water in 10 ml syringes for up to 24 hours. The sample volume ranges from 3-10 ml.

For GCs the procedure was similar. The work halves of gravity core segments were taken to the cooling lab after MSCL, splitting, porosity and head-space sampling. Depending on the length of the core it took up to 2 hours for the last segment to arrive in the cooling lab. Rhizons were attached every 10 cm and left in the core for extraction for up to 24 hours.

In Table 5.11.1 all taken samples and their location are shown.

**Table 5.11.1:** Overview of all collected samples.

Working area	Tool #	GeoB	First Sample [cm]	Last Sample [cm]	Sample Number	Resolution [cm]	Date
Sartori MV	GC 1	24302-02	10	200	20	10	22.10.2020
Sartori MV	GC 2	24303-01	0	485	50	10	22.10.2020
Sartori MV	MIC 2	24303-02	0	12,5	4	5	22.10.2020
Napoli MV	MIC 3	24306-01	0	13	4	5	26.10.2020
Napoli MV	GC 3	24310-01	5	255	26	10	27.10.2020
Bergamo MV	GC 4	24311-01	5	335	34	10	27.10.2020
Bergamo MV	MIC 4	24311-02	0	21	6	5	27.10.2020
fault zone	GC 6	24312-02	5	55	6	10	28.10.2020
fault zone	MUC 1	24312-03	0	19	5	5	28.10.2020
fault zone	GC 7	24315-01	5	385	39	10	29.10.2020

fault zone	MUC 2	24315-02	0	32	8	5	29.10.2020
fault zone	GC 8	24316-01	0	475	49	10	29.10.2020
fault zone	GC 9	24318-01	5	455	46	10	31.10.2020
fault zone	MUC 3	24318-02	0	35	8	5	31.10.2020
fault zone	GC 11	24320-01	5	505	51	10	31.10.2020
plateau of Bergamo	GC 12	24323-01	5	315	32	10	02.11.2020
plateau of Bergamo	MUC 4	24323-02	0	21,5	5	5	02.11.2020
West of Bergamo	MUC 5	24324-01	0	47	11	5	02.11.2020
West of Bergamo	GC 13	24324-02	5	435	44	10	02.11.2020
plateau of Bergamo	GC 14	24326-01	5	235	24	10	03.11.2020
plateau of Bergamo	MUC 6	24326-02	0	28	7	5	03.11.2020
Moscow MV	MUC 7	24327-01	4	29	6	5	03.11.2020
Moscow MV	GC 15	24327-02	5	205	21	10	03.11.2020
Maidstone MV	GC 16	24328-01	5	165	17	10	03.11.2020
Maidstone MV	MUC 8	24328-02	0	29	7	5	03.11.2020
Leipzig MV	GC 17	24333-01	5	25	3	10	05.11.2020
Leipzig MV	MUC 9	24333-02	0	28	7	5	05.11.2020
Dublin MV	GC 18	24337-01	5	165	17	10	07.11.2020
Dublin MV	MUC 10	24337-02	0	13	4	5	07.11.2020
Unnamed MV	GC 19	24340-01	5	115	12	10	09.11.2020
Unnamed MV	MUC 11	24340-02	0	26	7	5	09.11.2020
Nice MV	MUC 12	24341-01	0	39	9	5	09.11.2020
Nice MV	GC 20	24341-02	5	275	28	10	09.11.2020
Monza MV	GC 21	24343-01	5	305	31	10	10.11.2020
Monza MV	MUC 13	24343-02	0	33	8	5	10.11.2020
brine hole	MUC 14	24344-01	0	44	10	5	10.11.2020
Milano MV	MUC 15	24346-01	0	27	7	5	11.11.2020
Milano MV	GC 22	24346-02	5	245	25	10	11.11.2020
Subrosional pit	GC 23	24348-02	5	535	54	10	11.11.2020
Gelendzhik MV	GC 24	24351-01	5	275	28	10	13.11.2020
Gelendzhik MV	MUC 16	24351-02	0	45	10	5	13.11.2020
Heraklion MV	GC 25	24352-01	5	265	27	10	13.11.2020
Nice MV	GC 26	24355-01	5	75	8	10	14.11.2020
Nice MV	MUC 17	24355-02	0	23	6	5	14.11.2020
Unnamed MV	GC 27	24356-02	5	265	27	10	14.11.2020
Heraklion MV	MUC 19	24357-01	0	22	6	5	14.11.2020
Cobblestone area – MV #1	MUC 20	24359-01	0	28	7	5	16.11.2020
Cobblestone area – MV #1	GC 28	24359-02	5	245	25	10	16.11.2020
Cobblestone area – MV #2	GC 29	24360-01	5	25	3	10	16.11.2020

Cobblestone area – MV #2	MUC 21	24360-02	0	21	6	5	16.11.2020
Cobblestone area – MV #3	GC 30	24361-01	5	225	23	10	16.11.2020
Cobblestone area – Unnamed MV	MUC 22	24363-01	0	31	8	5	17.11.2020
Cobblestone area – Unnamed MV	GC 31	24364-01	5	195	20	10	17.11.2020
Sartori MV	MUC 23	24365-01	0	33	8	5	18.11.2020
Mud flow rim Sartori	GC 33	24370-01	5	305	31	10	18.11.2020
2nd Chimney Sartori	MUC 30	24376-01	0	32	8	5	19.11.2020
2nd Chimney Sartori	GC 38	24376-02	5	245	25	10	19.11.2020

All pore water samples have been splitted and / or diluted into subsamples to prepare them for further analysis at the University of Bremen and MARUM using ion chromatography (IC) and inductively coupled plasma-optical emission spectrometry (ICP-OES). Subsamples and their treatment are shown in Table 5.11.2.

**Table 5.11.2:** Subsample treatment.

Sample use	Amount [ml]	Properties/use	Storage
Original sample	1-7	Further isotope analysis	20 ml scintillation vials Cooling room
IC	0,04	Diluted 1:40 with deionized water	2 ml Eppendorf vials Cooling room
ICP-OES	0,4	Diluted 1:10 with 1 % nitric acid (HNO <sub>3</sub> )	20 ml scintillation vials Cooling room

During the cruise we analyzed the salinity and alkalinity of the samples.

Salinity was measured using an Atago master-s/mill $\alpha$  refractometer. The device allowed us to measure the salinity with a precision of 1 PSU. Due to its measurement range of 0 to 100 PSU and the high salinity of some samples made it necessary to dilute several samples to fit the scale. This led to an increase of uncertainty up to 3 PSU,

To measure the total alkalinity (TA), we placed 1 ml of sample in a stirring module with a pH-meter. Using an Eppendorf multipipette we titrated hydrochloric acid (HCl) of different concentrations ranging from 0.01 to 0.2 mol/l to the sample, lowering the pH to a value of preferably 3.8, but ranging in between 3.4 and 4.1. Using the measured pH values and the volume of hydrochloric acid titrated, alkalinities were calculated using equation (1) after Schulz and Zabel, (2005).

$$(1): TA \text{ (mol/l)} = [(v_{HCl} * c_{HCl}) - 10^{-pH_{final}} * (v_0 + v_{HCl})/f_h^+ + 10^{-pH_{start}} * v_0/f_h^+] / v_0$$

With:	$v_{HCl}$	volume HCl
	$c_{HCl}$	concentration HCl
	$v_0$	volume sample
	$f_h^+$	activity coefficient of water
	$pH_{start}$	pH of the sample at the start of titration
	$pH_{final}$	pH of the sample at the end of titration

The remarkably high alkalinity values in some samples and the limited volume capacity of the 2 ml vials on our stirring device made it necessary to use HCl with concentrations up to 0.2 mol/l. This led to an increase in uncertainty of the measurement and the occurring of over titration.

Most cores taken on the cruise contained relatively dry mud breccia which kept our sample volume on many cores relatively small. Resulting from that the alkalinity titration was done at a lower resolution of approximately every 20 cm, jumping over samples with too little volume.

### Preliminary results

The pore water salinity profiles from over 16 different mud volcanoes can be separated in two groups. The major number of sampled MVs show a water refreshing with depth down to approximately 10 PSU. Examples for fresh MVs are shown in Figure 5.11.1. Sartori and Nice MV show relatively sharp gradient and strong freshening, while the profile of Dublin MV exhibits less freshening and a slower change with depth. The shape of the freshening profiles differs strongly between the MVs. The depth of gradient change towards the freshening shows the influence of the seawater and therefore can be used as a parameter for the activity of the MVs.

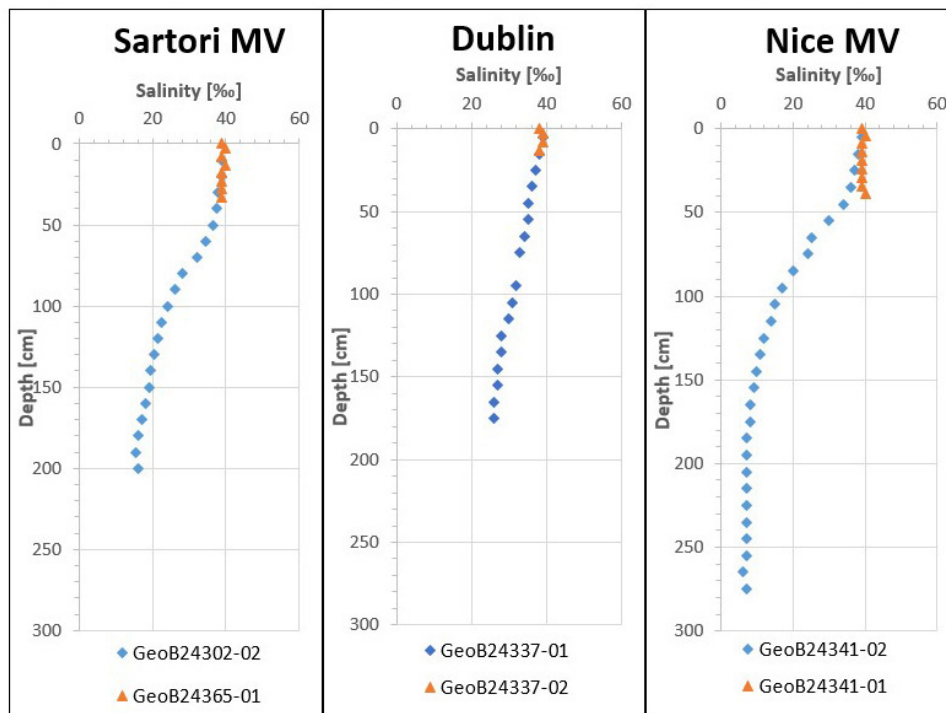


**Fig. 5.11.1:** Pore water profiles from Dublin, Sartori and Nice mud volcanoes. All three show water refreshing with depth.

However, those three MVs seem to have a different fluid source than the other sampled MVs and differ from each other as well, likely due to source mixing and/or other processes.

Besides cores from MVs several hemipelagic cores were taken from the fault zone of the Hellenic trench south of Crete. Those profiles show stable salinities around 40 PSU which is the mean salinity for the Mediterranean Sea (Fig. 5.11.3).

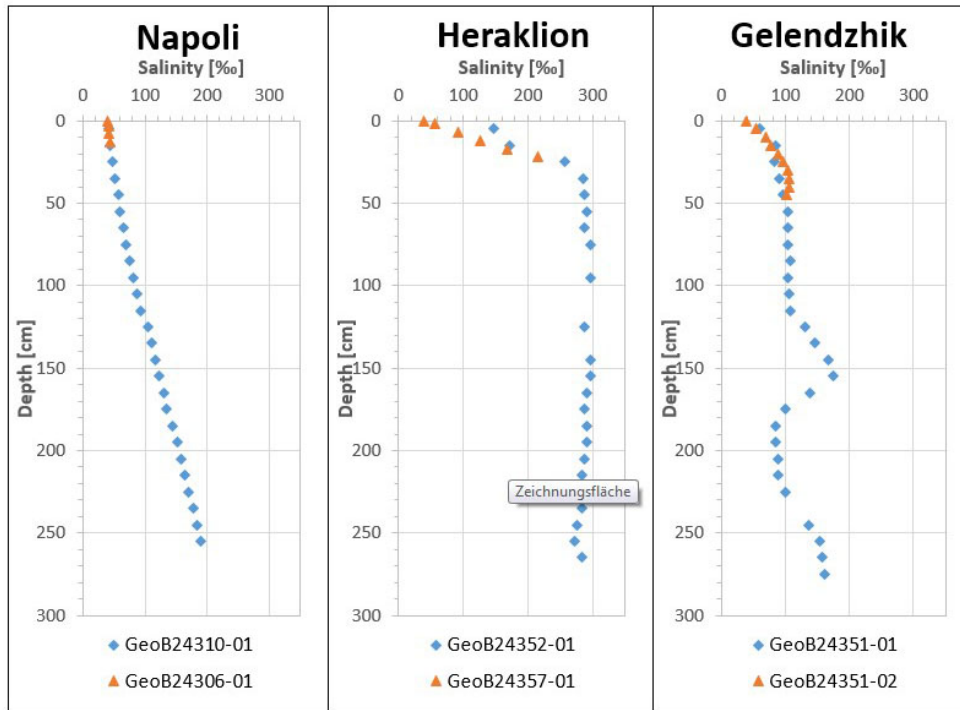


**Fig. 5.11.2:** Pore water salinity profiles from Napoli, Heraklion and Gelendzhik MV. All three show increasing salinity with depth.

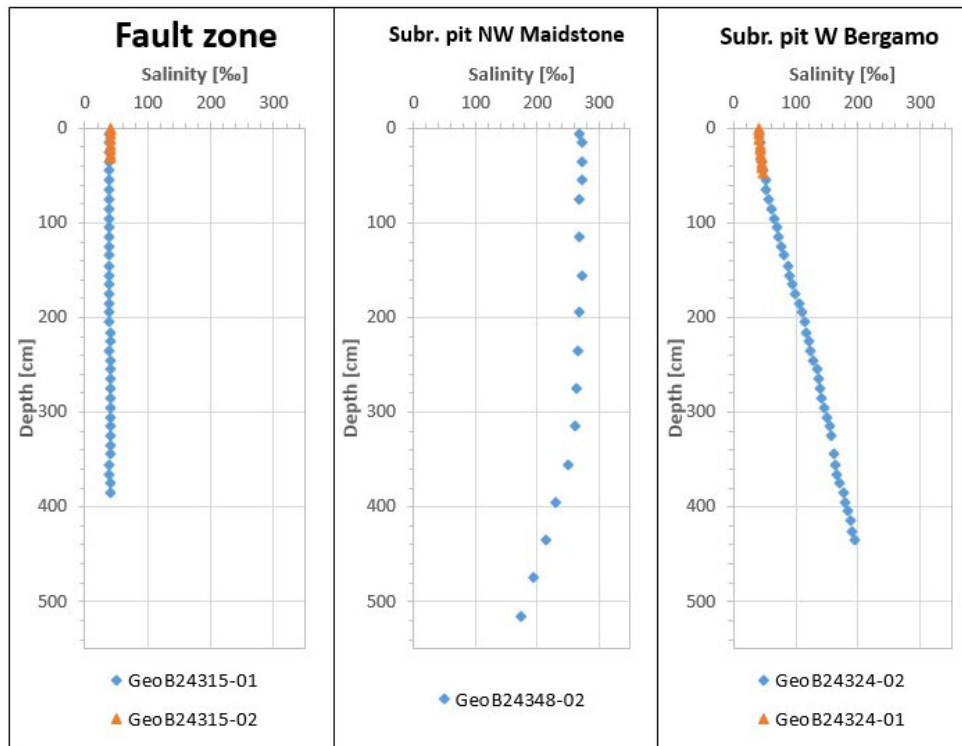


**Fig. 5.11.3:** Salinity profiles from the fault zone south of Crete and two subsrosional pits in the Olimpi field.

Two cores were taken from subsrosional holes in the Olimpi field. It was estimated that those pits are related to the Messinian salt deposits and contain brine. As shown in Figure 5.11.3 pore water salinity profiles from both cores revealed a remarkably high salinity up to 200 PSU. While salinity in the pit next to Bergamo MV starts at seawater mean salinity and increases with depth,

the pit next to Maidstone MV shows high values from the top throughout the first 3 meters of sediment. Salinity then begins to slowly decrease over the last 2 m of the GC. The high values on such shallow depth indicates the presence of a brine pool on the seafloor. This was also shown by temperature measurements of the heat flow team using thermal autonomous temperature loggers (MTLs) on the GCs outside, and a CTD station on the same location.

Alkalinity profiles on mud volcanos show mostly similar shapes but differ in range of values.

Compared to the hemipelagic cores MV cores show alkalinity values a magnitude higher. Hemipelagic cores show alkalinity values in between 2 and 10 meq/l, while the samples from MVs show values of 20 meq/l up to above 100 meq/l.

In hemipelagic cores the alkalinity increases to a certain depth and then starts to slowly decrease again, while in GC from MVs the alkalinity increases faster to higher values. But a later decrease is not visible, most likely due to the weaker penetration of the GC in MV sediments.

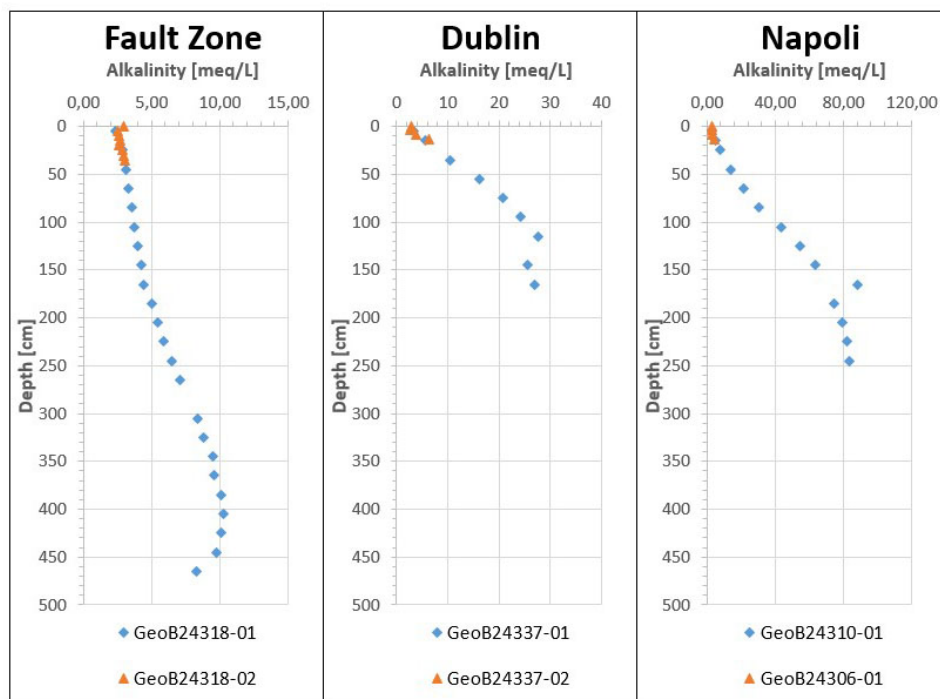


**Fig. 5.11.4:** Alkalinity profiles from 3 different stations. GeoB24318-01 from the fault zone south of Crete represent a hemipelagic profile, while profiles from Napoli and Dublin show the range of alkalinity values measured in MV.

## 5.12 Gas Analysis of Sediment Cores

(Y.-T. Tseng, J. Malnati)

### Introduction

Mud volcanoes are normally observed rooting to deep source mud fluids. In marine environment, gas from deeper methanogenesis zone is migrating to shallower depth, where the occurrence of sulphate leads to reactions of anaerobic oxidation of methane (AOM). Consequently, the sulphate methane interface (SMI) is showing the area where methane is consumed. Under certain temperature and pressure conditions, the formation of gas hydrate provides additional reservoir for preserving methane in the sediment. Thus, the study of gas chemistry in the sediment provides

us the information of mechanisms and cycles of hydrocarbon migrations and its effects to the environments.

During Cruise SO278, the recovery of sediment cores was not equipped with pressurized coring tubes which were used to preserve the sediment and fluids under in situ pressure of the formation. Vigorous degassing of gaseous and dissolved light hydrocarbon took place during the recovery, the measurements of ex-situ light hydrocarbons provide the profile showing the depth of SMI and the existing of methane within the subsurface pore fluid.

Measurements of the light carbon species and its ratio is crucial to distinguish sources of fluids. Biogenic gas produced via fermentation or degradation of organic matter generally characterized with mostly methane, while thermogenic gas produced via combustion has less fractionation of hydrocarbon. Thus, the ratio of methane (C1) to other higher hydrocarbon (C2+) indicate the source of the gas origin (e.g., Bernard et al., 1977). While the ratio of C1/C2+ is higher than 1000, the gas source is preferably from biogenic origins. The study of the isotopic carbon and hydrogen can further provide the information of its imprint (Whiticar, 1999). Additionally, depending on the structure type of hydrate, the guest gas will be varied, while type I and type II preferably hosting methane and ethane, respectively (Sloan, 2003). Consequently, the presence of gas hydrate is potentially causing variations in C1/C2 ratio.

## **Description of the methods**

### *Sampling and preparation*

For analysis of dissolved gas in pore water, a modified headspace technique after Kvenvolden and McDonald (1986) was used. Three ml of bulk sediment either retrieved with gravity core or multicorer or minicorer were transferred to 20 ml glass vials prefilled with 5 ml NaOH, thereby creating a headspace volume of 12 ml. For all gravity cores, sediment samples were taken from the lowest part of the core as soon as the core catcher was removed and from the lowermost part of each segment immediately after the PVC liners were cut in 1 m interval on deck. Additional samples were taken after each segment and were opened with respect to conspicuous lithological changes and/or with an approximate interval of ~25 cm. Cores obtained with the multicorer or minicorer were sampled in 2 cm intervals. In total 763 headspace samples and 704 subsamples, for light hydrocarbon concentration and isotopic measurements respectively, from 25 GCs, 20 MUCs, and 4 MICs were collected (Table 5.12.1). Methane concentrations in the headspace samples were measured by gas chromatography (Pape et al., 2010). Reported concentrations are ex-situ concentrations uncorrected for sediment porosity and Bunsen coefficient. Subsamples for isotopic composition of methane ( $\delta^{13}\text{C-CH}_4$ ,  $\delta^2\text{H-CH}_4$ ) will be analyzed by the onshore laboratory in MARUM.

### *Onboard analysis of concentrations of methane and molecular gas compositions*

Molecular compositions and methane concentrations of gas samples are analyzed via a three-channel gas chromatograph (7890B Angilent Technologies). Molecular of light hydrocarbon, methane (C1) to hexane (C6) were separated through a capillary column and then detected and quantified by a Flame Ionization Detector (FID), while methane and carbon dioxide were analyzed through a capillary column and then detected by Thermal Conductivity Detector (TCD).

Reported concentrations of dissolved methane are ex-situ concentration in headspace gas prepared from sediment samples and are uncorrected for sediment porosity and Bunsen coefficient.

**Table 5.12.1:** List of cores and samples for gas analysis and collected sub samples.

Station/ Device	GeoB No.	Area	Headspace gas	
			Conc. Analysis CH <sub>4</sub>	C + H isotop. Comp. CH <sub>4</sub>
GC-1	24302-2	Sartori MV	8	16
GC-2	24303-1	Sartori MV	20	40
MIC-2	24303-2	Sartori MV	7	
MIC-3	24306-1	Napoli MV	7	
GC-3	24310-1	Napoli MV	12	24
GC-4	24311-1	Bergamo MV	15	30
MIC-4	24311-2	Bergamo MV	9	
GC-6	24312-2	fault zone	3	6
MUC-1	24312-3	fault zone	13	
GC-7	24315-1	fault zone	18	36
MUC-2	24315-2	fault zone	18	
GC-8	24316-1	fault zone	20	40
GC-9	24318-1	fault zone	19	38
MUC-3	24318-2	fault zone	10	
GC-11	24320-1	fault zone	21	41
GC-12	24323-1	plateau of Bergamo MV	13	25
MUC-4	24323-2	plateau of Bergamo MV	20	
MUC-5	24324-1	West of Bergamo	24	
GC-13	24324-2	West of Bergamo	18	36
GC-14	24326-1	plateau of Bergamo MV	10	20
MUC-6	24326-2	plateau of Bergamo MV	15	
MUC-7	24327-1	Moscow MV	16	
GC-15	24327-2	Moscow MV	9	18
GC-16	24328-1	Maidstone MV	7	14
MUC-8	24328-2	Maidstone MV	17	
GC-17	24333-1	Leipzig MV	1	2
MUC-9	24333-2	Leipzig MV	16	
GC-18	24337-1	Dublin MV	8	16
MUC-10	24337-2	Dublin MV	11	
GC-19	24340-1	Unnamed MV1	6	12
MUC-11	24340-2	Unnamed MV1	16	
MUC-12	24341-1	Nice MV	17	
GC-20	24341-2	Nice MV	12	24
GC-21	24343-1	Monza MV	13	26
MUC-13	24343-2	Monza MV	19	
MUC-14	24344-1	brine hole	26	
MUC-15	24346-1	Milano MV	14	
GC-22	24346-2	Milano MV	11	22
GC-23	24348-2	Subrosional pit	22	44
GC-24	24351-1	Gelendzhik MV	11	22
MUC-16	24351-2	Gelendzhik MV	24	
GC-25	24352-1	Heraklion MV	11	22
GC-26	24355-1	Nice MV	3	6
MUC-17	24355-2	Nice MV	14	
MUC-18	24356-1	Unnamed MV	empty	
GC-27	24356-2	Unnamed MV	11	22
MUC-19	24357-1	Heraklion MV	16	
MUC-20	24359-1	Helios MV	15	
GC-28	24359-2	Helios MV	10	20

GC-29	24360-1	Unnamed MV 2	1	2
MUC-21	24360-2	Unnamed MV 2	8	
GC-30	24361-1	Helios MV	10	20
MUC-22	24363-1	Helios MV	17	
GC-31	24364-1	SE flank of Helios MV	8	16
MUC-23	24365-1	South of Sartori MV	20	
GC-33	24370-1	Mud flow rim Sartori	13	26
MUC-30	24376-1	2nd chimney Sartori	21	
GC-38	24376-2	2nd chimney Sartori	9	18
		<b>Total</b>	<b>763</b>	<b>704</b>

### Preliminary results

In total, 18 locations (15 mud volcanoes, 2 subrosional pit and 1 fault zone) were analyzed. 14 mud volcanoes and both subrosional pit sites show the variations of methane concentration. 11 mud volcanoes and both brine hole related sites were measured with the involving of ethane (Table 5.12.2).

**Table 5.12.2:** Preliminary results of light hydrocarbon species detected in different locations.

Work area	Mud volcano/pit/hole/fault zone	CH <sub>4</sub>	C <sub>2</sub> H <sub>6</sub>
3	Sartori MV	x	x
1	Napoli MV	x	
1	Bergamo MV	x	x
1	Fault zone	x	
1	Moscow MV	x	x
1	Maidstone MV	x	x
1	Leipzig MV	x	
1	Dublin MV	x	x
1	Unnamed MV1	x	x
1	Nice MV	x	x
1	Monza MV	x	
1	Brine hole	x	x
1	Milano MV	x	x
1	Subrosional pit	x	x
1	Gelendzhik MV	x	x
1	Heraklion MV	x	x
2	Helios MV	x	x
2	Unnamed MV2	x	

### *Methane consumption and SMI*

Methane concentration profiles from multicorer minimized the disturbing of the sediment during the coring processes. The occurrence of where methane was consumed indicates the sulphate-methane interface (SMI). Shallow SMI can be observed in Bergamo MV, Moscow MV, Sartori MV, and Helios MV. SMIs of each independent core (MIC-4, MUC-4, and MUC-6) in Bergamo MV area show spatial variation, where the center is showing the shallowest SMI and then MV west while the MV north shows most likely the result from diffusion (Fig. 5.12.1).

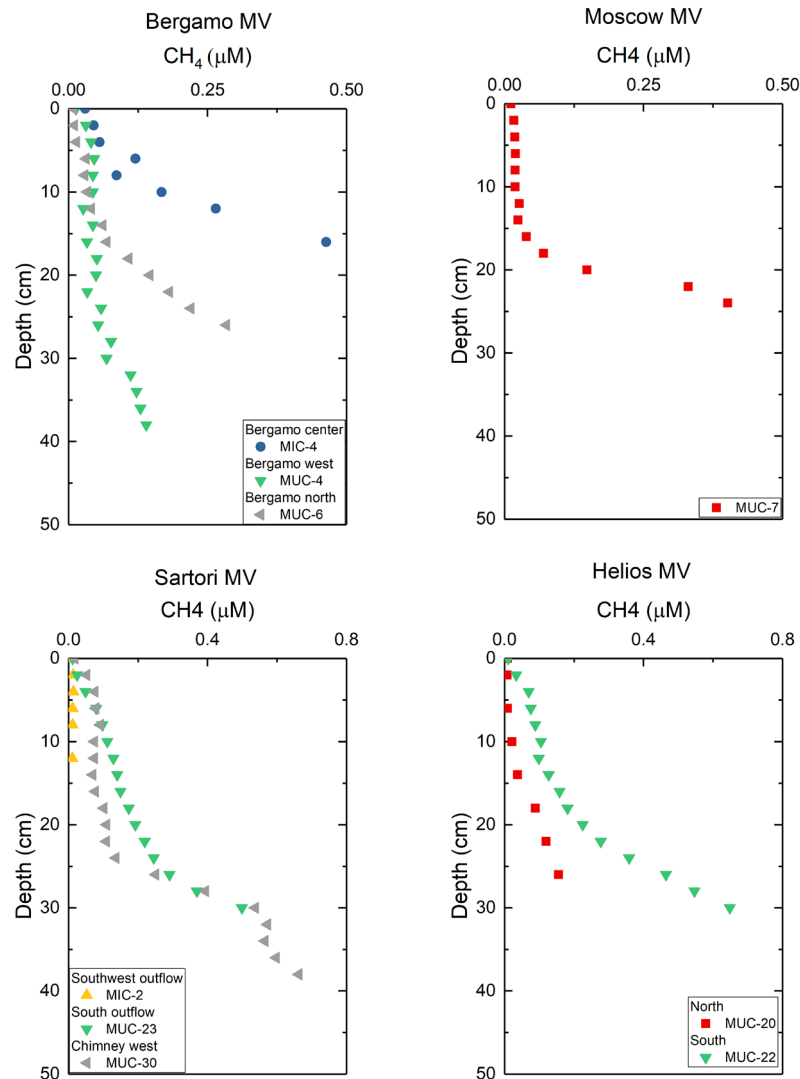


**Fig 5.12.1:** Ex-situ shallow depth methane concentration profile of mud volcanos recovered in multicorer cores.

#### *Variation of gas source and gas species variation*

Bergamo MV seems to be one of the most active mud volcanoes in this area. From the methane concentration profiles in correlation to C1/C2 profile, mechanisms that effect the gas migration can be observed. Most shallow and highest concentration of methane can be observed at the mud volcano center, showing the value of 100 µM at 56 cmbsf. The second peak located at the depth of 281 cmbsf with the value of 97 µM and at the bottom of the core is showing increasing methane up to values of 77 µM. Mud volcano plateau shows the increasing trends at approximately 70 cmbsf. At the west of Bergamo MV, methane was consumed above 100 cmbsf. As the C1/C2 ratio varied between different locations indicating the variation of different gas sources in different parts of the MV. GC-4 shows the C1/C2 ratio up to 1000 suggesting the biogenic dominated gas origin while GC-13 shows mostly thermogenic gas origin and GC-12 is in between. In addition, the fluctuation of GC-4 likely reflects the composition of volatiles that were formerly in the gas hydrate.

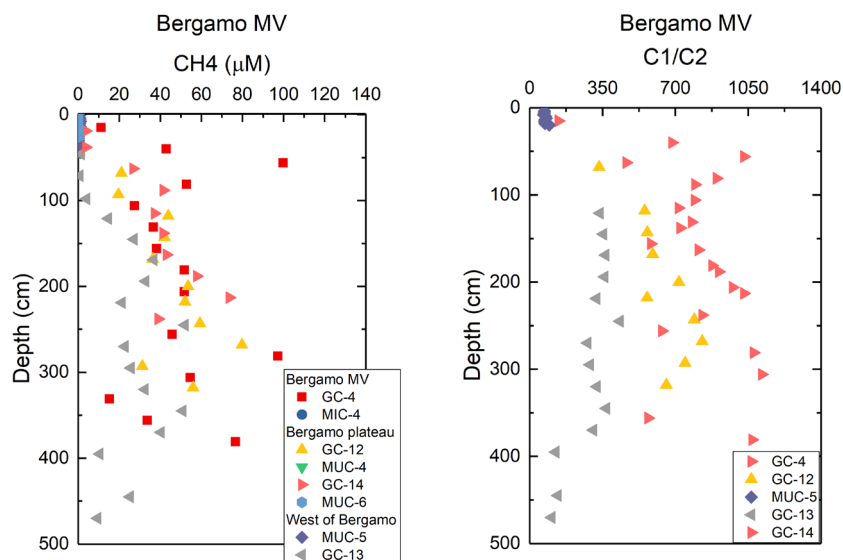


**Fig. 5.12.2:** Ex-situ concentration profiles of dissolved methane in headspace gas samples from the Bergamo MV. (Left: methane concentration profile; right: methane C1/ethane C2 ratio profile.)

As an example of biogenic gas dominated site, methane concentration at GC-27 shows the fluctuation between 32-72  $\mu\text{M}$ . Biogenic source fluids are normally characterized by methane dominated gas. Thus, the over 1000 high C1/C2 ratio is suggesting the potentially biogenic gas in this area.

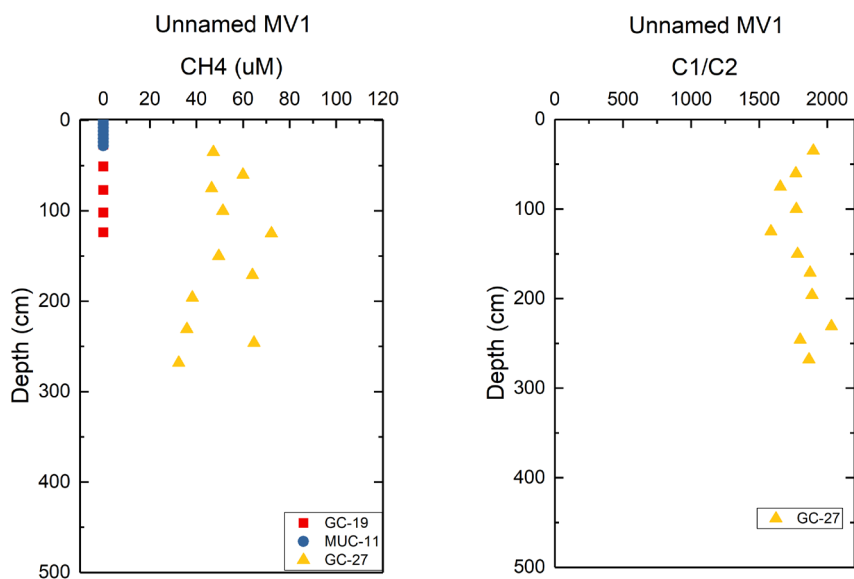


**Fig 5.12.3:** Ex-situ concentration profiles of dissolved methane in headspace gas samples from the unnamed MV 1. (Left: methane concentration profile; right: methane C1/ethane C2 ratio profile.)

At Nice MV, an example of thermogenic dominated MV, an increasing methane concentration trend can be found at the depth of 75 cmbsf. A peak of 60  $\mu\text{M}$  is located at 100 cmbsf. A general increasing of methane can be observed until the bottom of the core (282 cmbsf). Low C1/C2 ratio observed in this area suggests the dominated thermogenic gas source.

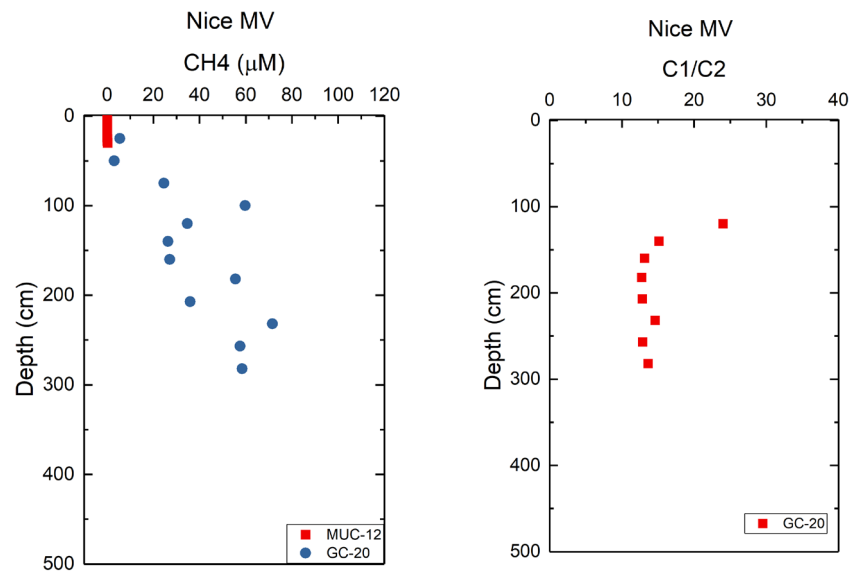


**Fig 5.12.4:** Ex-situ concentration profiles of dissolved methane in headspace gas samples from the Nice MV. (Left: methane concentration profile; right: methane C1/ethane C2 ratio profile.)

#### *Gas hydrate bearing layer and gas species variation*

A shallow and high concentration methane peak can be found at the depth of 25 cmbsf within the MUC-19 from Heraklion MV. In GC-25, highest methane concentration is at the depth of 132 cmbsf, showing the value of 148  $\mu\text{M}$ . Ethane can be measured in samples of MUC-19. The wide variation of C1/C2 ratio (from 28 to 3200) correlates to gas crack and soupy layer observed around 24 cm. This suggests the potential effect of former type I gas hydrate bearing layer preferably hosting methane at the near surface area.

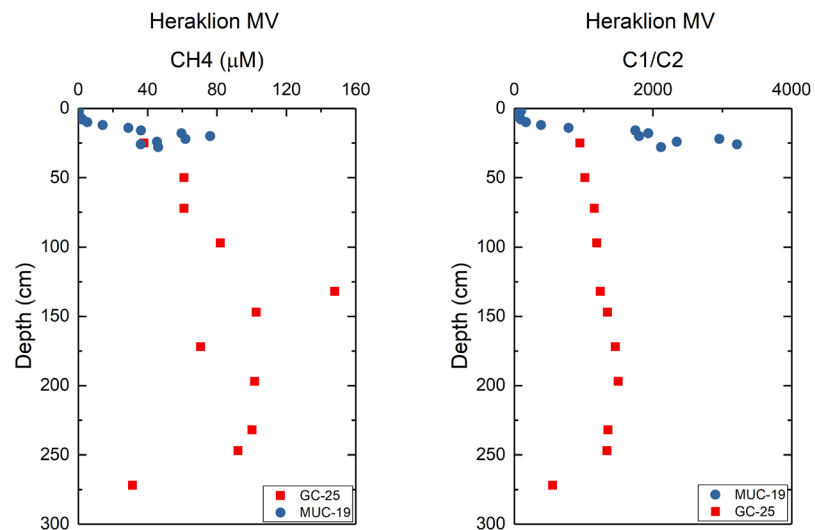


**Fig. 5.12.5:** Ex-situ concentration profiles of dissolved methane in headspace gas samples from the Heraklion MV. (Left: methane concentration profile; right: methane C1/ethane C2 ratio profile.)

6 Station List SO278

SONNE SO278													Station List												
Date	St. SO278/	Instrument	GeoB Number	Location	Time (UTC)		Begin / on seafloor			End / off seafloor			Water depth (m)	Remarks											
					Begin seafloor	on	off	End	Latitude N	Longitude E	Water depth (m)	Latitude N			Longitude E										
10.21.20	001-1	HF-20-1	24301-1	Sartori MV	04:00	04:40	04:57	38° 12.0120	17° 37.6758	1910															
10.21.20	001-2	HF-20-2	24301-2	Sartori MV	05:23	05:40	05:40	38° 12.1105	17° 37.4922	1904															
10.21.20	001-3	HF-20-3	24301-3	Sartori MV	06:10	06:26	06:26	38° 12.2112	17° 37.3074	1872															
10.21.20	001-4	HF-20-4	24301-4	Sartori MV	06:48	06:56	06:56	38° 12.2706	17° 37.1958	1866															
10.21.20	001-5	HF-20-5	24301-5	Sartori MV	07:16	07:32	07:32	38° 12.3180	17° 37.1208	1862															
10.21.20	001-6	HF-20-6	24301-6	Sartori MV	07:49	08:05	08:05	38° 12.3528	17° 37.0590	1864															
10.21.20	001-7	HF-20-7	24301-7	Sartori MV	08:26	08:42	08:42	38° 12.3840	17° 36.9978	1862															
10.21.20	001-8	HF-20-8	24301-8	Sartori MV	09:12	09:28	09:28	38° 12.4488	17° 36.8748	1870															
10.21.20	001-9	HF-20-9	24301-9	Sartori MV	09:53	10:10	10:10	38° 12.5310	17° 36.7374	1902															
10.21.20	001-10	HF-20-10	24301-10	Sartori MV	10:45	11:02	11:02	38° 12.6492	17° 36.5100	1929															
10.22.20	002-1	MIC-01	24302-1	Sartori MV	04:10	05:25	05:25	38° 12.3231	17° 37.1254	1856															
10.22.20	002-2	GC-01	24302-2	Sartori MV	06:18	07:04	07:04	38° 12.3211	17° 37.1133	1856			2.05 m recovery												
10.22.20	003-1	GC-02	24303-1	South of Sartori MV	08:40	09:28	09:28	38° 10.5465	17° 35.0194	2006			4.88 m recovery												
10.22.20	003-2	MIC-02	24303-2	South of Sartori MV	10:37	11:49	11:49	38° 10.5379	17° 35.0232	2006															
10.24.20	004-1	CTD-01	24304-1	Napoli MV	17:56	18:51	18:51	33° 43.4037	24° 41.2066	1932															
10.25.20	005-1	AUV-01	24305-1	Bergamo MV	05:12	07:02	14:30	33° 44.8480	24° 44.9679	2000															
10.26.20	006-1	MIC-03	24306-1	Napoli MV	07:55	09:05	09:05	33° 43.4002	24° 41.1968	1932															
10.26.20	007-1	OFOS-01	24307-1	Bergamo MV	10:30	12:39	16:16	33° 44.3669	24° 45.1340	1929															
10.26.20	008-1	HF-21-1	24308-1	Bergamo MV	17:35	18:20	18:36	33° 44.5927	24° 45.9459	2038															
10.26.20	008-2	HF-21-2	24308-2	Bergamo MV		19:05	19:12	33° 44.4855	24° 45.7387	2019															
10.26.20	008-3	HF-21-3	24308-3	Bergamo MV		19:39	19:46	33° 44.4005	24° 45.5411	2006															
10.26.20	008-4	HF-21-4	24308-4	Bergamo MV		20:14	20:29	33° 44.3310	24° 45.3604	1979															
10.26.20	008-5	HF-21-5	24308-5	Bergamo MV		20:54	21:00	33° 44.3155	24° 45.2000	1939															
10.26.20	008-6	HF-21-6	24308-6	Bergamo MV		21:15	21:32	33° 44.3137	24° 45.1447	1935															
10.26.20	008-7	HF-21-7	24308-7	Bergamo MV		21:51	22:07	33° 44.3154	24° 45.0501	1932															
10.26.20	008-8	HF-21-8	24308-8	Bergamo MV		22:33	22:57	33° 44.3083	24° 44.8685	1936															
10.26.20	008-9	HF-21-9	24308-9	Bergamo MV		23:20	23:27	33° 44.2887	24° 44.7265	1964															
10.27.20	008-10	HF-21-10	24308-10	Bergamo MV		00:00	00:16	33° 44.2720	24° 44.5054	2020															
10.27.20	008-11	HF-21-11	24308-11	Bergamo MV		00:44	01:01	33° 44.2727	24° 44.3632	2047															
10.27.20	008-12	HF-21-12	24308-12	Bergamo MV		01:31	01:47	33° 44.2699	24° 44.1883	2039															
10.27.20	008-13	HF-21-13	24308-13	Bergamo MV		02:24	02:40	33° 44.0896	24° 44.3852	2038															
10.27.20	009-1	AUV-92	24309-1	Monza MV	04:29	05:40	15:00	33° 43.9426	24° 45.5397	2000			Failure: no data												
10.27.20	010-1	GC-03	24310-1	Napoli MV	16:49	17:28	17:28	33° 43.4011	24° 41.1959	1933			2.81 m recovery												
10.27.20	011-1	GC-04	24311-1	Bergamo MV	19:17	19:56	19:56	33° 44.3279	24° 45.0576	1930			3.56 m recovery												
10.27.20	011-2	MIC-04	24311-2	Bergamo MV	21:02	22:08	22:08	33° 44.3282	24° 45.0503	1930															
10.28.20	012-1	GC-05	24312-1	Fault zone	10:25	11:26	11:26	34° 5.6769	24° 58.3945	3346			0.20 m recovery, carbonates												
10.28.20	012-2	GC-06	24312-2	Fault zone	12:47	13:47	13:47	34° 5.6740	24° 58.3909	3320			0.61 m recovery												
10.28.20	012-3	MUC-01	24312-3	Fault zone	15:04	16:34	16:34	34° 5.6692	24° 58.4002	3354															
10.28.20	013-1	HF-22-1	24313-1	Fault zone	18:30	19:34	19:49	34° 7.9152	24° 55.6191	3062															
10.28.20	013-2	HF-22-2	24313-2	Fault zone		21:22	21:29	34° 6.8834	24° 55.6205	3059															

Continuation Station List

SONNE SO278		Station List											
		Date	St. SO278/	Instrument	Geob Number	Location	Begin on seafloor	Time (UTC)	End	Latitude N	Longitude E	Water depth (m)	Remarks
10/28/20	013-3	HF-22-3	24313-3	Fault zone		23:34	23:39		34° 5.5100	24° 55.6182	3527		
10/29/20	013-4	HF-22-4	24313-4	Fault zone		00:37	00:52		34° 5.0807	24° 55.6251	3522		
10/29/20	013-5	HF-22-5	24313-5	Fault zone		02:33	02:47		34° 3.9038	24° 55.6193	3105		
10/29/20	013-6	HF-22-6	24313-6	Fault zone		04:14	04:21	05:27	34° 2.9328	24° 55.6252	3194		
10/29/20	014-1	CTD-02	24314-1	Fault zone		06:15		09:14	34° 5.2402	24° 55.6173	3526		
10/29/20	015-1	GC-07	24315-1	Fault ridge		10:24	11:13	11:59	34° 7.2990	24° 59.3087	2501	3.93 m recovery	
10/29/20	015-2	MUC-02	24315-2	Fault ridge		12:05	13:14	14:05	34° 7.3095	24° 59.3080	2501		
10/29/20	016-1	GC-08	24316-1	Fault zone		15:02	16:00	17:02	34° 3.8940	24° 55.6230	3105	4.80 m recovery	
10/30/20	017-1	AUV-93	24317-1	Inner ridge transect		15:25	15:49	03:55	34° 2.1918	24° 56.2485			
10/31/20	018-1	GC-09	24318-1	Fault zone		06:34	07:36	08:42	34° 5.5130	24° 55.6306	3530	4.82 m recovery	
10/31/20	018-2	MUC-03	24318-2	Fault zone		08:56	10:23	11:32	34° 5.5121	24° 55.6238	3552		
10/31/20	019-1	GC-10	24319-1	Fault zone		12:16	13:21	14:24	34° 5.3641	24° 58.3380	3532	Banana, no sediment	
10/31/20	020-1	GC-11	24320-1	Fault zone		15:13	16:24	17:25	34° 5.0841	24° 55.6292	3521	5.19 m recovery	
10/31/20	021-1	HF-23-1	24321-1	Inner ridge transect		18:15	19:13	19:27	34° 2.1656	24° 55.5223	3045		
10/31/20	021-2	HF-23-2	24321-2	Inner ridge transect		20:18	20:24		34° 1.7800	24° 55.5286	3085		
10/31/20	021-3	HF-23-3	24321-3	Inner ridge transect		21:04	21:10		34° 1.5560	24° 55.5314	3080		
10/31/20	021-4	HF-23-4	24321-4	Inner ridge transect		21:51	22:05		34° 1.3306	24° 55.5255	3103		
10/31/20	021-5	HF-23-5	24321-5	Inner ridge transect		22:30	22:37		34° 1.2058	24° 55.5265	3109		
11/01/20	021-6	HF-23-6	24321-6	Inner ridge transect		23:39	23:54		34° 0.7575	24° 55.5385	3004		
11/01/20	021-7	HF-23-7	24321-7	Inner ridge transect		01:01			34° 0.2459	24° 55.5179	-		
11/01/20	021-8	HF-23-8	24321-8	Inner ridge transect		01:54	02:09	03:15	33° 59.8672	24° 55.5059	2832		
11/01/20	022-1	AUV-94	24322-1	Fault zone		04:30	06:00	16:10	34° 5.4704	24° 51.4182	3500	34° 4.8799 24° 55.8610 3500	
11/02/20	023-1	GC-12	24323-1	Bergamo plateau		08:07	08:47	09:29	33° 44.3047	24° 44.8789	1934	3.18 m recovery	
11/02/20	023-2	MUC-04	24323-2	Bergamo plateau		09:40	10:31	11:11	33° 44.3047	24° 44.8756	1936		
11/02/20	024-1	MUC-05	24324-1	West of Bergamo		11:29	12:28	13:10	33° 44.3240	24° 44.2685	2041		
11/02/20	024-2	GC-13	24324-2	West of Bergamo		13:17	14:04	14:45	33° 44.3252	24° 44.2721	2038	4.45 m recovery	
11/02/20	025-1	AUV-95	24325-1	Monza MV		15:30	16:55	04:00	33° 43.8375	24° 45.9512	2000	33° 43.5673 24° 42.8232 2000	
11/03/20	026-1	GC-14	24326-1	Bergamo NE plateau		05:40	06:19	06:59	33° 44.4080	24° 45.0100	1937	2.38 m recovery	
11/03/20	026-2	MUC-06	24326-2	Bergamo NE plateau		07:05	07:55	08:36	33° 44.4053	24° 45.0041	1936		
11/03/20	027-1	MUC-07	24327-1	Moscow MV		09:54	10:49	11:26	33° 40.5950	24° 31.7173	1824		
11/03/20	027-2	GC-15	24327-2	Moscow MV		11:36	12:10	12:55	33° 40.5934	24° 31.7192	1824	2.19 m recovery	
11/03/20	028-1	GC-16	24328-1	Maidstone MV		14:09	14:50	15:35	33° 37.1155	24° 40.6466	1934	1.85 m recovery	
11/03/20	028-2	MUC-08	24328-2	Maidstone MV		15:51	16:43	17:27	33° 37.1199	24° 40.6550	1933		
11/03/20	029-1	HF-24-1	24329-1	Monza MV		18:47	19:34	19:48	33° 44.1768	24° 44.4378	2064		
11/03/20	029-2	HF-24-2	24329-2	Monza MV		20:10	20:16		33° 44.1425	24° 44.3526	2059		
11/03/20	029-3	HF-24-3	24329-3	Monza MV		20:56	21:12		33° 44.0972	24° 43.9019	2017		
11/03/20	029-4	HF-24-4	24329-4	Monza MV		21:42	21:49		33° 44.0684	24° 43.6407	1932		
11/03/20	029-5	HF-24-5	24329-5	Monza MV		22:13	22:20		33° 44.0654	24° 43.5168	1922		
11/03/20	029-6	HF-24-6	24329-6	Monza MV		22:36	22:51		33° 44.0608	24° 43.4784	1928		
11/03/20	029-7	HF-24-7	24329-7	Monza MV		23:08	23:15		33° 44.0584	24° 43.4408	1932		

Continuation Station List

SONNE SO278		Station List												
Date	St. SO278/	Instrument	GeoB Number	Location	Time (UTC)		Begin / on seafloor			End / off seafloor			Water depth (m)	Remarks
					Begin seafloor	on off seafloor	Latitude N	Longitude E	Water depth (m)	Latitude N	Longitude E	Water depth (m)		
11.03.20	029-8	HF-24-8	24329-8	Monza MV	23:33	23:40	33° 44.0512	24° 43.3801	1946					
11.04.20	029-9	HF-24-9	24329-9	Monza MV	00:06	00:21	33° 44.0407	24° 43.2676	1987					
11.04.20	029-10	HF-24-10	24329-10	Monza MV	00:52	00:59	33° 44.0197	24° 43.0477	2017					
11.04.20	030-1	OFOS-02	24330-1	Monza MV	03:10	11:39	33° 44.1048	24° 43.3641	1962	33° 44.1146	24° 44.4321	2059	Verified seep structures	
11.04.20	031-1	CTD-03	24331-1	Milano MV	12:55	13:51	33° 44.0551	24° 46.7760	1950					
11.04.20	032-1	AUV-96	24332-1	Milano MV	15:29	16:27	33° 44.2930	24° 45.6660	1929	33° 45.0990	24° 47.2920	1929	0.30 m recovery	
11.05.20	033-1	GC-17	24333-1	Leipzig MV	05:42	06:25	33° 46.7619	24° 40.0083	1933					
11.05.20	033-2	MUC-09	24333-2	Leipzig MV	07:14	08:06	33° 46.7698	24° 40.0135	1936					
11.06.20	034-1	CTD-04	24334-1	Dublin MV	16:09	17:15	33° 30.6020	25° 29.2834	2260					
11.06.20	035-1	HF-25-1	24335-1	Dublin MV	18:55	20:00	33° 30.6255	25° 30.8340	2424					
11.06.20	035-2	HF-25-2	24335-2	Dublin MV	21:09	21:16	33° 30.6139	25° 30.2533	2357					
11.06.20	035-3	HF-25-3	24335-3	Dublin MV	22:02	22:09	33° 30.6108	25° 29.8303	2322					
11.06.20	035-4	HF-25-4	24335-4	Dublin MV	22:54	23:09	33° 30.5973	25° 29.4382	2283					
11.06.20	035-5	HF-25-5	24335-5	Dublin MV	23:39	00:10	33° 30.5905	25° 29.2848	2266					
11.07.20	035-6	HF-25-6	24335-6	Dublin MV	01:04	01:19	33° 30.5801	25° 28.6208	2370					
11.07.20	035-7	HF-25-7	24335-7	Dublin MV	02:05	02:11	33° 30.5693	25° 28.1130	2390					
11.07.20	035-8	HF-25-8	24335-8	Dublin MV	03:08	03:15	33° 30.5596	25° 27.5161	2384					
11.07.20	036-1	OFOS-03	24336-1	Dublin MV	04:57	06:03	33° 30.6133	25° 30.2584	2353	33° 30.6992	25° 29.3833	2291	1.83 m recovery	
11.07.20	037-1	GC-18	24337-1	Dublin MV	11:56	12:35	33° 30.5300	25° 29.3488	2269					
11.07.20	037-2	MUC-10	24337-2	Dublin MV	13:25	14:30	33° 30.5338	25° 29.3433	2265					
11.08.20	038-1	AUV-97	24338-1	Nice MV	15:11	15:56	34° 3.2407	24° 19.7522	1770	34° 3.3034	24° 17.1299	1770		
11.09.20	039-1	CTD-05	24339-1	Flare position	06:55	07:59	34° 9.8608	24° 18.8319	1865					
11.09.20	040-1	GC-19	24340-1	Unnamed MV	09:50	10:29	34° 8.6759	24° 19.8500	1813					1.24 m recovery
11.09.20	040-2	MUC-11	24340-2	Unnamed MV	11:18	12:09	34° 8.6704	24° 19.8469	1812					
11.09.20	041-1	MUC-12	24341-1	Nice MV	13:58	14:52	34° 4.0199	24° 18.3729	1721					
11.09.20	041-2	GC-20	24341-2	Nice MV	15:36	16:14	34° 4.0197	24° 18.3724	1737					2.82 m recovery
11.09.20	042-1	HF-26-1	24342-1	Nice MV	17:25	18:09	34° 2.2030	24° 19.7304	1862					
11.09.20	042-2	HF-26-2	24342-2	Nice MV	18:55	19:01	34° 2.3640	24° 19.5954	1890					
11.09.20	042-3	HF-26-3	24342-3	Nice MV	19:47	19:54	34° 2.6683	24° 19.3503	1863					
11.09.20	042-4	HF-26-4	24342-4	Nice MV	20:46	21:02	34° 3.1060	24° 19.0236	1826					
11.09.20	042-5	HF-26-5	24342-5	Nice MV	21:49	21:56	34° 3.4949	24° 18.7209	1778					
11.09.20	042-6	HF-26-6	24342-6	Nice MV	22:50	23:05	34° 3.9654	24° 18.3559	1724					
11.09.20	042-7	HF-26-7	24342-7	Nice MV	23:22	23:39	34° 4.0183	24° 18.3670	1719					
11.10.20	042-8	HF-26-8	24342-8	Nice MV	00:16	00:23	34° 4.0851	24° 18.0321	1778					
11.10.20	042-9	HF-26-9	24342-9	Nice MV	01:17	01:32	34° 4.1688	24° 17.534	1813					
11.10.20	042-10	HF-26-10	24342-10	Nice MV	02:21	02:35	34° 4.253	24° 17.055	1730					
11.10.20	042-11	HF-26-11	24342-11	Nice MV	03:22	03:29	34° 4.369	24° 16.395	1828					
11.10.20	043-1	GC-21	24343-1	Monza MV	08:40	09:19	33° 44.0642	24° 43.4720	1921					3.18 m recovery
11.10.20	043-2	MUC-13	24343-2	Monza MV	10:06	11:00	33° 44.0555	24° 43.4649	1926					
11.10.20	044-1	MUC-14	24344-1	Brine hole	11:58	12:57	33° 44.1332	24° 44.3584	2077					

Continuation Station List

SONNE SO278		Station List													
Date	St.	Instrument	GeOB Number	Location	Time (UTC)		Begin / on seafloor			End / off seafloor			Remarks		
	SO278/				Begin seafloor	on	off	Latitude N	Longitude E	Water depth (m)	Latitude N	Longitude E	Water depth (m)		
11.11.20	045-1	AUV-98	24345-1	Nadir brine lake	15:00	15:54	04:48	05:50	33° 38.8321	24° 39.4741	1900	33° 40.5643	24° 39.1117	1900	
11.11.20	046-1	MUC-15	24346-1	Milano MV	06:56	07:50		08:34	33° 43.9413	24° 46.6527	1947				
11.11.20	046-2	GC-22	24346-2	Milano MV	08:41	09:22		10:03	33° 43.9440	24° 46.6507	1956				2.74 m recovery
11.11.20	047-1	OFOS-04	24347-1	Milano MV	10:35	11:28	15:00	15:41	33° 43.6734	24° 46.7582	1974	33° 43.7695	24° 46.1661	2014	
11.11.20	048-1	CTD-06	24348-1	Subrosional pit	16:50	17:52		18:57	33° 38.3470	24° 38.8813	2066				
11.11.20	048-2	GC-23	24348-2	Subrosional pit	19:10	20:02		20:55	33° 38.3396	24° 38.8854	2081				
11.11.20	049-1	AUV-99	24349-1	Flare position	05:21	06:31	15:51	17:02	34° 10.3020	24° 19.6680	1880	34° 10.4639	24° 18.6540	1880	
11.11.20	050-1	HF-27-1	24350-1	Nice MV	17:55	18:37	18:52		34° 3.1401	24° 19.5456	1835				5.37 m recovery, with MTLs
11.11.20	050-2	HF-27-2	24350-2	Nice MV		19:23	19:30		34° 3.1081	24° 19.2642	1852				
11.11.20	050-3	HF-27-3	24350-3	Nice MV		20:10	20:16		34° 3.0782	24° 18.8448	1798				
11.11.20	050-4	HF-27-4	24350-4	Nice MV		20:47	21:01		34° 3.0783	24° 18.6277	1779				
11.11.20	050-5	HF-27-5	24350-5	Nice MV		21:28	21:34		34° 3.0600	24° 18.4096	1782				
11.11.20	050-6	HF-27-6	24350-6	Nice MV		22:06	22:13		34° 3.0394	24° 18.1671	1812				
11.11.20	050-7	HF-27-7	24350-7	Nice MV		22:46	23:01		34° 3.0307	24° 17.9774	1862				
11.11.20	050-8	HF-27-8	24350-8	Nice MV		23:44	23:59		34° 3.0145	24° 17.6826	1861				
11/11/20	050-9	HF-27-9	24350-9	Nice MV		00:38	00:44		34° 2.9850	24° 17.3367	1870				
11/11/20	050-10	HF-27-10	24350-10	Nice MV		01:20	01:34		34° 2.9675	24° 17.1417	1835				
11/11/20	050-11	HF-27-11	24350-11	Nice MV		02:12	02:18		34° 2.9398	24° 16.7831	1863				
11/11/20	050-12	HF-27-12	24350-12	Nice MV		02:51	03:06		34° 2.9224	24° 16.5109	1850				
11/11/20	051-1	GC-24	24351-1	Gelendzhik MV	04:58	05:37		06:20	33° 54.175	24° 16.155	1709				2.84 m recovery
11/11/20	051-2	MUC-16	24351-2	Gelendzhik MV	06:27	07:13		07:55	33° 54.175	24° 16.155	1696				
11/11/20	052-1	GC-25	24352-1	Heraklion MV	08:48	09:25		10:09	33° 56.195	24° 06.918	1714				2.72 m recovery
11/11/20	053-1	OFOS-05	24353-1	Flare position	11:55	12:39	17:02	17:43	34° 9.8767	24° 18.8252	1845	34° 9.7604	24° 18.3692	1830	
11/11/20	054-1	AUV-100	24354-1	Nice MV	19:18	20:15	08:27	09:10	34° 1.5900	24° 17.7840	1900	34° 1.9260	24° 18.7380	1900	
11/11/20	055-1	GC-26	24355-1	Nice MV	09:55	10:34		11:10	34° 3.0369	24° 18.1749	1819				0.78 m recovery, banana
11/11/20	055-2	MUC-17	24355-2	Nice MV	11:17	12:07		12:44	34° 3.0423	24° 18.1853	1811				
11/11/20	056-1	MUC-18	24356-1	Unnamed MV	13:31	14:24		15:05	34° 8.4602	24° 19.4397	1803				Failure: all liners empty
11/11/20	056-2	GC-27	24356-2	Unnamed MV	15:11	15:52		16:33	34° 8.4602	24° 19.4452	1812				2.68 m recovery
11/11/20	057-1	MUC-19	24357-1	Heraklion MV	18:21	19:10		19:56	33° 56.1979	24° 6.9129	1722				
11/11/20	058-1	AUV-101	24358-1	Helios MV	16:10	17:30	05:22	06:48	35° 56.1453	20° 46.1814	2900	35° 57.6592	20° 46.3011	2900	
11/11/20	059-1	MUC-20	24359-1	Helios MV	07:03	08:20		09:21	35° 58.1876	20° 47.1307	2754				
11/11/20	059-2	GC-28	24359-2	Helios MV	09:26	10:20		11:20	35° 58.1830	20° 47.1349	2753				2.51 m recovery
11/11/20	060-1	GC-29	24360-1	Unnamed MV 2	11:58	12:52		13:49	35° 56.6328	20° 46.4209	2762				0.25 m recovery
11/11/20	060-2	MUC-21	24360-2	Unnamed MV 2	13:54	15:09		16:07	35° 56.6307	20° 46.4177	2758				
11/11/20	061-1	GC-30	24361-1	Helios MV	16:36	17:30		18:26	35° 58.1104	20° 47.1807	2751				2.47 m recovery
11/11/20	062-1	HF-28-1	24362-1	Helios MV	18:55	19:55	20:09		35° 56.6163	20° 46.3936	2752				-
11/11/20	062-2	HF-28-2	24362-2	Helios MV		21:10	21:16		35° 56.9206	20° 46.8480	2857				
11/11/20	062-3	HF-28-3	24362-3	Helios MV		22:15	22:30		35° 57.2829	20° 47.2499	2896				
11/11/20	062-4	HF-28-4	24362-4	Helios MV		23:21	23:27		35° 57.6615	20° 47.2093	2857				

Continuation Station List

SONNE SO278										Station List									
Date	St.	Instrument	GeoB Number	Location	Begin on seafloor	Time (UTC)	End	Latitude N	Longitude E	Water depth (m)	Latitude N	Longitude E	Water depth (m)	Remarks					
11/17/20	SO278/062-5	HF-28-5	24362-5	Helios MV	00:18	00:33		35° 58.1142	20° 47.1804	2759									
11/17/20	062-6	HF-28-6	24362-6	Helios MV	00:48	00:54		35° 58.1663	20° 47.1516	2753									
11/17/20	062-7	HF-28-7	24362-7	Helios MV	01:10	01:24		35° 58.2332	20° 47.1467	2754									
11/17/20	062-8	HF-28-8	24362-8	Helios MV	02:14	02:20		35° 58.6275	20° 47.0925	2897									
11/17/20	062-9	HF-28-9	24362-9	Helios MV	03:07	03:13		35° 58.9949	20° 47.0373	2924									
11/17/20	062-10	HF-28-10	24362-10	Helios MV	04:07	04:14	05:15	35° 59.4604	20° 46.9801	2950									
11/17/20	063-1	MUC-22	24363-1	Helios MV	05:39	06:58	07:56	35° 58.1122	20° 47.1714	2753									
11/17/20	064-1	GC-31	24364-1	E flank of Helios MV	08:19	09:14	10:07	35° 57.7990	20° 47.5806	2867				1.98 mrecovery					
11/18/20	065-1	MUC-23	24365-1	Sartori MV	06:35	07:30	08:10	38° 12.3198	17° 37.1085	1856									
11/18/20	066-1	GC-32	24366-1	South of Sartori MV	08:39	09:20	10:02	38° 10.9078	17° 36.8892	1967				5.74 mrecovery					
11/18/20	066-2	MUC-24	24366-2	South of Sartori MV	10:08	11:05	11:51	38° 10.9078	17° 36.8900	1950									
11/18/20	067-1	MUC-25	24367-1	Mud flow Sartori MV	12:15	13:05	13:44	38° 12.6008	17° 36.7804	1894									
11/18/20	068-1	MUC-26	24368-1	Mud flow rim Sartori	13:55	14:46	15:25	38° 12.3558	17° 36.7506	1865									
11/18/20	069-1	MUC-27	24369-1	Outflow west Sartori	15:35	16:30		38° 12.3759	17° 36.6447	1888				Failure: all liners empty					
11/18/20	070-1	GC-33	24370-1	Mud flow rim Sartori	17:18	17:58	18:38	38° 12.3616	17° 36.7491	1867				3.24 mrecovery					
11/18/20	071-1	HF-29-1	24371-1	Sartori MV	18:54	19:35	19:50	38° 12.6143	17° 37.5099	1882									
11/18/20	071-2	HF-29-2	24371-2	Sartori MV	20:07	20:14		38° 12.5607	17° 37.4466	1887									
11/18/20	071-3	HF-29-3	24371-3	Sartori MV	20:29	20:44		38° 12.5069	17° 37.3907	1892									
11/18/20	071-4	HF-29-4	24371-4	Sartori MV	21:08	21:23		38° 12.3872	17° 37.2384	1865									
11/18/20	071-5	HF-29-5	24371-5	Sartori MV	21:48	22:02		38° 12.3290	17° 37.1273	1857									
11/18/20	071-6	HF-29-6	24371-6	Sartori MV	22:38	23:11		38° 12.3525	17° 36.8520	1862									
11/18/20	071-7	HF-29-7	24371-7	Sartori MV	23:29	23:44		38° 12.3579	17° 36.7617	1866									
11/19/20	071-8	HF-29-8	24371-8	Sartori MV	00:04	00:20		38° 12.3745	17° 36.6502	1885									
11/19/20	071-9	HF-29-9	24371-9	Sartori MV	00:59	01:13		38° 12.3898	17° 36.2472	1928									
11/19/20	071-10	HF-29-10	24371-10	Sartori MV	01:53	02:08		38° 12.1337	17° 35.9655	1952									
11/19/20	071-11	HF-29-11	24371-11	Sartori MV	02:53	03:07		38° 11.7104	17° 35.9710	1964									
11/19/20	071-12	HF-29-12	24371-12	Sartori MV	03:42	03:58	04:40	38° 11.3961	17° 36.0058	1955									
11/19/20	072-1	GC-34	24372-1	Mud flow Sartori MV	05:16	05:49	06:33	38° 12.3766	17° 36.6434	1888				Failure: empty liner					
11/19/20	073-1	GC-35	24373-1	SW of Sartori MV	07:13	07:52	08:37	38° 11.3728	17° 35.6644	1961				5.64 mrecovery					
11/19/20	073-2	MUC-28	24373-2	SW of Sartori MV	08:46	09:39	10:24	38° 11.3741	17° 35.6650	1980									
11/19/20	074-1	GC-36	24374-1	SW of Sartori MV	10:42	11:23	12:12	38° 11.6180	17° 36.1995	1977				4.43 mrecovery					
11/19/20	074-2	MUC-29	24374-2	SW of Sartori MV	12:34	13:29	14:13	38° 11.6248	17° 35.2064	1976									
11/19/20	075-1	GC-37	24375-1	SW of Sartori MV	14:24	15:06	15:53	38° 12.3388	17° 35.5201	1976				4.64 mrecovery					
11/19/20	076-1	MUC-30	24376-1	2nd chimney Sartori	16:14	17:07	17:51	38° 12.3862	17° 36.9991	1858									
11/19/20	076-2	GC-38	24376-2	2nd chimney Sartori	17:55	18:33	19:17	38° 12.3883	17° 37.0010	1858				2.54 mrecovery					

AUV Seal 5000: AUV  
 Gravity corer: GC  
 Minicorer: MIC  
 TV-Multicorer: TV-MUC  
 CTD+Rosette: CTD  
 Ocean floor observation system: OFOS  
 Heat flow lance: HF  
 \* coordinates of the vessel

## 7 Data and Sample Storage and Availability

Metadata of the cruise as well as the station list were submitted to Pangaea data bank (<https://www.pangaea.de/>). Sediment cores recovered during the SO278 cruise are stored at the University of Bremen in the MARUM/GeoB Core Repository: (<https://www.marum.de/Infrastruktur/MARUM-GeoB-Kernlager.html>).

Samples from these cores are available upon request to the co-chief scientist Gerhard Bohrmann ([gbohrmann@marum.de](mailto:gbohrmann@marum.de)). Non-cruise participants can request samples after the moratorium of three years. In addition, data (raw and processed) will be submitted to Pangaea along with the scientific publication.

**Table 7.1** Overview of data availability.

Type	Database	Available	Free Access	Contact
Station list	PANGAEA	March 2021	April 2024	<a href="mailto:gbohrmann@marum.de">gbohrmann@marum.de</a>
Hydroacoustic data (EM122, Parasound)	PANGAEA	March 2021	April 2024	<a href="mailto:gbohrmann@marum.de">gbohrmann@marum.de</a>
Core logs	PANGAEA	March 2021	April 2024	<a href="mailto:gbohrmann@marum.de">gbohrmann@marum.de</a>
CTD data	PANGAEA	March 2021	April 2024	<a href="mailto:gbohrmann@marum.de">gbohrmann@marum.de</a>

## 8 Acknowledgements

RV SONNE cruise SO278 to the Mediterranean Ridge was planned, coordinated and carried out by MARUM “Center for Marine Environmental Sciences” at the University of Bremen. The cruise was financed by the “Deutsche Forschungsgemeinschaft” (DFG) through the cluster of excellence “The Ocean Floor – Earth’s Uncharted Interface” (EXC 2077) and through funds related to the GPF review procedure (GPF 20\_1\_054, Sartori MV plus). We would like to specially acknowledge the master of the vessel, Lutz Mallon and his crew for their continued contribution to a pleasant and professional atmosphere aboard RV SONNE. Many thanks to the staff of the Control Station German Research Vessels and to the Logistic Department of MARUM (Marco Klann and Götz Ruhland). We also would like to thank our colleagues of the German embassies in Greece and Italy for supporting our request of research at the foreign ministries.

## 9 References

- Behrmann, J.H., Lewis, S.D., Musgrave, R.J. and Shipboard Scientific Party Leg 141, 1992. Proc. ODP, Init. Repts., 141, College Station, TX (Ocean Drilling Program), 709 pp.
- Bernard, B., Brooks, J.M., Sackett, W.M., 1977. A geochemical model for characterization of hydrocarbon gas sources in marine sediments. paper presented at Offshore Technology Conference, Houston, Texas, 02.-05.05.1977.doi:10.4043/2934-ms.
- Blum, P., 1997. Physical properties handbook: a guide to the shipboard measurement of physical properties of deep-sea cores. College Station, Texas, USA. Strength 9, 1-3.
- Bohrmann, G. and cruise participants, 2016. Report and preliminary results of R/V POSEIDON cruise POS499, Calabrian Mud Volcanoes, Catania (Italy) – Catania (Italy), May 4 – May 22,

2016. Berichte, MARUM – Zentrum für Marine Umweltwissenschaften, Fachbereich Geowissenschaften, Universität Bremen.
- Bohrmann, G. and cruise participants, 2015. Report and preliminary results of R/V METEOR cruise M112, Dynamic of Mud Volcanoes and Seeps in the Calabrian Accretionary Prism, Ionian Sea, Catania (Italy) – Catania (Italy), November 6 – December 15, 2014. Berichte, MARUM – Zentrum für Marine Umweltwissenschaften, Fachbereich Geowissenschaften, Universität Bremen.
- Caress, D.W., Chayes, D.N., 1995. Current Status of MB-System. Version 4.2, February 28, 1995. Lamont-Doherty Earth Observatory of Columbia University. (<http://www.ldeo.columbia.edu/res/pi/MB-System/>).
- Ceramicola, S., Praeg, D., Cova, A., Accetella, D. and Zecchin, M., 2014. Seafloor distribution and last glacial to postglacial activity of mud volcanoes on the Calabrian accretionary prism, Ionian Sea. *Geo-Marine Letters* 34, 111-129.
- Ceramicola, S., Praeg, D. and the OGS EXPLORA Scientific Party, 2006. Mud volcanoes discovered on the Calabrian Arc: preliminary results from the HERMES-HYDRAMED IONIO 2005 campaign. *CIESM Workshop Monographs* 29, 35–39.
- Cita, M.B., Erba, E., Lucchi, R., Pott, M., van der Meer, R., Nieto, L., 1996. Stratigraphy and sedimentation in the Mediterranean Ridge diapiric belt. *Marine Geology* 132, 131-150.
- Cita, M.B., Wright, R.C., Ryan, W.B.F. and Longinelli, A., 1978. Messinian Paleoenvironments. In Hsü, K.J., Montadert, L. et al. *Init. Repts. DSDP, 42A: Washington (U.S. Govt. Printing Office)*, 1003-1035.
- Dählmann, A., de Lange, G.J., 2003. Fluid-sediment interactions at Eastern Mediterranean mud volcanoes: a stable isotope study from ODP Leg 160. *Earth Planet. Sci. Letts.*, 212: 377-391.
- De Lange, G., Thomson, J., Reitz, A., Slomp, C.P., Speranza Principato, M., Erba, E., Corselli, C., 2008. Synchronous basin-wide formation and redox-controlled preservation of a Mediterranean sapropel. *Nature Geoscience* 1, 606-610.
- Deyhle, A., Kopf, A., 2001. Deep fluids and ancient pore waters at the backstop: Stable isotope systematics (C, B, O) of mud volcano deposits on the Mediterranean Ridge accretionary wedge. *Geology*, 29/11, 1031-1034.
- Emeis, K.-C., Robertson, A.H.F., Richter, C., Shipboard Scientific Party, 1996. *Proc. ODP, Init. Repts.*, 160, College Station, TX (Ocean Drilling Program), 972 pp.
- Faccenna, C., Molin, P., Orecchio, B., Olivetti, V., Bellier, O., Funiciello, F., Minelli, L., Piromallo, C., Billi, A., 2011. Topography of the Calabria subduction zone (southern Italy): clues for the origin of Mt. Etna. *Tectonics* 30, TC1003. doi:10.1029/2010TC002694.
- Faccenna, C., Piromallo, C., Crespo-Blanc, A., Jolivet, L., Rossetti, F., 2004. Lateral slab deformation and the origin of the western Mediterranean arcs. *Tectonics* 23, TC1012, doi:10.1029/2002TC001488.
- Fusi, N., Kenyon, N.H., 1996. Distribution of mud diapirism and other geological structures from long-range sidescan sonar (GLORIA) data, Eastern Mediterranean Sea. *Marine Geology* 132, 21–38.
- Goes, S., Giardini, D., Jenny, S., Hollenstein, C., Kahle, H.-G., Geiger, A., 2004. A recent tectonic reorganization in the south-central Mediterranean. *Earth and Planetary Science Letters* 226, 335–345. doi:10.1016/j.epsl.2004.07.038.

- Grevenmeyer, I., Kopf, A., Fekete, N., Kaul, N., Villinger, H.W., Heesemann, M., Wallmann, K., Spiess, V., Gennerich, H.-H., Müller M. and Weinrebe, W., 2004. Fluid flow through active mud dome Mound Culebra offshore Nicoya Peninsula, Costa Rica: evidence from heat flow surveying. *Marine Geology*, 207, 145-157.
- Gutscher, M.A., Kopp, H., Krastel, S., Bohrmann, G., Garlan, T., Zaragosi, S., Klaucke, I., Wintersteller, P., Loubrieu, B., Le Faou, Y., San Pedro, L., Dominguez, S., Rovere, M., Mercier de Lepinay, B., Ranero, C. and Sallares, V., 2017. Active tectonics of the Calabrian subduction revealed by new multi-beam bathymetric data and high-resolution seismic profiles in the Ionian Sea (Central Mediterranean). *Earth and Planetary Science Letters*, 461, 61-72. doi:10.1016/j.epsl.2016.12.020.
- Hansbo, S., 1957. A new approach to the determination of the shear strength of clay by the fall-cone test. *Geotechnical Institute Proceedings* no. 14, Stockholm 1957, 50.
- Hartmann, A., Villinger, H., 2002. Inversion of marine heat flow measurements by expansion of the temperature decay function. *Geophysical Journal International* 148 (3), 628–636.
- Huguen, C., Chamot-Rooke, N., Loubrieu, B., Mascle, J., 2006. Morphology of a pre-collisional, salt-bearing, accretionary complex: The Mediterranean Ridge (Eastern Mediterranean). *Mar Geophys Res* 27(1) 61–75.
- Huguen, C., Mascle, J., Woodside, J., Zitter, T., & Foucher, J. P., 2005. Mud volcanoes and mud domes of the Central Mediterranean Ridge: near-bottom and in situ observations. *Deep Sea Research Part I: Oceanographic Research Papers*, 52(10), 1911-1931.
- Huguen, C., Mascle, J., Chaumillon, E., Kopf, A., Woodside, J., Zitter, T., 2004. Structural setting and tectonic control of mud volcanoes from the Central Mediterranean Ridge (Eastern Mediterranean). *Mar Geol* 209(1–4), 245–263, doi:10.1016/j.margeo.2004.05.002.
- Hyndman, R., Davis, E., Wright, J., 1979, The measurements of marine geothermal heat flow by a multipenetration probe with digital acoustic telemetry and insitu thermal conductivity. *Marine Geophysical Researches* 4 (2), 181–205.
- Keller, J., Ryan, W.B.F., Nikovich, D., Altherr, R., 1978. Explosive volcanic activity in the Mediterranean over the past 200,000 yr as recorded in deep-sea sediments. *Geological Society of America Bulletin* 89, 591-604.
- Kopf, A. and cruise participants, 2012a. Report and preliminary results of R/V POSEIDON cruise P410: MUDFLOW (Mud volcanism, Faulting and Fluid Flow on the Mediterranean Ridge Accretionary Complex), Heraklion/ Greece, 12.02.2011 – Taranto/ Italy, 01.04.2011. *Berichte, Fachbereich Geowissenschaften, Universität Bremen*, No. 284, 128 pages, Bremen, 2012.
- Kopf, A. and cruise participants, 2012b. Report and preliminary results of R/V POSEIDON cruise P429: MEDFLUIDS: Slope Stability, Mud volcanism, Faulting and Fluid Flow in the Eastern Mediterranean Sea (Cretan Sea, Mediterranean Ridge) and Ligurian Margin (Nice slope), Heraklion / Greece, 22.03.2012 – La Seyne sur Mer/ France, 06.04.2012. *Berichte, Fachbereich Geowissenschaften, Universität Bremen*, No. 286, 80 pages. Bremen, 2012.
- Kopf, A., Mascle, J., Klaeschen, D., 2003. The Mediterranean Ridge: A mass balance across the fastest growing accretionary complex on Earth. *J. Geophys. Research* 108, 2372-2403, doi:10.1029/2001JB000473.
- Kopf, A.J., Deyhle, A., 2002. Back to the roots: Source depths of mud volcanoes and diapirs using boron and B isotopes. *Chem. Geology*, 192, 195-210.

- Kopf, A., 2002. Significance of mud volcanism. *Reviews of Geophysics*, 40/2, 52 pp. [DOI 10.1029/2000RG000093].
- Kopf, A., Klaeschen, D., Mascle, J., 2001. Extreme efficiency of mud volcanism in dewatering accretionary prisms. *Earth Planet. Sci. Letters*, 189/3-4, 295-313.
- Kvenvolden, K.A. and McDonald, T.J., 1986. Organic geochemistry on the Joides Resolution: An Assay, Tech. Note. *Ocean Drill. Prog.*, Texas A&M Univ, College Station, Tex., 147 pp.
- Limonov, A., Woodside, J., Cita, M., Ivanov, M., 1996. The Mediterranean Ridge and related mud diapirism; a background. *Mar Geol.* 132(1-4), 7-19.
- Lister, C. R. B., 1979. The pulse-probe method of conductivity measurement. *Geophys. J. R. Astr. Soc.* 57, 451-461.
- Loher, M., Ceramicola, S., Wintersteller, P., Meinecke, G., Sahling, H. and Bohrmann, G., 2018. Mud volcanism in a canyon: morphodynamic evolution of the active Venere mud volcano and its interplay with Squillace Canyon, Central Mediterranean. *Geochemistry, Geophysics, Geosystems*. doi:10.1002/2017GC007166.
- Lykousis, V., Alexandri, S., Woodside, J., de Lange, G., Dählmann, A., Perissoratis, C., Heeschen, K., Ioakim, C., Sakellariou, D., Nomikou, P., Rousakis, G., Casas, D., Ballas, D., Ercilla, G., 2009. Mud volcanoes and gas hydrates in the Anaximander mountains (Eastern Mediterranean Sea). *Mar. Pet. Geol.* 26, 854-872.
- Mascle, J., Mar, y F., Prae, g D., Brosolo, L., Camera, L., Ceramicola, .S, Dupré, S., 2014. Distribution and geological control of mud volcanoes and other fluid/free gas seepage features in the Mediterranean Sea and nearby Gulf of Cadiz, *Geo-Marine Let.*, doi 10.1007/s00367-014-0356-4.
- Malinverno, A., Ryan, W.B.F., 1986. Extension in the Tyrrhenian Sea and shortening in the Apennines as result of arc migration driven by sinking of the lithosphere. *Tectonics* 5 (2), 227-245.
- Marsaglia, K., Milliken, K., Leckie, R., M., Tentori, D., Doran, L., 2015. IODP Smear Slide Digital Reference for Sediment Analysis of Marine Mud. Part 2: Methodology and Atlas of Biogenic Components. IODP Technical Note 2. doi:10.14379/iodp.tn.2.2015.
- Marsaglia, K., Milliken, K., and Doran, L., 2013. Smear slides of marine mud for IODP core description, Volume I. Part 1: Methodology and atlas of siliciclastic and volcanogenic components. IODP Technical Note 1. doi:10.2204/iodp.tn.1.2013.
- Mercone, D., Thomson, J., Croudance, I.W., 2000. Duration of S1, the most recent sapropel in the eastern Mediterranean Sea, as indicated by accelerator mass spectrometry radiocarbon and geochemical evidence. *Paleoceanography* 3, 336-347.
- Minelli, L., Faccenna, C., 2010. Evolution of the Calabrian accretionary wedge (central Mediterranean). *Tectonics* 29, TC4004; doi:10.1029/2009TC002562.
- Moore, J.C., Saffer, D., 2001. Updip limit of the seismogenic zone beneath the accretionary prism of southwest Japan: An effect of diagenetic to low-grade metamorphic processes and increasing effective stress. *Geology*, 29, 183-186.
- Narcisi, B., Vezzoli, L., 1999. Quaternary stratigraphy of distal tephra layers in the Mediterranean – an overview. *Global and Planetary Change* 21, 35-50.
- Pape, T., Bahr, A., Rethemeyer, J., Kessler, J.D., Sahling, H., Hinrichs, K.-U., Klapp, S.A., Reeburgh, W.S., Bohrmann, G., 2010. Molecular and isotopic partitioning of low-molecular

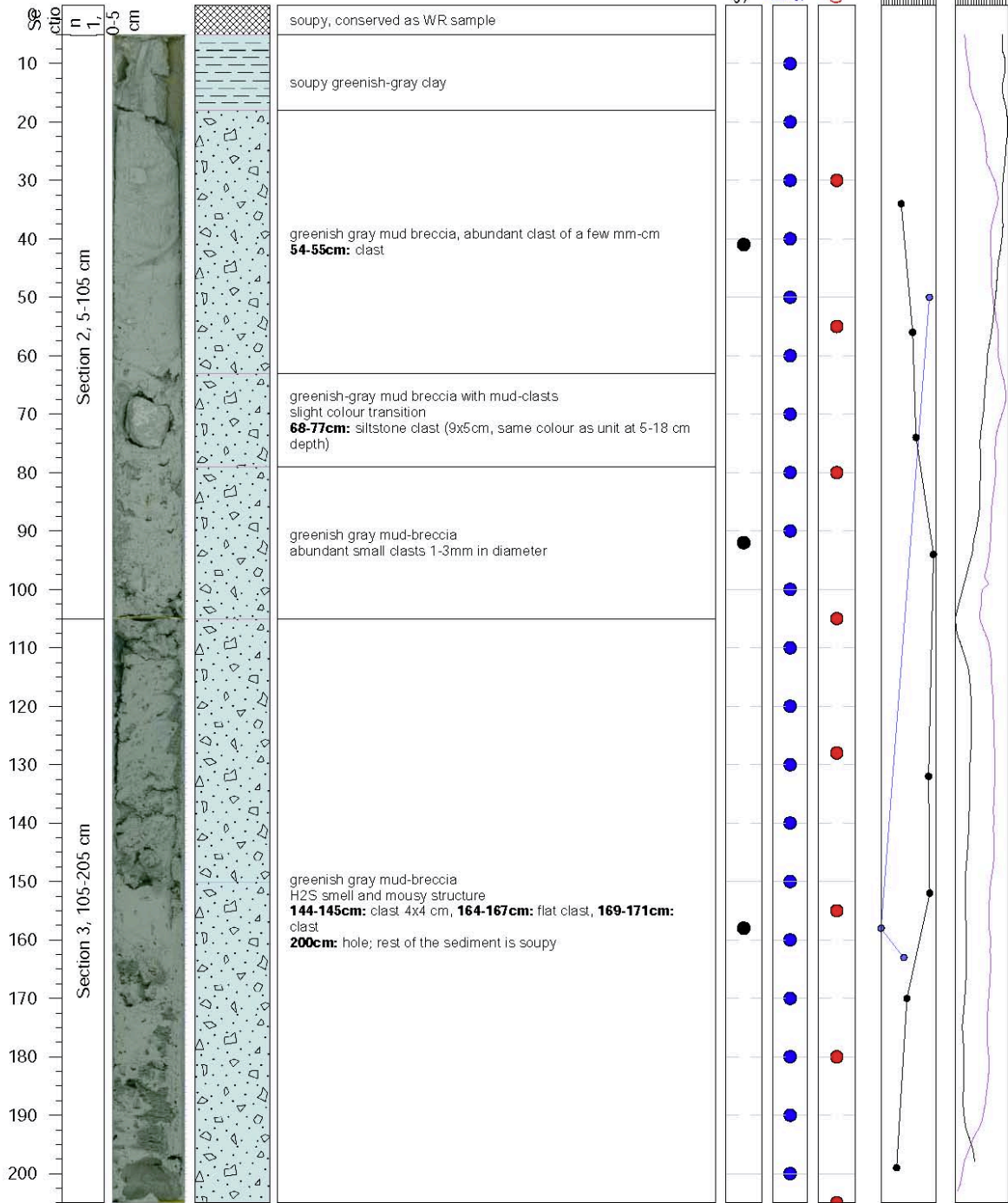
- weight hydrocarbons during migration and gas hydrate precipitation in deposits of a high-flux seepage site. *Chemical Geology* 269, 350-363. doi: 10.1016/j.chemgeo.2009.10.009.
- Polonia, A., Romano, S., Çağatay, M.N., Capotondi, L., Gasparotto, G., Gasperini, L., Panieri, G., Torelli, L., 2015. Are repetitive slumpings during sapropel S1 related to paleo-earthquakes? *Marine Geology* 361, 41-52.
- Polonia, A., Torelli, L., Mussoni, P., Gasperini, L., Artoni, A., Klaeschen, D., 2011. The Calabrian Arc subduction complex in the Ionian Sea: regional architecture, active deformation and seismic hazard. *Tectonics* 30, TC5018.
- Praeg, D., Ceramicola, S., Barbieri, R., Unnithan, V., Wardell, N., 2009. Tectonically-driven mud volcanism since the late Pliocene on the Calabrian accretionary prism, central Mediterranean Sea, *J. of Marine and Petroleum Geology* 26, 1849–186.
- Rabaute, A., Chamot-Rooke, N., 2007. Quantitative mapping of active mud volcanism at the western Mediterranean Ridge-backstop contact. *Mar. Geophys. Res.* 28, 271–295.
- Rothwell, R.G., 1989. *Minerals and Mineraloids in Marine Sediments: an optical identification guide*. Elsevier Science Publishers, 10.1007/978-94-009-1133-8.
- Rossi, S., Sartori, R., 1981. A seismic reflection study of the external Calabrian Arc in the northern Ionian Sea (eastern Mediterranean). *Marine Geophysical Researches* 4, 403–426.
- Schulz, H., Zabel, M., 2005. *Marine Geochemistry* (2nd edition). Berlin Heidelberg, Germany, Springer-Verlag.
- Sloan, E.D., 2003. Fundamental principles and applications of natural gas hydrates. *Nature*, 426(6964), 353-359.
- Tomlinson, E.L., Smith, V.C., Albert, P.G., Aydar, E., Civetta, L., Cioni, R., Çubukçu, E., Gertisser, R., Isaia, R., Menzies, M.A., Orsi, G., Rosi, M., 2015. The major trace element glass compositions of the productive Mediterranean volcanic source: tools for correlating distal tephra layers in and around Europe. *Quaternary Science Reviews* 118, 48-66.
- Villinger, H., Trehu, A.M., Grevemeyer, I., 2010. Seafloor marine heat flux measurements and estimation of heat flux from seismic observations of bottom simulating reflectors, In: *Geophysical Characterization of Gas Hydrates special volume*, ISBN (13) 9181560802181, Society of Exploration Geophysicists, 279-298.
- Whiticar, M.J., 1999. Carbon and hydrogen isotope systematics of bacterial formation and oxidation of methane. *Chemical Geology*, 161, 291-314.
- Wood, D.M., 1985. Some fall-cone tests. *Geotechnique* 35, 64-68.

10 Appendices

10.1 Gravity Cores: Strater Profiles and Core Photos



**SO278**  
**GC-01 GeoB24302-02 Sartori MV**  
 Latitude: 38° 12.3211 N Longitude: 17° 37.1133 E  
 Length of core: 205 cm Water depth: 1856 m



Comments: Mud with mud clasts

32  
52  
72  
92  
Mag. Sus

### Continuation Strater Profiles and Core Photos



SO278

GC-01 GeoB24302-02

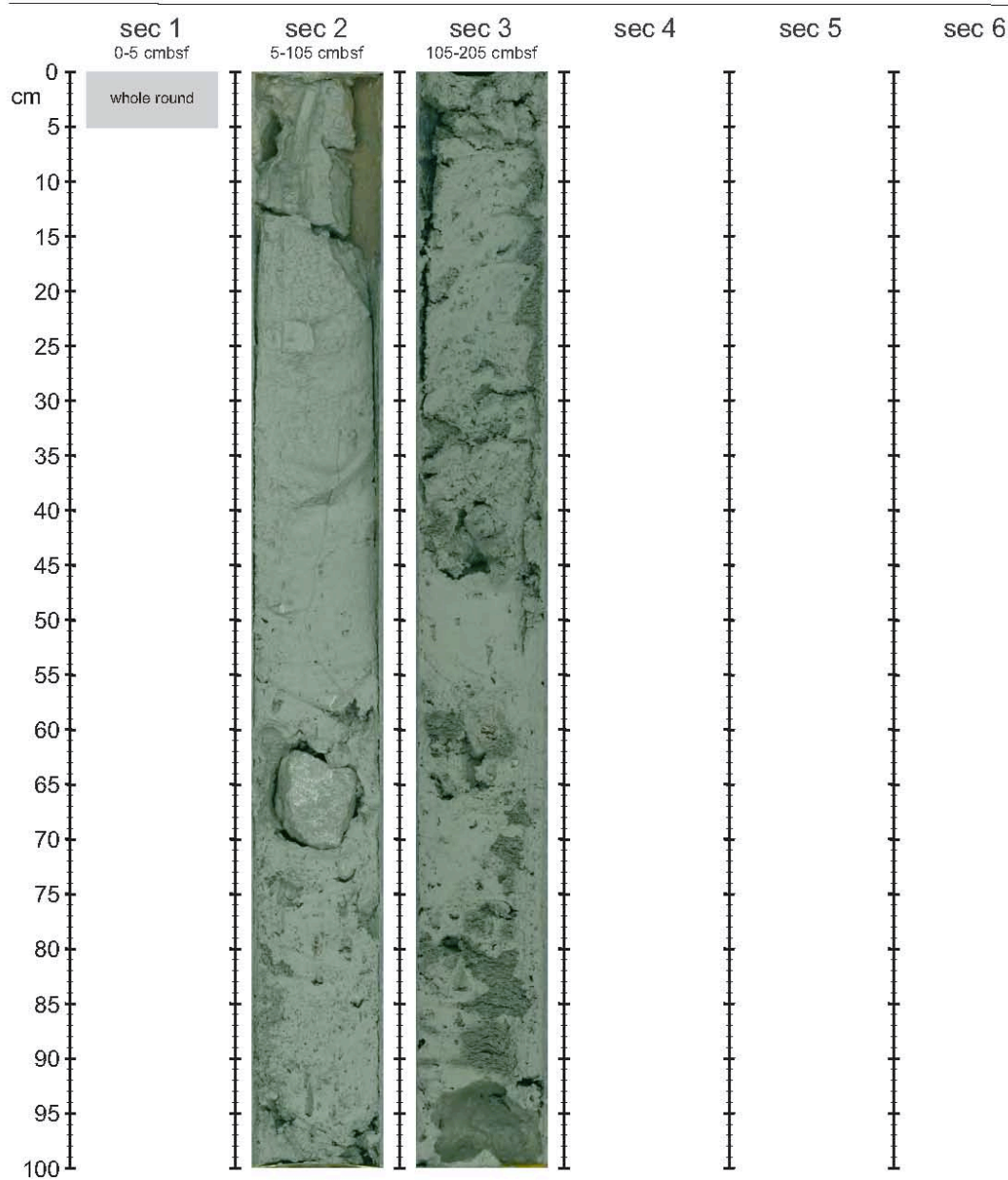
Sartori MV

Latitude: 38° 12.3211 N

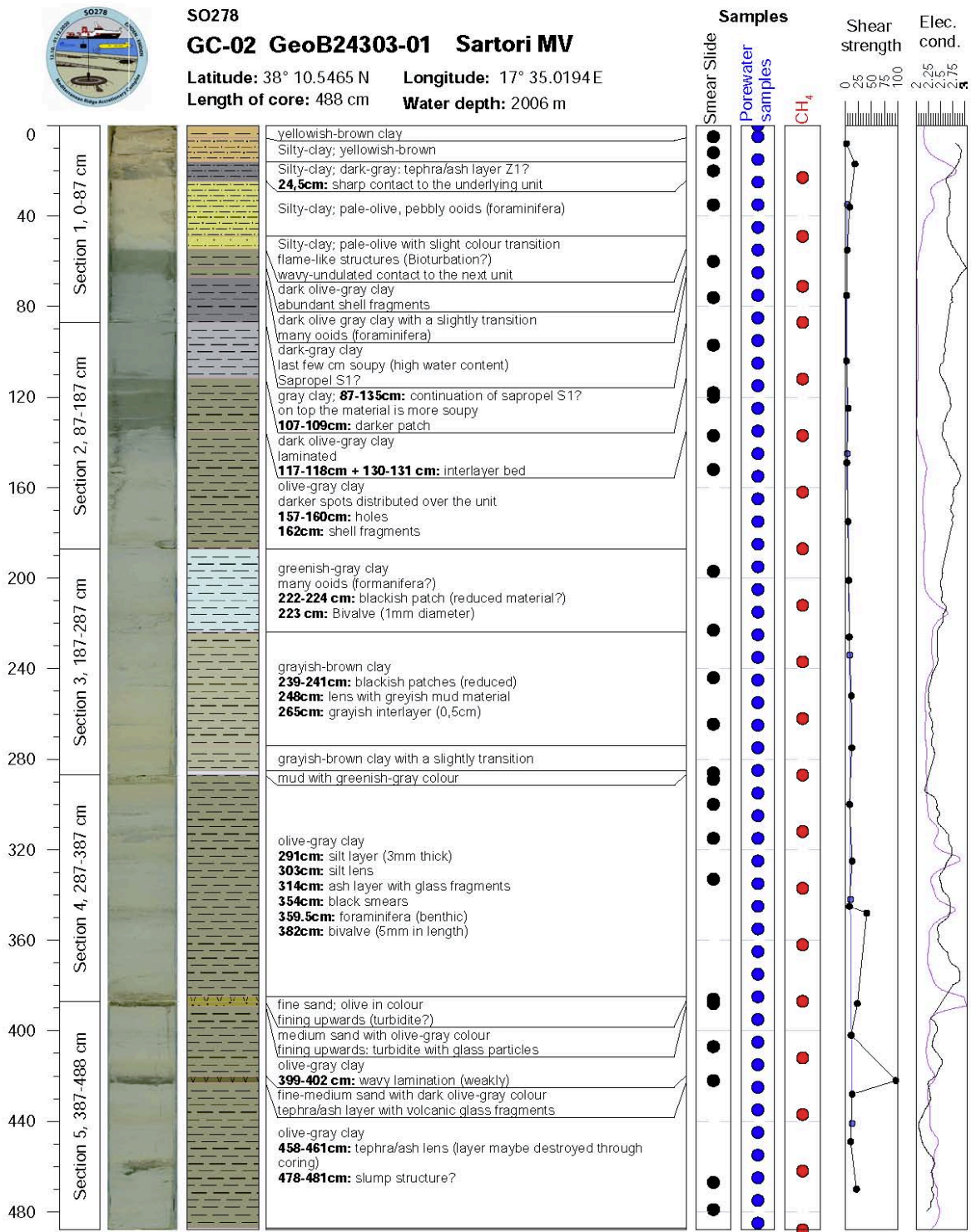
Longitude: 17° 37.1133 E

Length of core: 205 cm

Water depth: 1856 m



Continuation Strater Profiles and Core Photos



Comments: -

250  
500  
750  
Mag. Su

### Continuation Strater Profiles and Core Photos

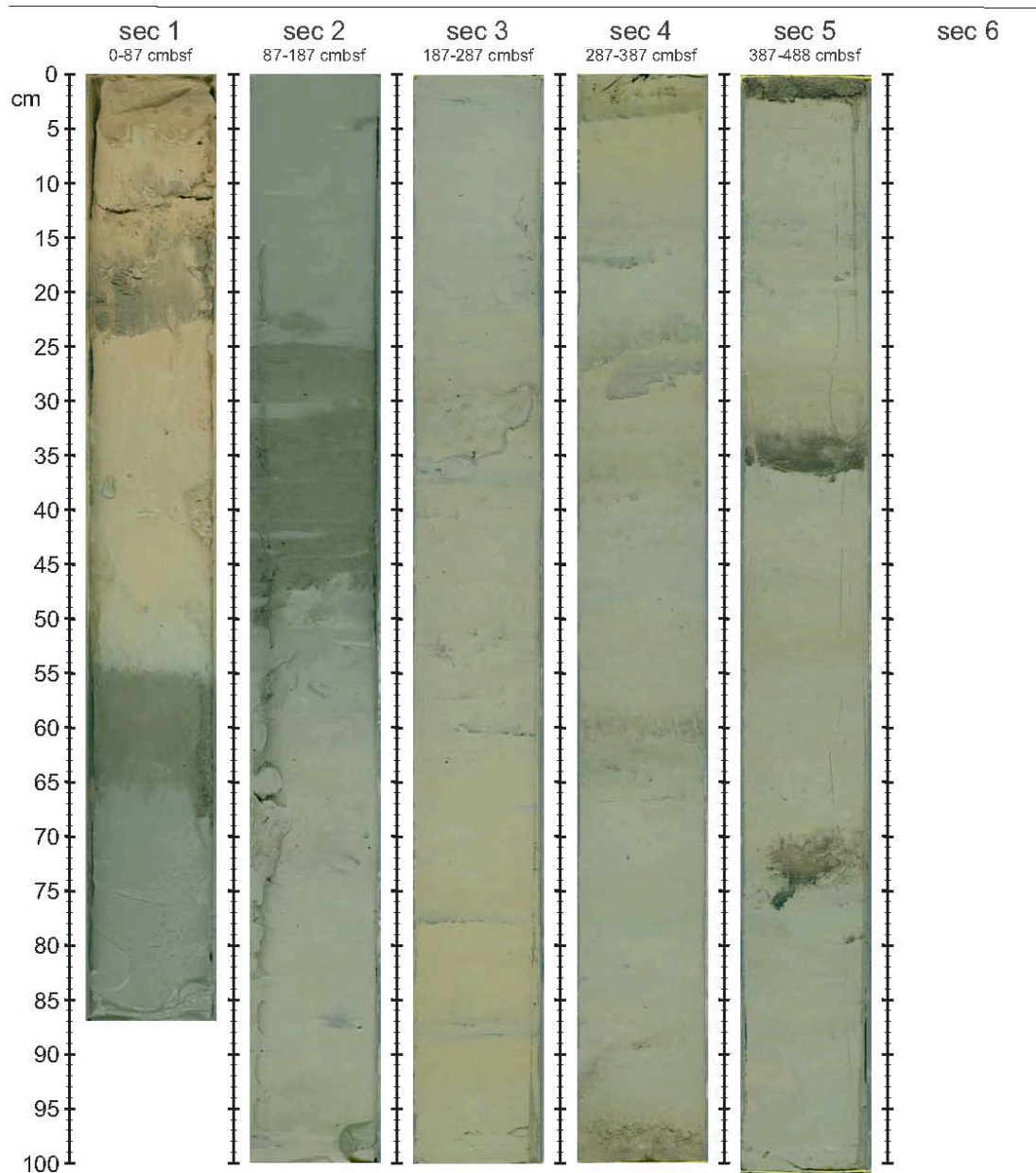


SO278

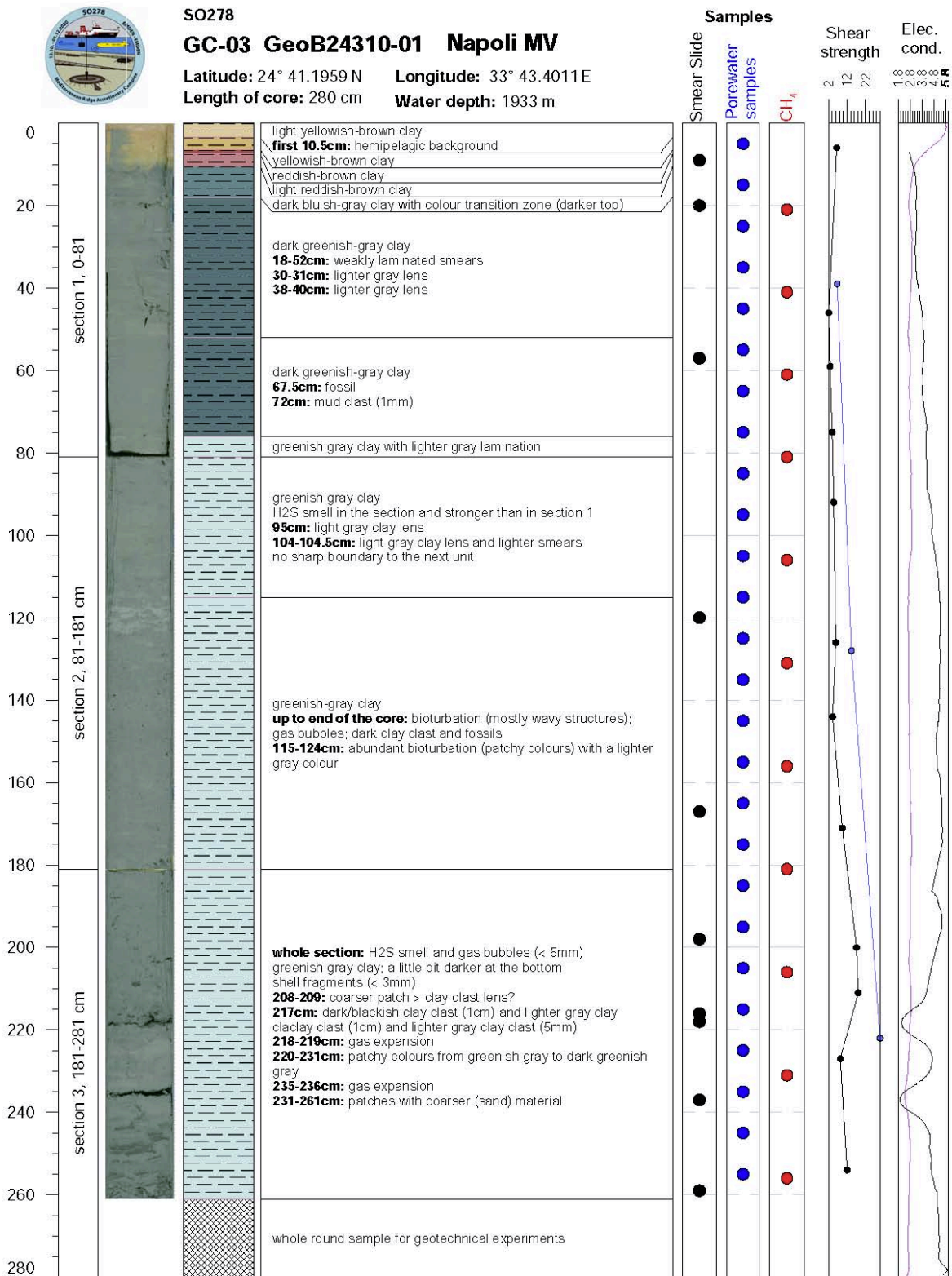
GC-02 GeoB24303-01 South of Sartori MV

Latitude: 38° 10.5465 N Longitude: 17° 35.0194 E

Length of core: 488 cm Water depth: 2006 m



Continuation Strater Profiles and Core Photos



Comments: core catcher: mossy grey mud breccia with strong H<sub>2</sub>S smell

20  
70  
120  
170  
Mag. Su

### Continuation Strater Profiles and Core Photos



SO278

GC-03 GeoB24310-01

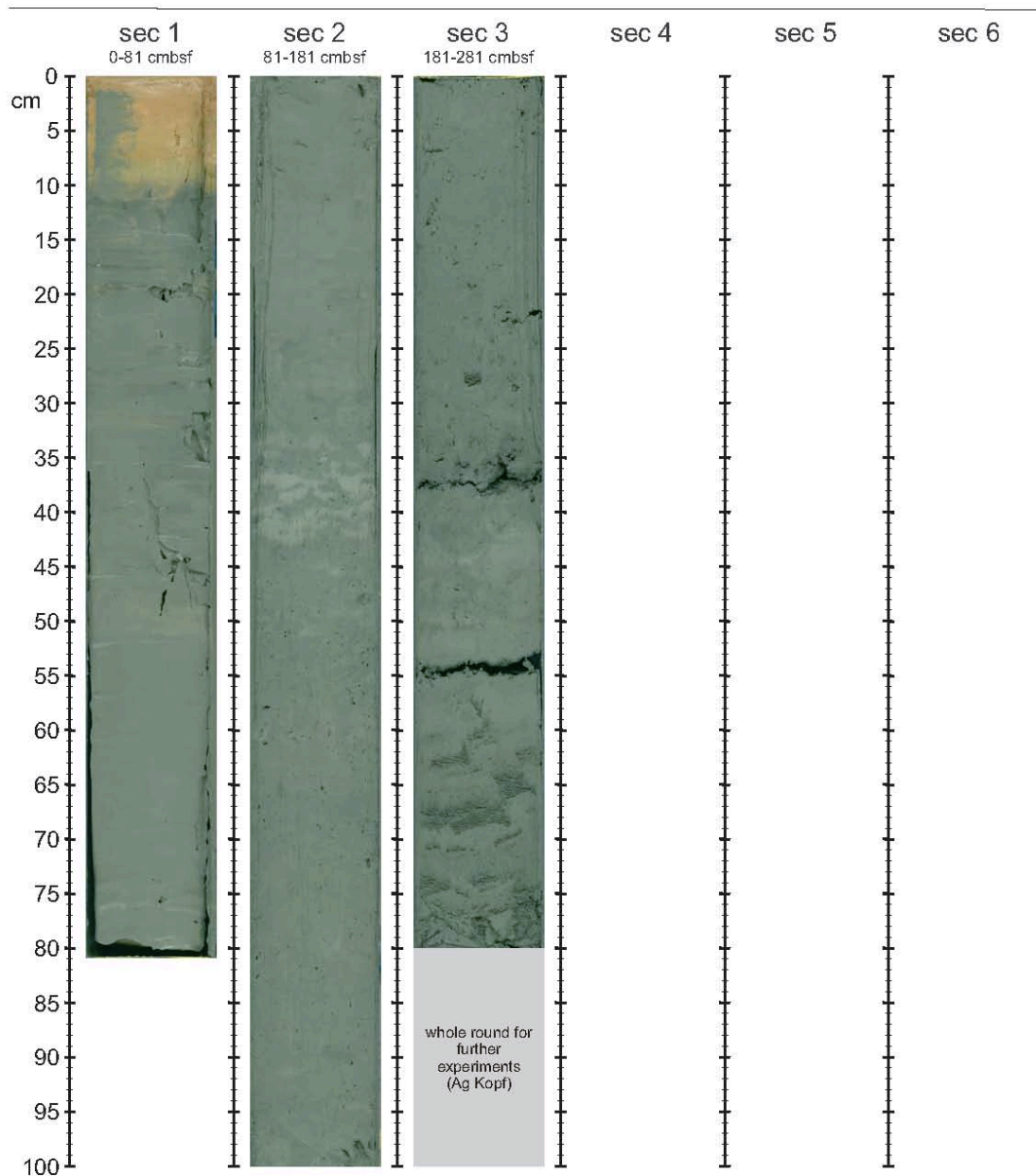
Napoli MV

Latitude: 33° 43.4011 N

Longitude: 24° 41.1959 E

Length of core: 281 cm

Water depth: 1933 m





### Continuation Strater Profiles and Core Photos



SO278

GC-04 GeoB24311-01

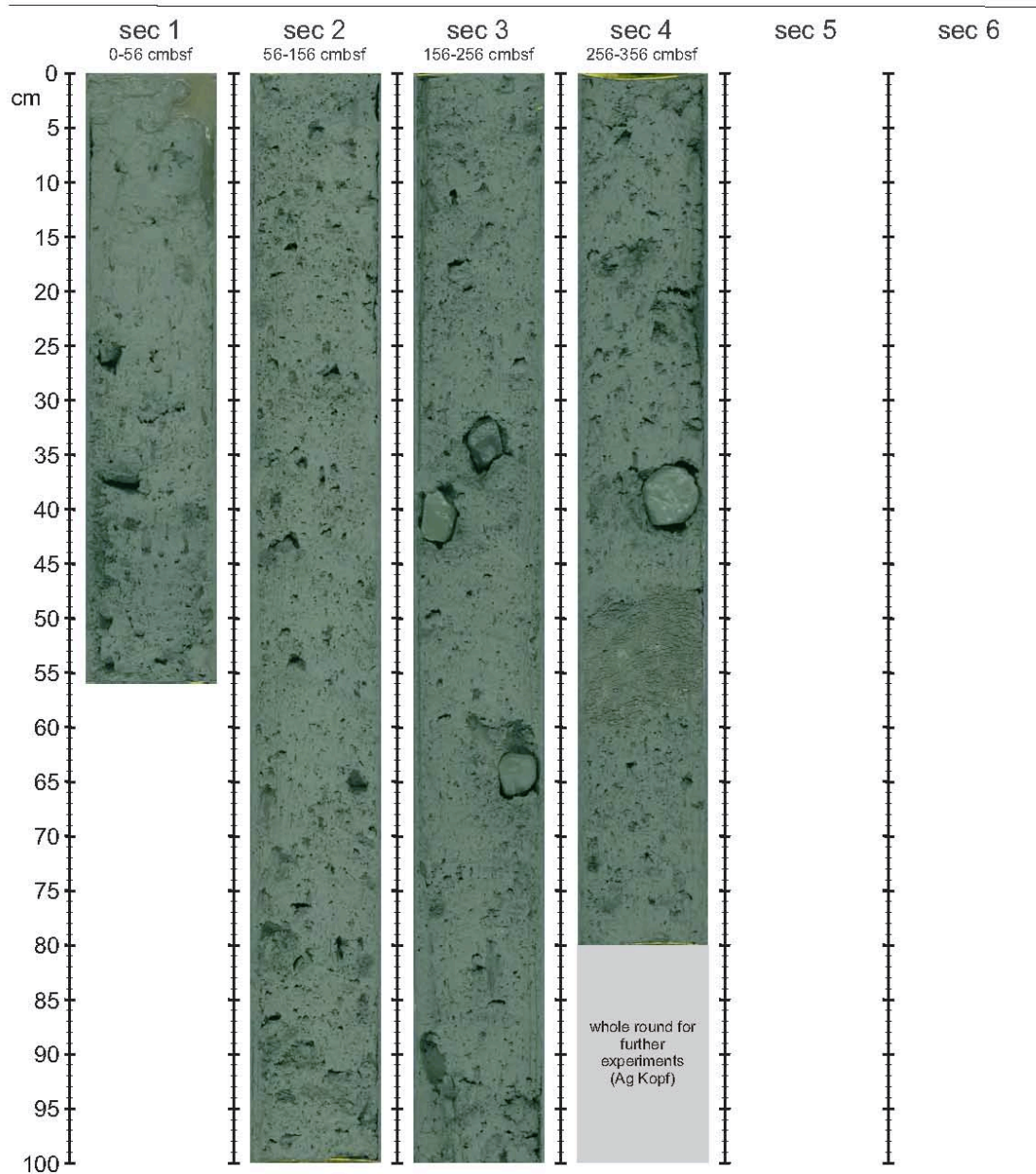
Bergamo MV

Latitude: 33° 44.3279 N

Longitude: 24° 45.0576 E

Length of core: 356 cm

Water depth: 1930 m





### Continuation Strater Profiles and Core Photos



SO278

GC-05 GeoB24312-01

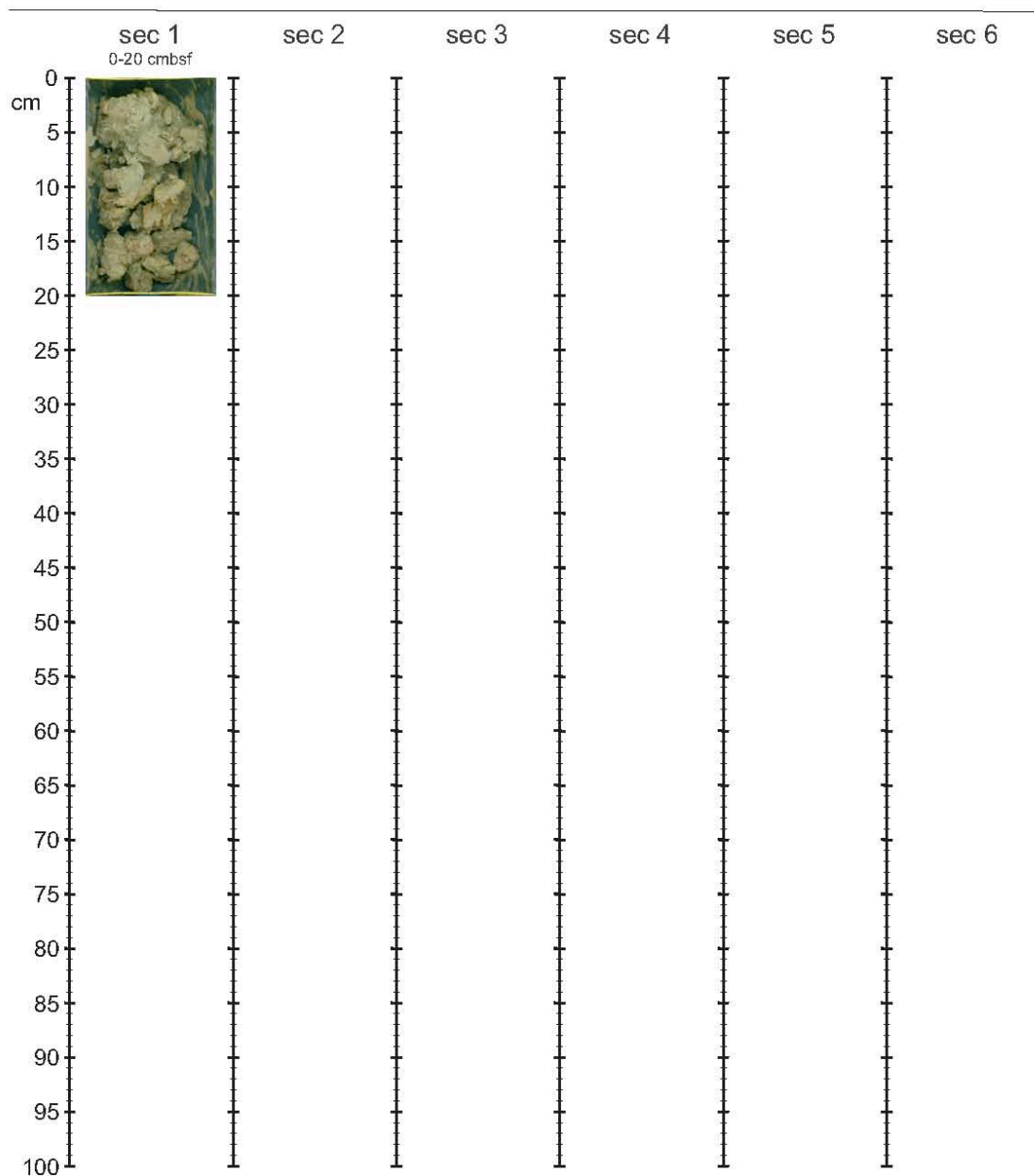
Fault zone

Latitude: 34° 05.6769 N

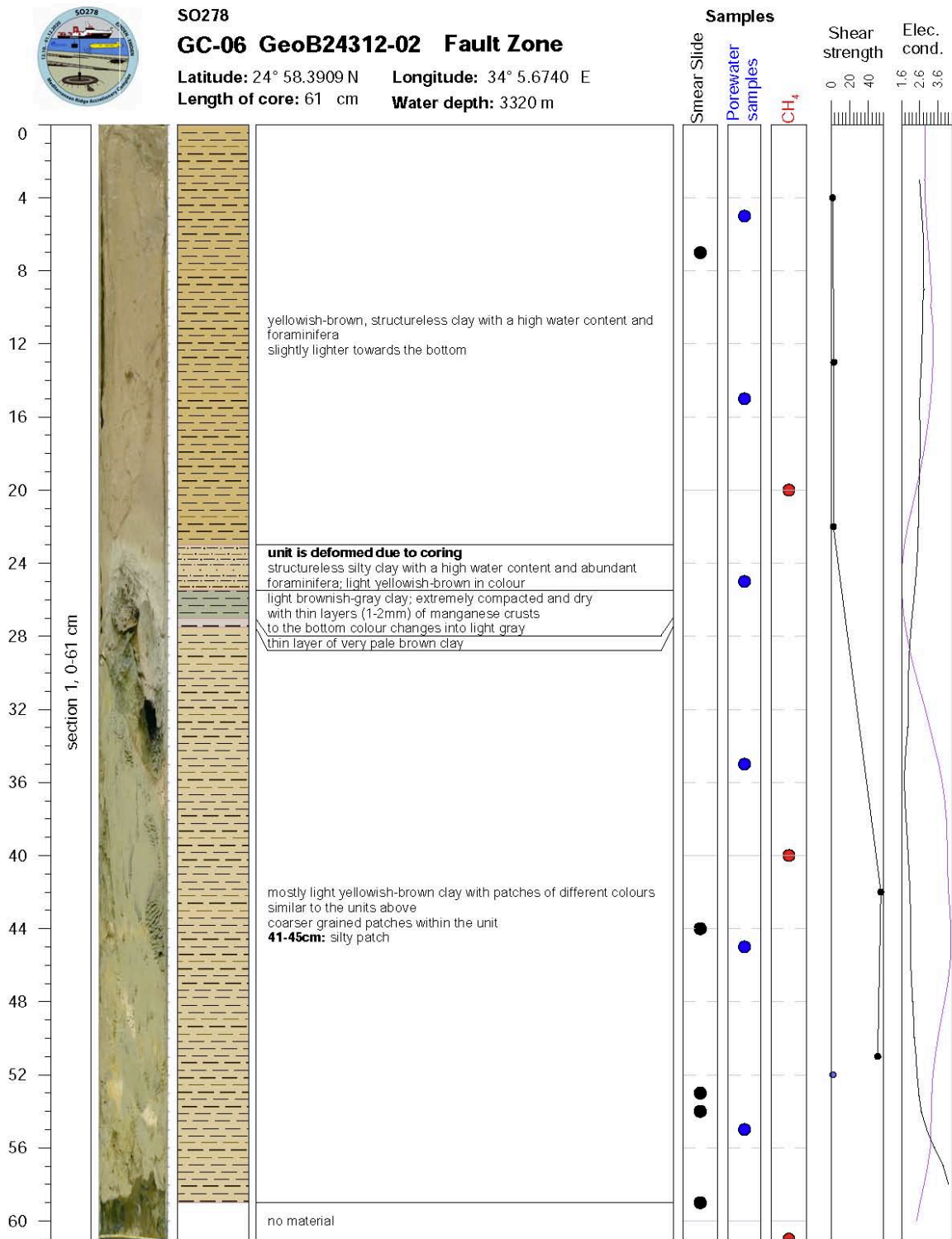
Longitude: 24° 58.3945 E

Length of core: 20 cm

Water depth: 3346 m



Continuation Strater Profiles and Core Photos



Comments: -

### Continuation Strater Profiles and Core Photos



SO278

GC-06 GeoB24312-02

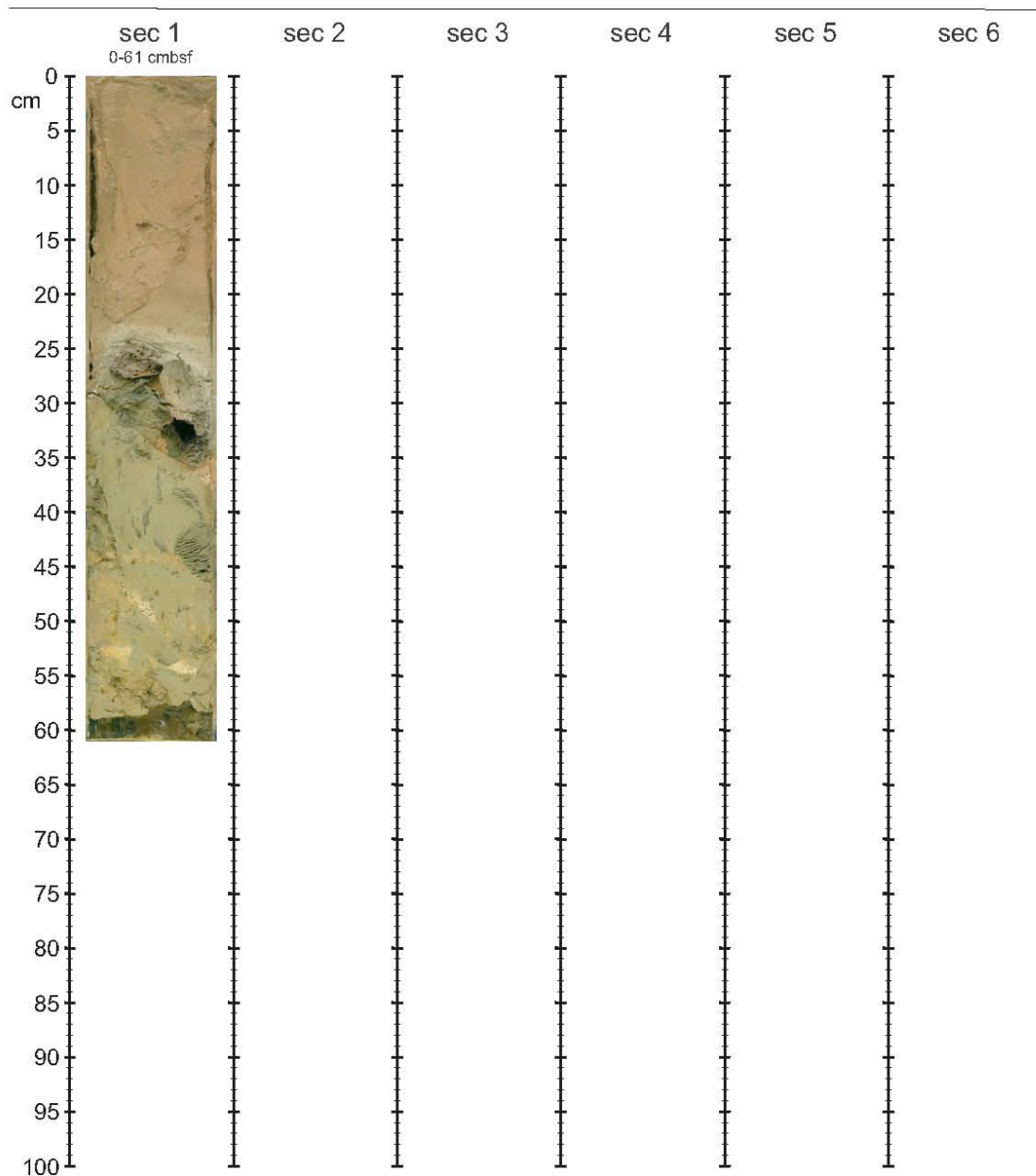
Fault zone

Latitude: 34° 05.6740 N

Longitude: 24° 58.3909 E

Length of core: 61 cm

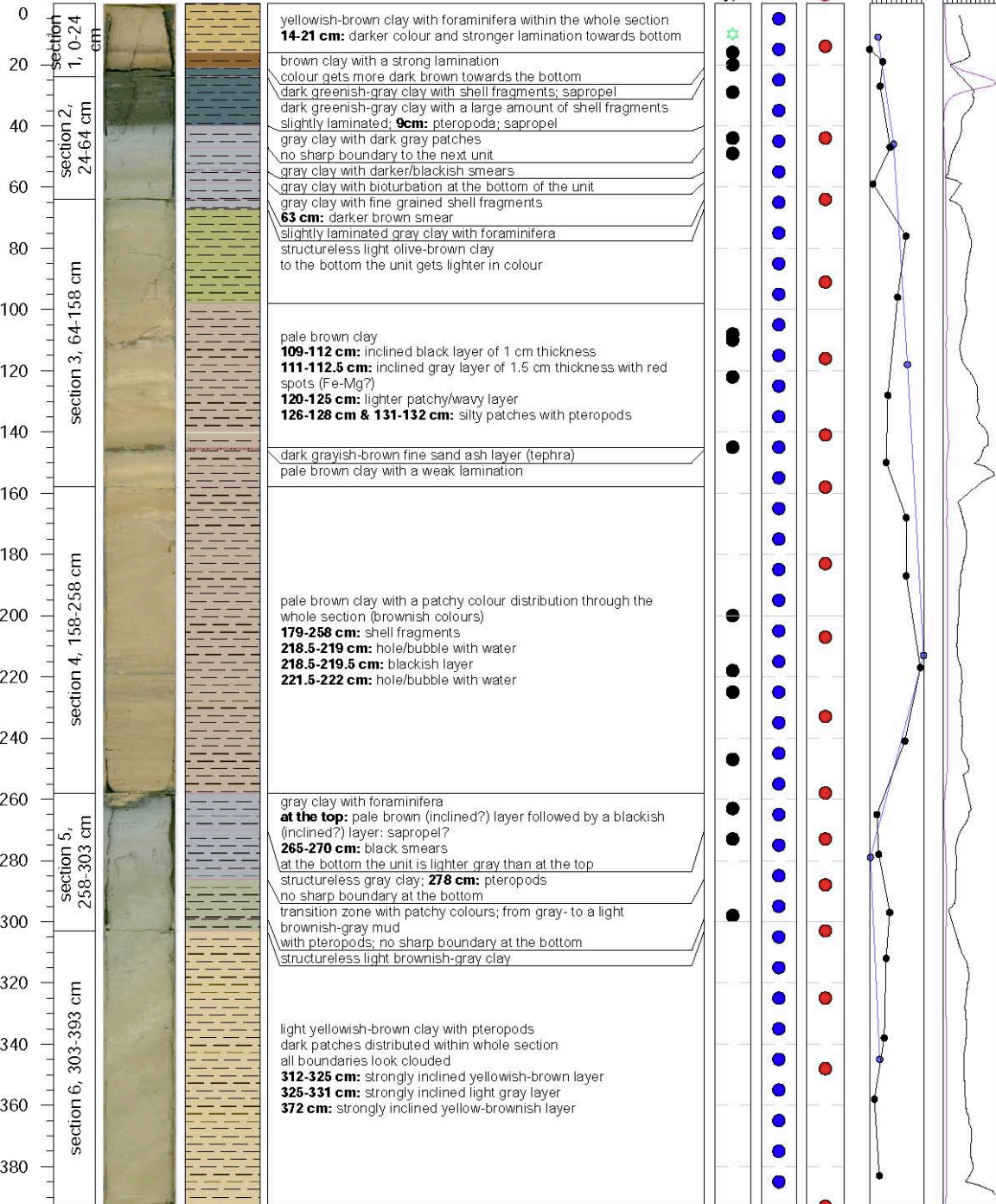
Water depth: 3320 m



Continuation Strater Profiles and Core Photos



**SO278**  
**GC-07 GeoB24315-01 Fault Zone**  
 Latitude: 24° 59.3087 N Longitude: 34° 7.2990 E  
 Length of core: 393 cm Water depth: 2501 m



Comments: core catcher: clay with foraminifera

0  
1000  
2000  
3000  
4000  
Mag. Su

### Continuation Strater Profiles and Core Photos



SO278

GC-07 GeoB24315-01

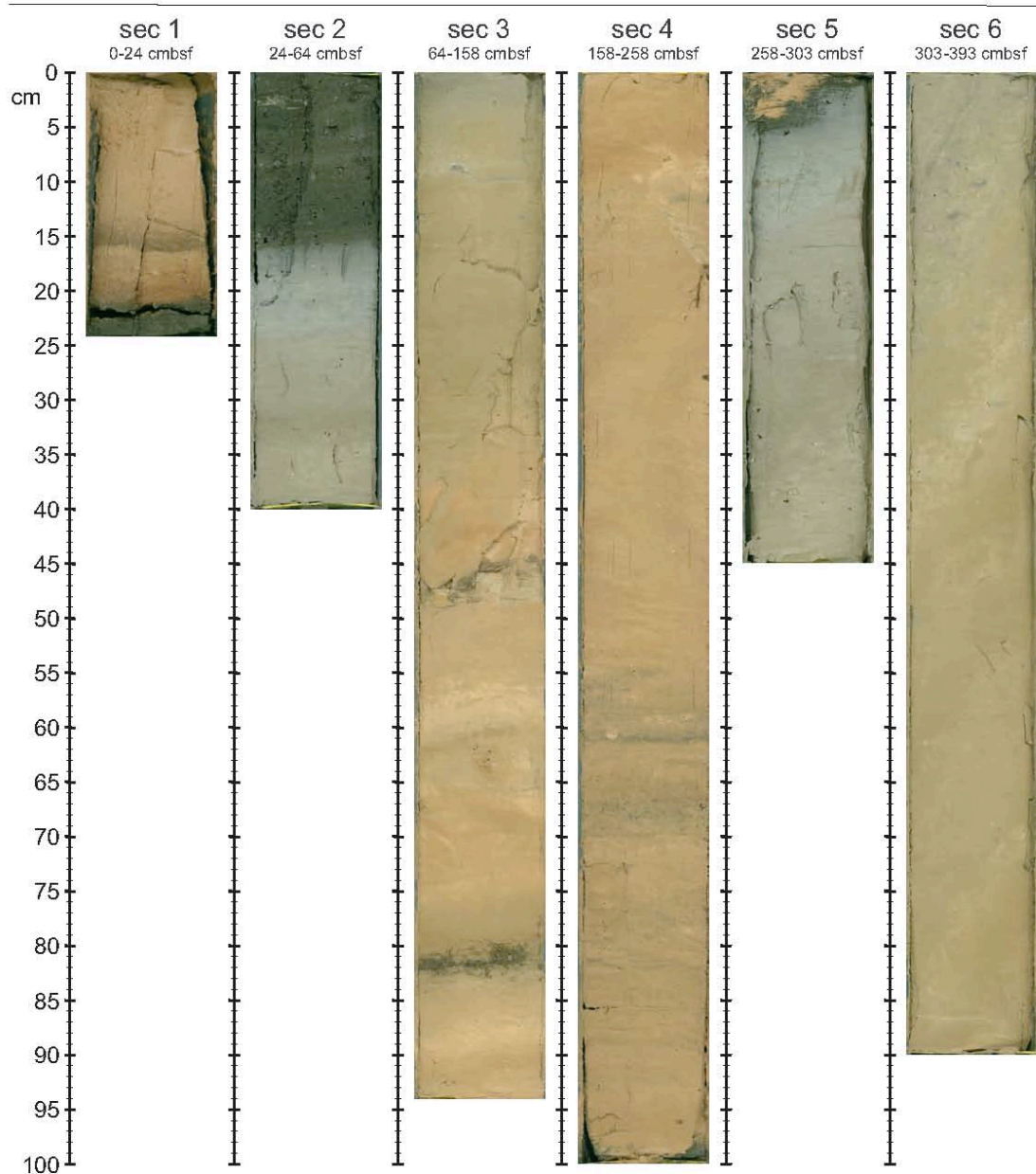
Fault ridge

Latitude: 34° 07.2990 N

Longitude: 24° 59.3087 E

Length of core: 393 cm

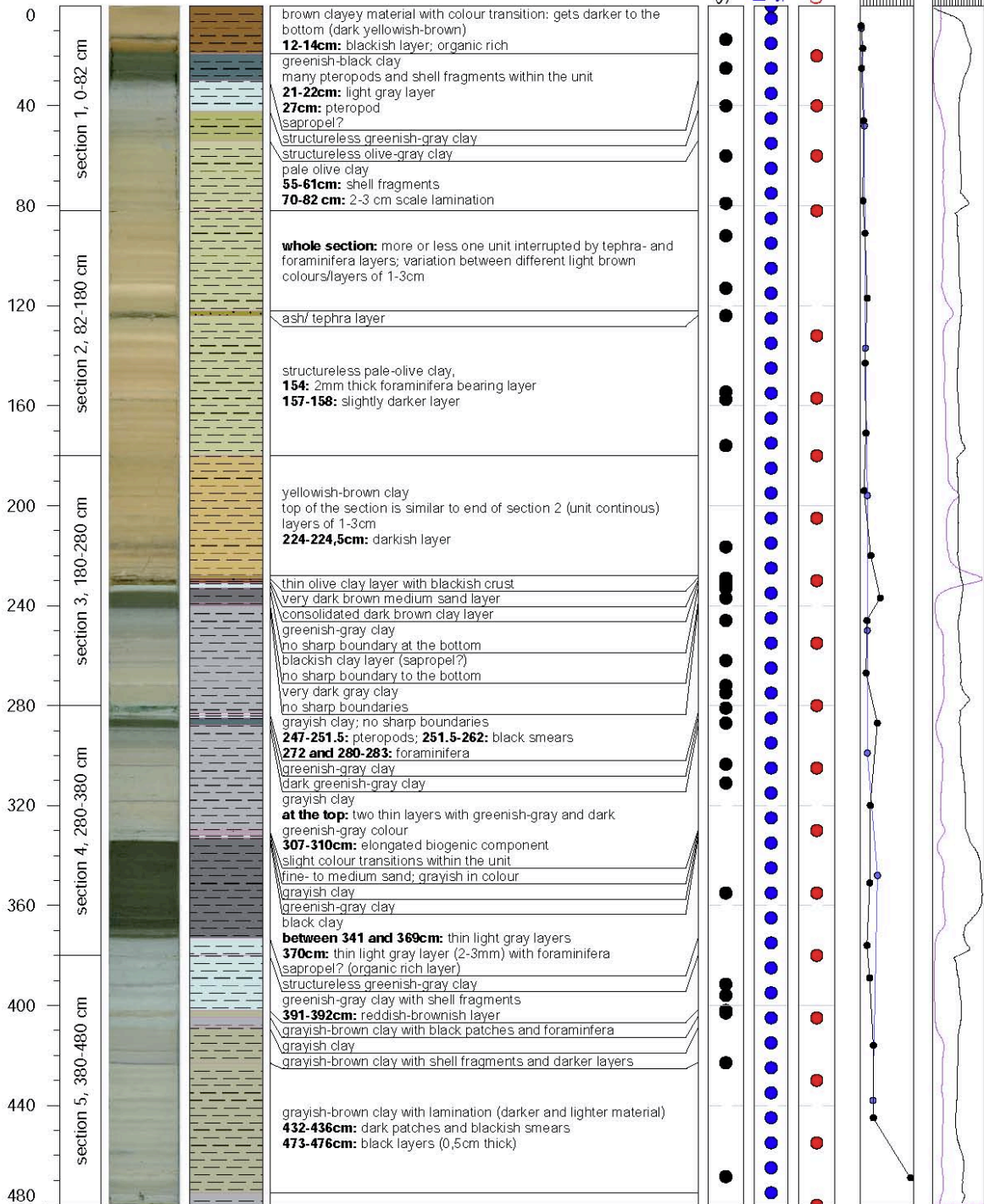
Water depth: 2501 m



Continuation Strater Profiles and Core Photos



**SO278**  
**GC-08 GeoB24316-01 Fault Zone**  
 Latitude: 24° 55.6230 N Longitude: 34° 3.8940 E  
 Length of core: 480 cm Water depth: 3105 m



Comments: core catcher: clay with pteropods

Mag. Sus

### Continuation Strater Profiles and Core Photos



SO278

GC-08 GeoB24316-01

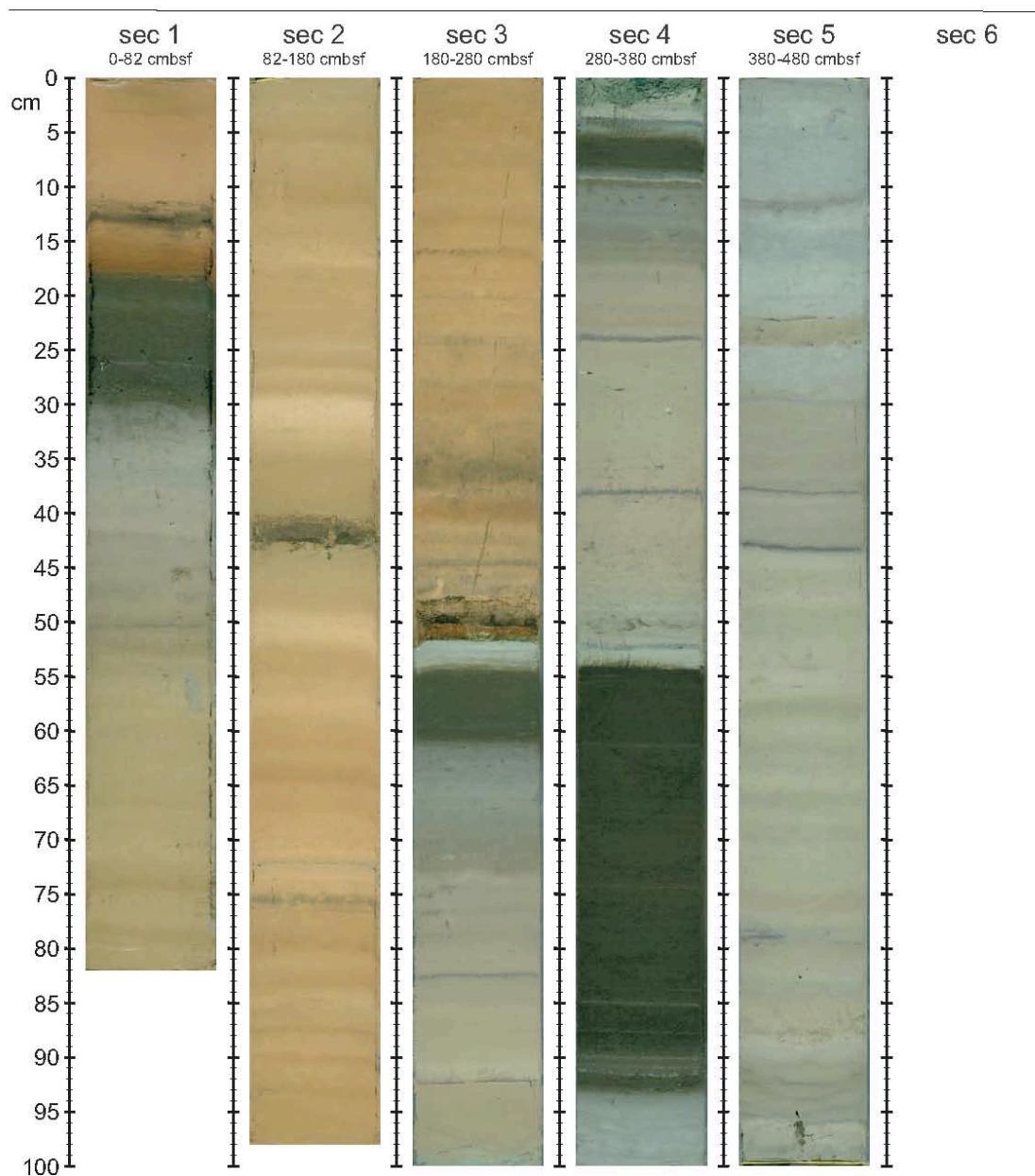
Fault zone

Latitude: 34° 03.8940 N

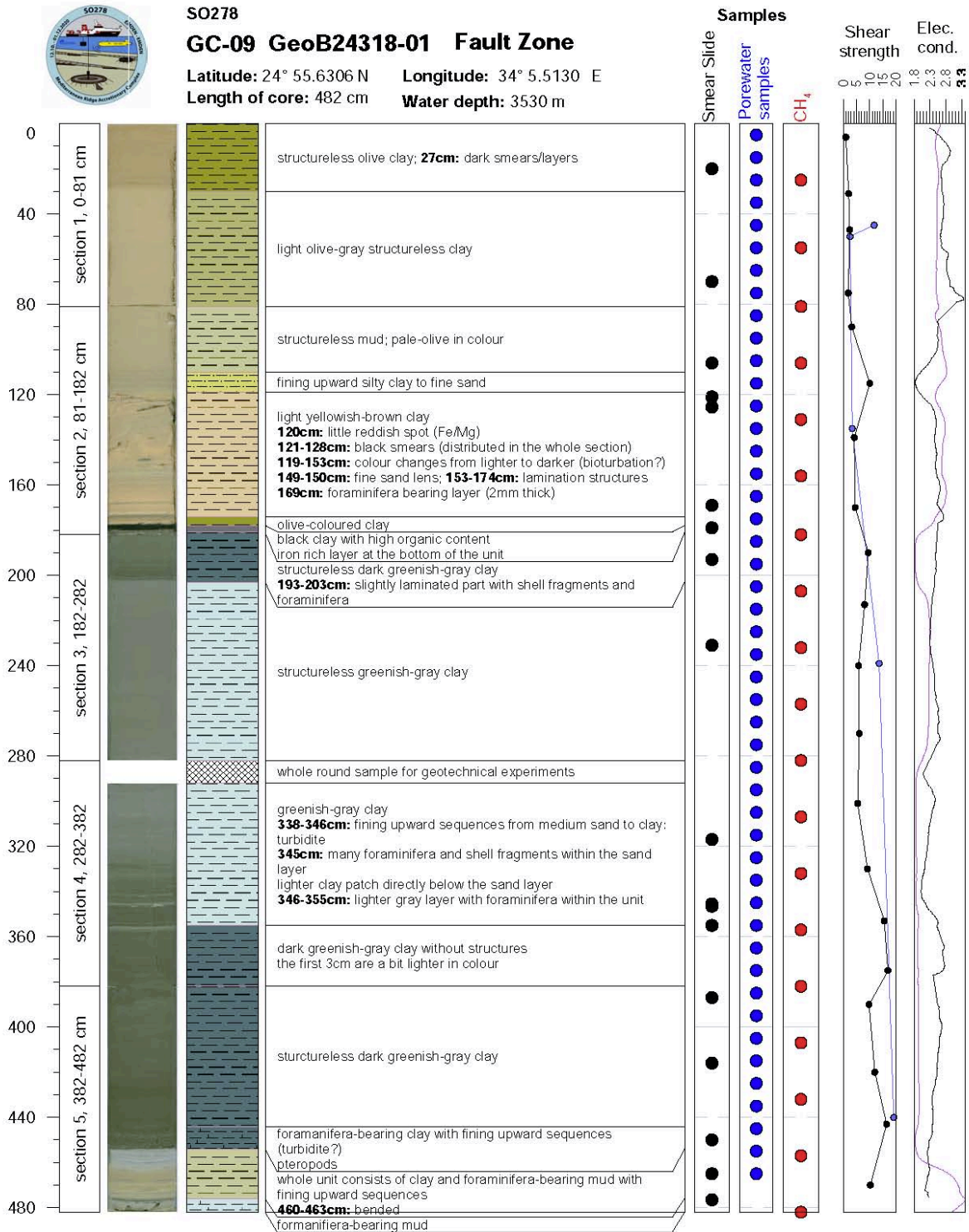
Longitude: 24° 55.6230 E

Length of core: 480 cm

Water depth: 3105 m



Continuation Strater Profiles and Core Photos



Comments: core catcher: clay with fine sand, shell fragments



### Continuation Strater Profiles and Core Photos



SO278

GC-09 GeoB24318-01

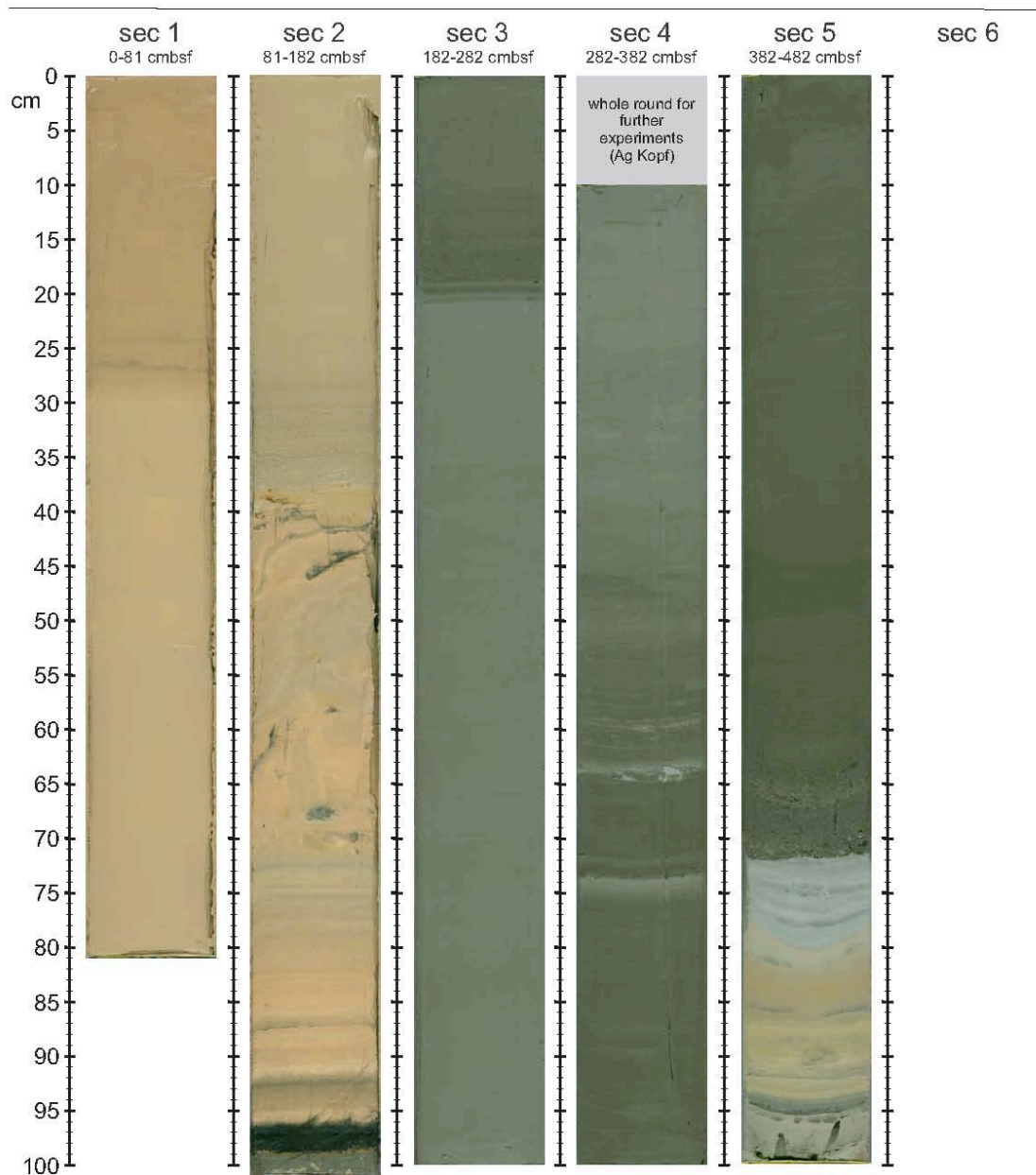
Fault zone

Latitude: 34° 05.5130 N

Longitude: 24° 55.6306 E

Length of core: 482 cm

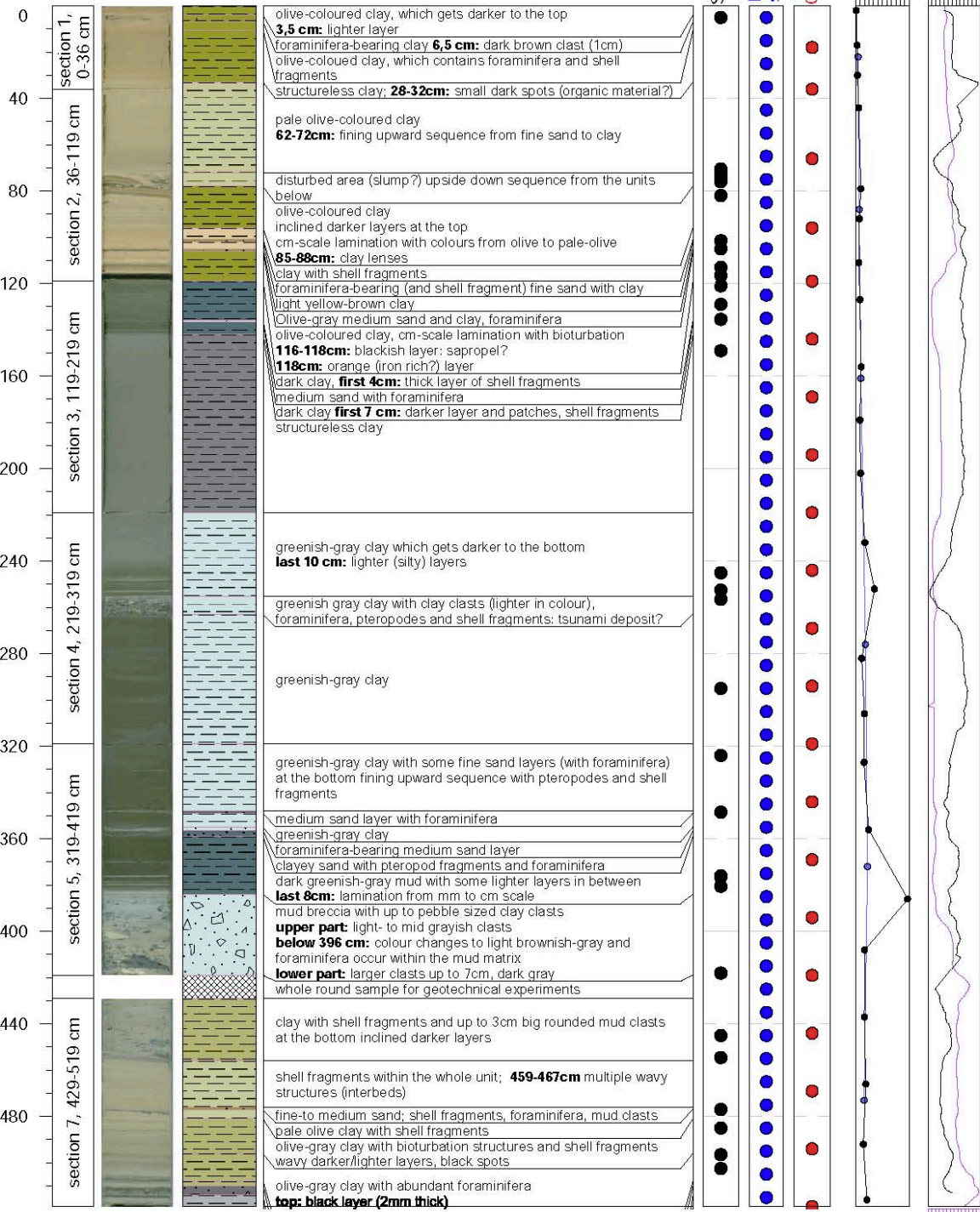
Water depth: 3530 m



Continuation Strater Profiles and Core Photos



**SO278**  
**GC-11 GeoB24320-01 Fault Zone**  
 Latitude: 24° 55.6292 N Longitude: 34° 5.0841 E  
 Length of core: 519 cm Water depth: 3521 m



Comments: -

Mag. Sus

### Continuation Strater Profiles and Core Photos

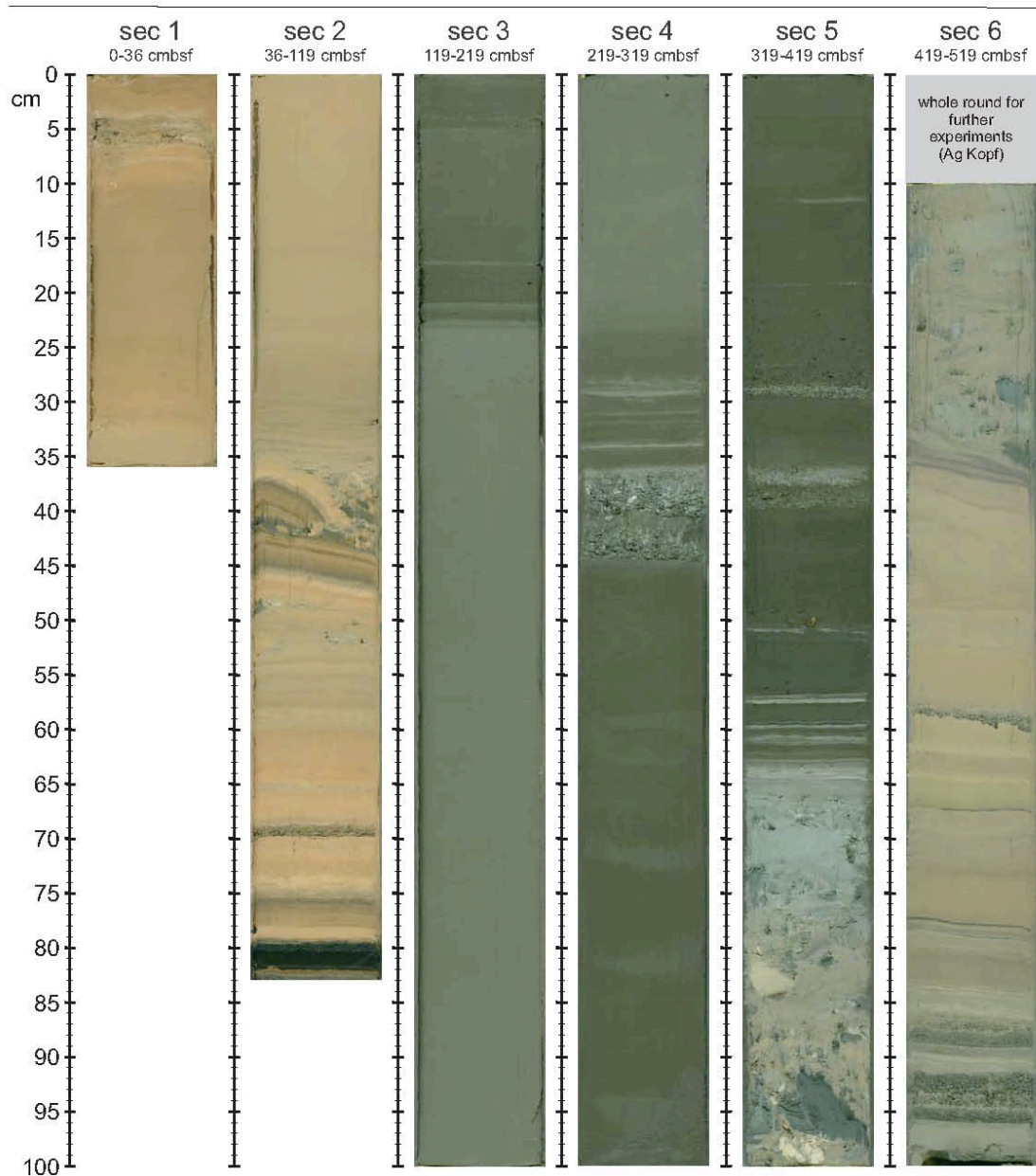


SO278

GC-11 GeoB24320-01      Fault zone

Latitude: 34° 05.0841 N      Longitude: 24° 55.6292 E

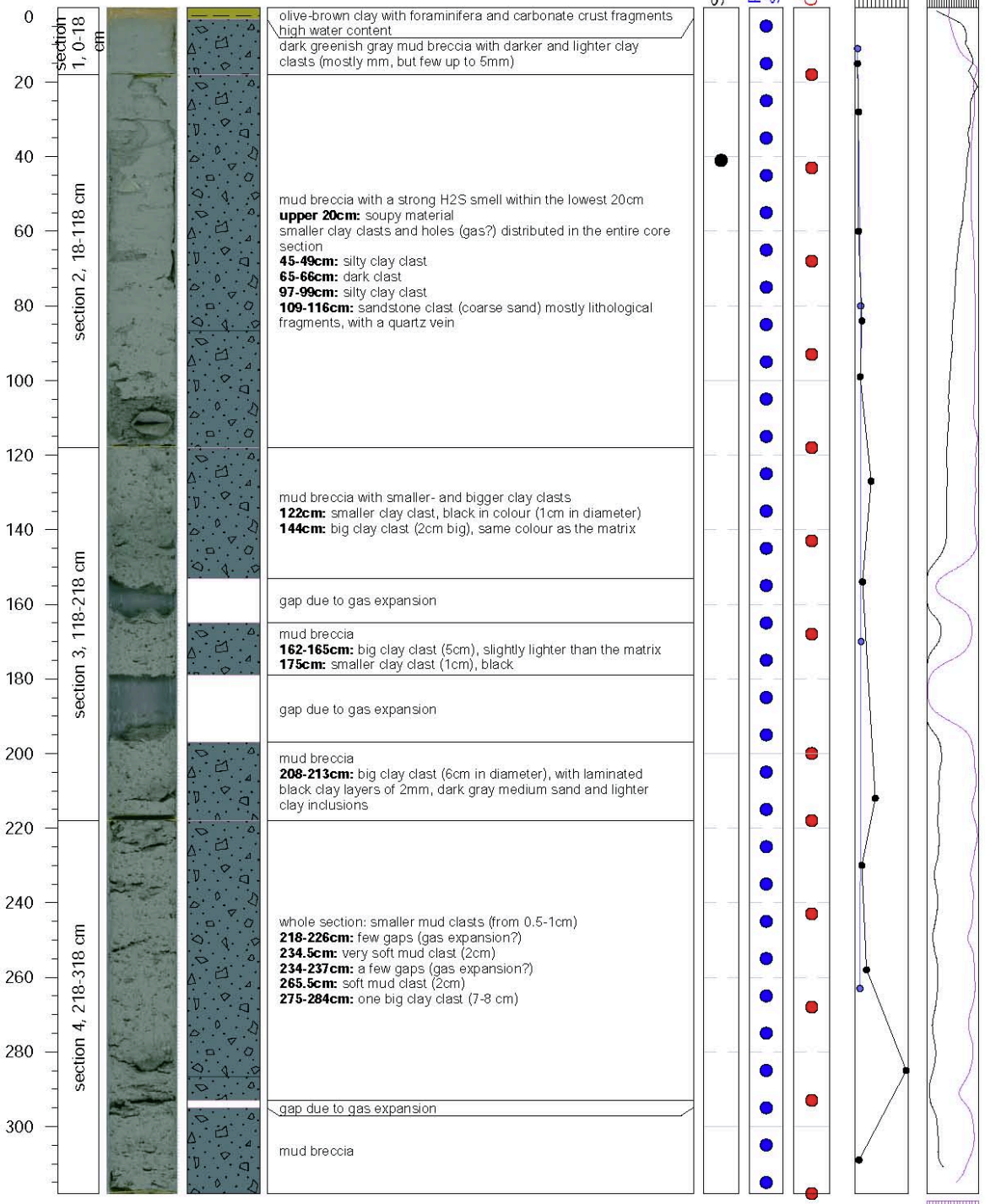
Length of core: 519 cm      Water depth: 3521 m



Continuation Strater Profiles and Core Photos



**SO278**  
**GC-12 GeoB24323-01 Bergamo MV plateau**  
 Latitude: 24° 44.8789 N Longitude: 33° 44.3047 E  
 Length of core: 318 cm Water depth: 1934 m



Comments: top of section 2 had 2 cm foam that moved inside the core material during MSCL scanning

0 50 100 150  
 Mag. Sus

### Continuation Strater Profiles and Core Photos



SO278

GC-12 GeoB24323-01

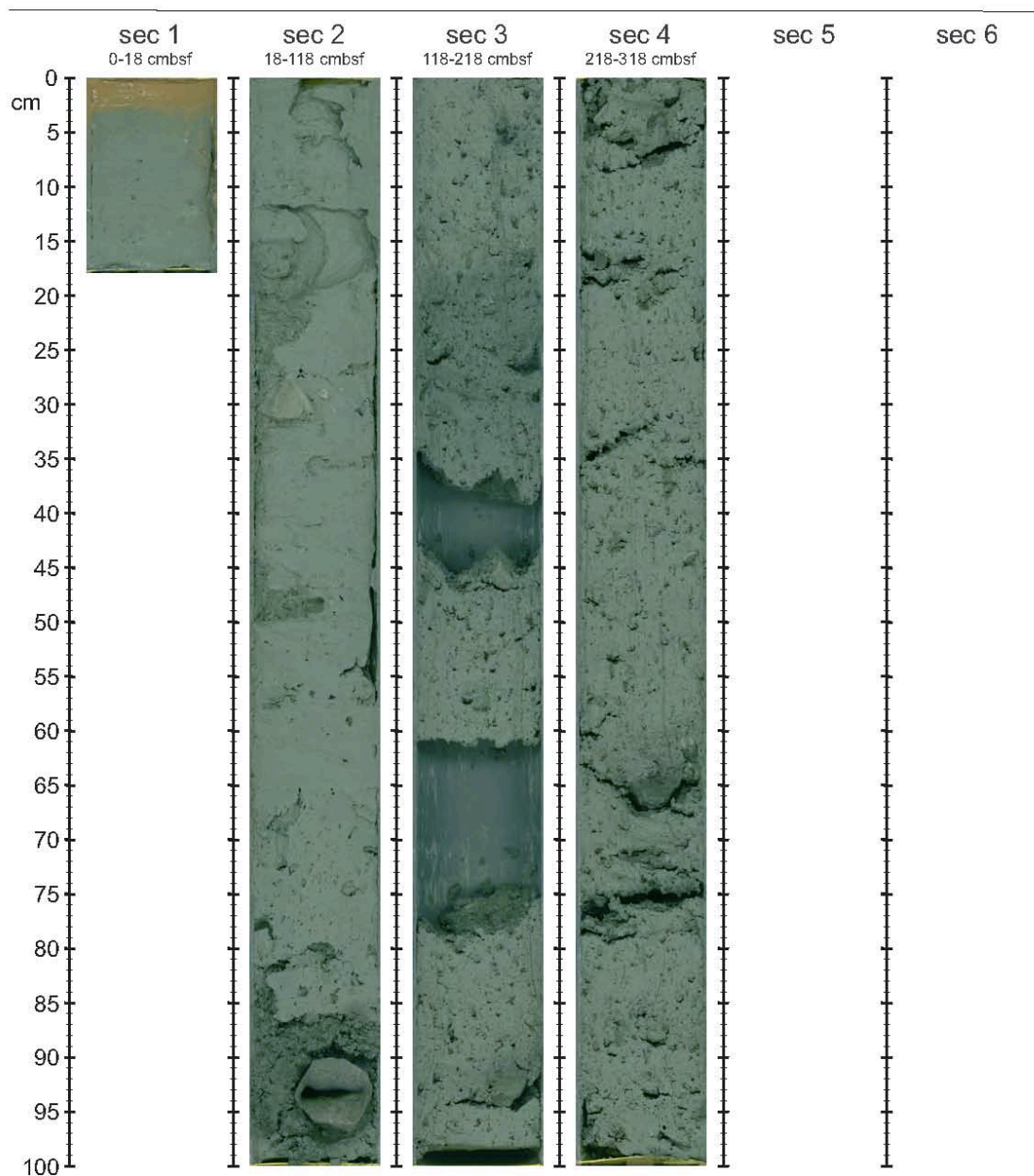
Bergamo plateau

Latitude: 33° 44.3047 N

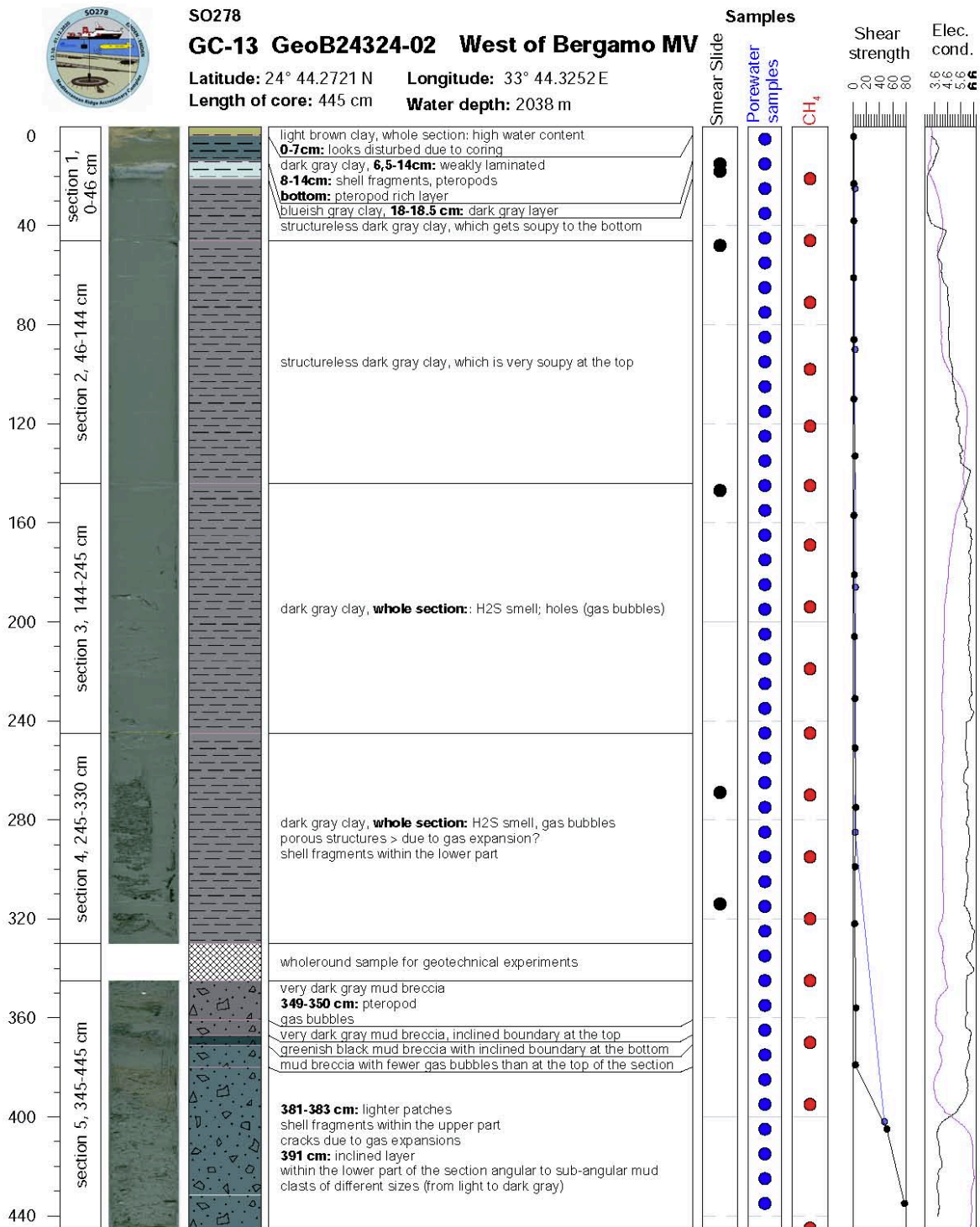
Longitude: 24° 44.8789 E

Length of core: 318 cm

Water depth: 1934 m



Continuation Strater Profiles and Core Photos



Comments: **core catcher:** mud breccia with dark and light gray clasts (<5 cm) and gypsum fragment



### Continuation Strater Profiles and Core Photos



SO278

GC-13 GeoB24324-02

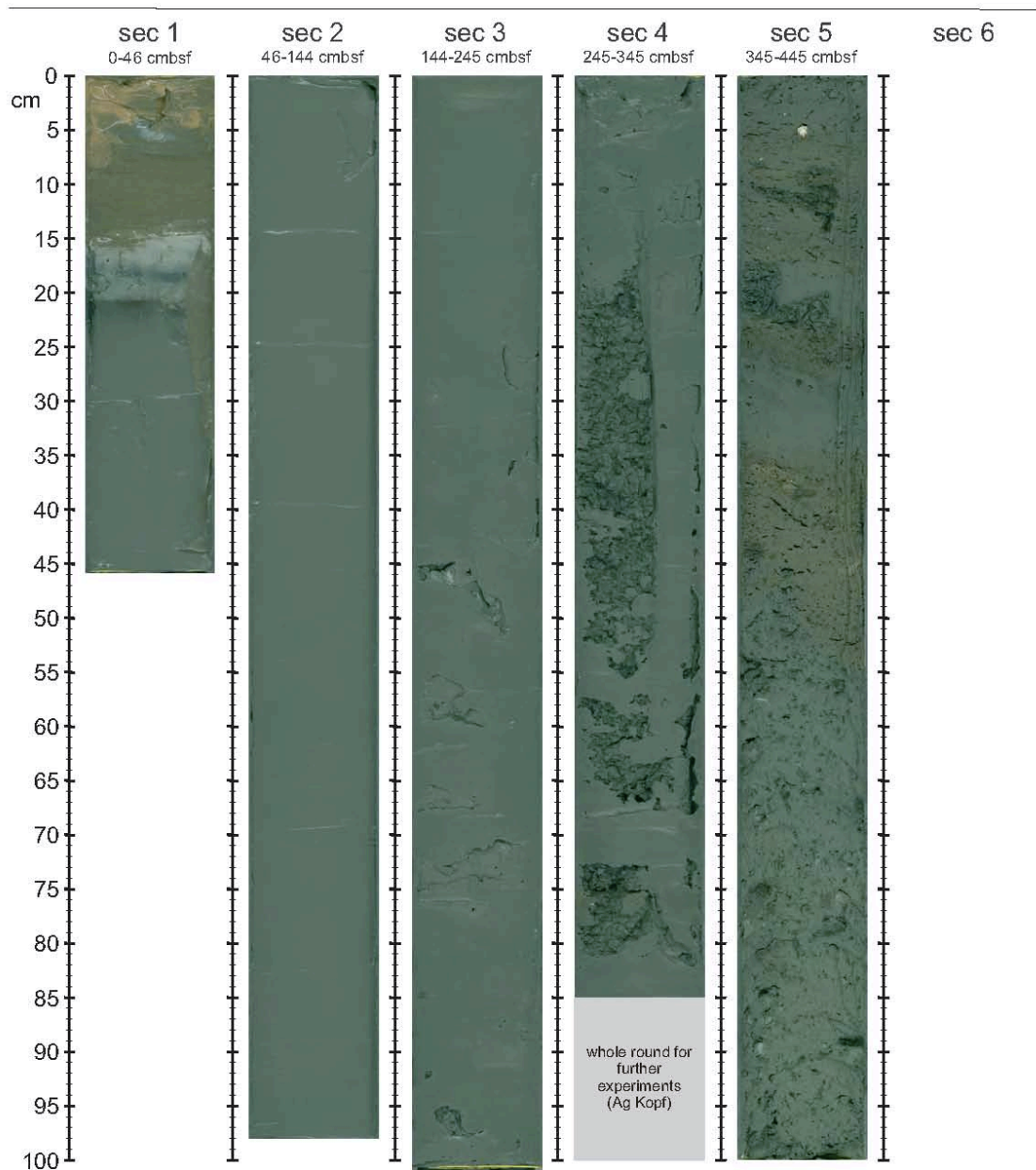
West of Bergamo

Latitude: 33° 44.3252 N

Longitude: 24° 44.2721 E

Length of core: 445 cm

Water depth: 2038 m



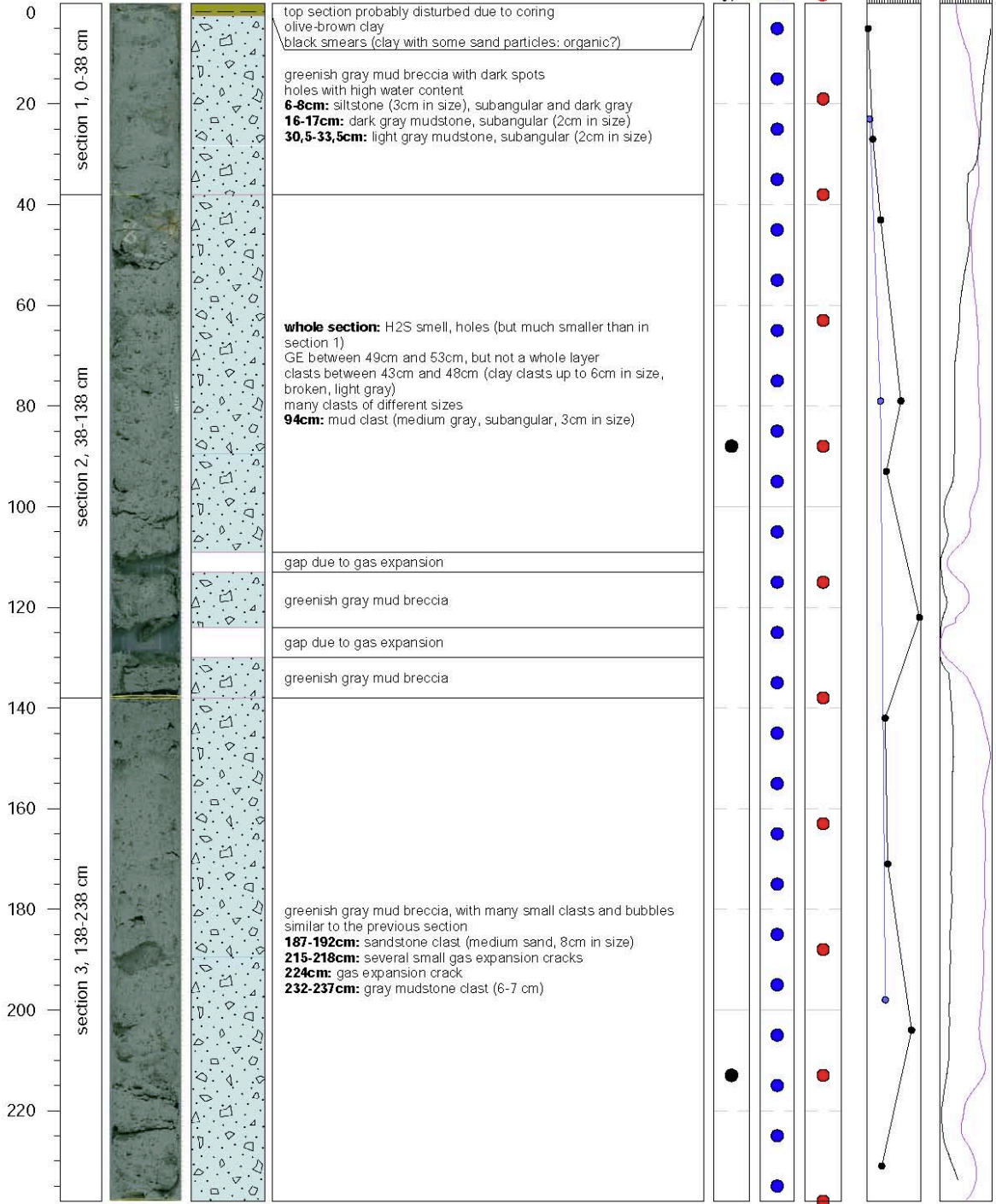
Continuation Strater Profiles and Core Photos



SO278

GC-14 GeoB24326-01 Bergamo NE plateau

Latitude: 24° 45.0100 N Longitude: 33° 44.4080 E  
 Length of core: 238 cm Water depth: 1937 m



Comments: -

50  
100  
150  
Mag. Sus

### Continuation Strater Profiles and Core Photos

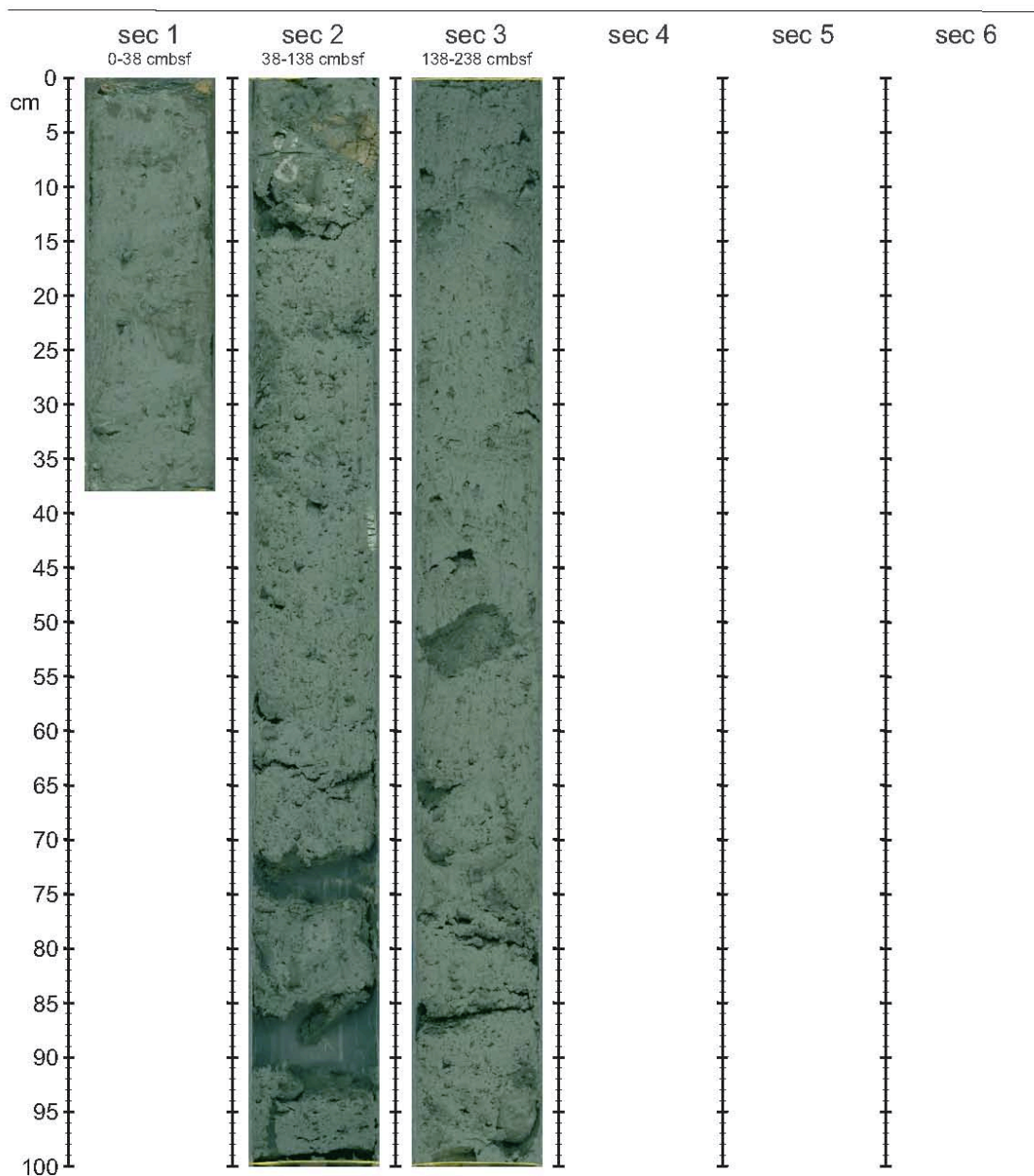


SO278

GC-14 GeoB24326-01 Bergamo NE plateau

Latitude: 33° 44.4080 N Longitude: 24° 45.0100 E

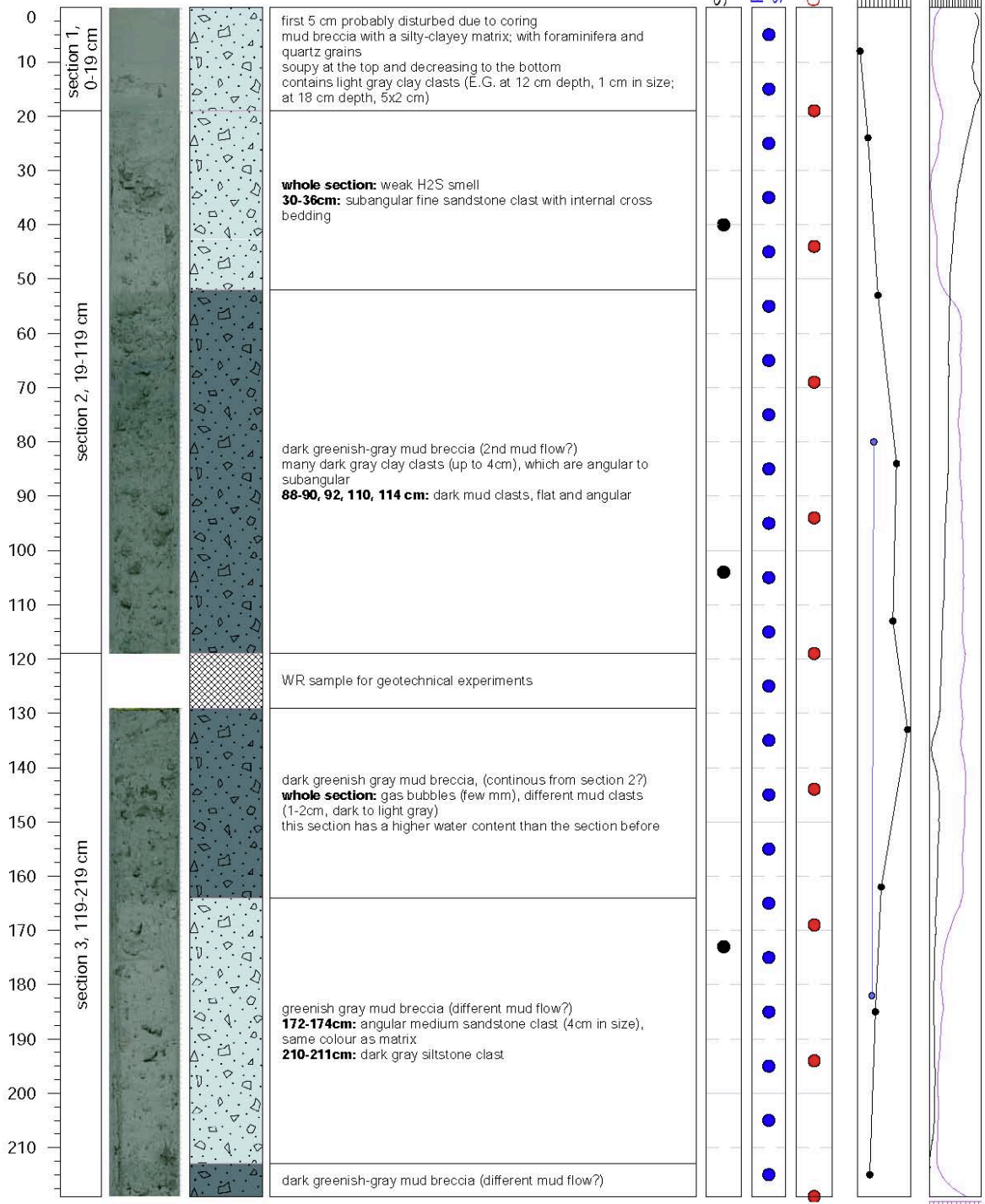
Length of core: 238 cm Water depth: 1937 m



### Continuation Strater Profiles and Core Photos



**SO278**  
**GC-15 GeoB24327-02 Moscow MV**  
 Latitude: 24° 31.7192 N Longitude: 33° 40.5934 E  
 Length of core: 219 cm Water depth: 1824 m



Comments: -

100  
150  
200  
Mag. Sus

### Continuation Strater Profiles and Core Photos



SO278

GC-15 GeoB24327-02

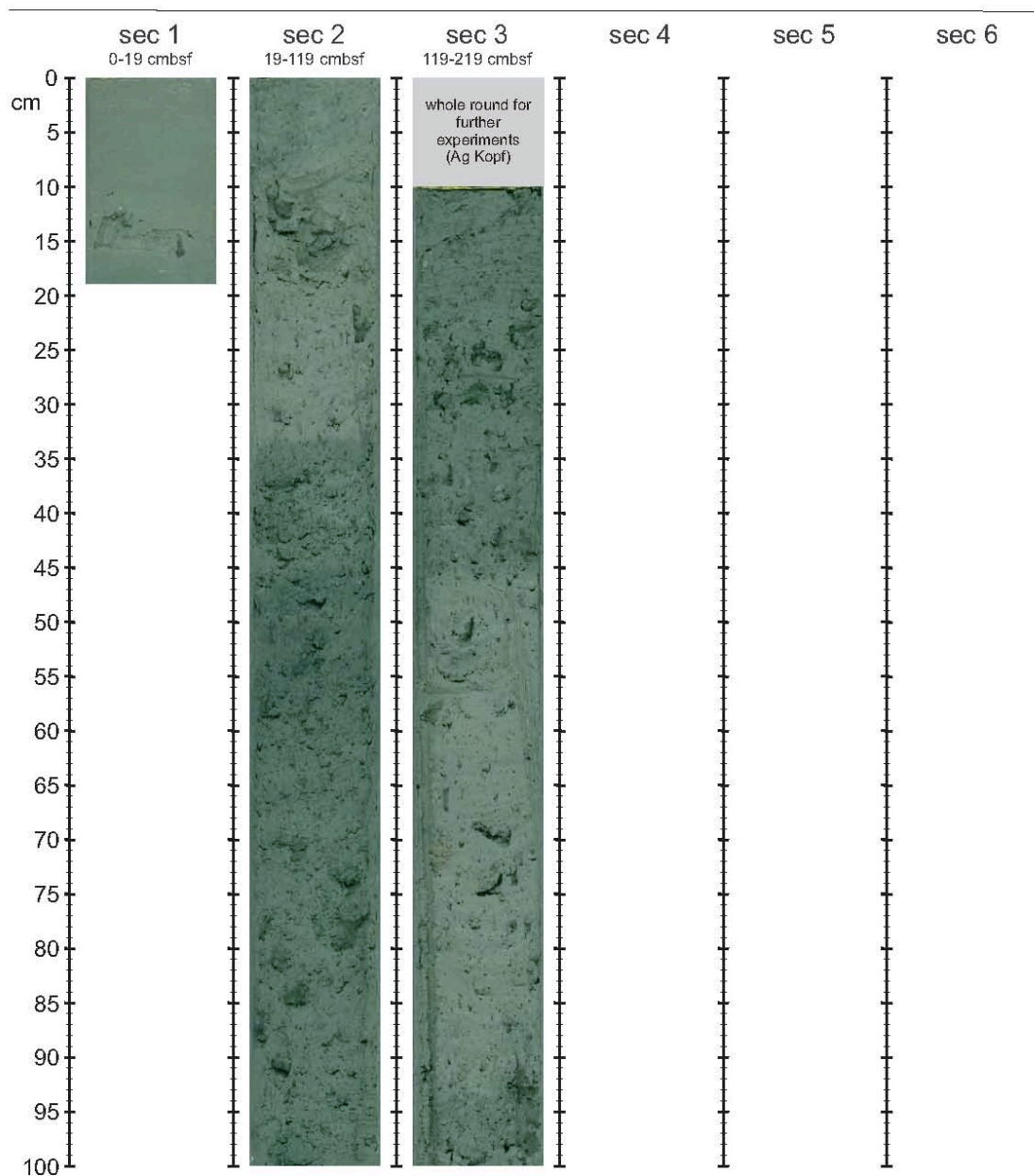
Moscow MV

Latitude: 33° 40.5934 N

Longitude: 24° 31.7192 E

Length of core: 219 cm

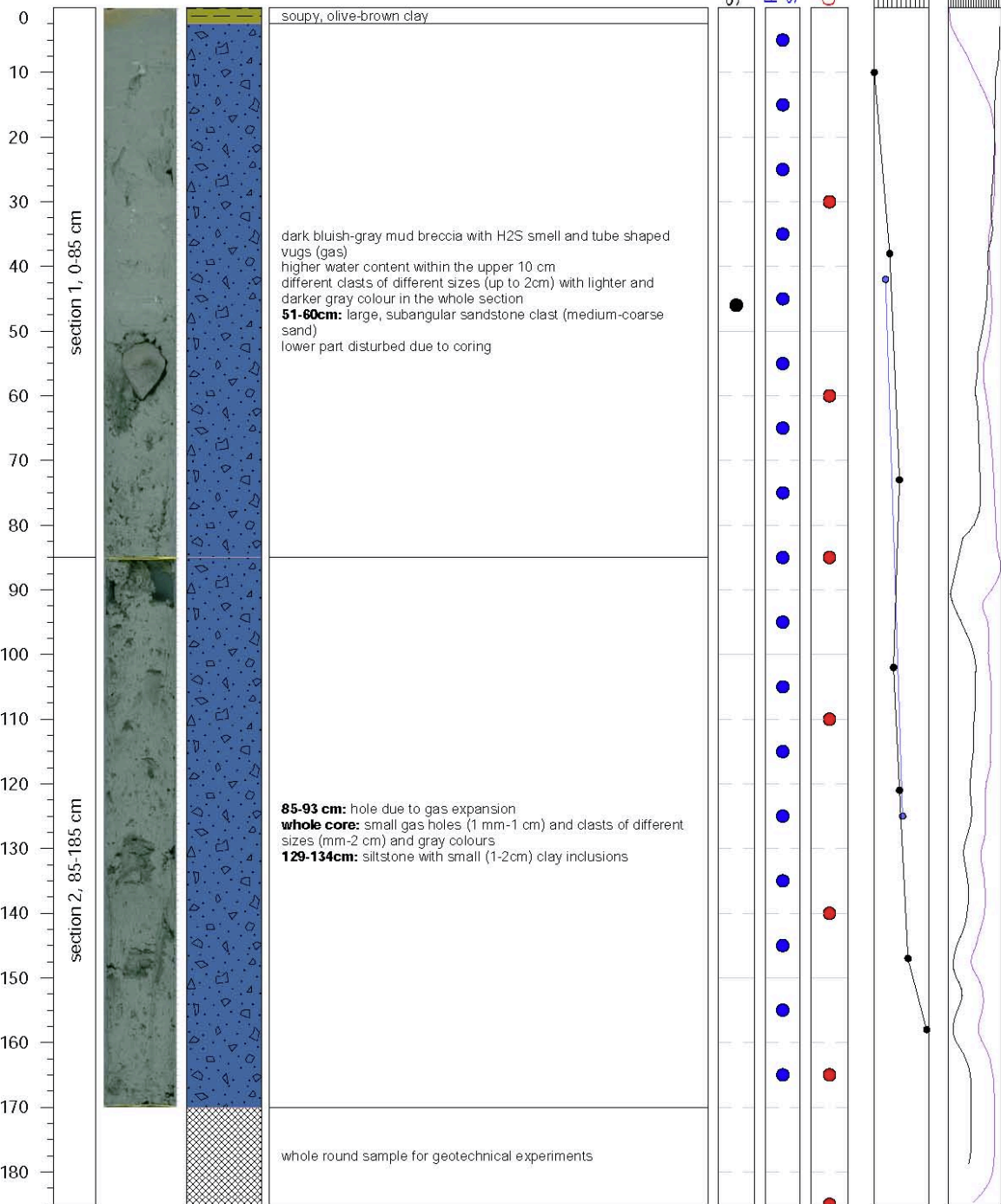
Water depth: 1824 m



Continuation Strater Profiles and Core Photos



**SO278**  
**GC-16 GeoB24328-01 Maidstone MV**  
 Latitude: 24° 40.6466 N Longitude: 33° 37.1155 E  
 Length of core: 185 cm Water depth: 1934 m



Comments: **core catcher:** mud breccia

55  
80  
105  
130  
Mag. Sus

### Continuation Strater Profiles and Core Photos



SO278

GC-16 GeoB24328-01

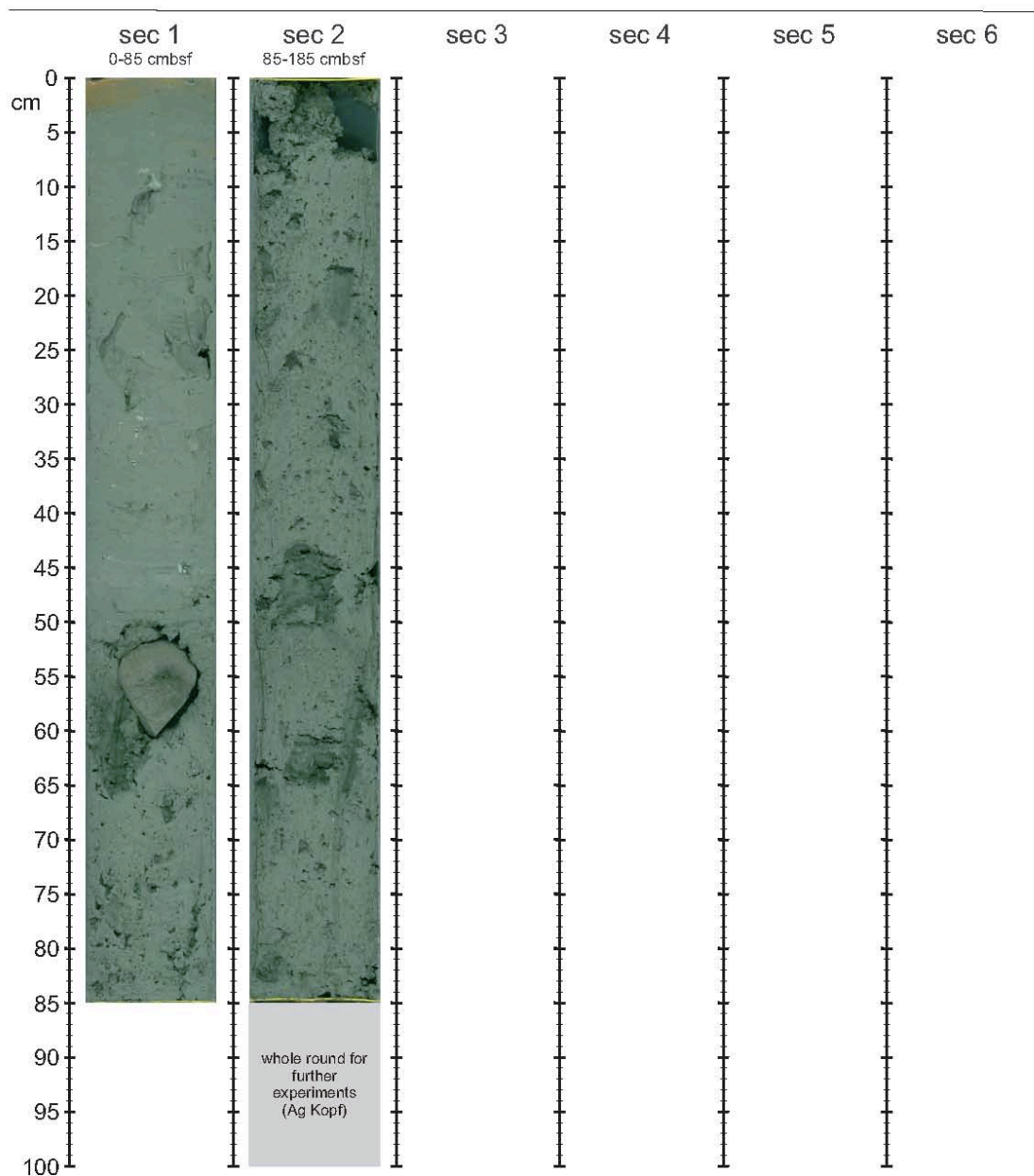
Maidstone MV

Latitude: 33° 37.1155 N

Longitude: 24° 40.6466 E

Length of core: 185 cm

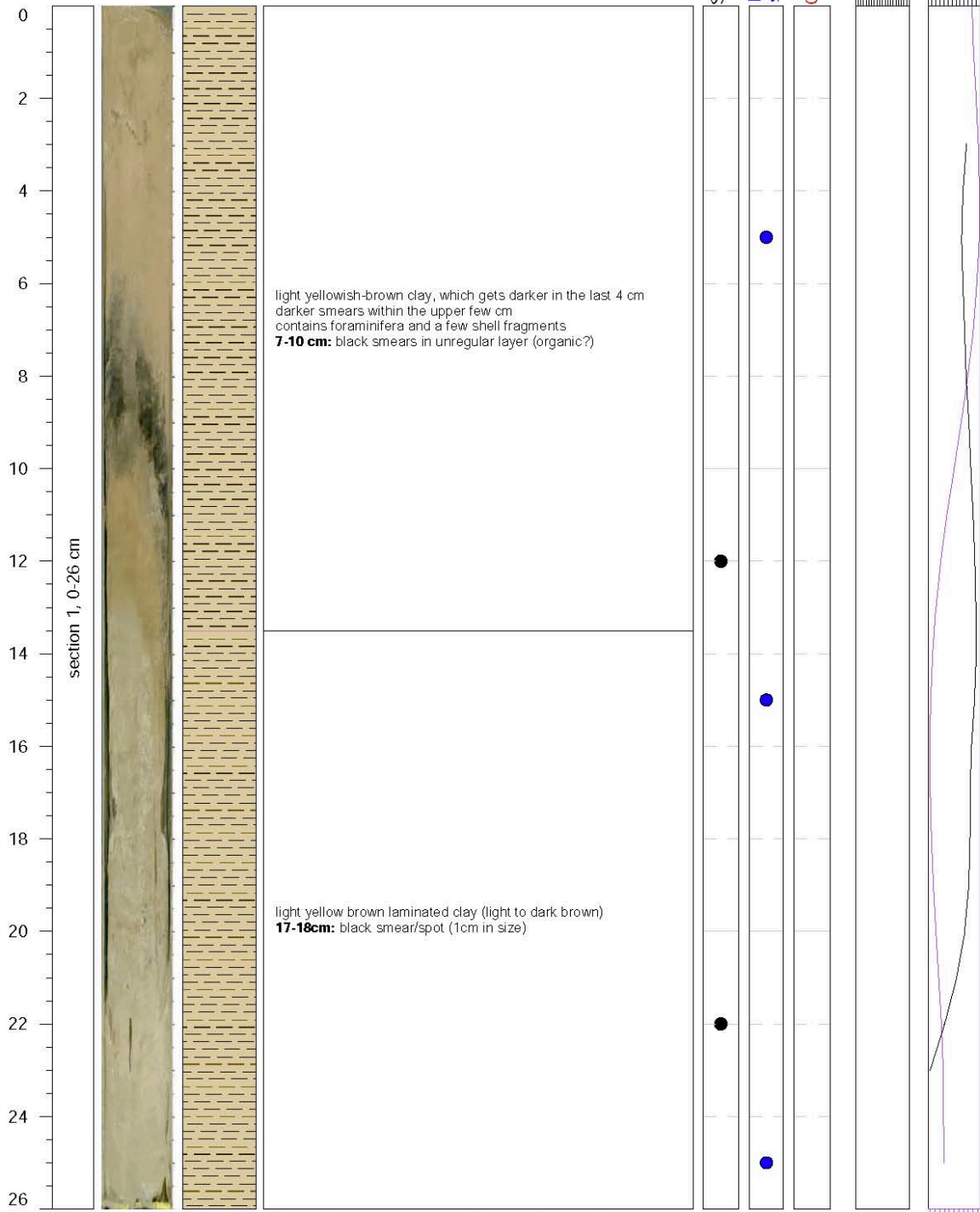
Water depth: 1934 m



Continuation Strater Profiles and Core Photos



**SO278**  
**GC-17 GeoB24333-01 Leipzig MV**  
 Latitude: 24° 40.0083 N Longitude: 33° 46.7619E  
 Length of core: 26 cm Water depth: 1933 m



Comments: outside of gravity core covered in mud breccia

Mag. Su

### Continuation Strater Profiles and Core Photos



SO278

GC-17 GeoB24333-01

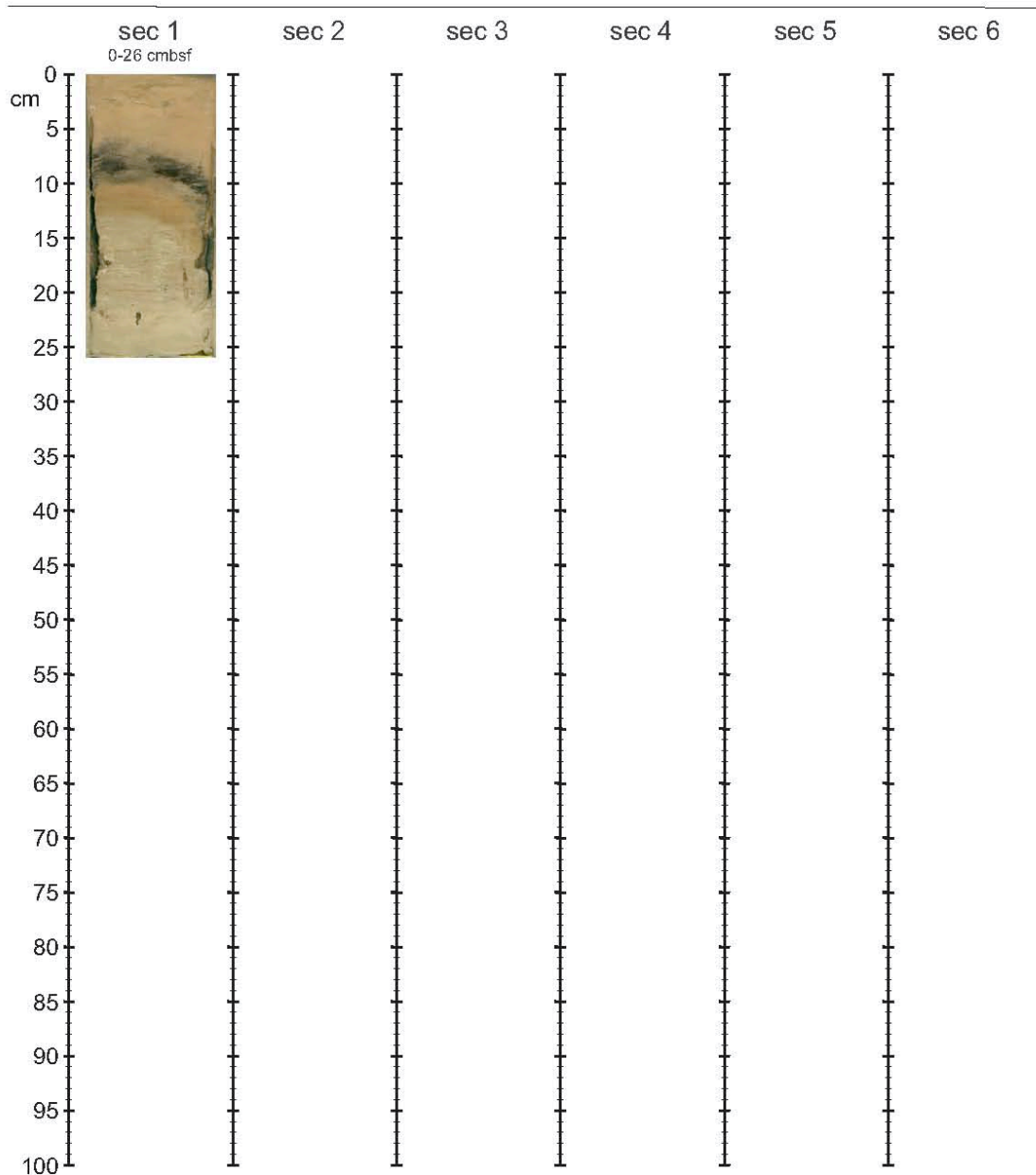
Leipzig MV

Latitude: 33° 46.7619 N

Longitude: 24° 40.0083 E

Length of core: 26 cm

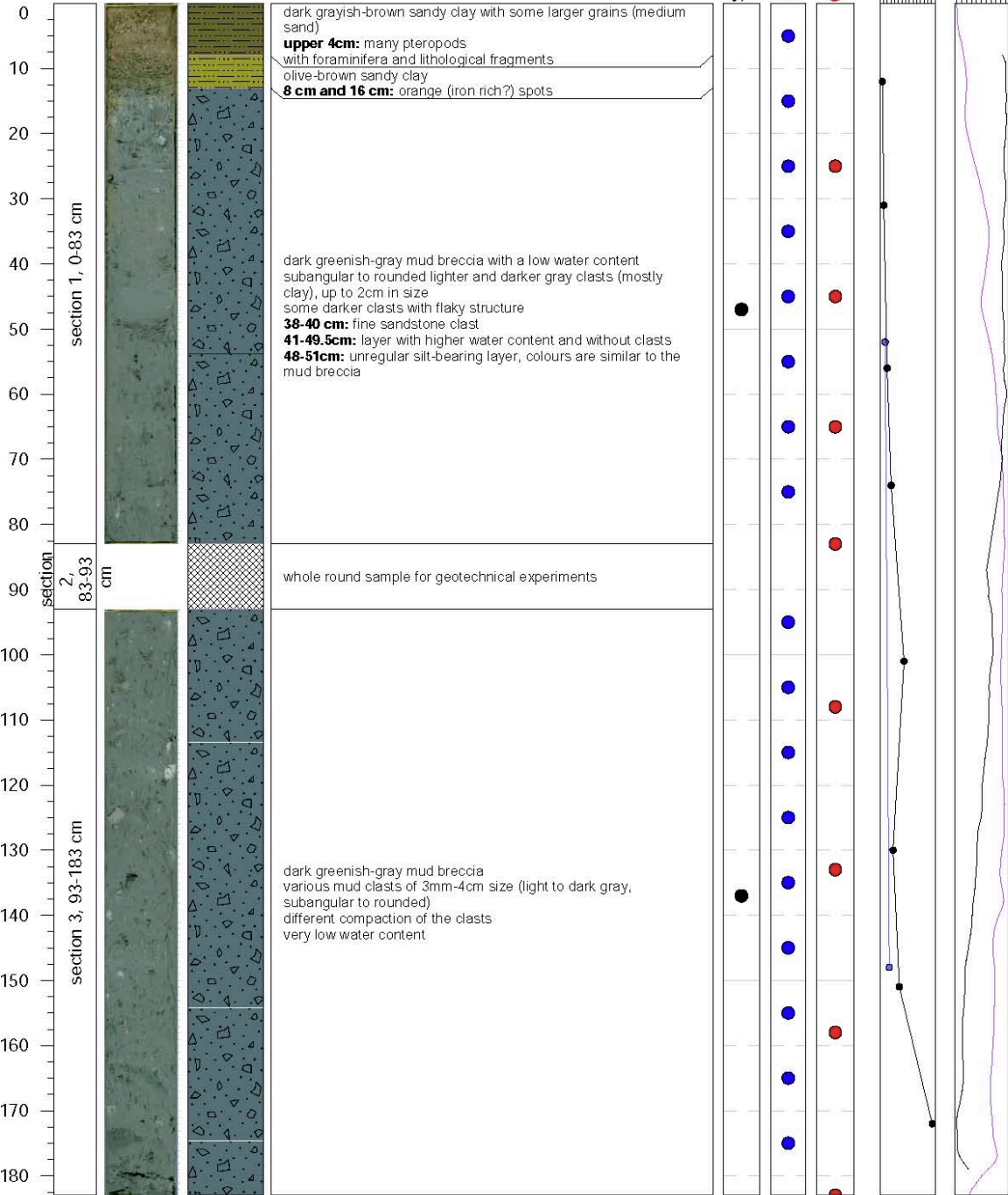
Water depth: 1933 m



Continuation Strater Profiles and Core Photos



**SO278**  
**GC-18 GeoB24337-01 Dublin MV**  
 Latitude: 25° 29.3488 N Longitude: 33° 30.5300 E  
 Length of core: 183 cm Water depth: 2269 m



Comments: -

70 120 170 220  
 Mag. Su

### Continuation Strater Profiles and Core Photos



SO278

GC-18 GeoB24337-01

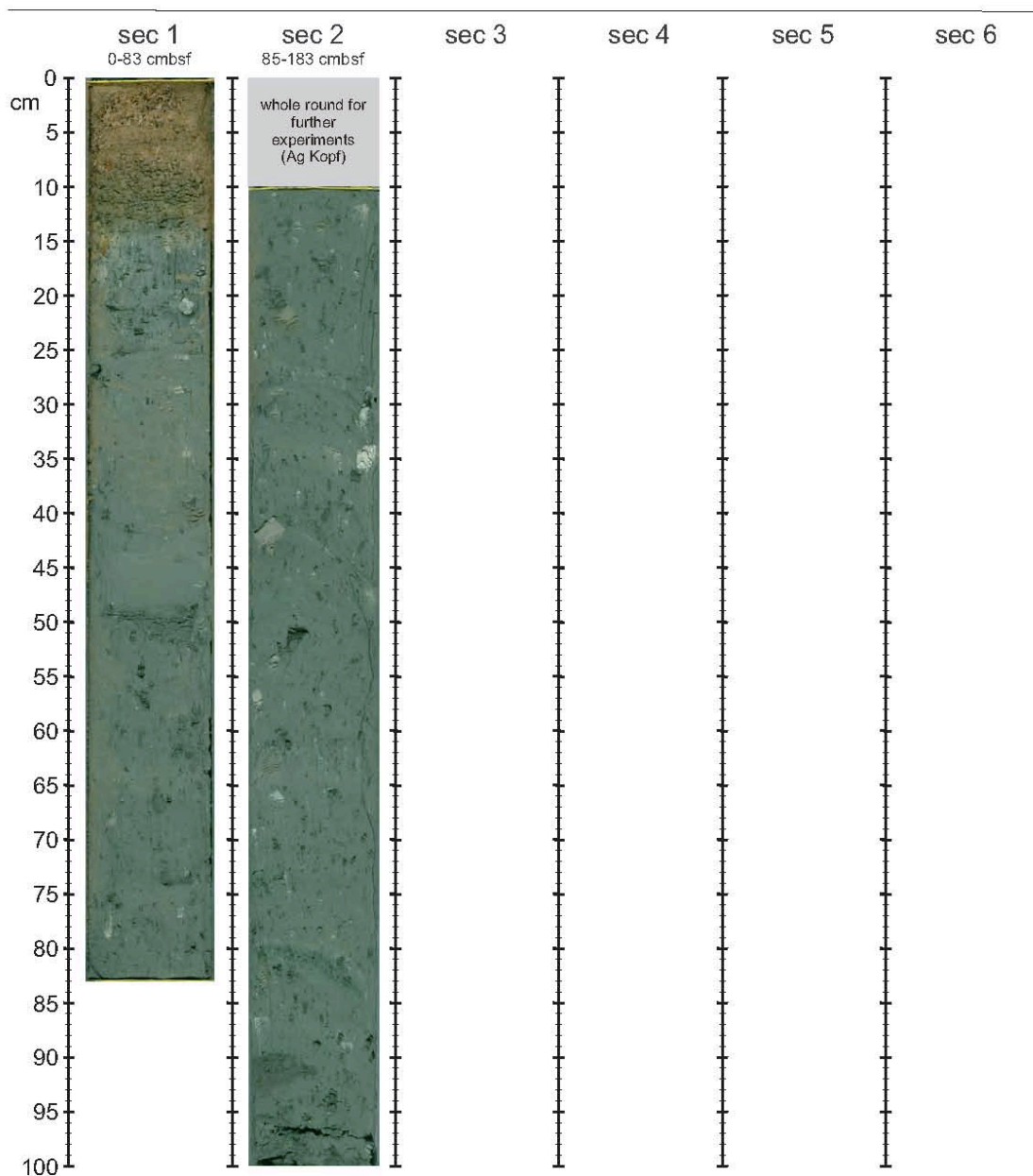
Dublin MV

Latitude: 33° 30.5300 N

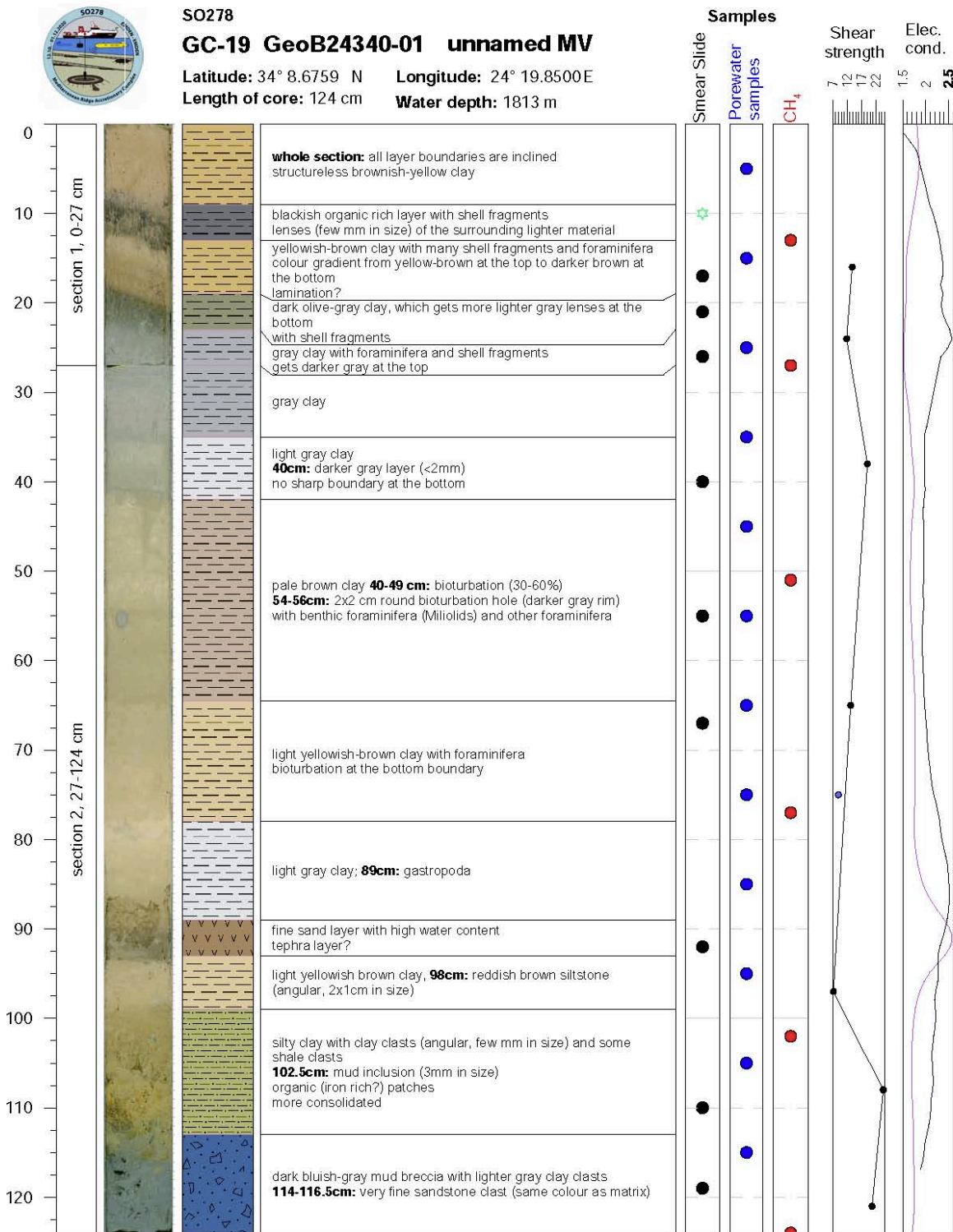
Longitude: 25° 29.3488 E

Length of core: 183 cm

Water depth: 2269 m



Continuation Strater Profiles and Core Photos



Comments: core catcher: mud breccia with subangular clasts (<4cm, light to dark gray)



### Continuation Strater Profiles and Core Photos



SO278

GC-19 GeoB24340-01

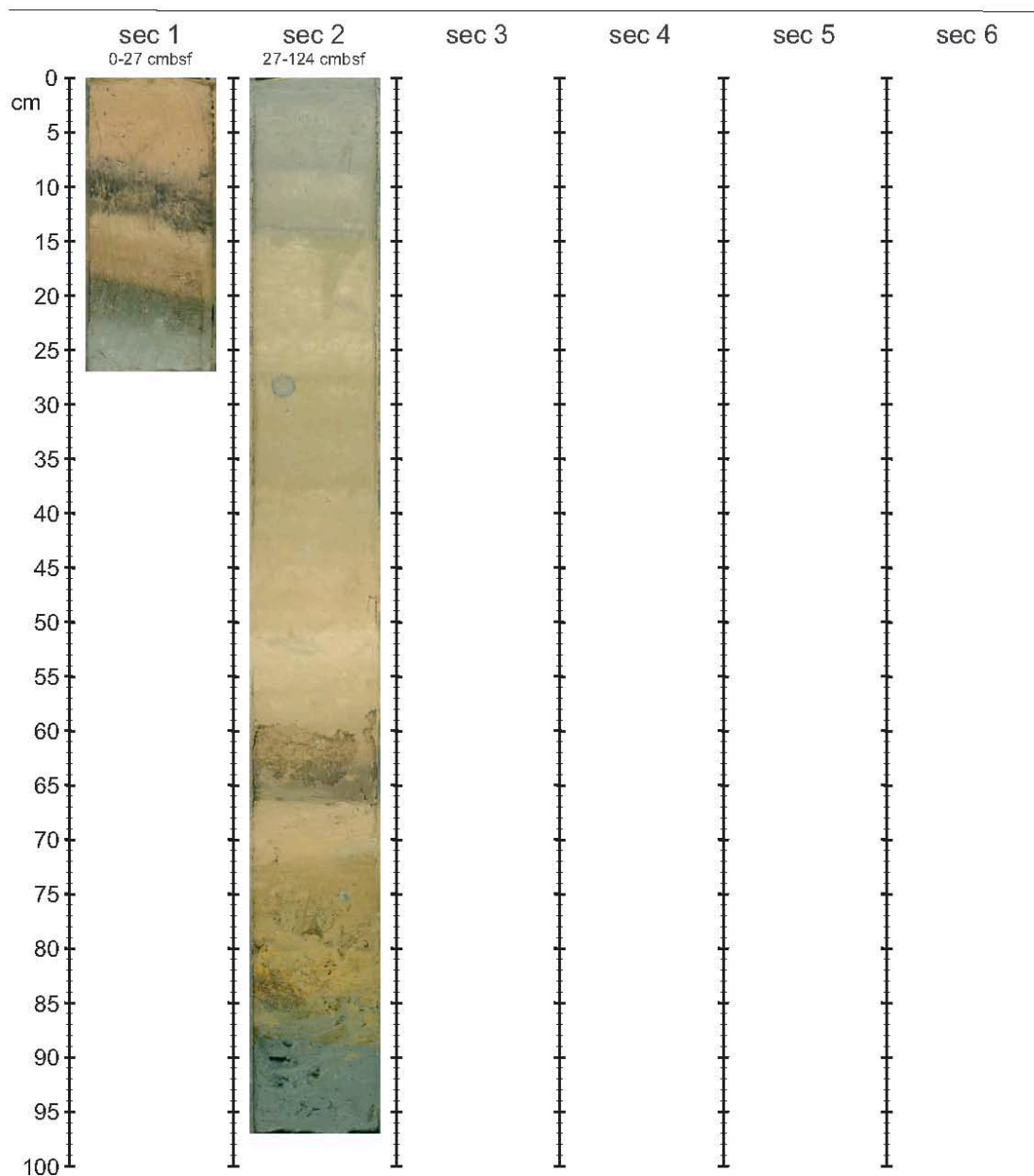
Unnamed MV

Latitude: 34° 08.6759 N

Longitude: 24° 19.8500 E

Length of core: 124 cm

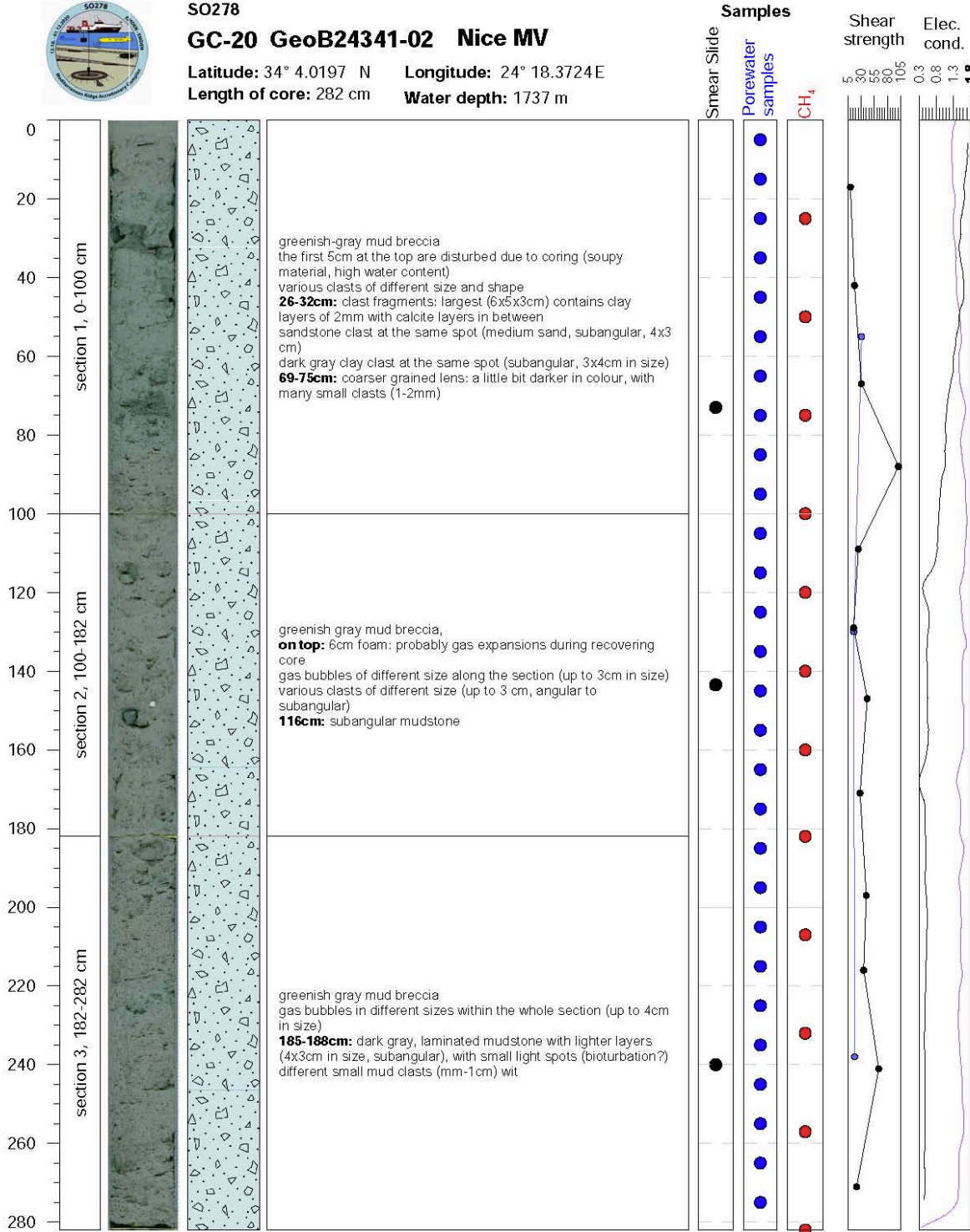
Water depth: 1813 m



Continuation Strater Profiles and Core Photos



**SO278**  
**GC-20 GeoB24341-02 Nice MV**  
 Latitude: 34° 4.0197 N Longitude: 24° 18.3724 E  
 Length of core: 282 cm Water depth: 1737 m



Comments: **core catcher**: mud breccia with small gypsum clast, different mud clasts, calcite clast with slickenside



### Continuation Strater Profiles and Core Photos



SO278

GC-20 GeoB24341-02

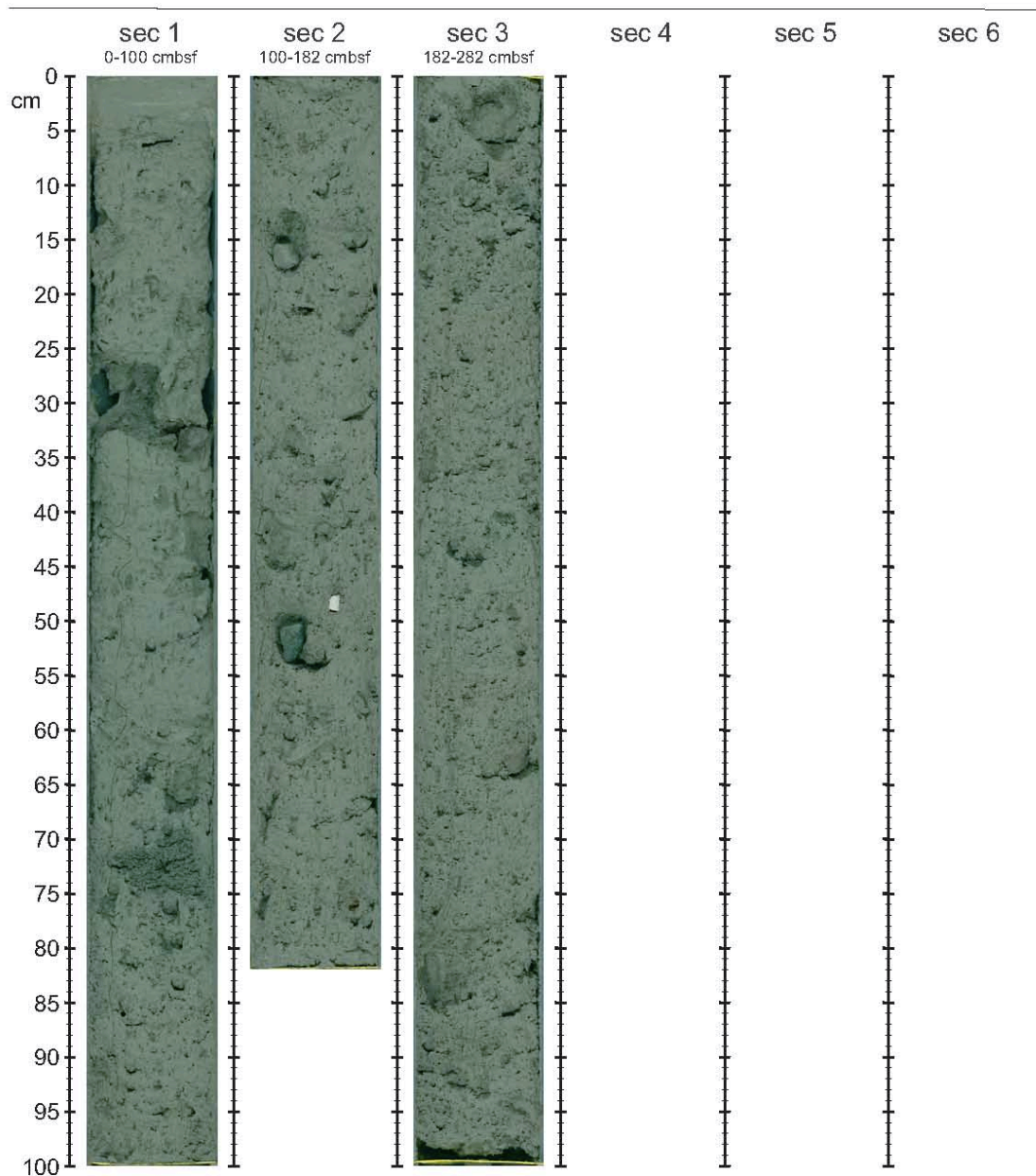
Nice MV

Latitude: 34° 04.0197 N

Longitude: 24° 18.3724 E

Length of core: 282 cm

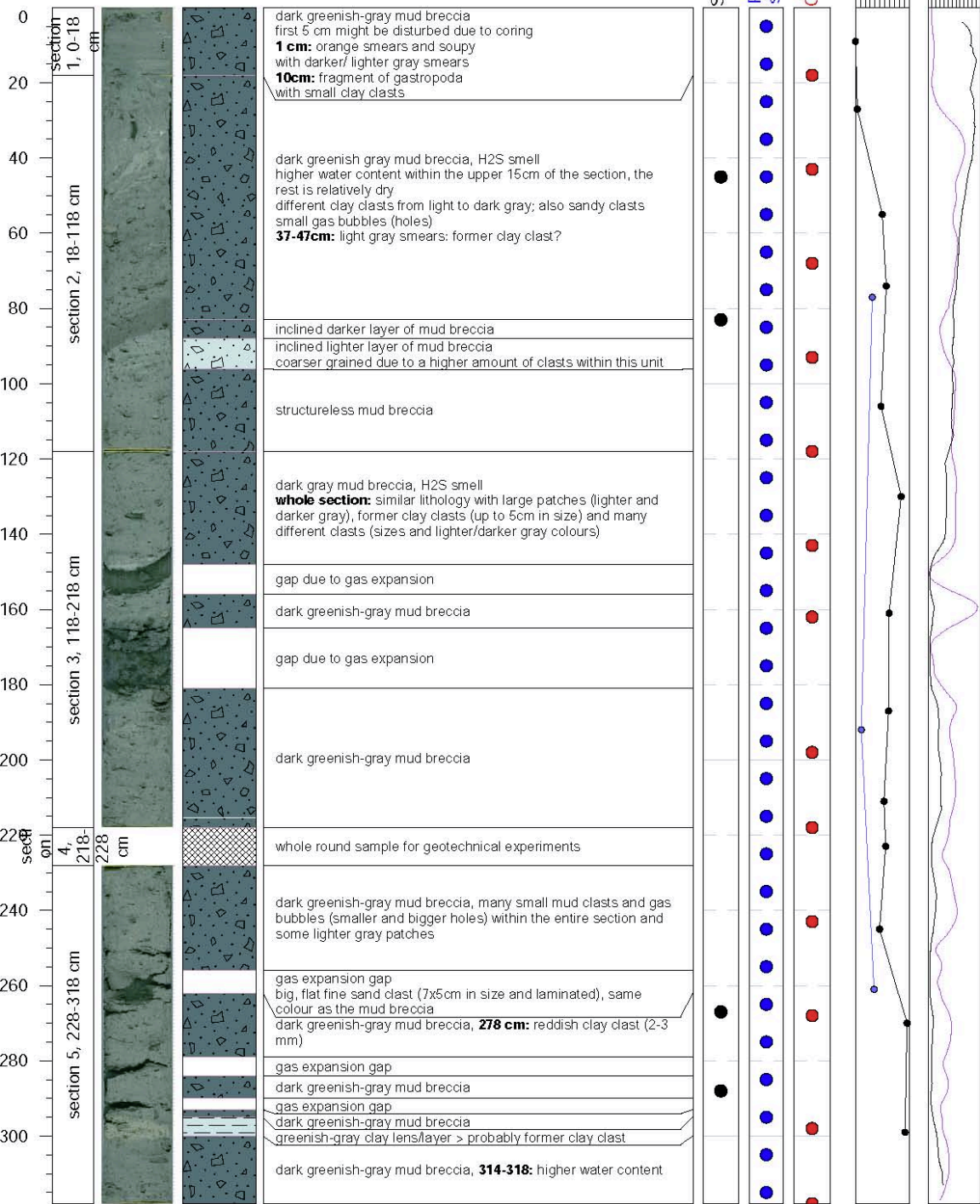
Water depth: 1737 m



Continuation Strater Profiles and Core Photos



**SO278**  
**GC-21 GeoB24343-01 Monza MV**  
 Latitude: 33° 44.0642 N Longitude: 24° 43.4720 E  
 Length of core: 318 cm Water depth: 1921 m



Comments: **core catcher:** mud breccia with single laminated siltstone clast (subangular, 3x2)

Mag. Su

### Continuation Strater Profiles and Core Photos



SO278

GC-21 GeoB24343-01

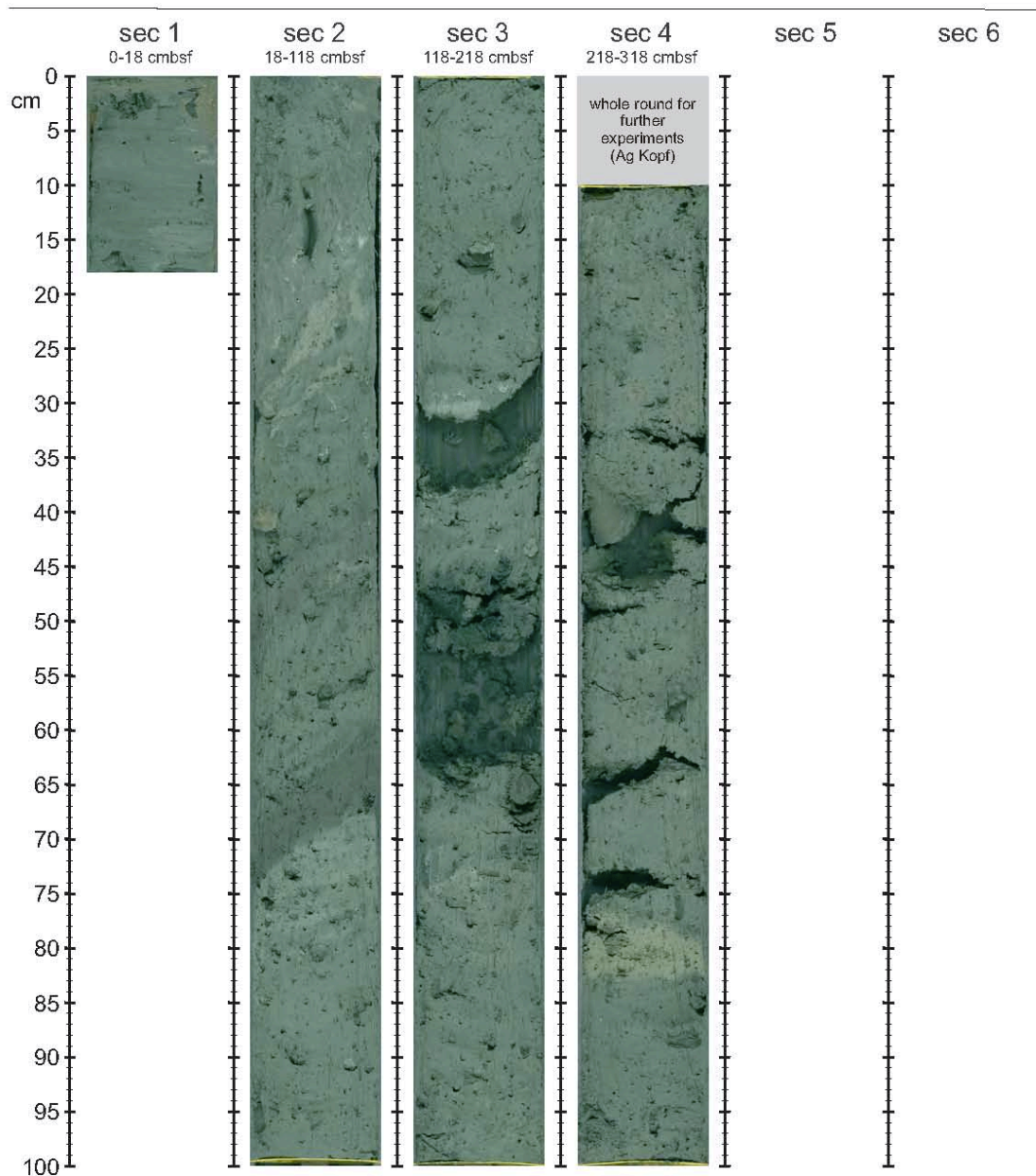
Monza MV

Latitude: 33° 44.0642 N

Longitude: 24° 43.4720 E

Length of core: 318 cm

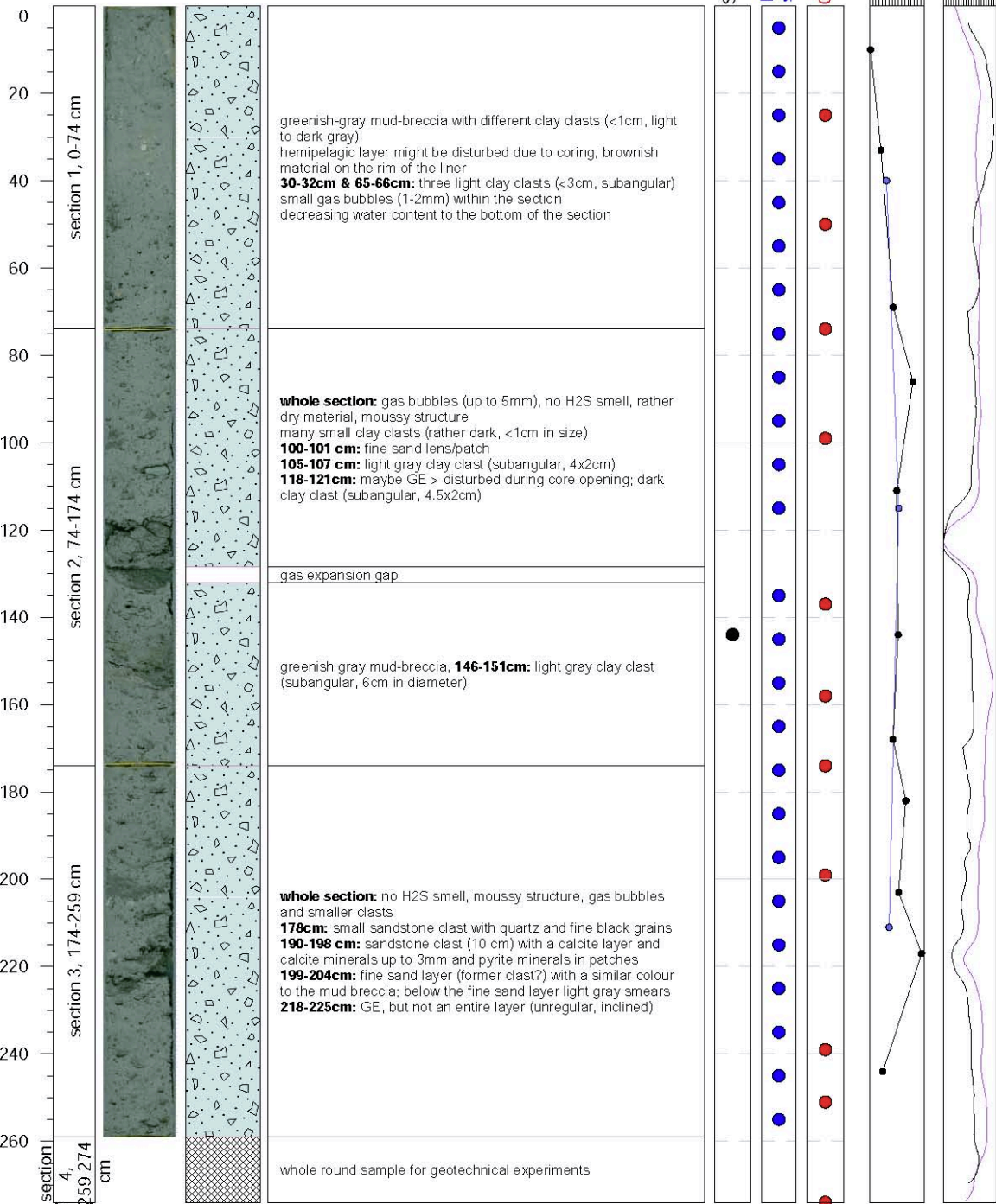
Water depth: 1921 m



Continuation Strater Profiles and Core Photos



**SO278**  
**GC-22 GeoB24346-02 Milano MV**  
 Latitude: 33° 43.9440 N Longitude: 24° 46.6507 E  
 Length of core: 274 cm Water depth: 1956 m



Comments: **core catcher:** mud breccia including subangular fine sandstone clasts (5x3x4)

Mag. Su.

### Continuation Strater Profiles and Core Photos



SO278

GC-22 GeoB24346-02

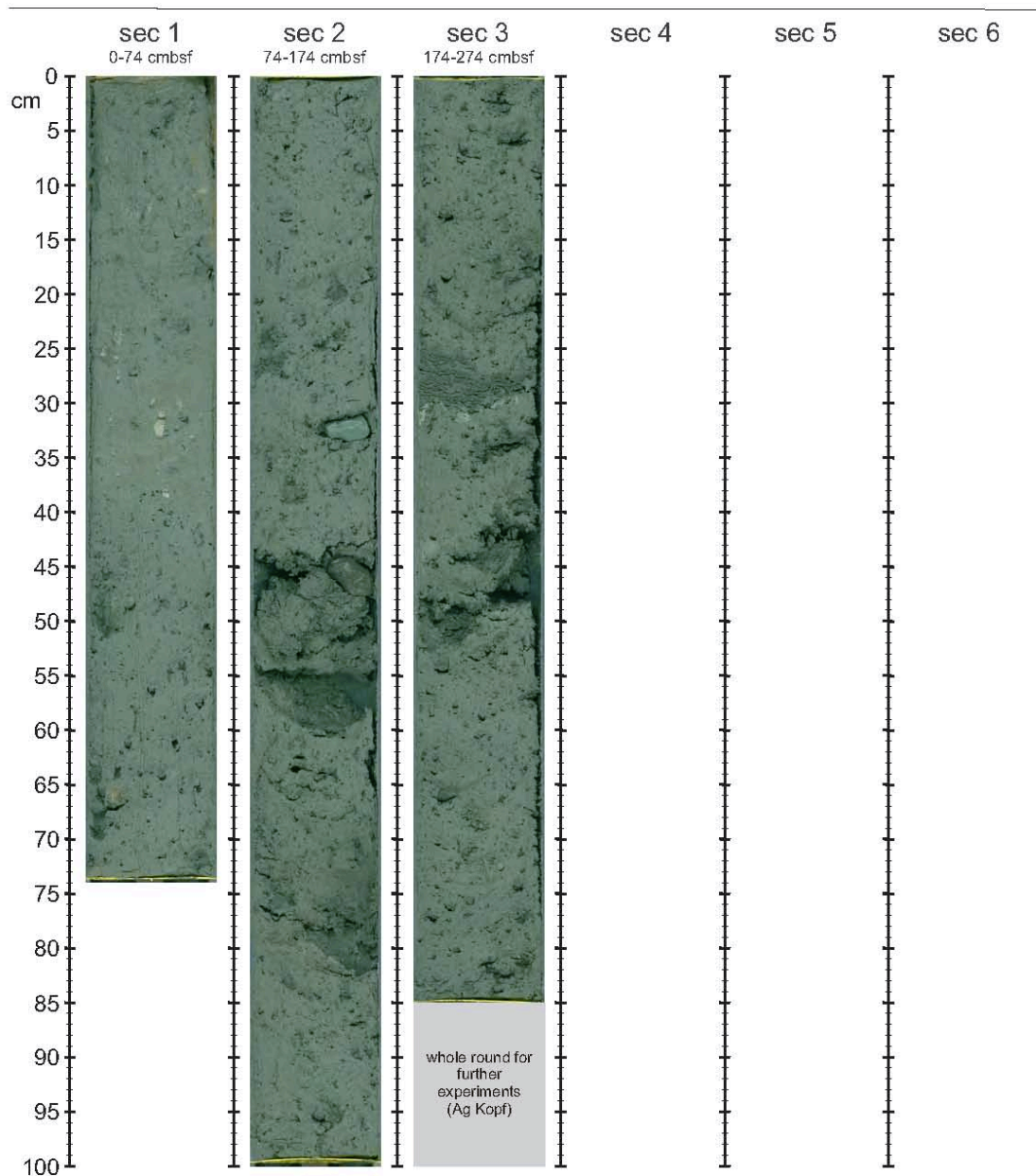
Milano MV

Latitude: 33° 43.9440 N

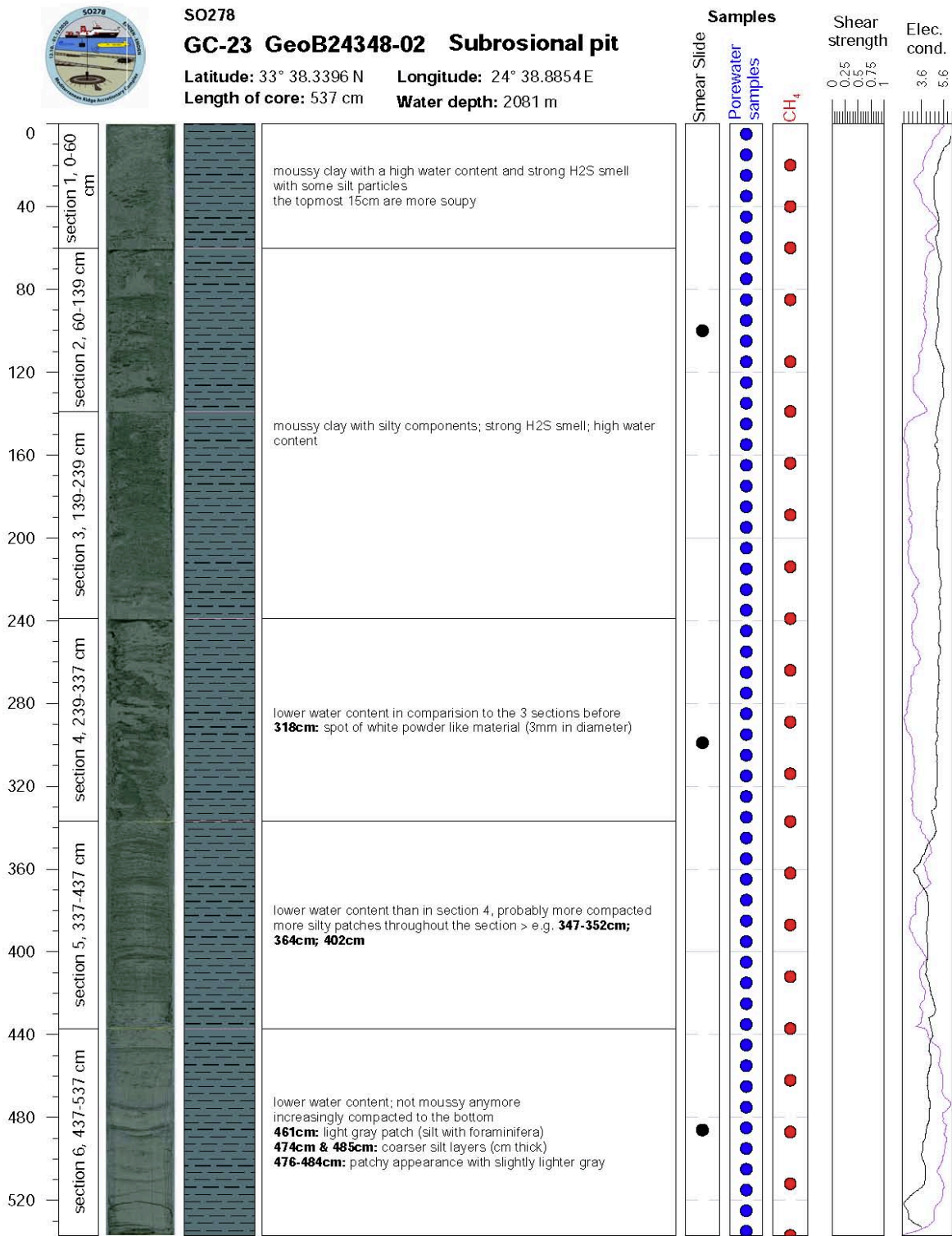
Longitude: 24° 46.6507 E

Length of core: 274 cm

Water depth: 1956 m



Continuation Strater Profiles and Core Photos



Comments: H2S smell so strong core was left to degass overnight, description ~12 hours later

36 46 56 66  
 Mag. Su

### Continuation Strater Profiles and Core Photos



SO278

GC-23 GeoB24348-02

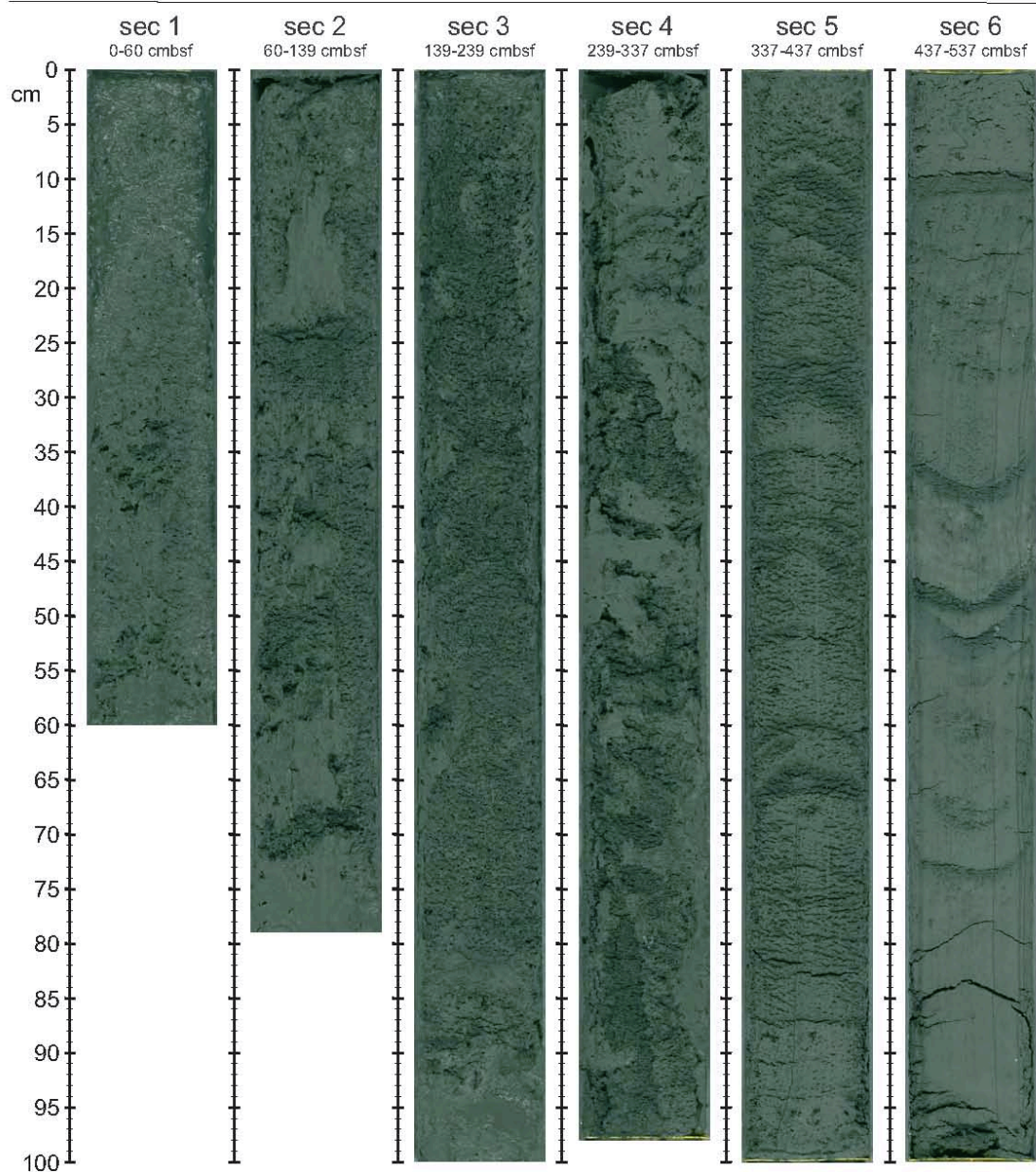
Subrosional pit

Latitude: 33° 38.3396 N

Longitude: 24° 38.8854 E

Length of core: 537 cm

Water depth: 2081 m

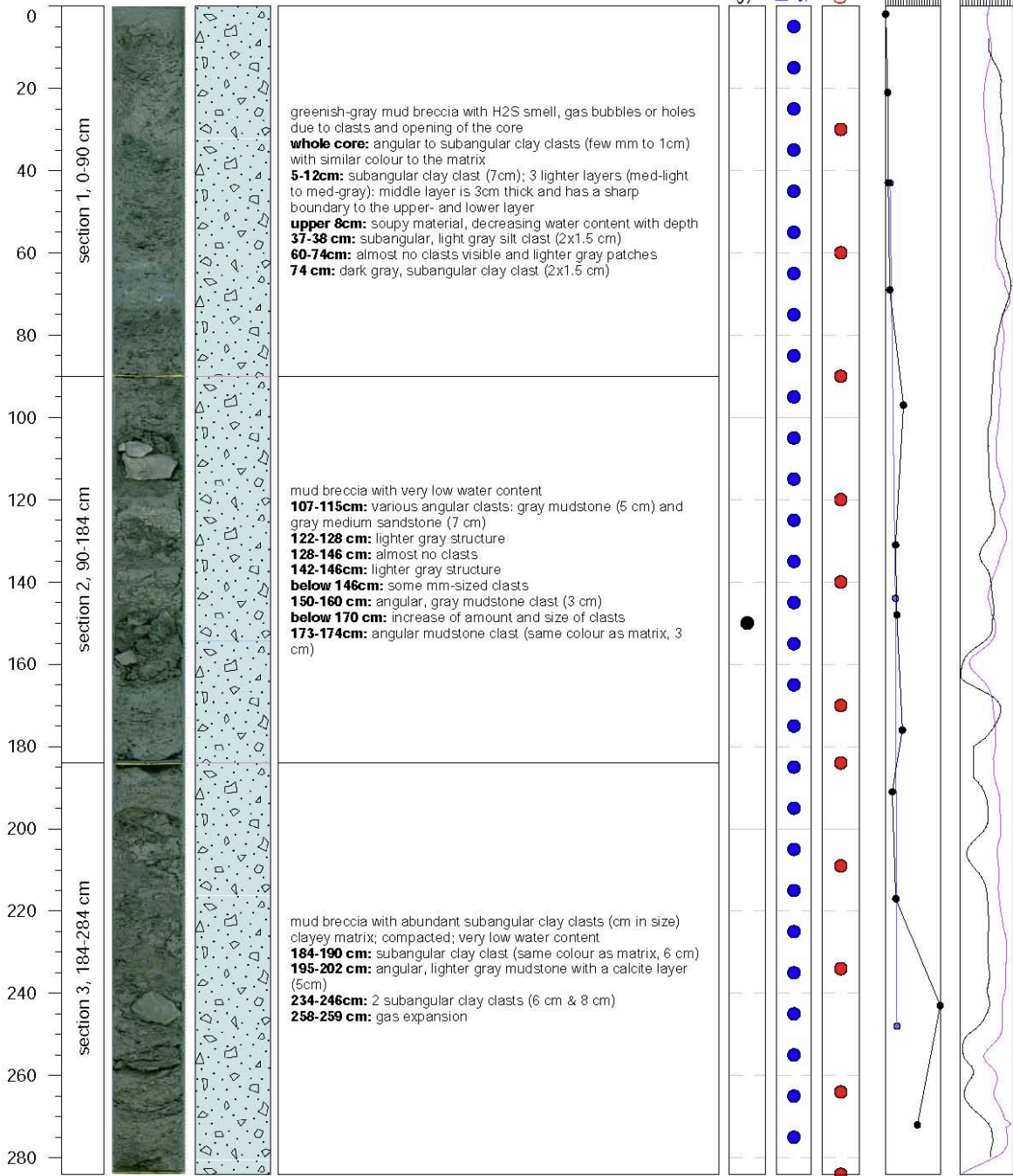


Continuation Strater Profiles and Core Photos



**SO278**  
**GC-24 GeoB24351-01 Gelendzhik MV**

**Latitude:** 33° 54.175 N **Longitude:** 24° 16.155 E  
**Length of core:** 284 cm **Water depth:** 1709 m



Comments: -



### Continuation Strater Profiles and Core Photos



SO278

GC-24 GeoB24351-01

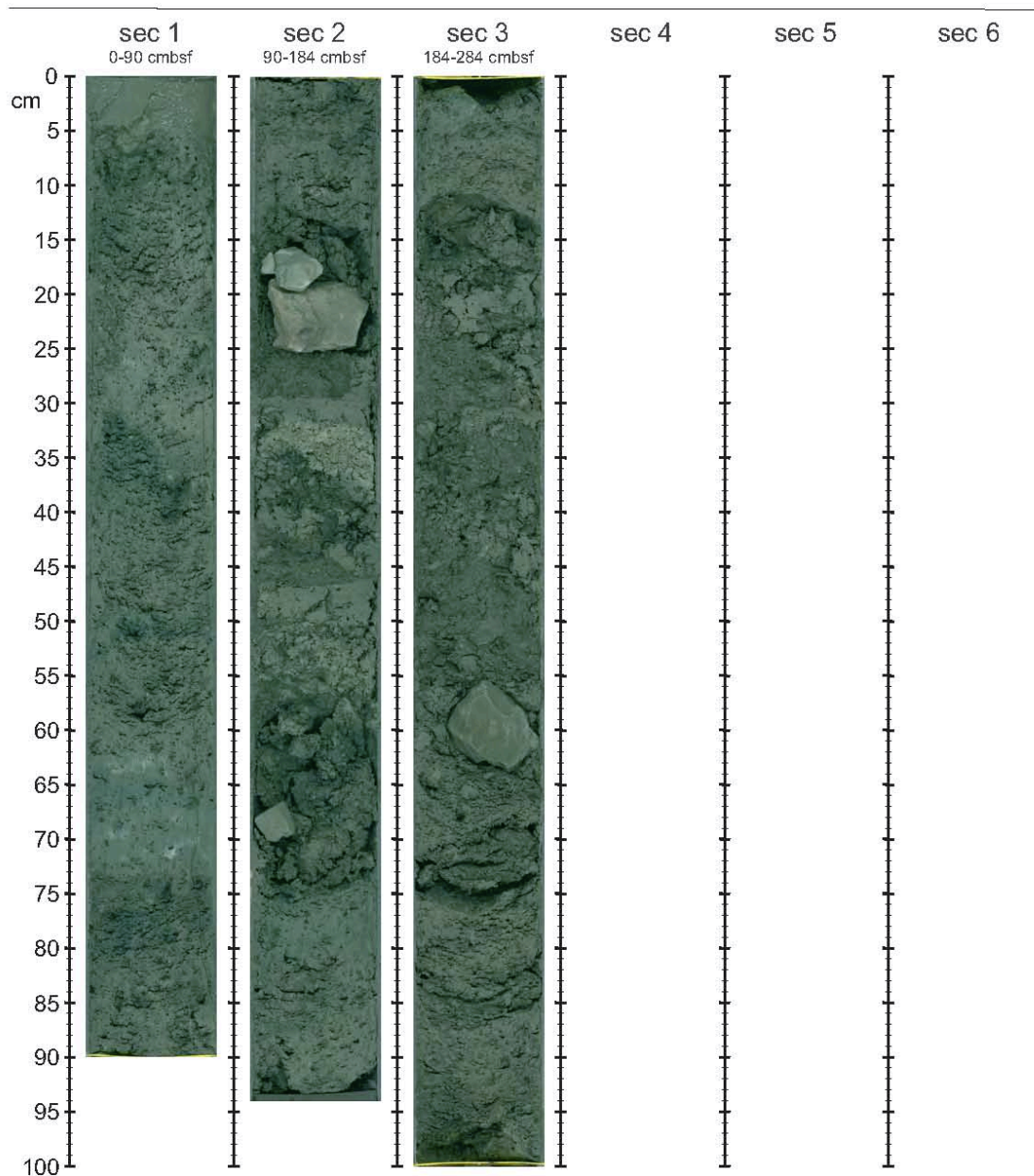
Gelendzhik MV

Latitude: 33° 54.175 N

Longitude: 24° 16.155 E

Length of core: 284 cm

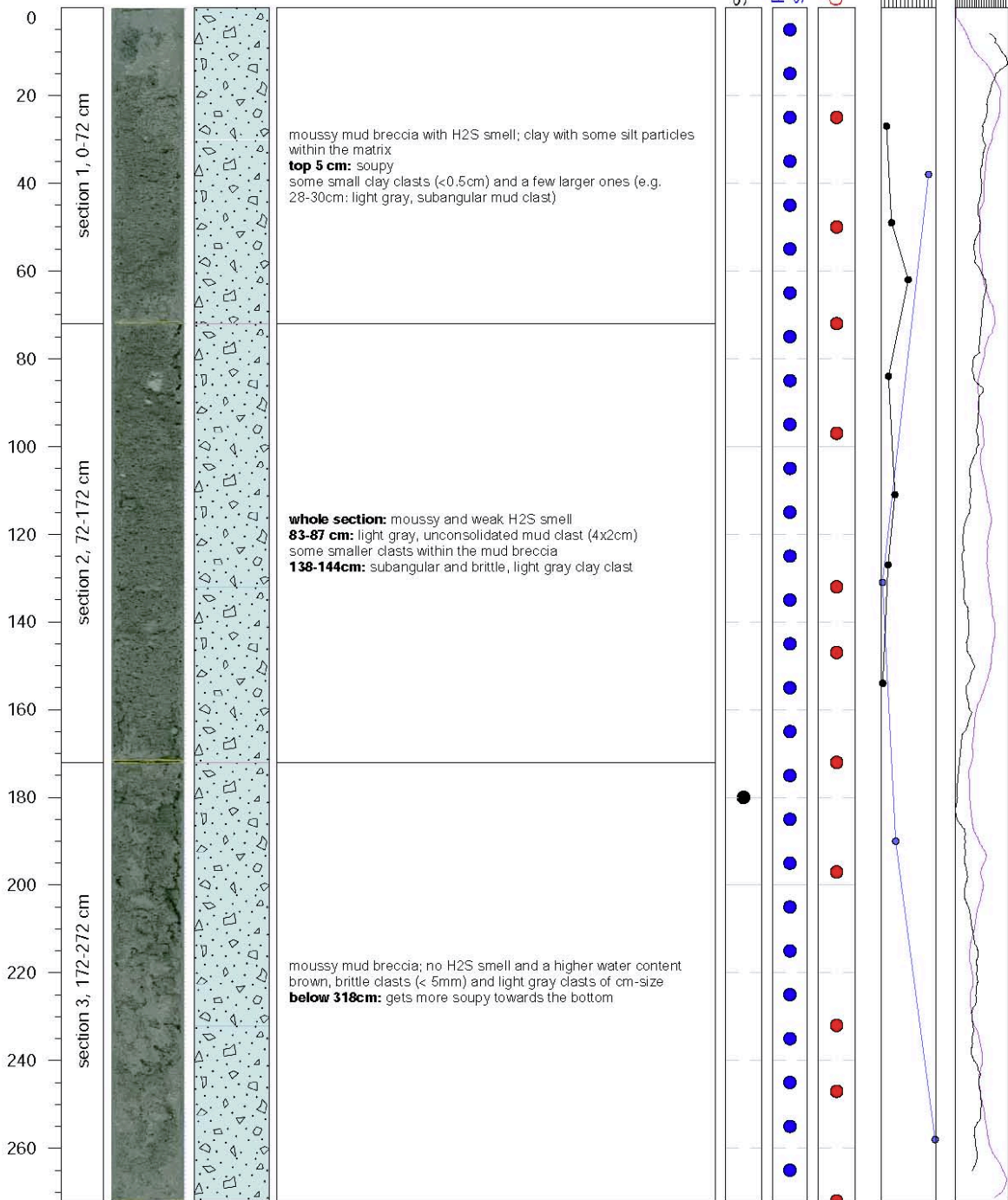
Water depth: 1709 m



Continuation Strater Profiles and Core Photos



**SO278**  
**GC-25 GeoB24352-01 Heraklion MV**  
 Latitude: 33° 56.195 N Longitude: 24° 06.918 E  
 Length of core: 272 cm Water depth: 1714 m



Comments: lower half too soupy for fall cone measurements

64 84  
 Mag. Su

### Continuation Strater Profiles and Core Photos



SO278

GC-25 GeoB24352-01

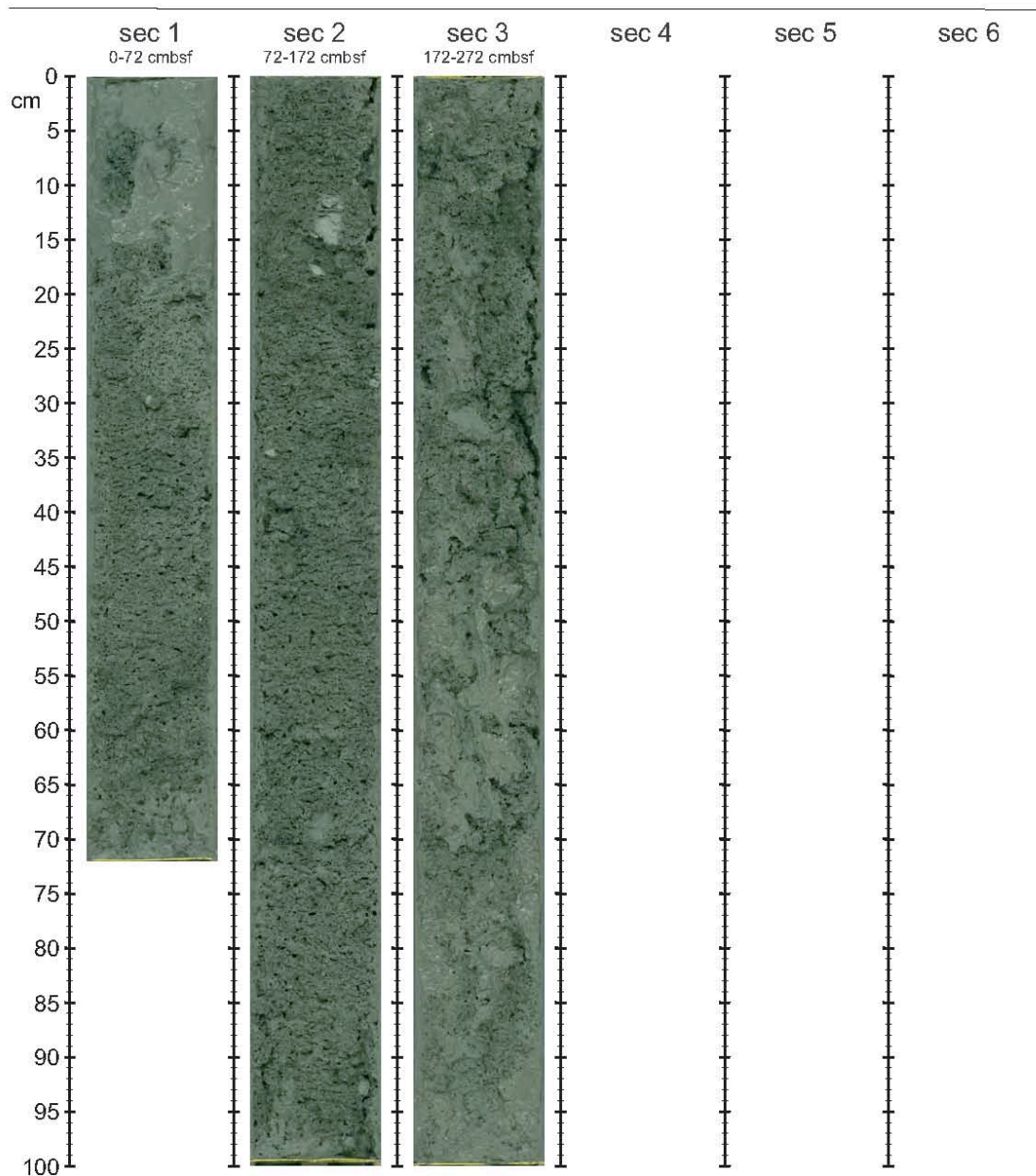
Heraklion MV

Latitude: 33° 56.195 N

Longitude: 24° 06.918 E

Length of core: 272 cm

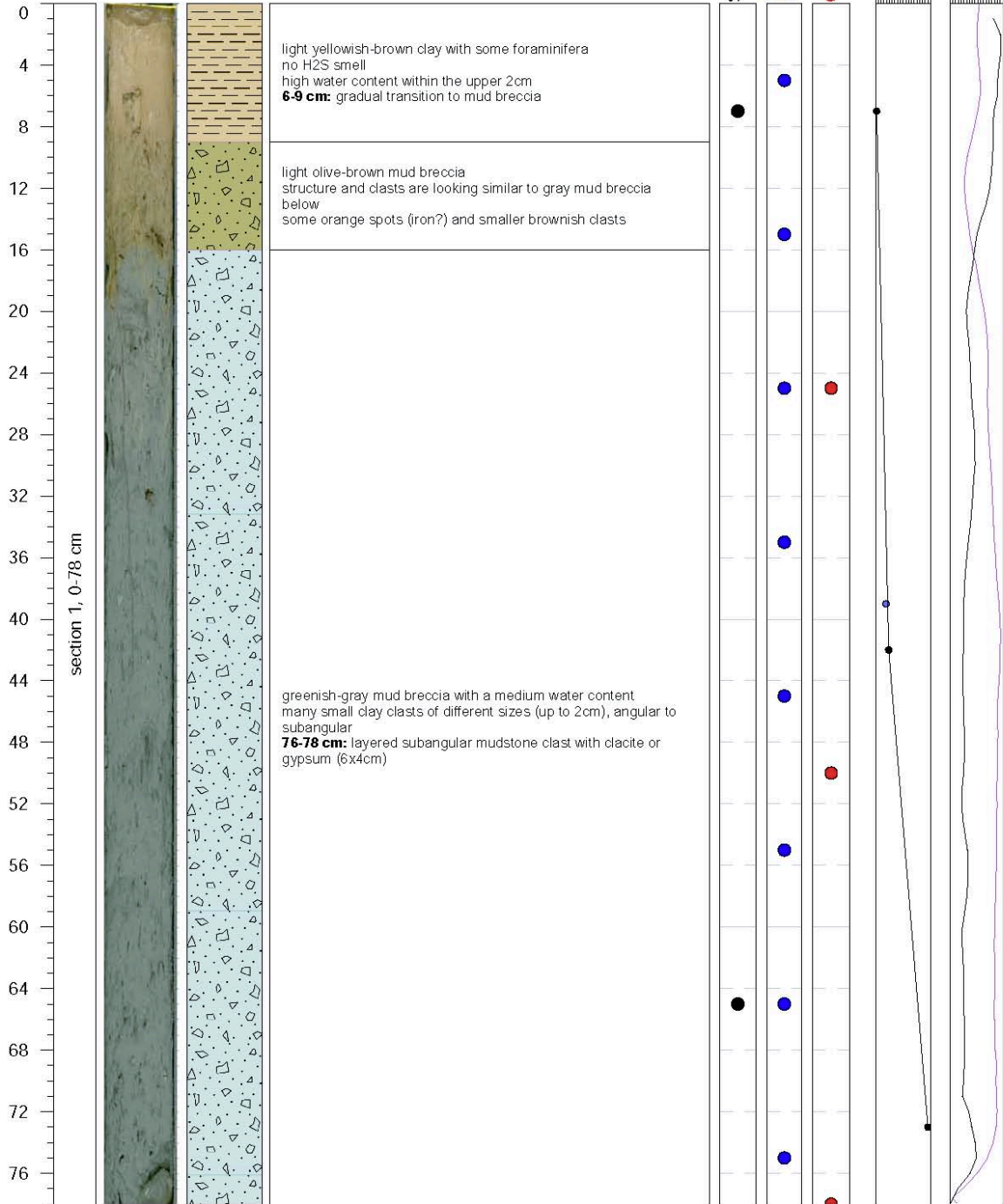
Water depth: 1714 m



Continuation Strater Profiles and Core Photos



**SO278**  
**GC-26 GeoB24355-01 Nice MV**  
 Latitude: 34° 3.0369 N Longitude: 24° 18.1749E  
 Length of core: 78 cm Water depth: 1819 m



Comments: -



### Continuation Strater Profiles and Core Photos



SO278

GC-26 GeoB24355-01

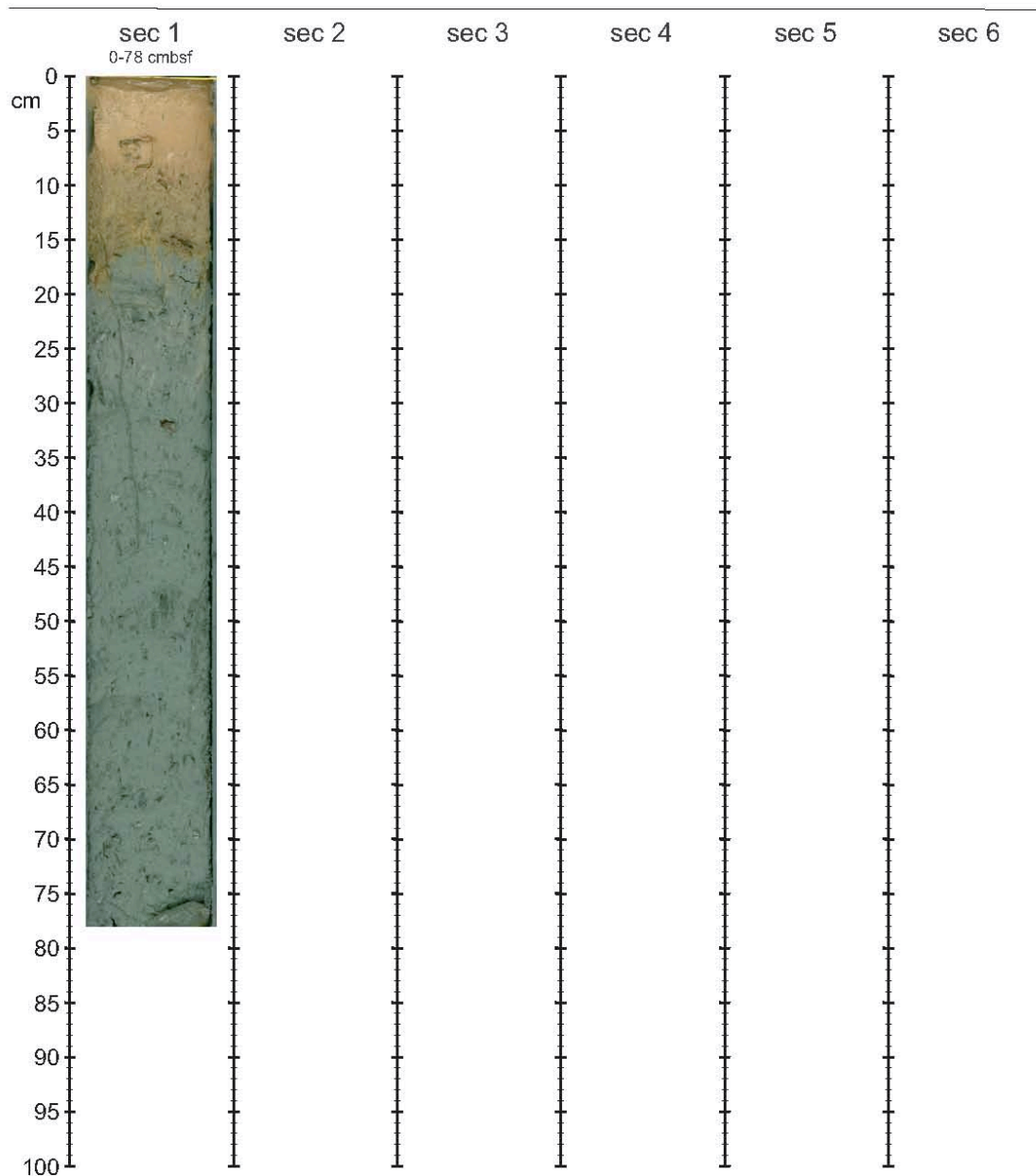
Nice MV

Latitude: 34° 03.0369 N

Longitude: 24° 18.1749 E

Length of core: 78 cm

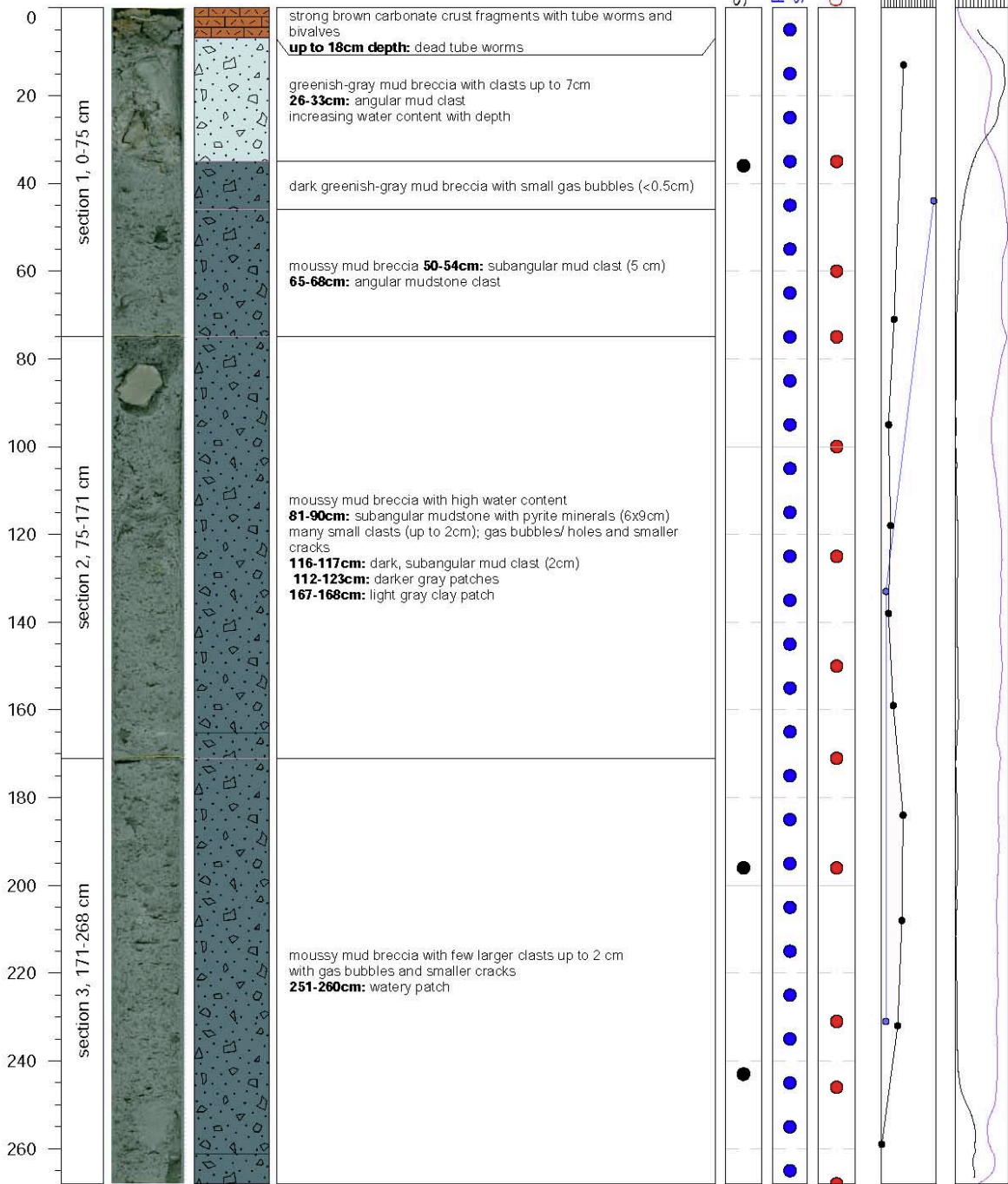
Water depth: 1819 m



Continuation Strater Profiles and Core Photos



**SO278**  
**GC-27 GeoB24356-02 unnamed MV**  
 Latitude: 34° 8.4602 N Longitude: 24° 19.4452 E  
 Length of core: 268 cm Water depth: 1812 m



Comments: -

20 70 120 170  
 Mag. Sus

### Continuation Strater Profiles and Core Photos



SO278

GC-27 GeoB24356-02

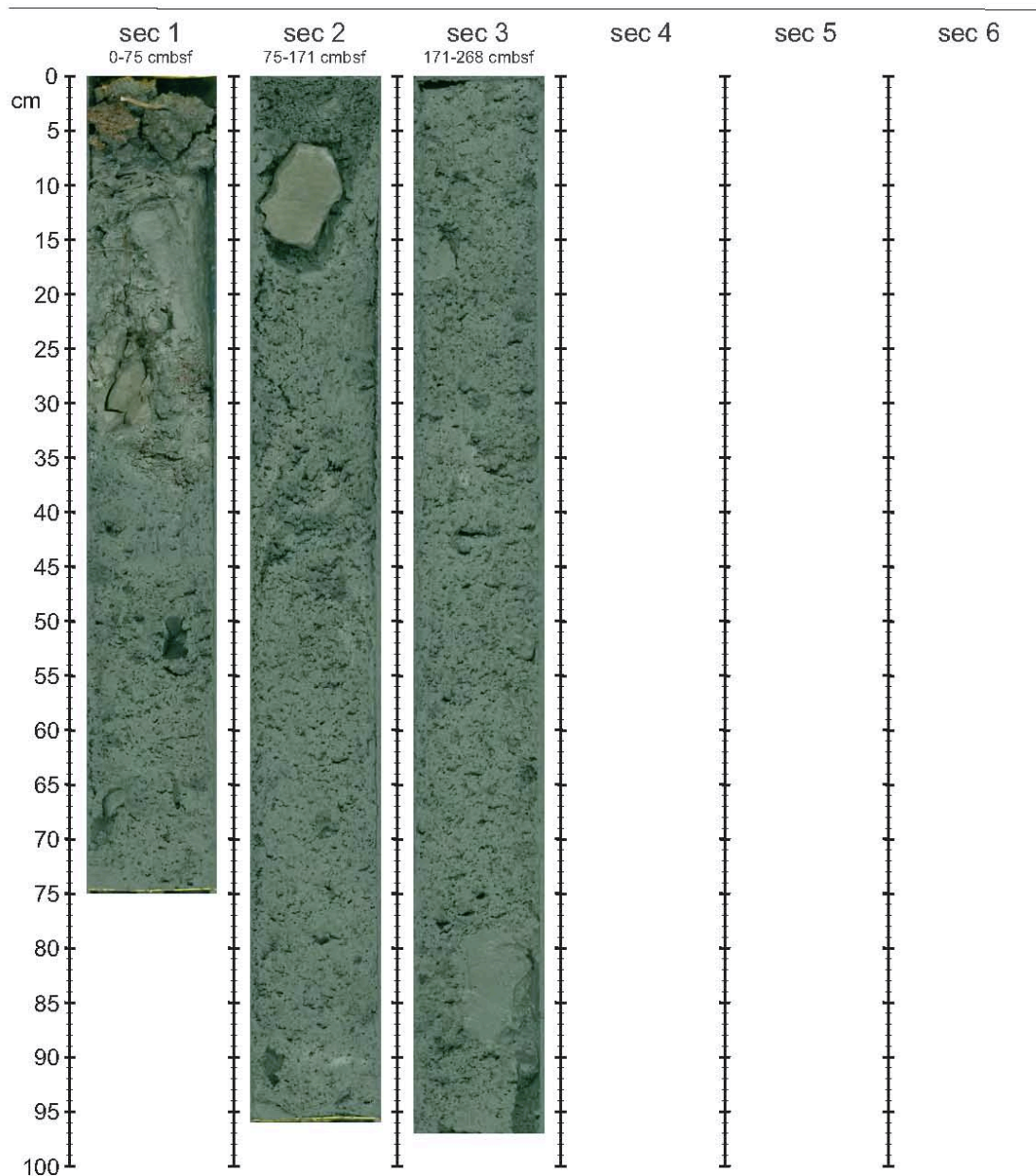
Unnamed MV

Latitude: 34° 08.4602 N

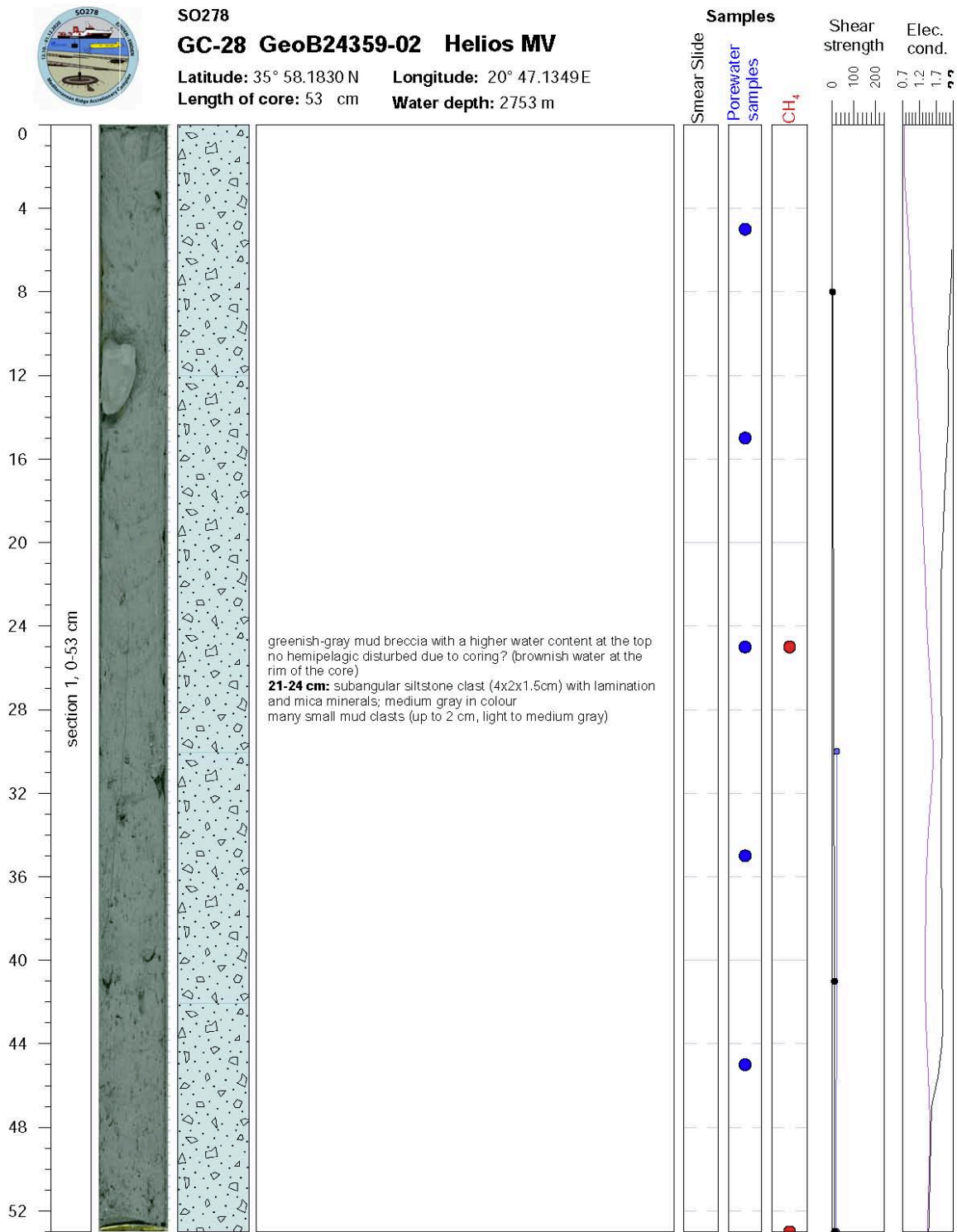
Longitude: 24° 19.4452 E

Length of core: 268 cm

Water depth: 1812 m



Continuation Strater Profiles and Core Photos



Comments: **core catcher:** mud breccia with higher H<sub>2</sub>O content and many smaller mud clasts (<2cm)

80  
130  
180  
230  
Mag. Su:

### Continuation Strater Profiles and Core Photos



SO278

GC-28 GeoB24359-02

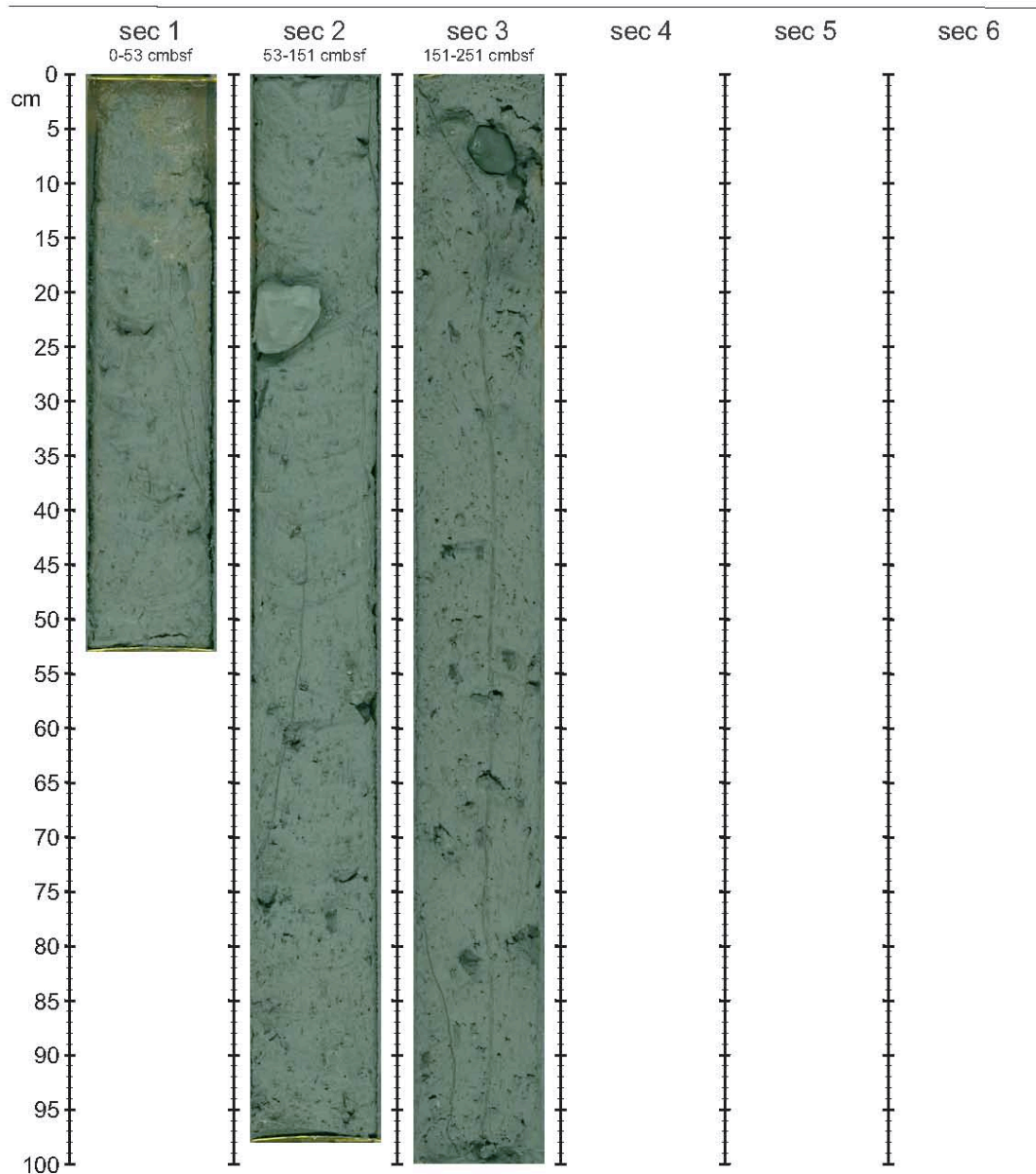
Helios MV

Latitude: 35° 58.1830 N

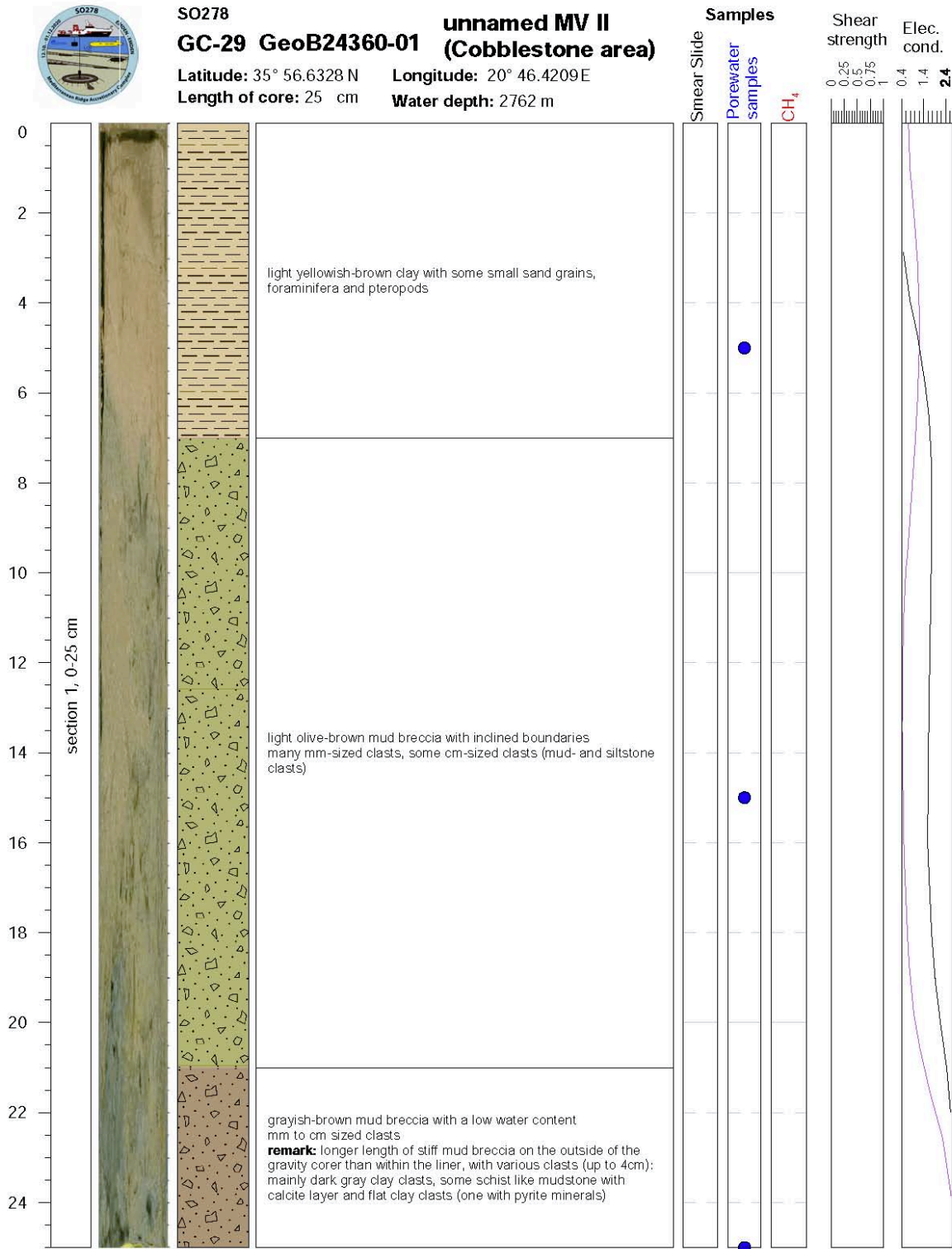
Longitude: 20° 47.1349E

Length of core: 251 cm

Water depth: 2753 m



Continuation Strater Profiles and Core Photos



**Comments:** outside of gravity core covered in stiff mud beccia, with many different clasts: mainly dark gray mud clasts (<4 cm), schist-like mudstones with calcite layers, flat clay clasts (2 mm), of which one contains pyrite.

### Continuation Strater Profiles and Core Photos



SO278

GC-29 GeoB24360-01

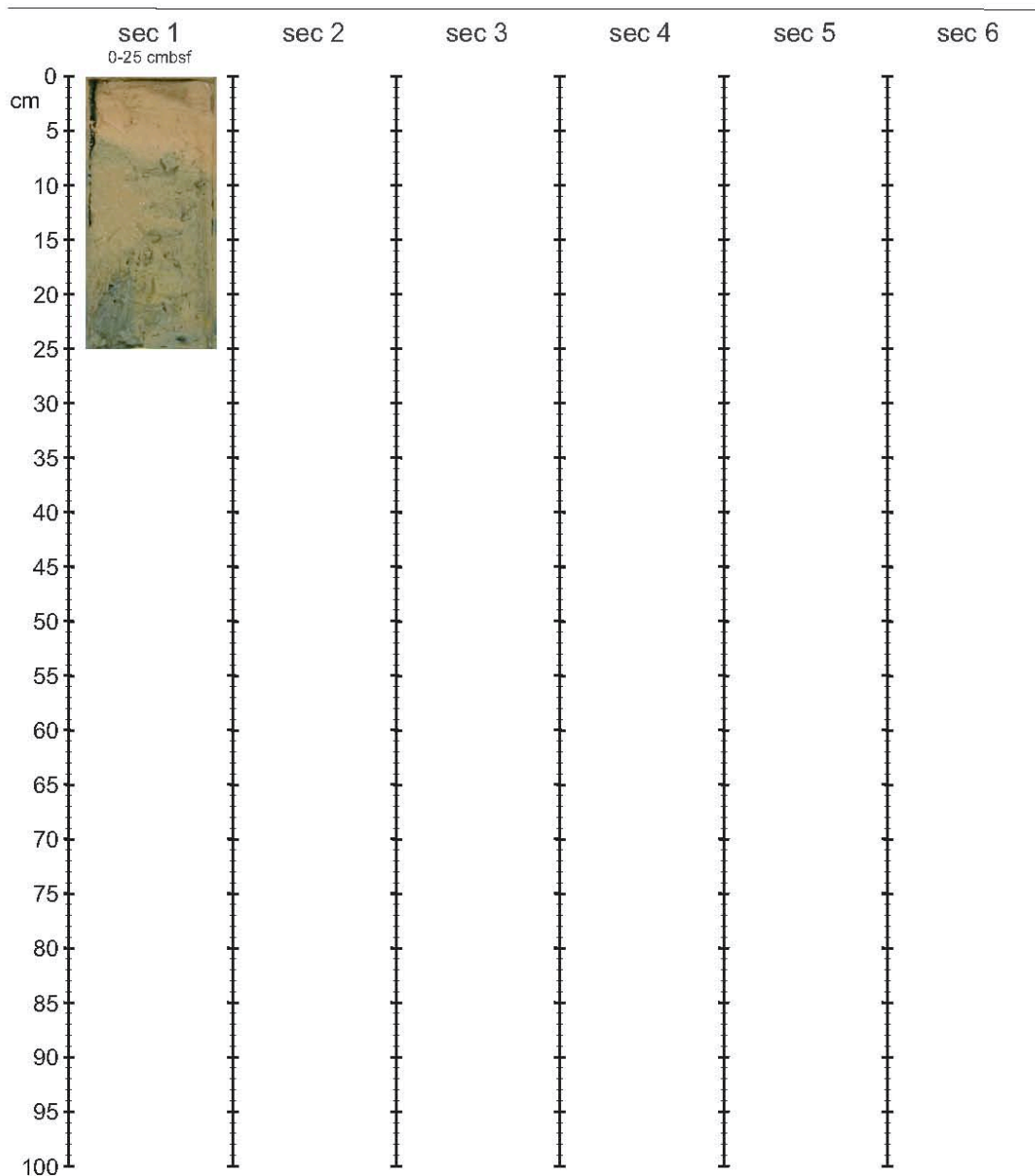
Unnamed MV 2

Latitude: 35° 56.6328 N

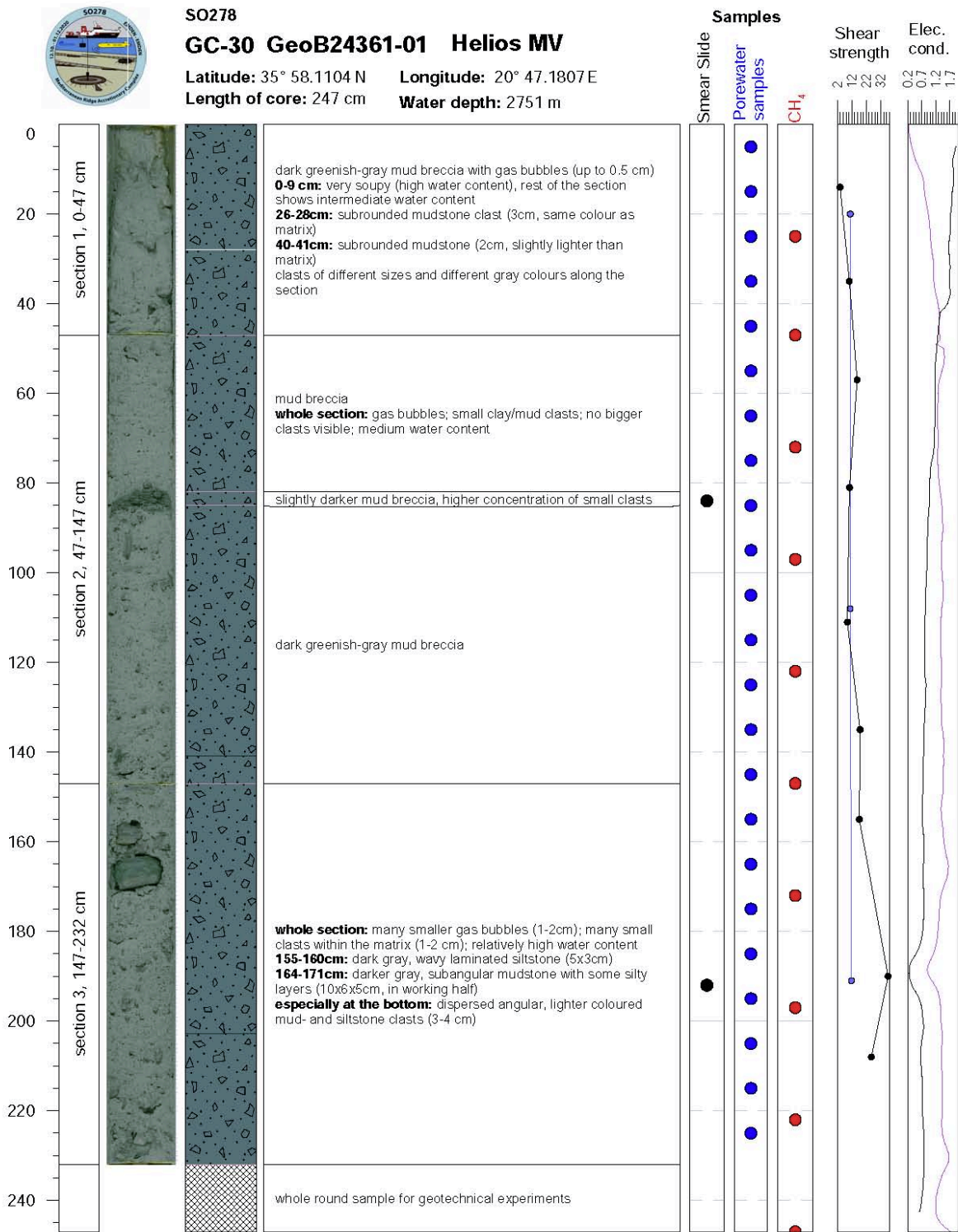
Longitude: 20° 46.4209 E

Length of core: 25 cm

Water depth: 2762 m



Continuation Strater Profiles and Core Photos



Comments: due to gas expansion, section 3 lost end cap: ca. 5 cm was taken out and stored separately;  
**core catcher:** mud breccia with different mud clasts up to 4 cm



### Continuation Strater Profiles and Core Photos



SO278

GC-30 GeoB24361-01

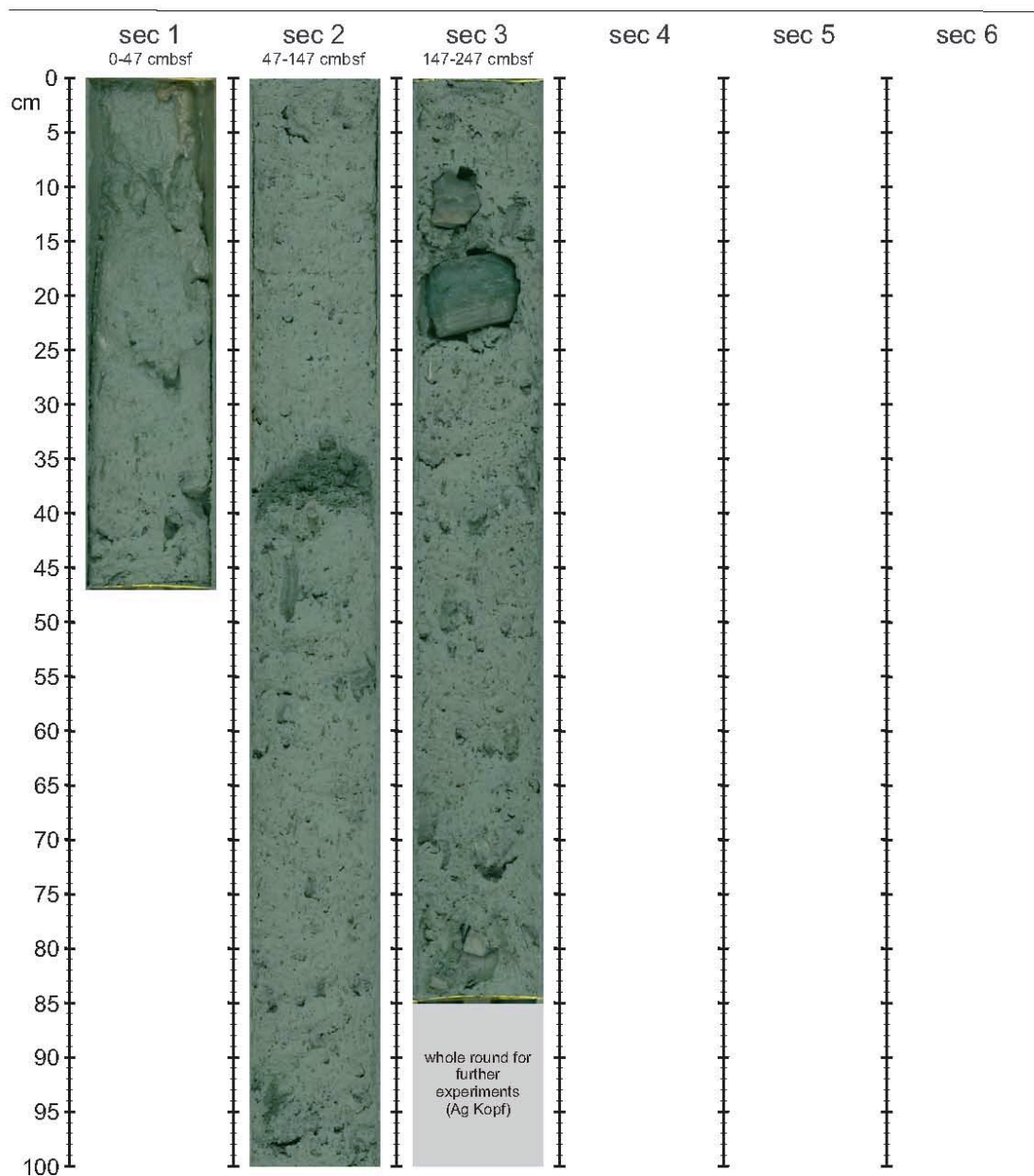
Helios MV

Latitude: 35° 58.1104 N

Longitude: 20° 47.1807 E

Length of core: 519 cm

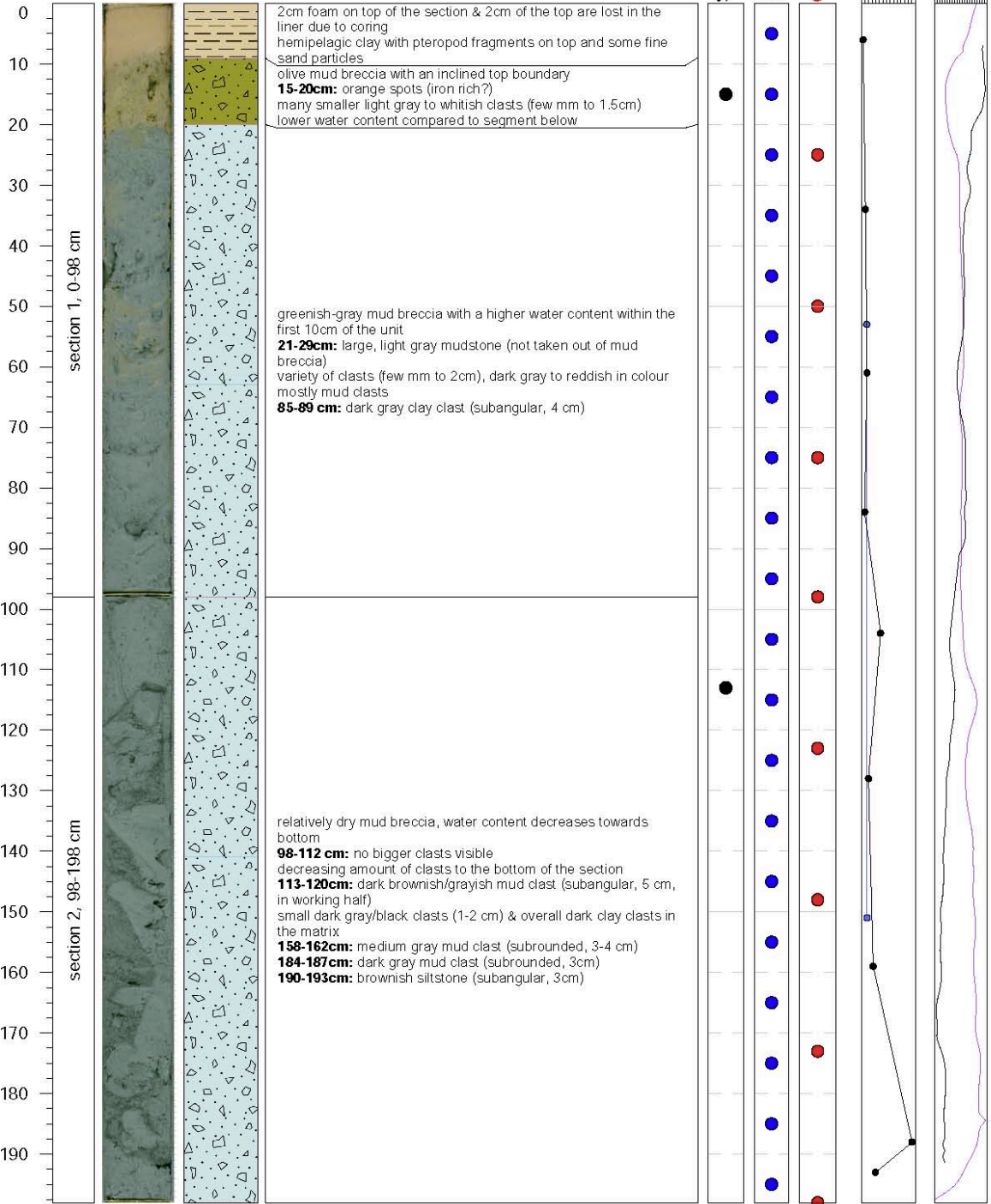
Water depth: 2751 m



Continuation Strater Profiles and Core Photos



**SO278**  
**GC-31 GeoB24364-01 Helios MV**  
 Latitude: 35° 57.7990 N Longitude: 20° 47.5806 E  
 Length of core: 198 cm Water depth: 2867 m



Comments: **core catcher:** highly compacted mud breccia, with mudstone and brown mud clasts up to 3 cm

100 150 200 cm  
 Mag. Su

### Continuation Strater Profiles and Core Photos

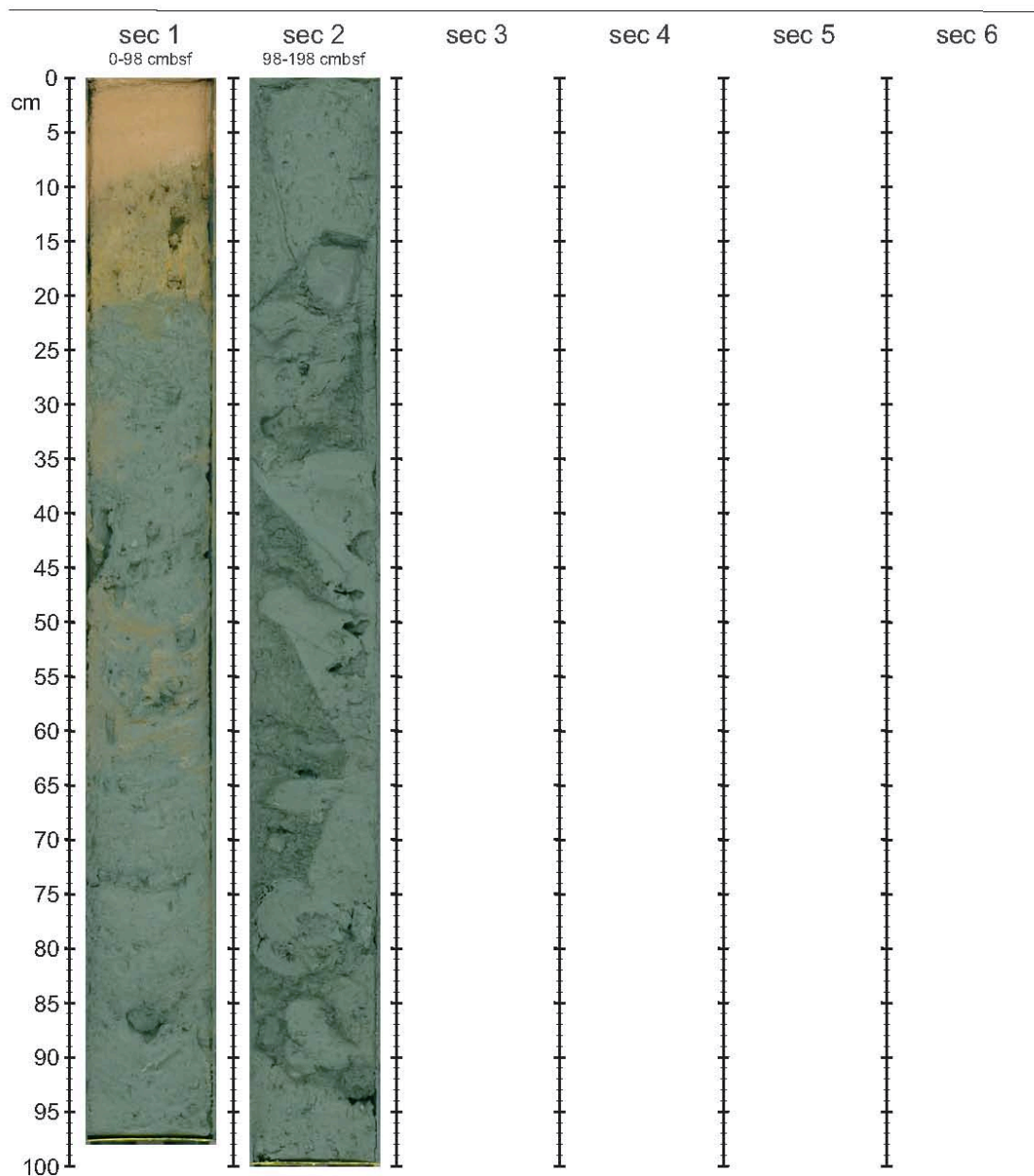


SO278

GC-31 GeoB24364-01 SE flank of Helios MV

Latitude: 35° 57.7990 N Longitude: 20° 47.5806 E

Length of core: 198 cm Water depth: 2867 m



Continuation Strater Profiles and Core Photos

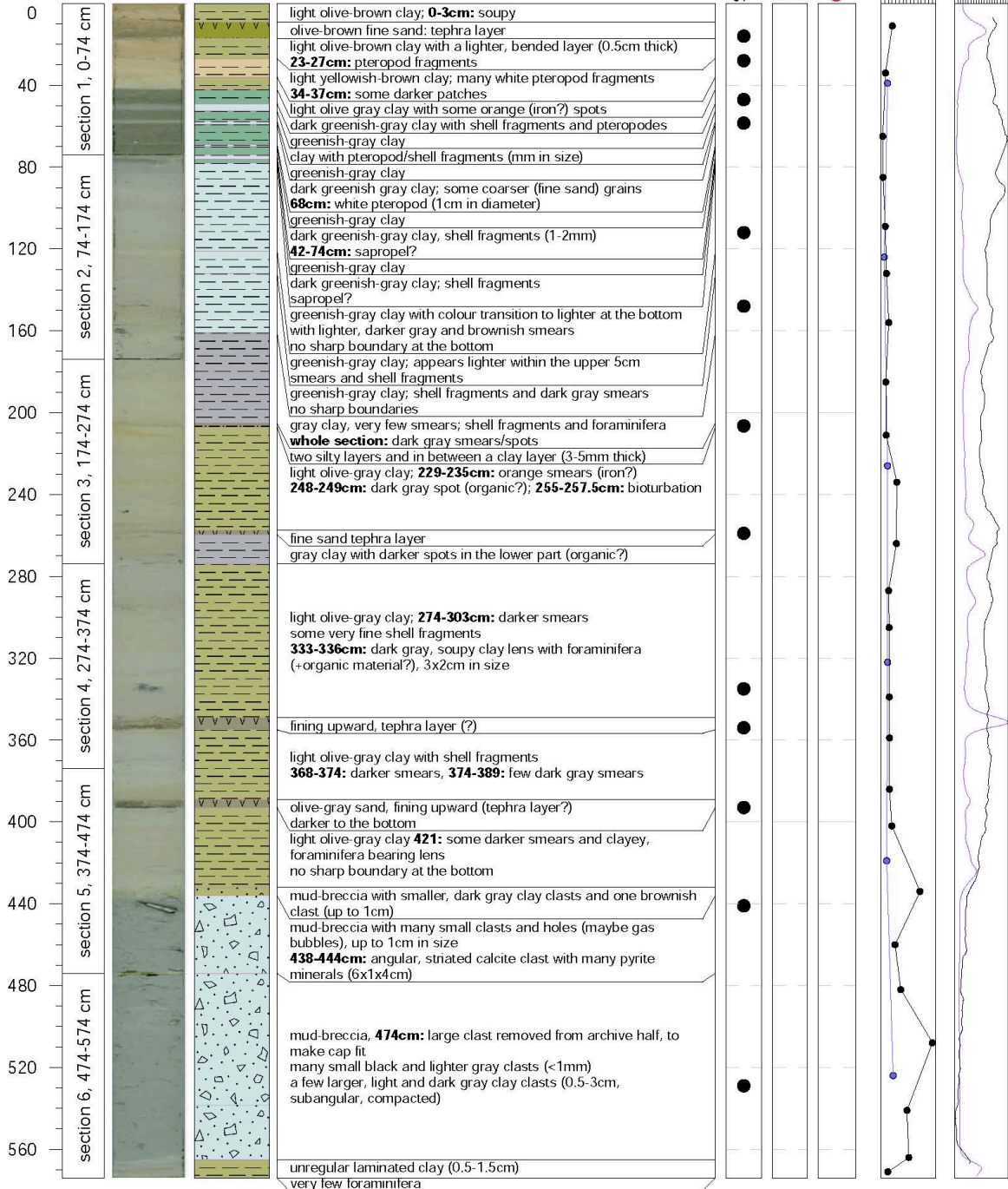


SO278

GC-32 GeoB24366-01 South of Sartori MV

Latitude: 38° 10.9078 N Longitude: 17° 36.8892 E  
 Length of core: 574 cm Water depth: 1967 m

Samples



Comments: core catcher: -6 cm material preserved undisturbed in liner



Mag. Sus

### Continuation Strater Profiles and Core Photos

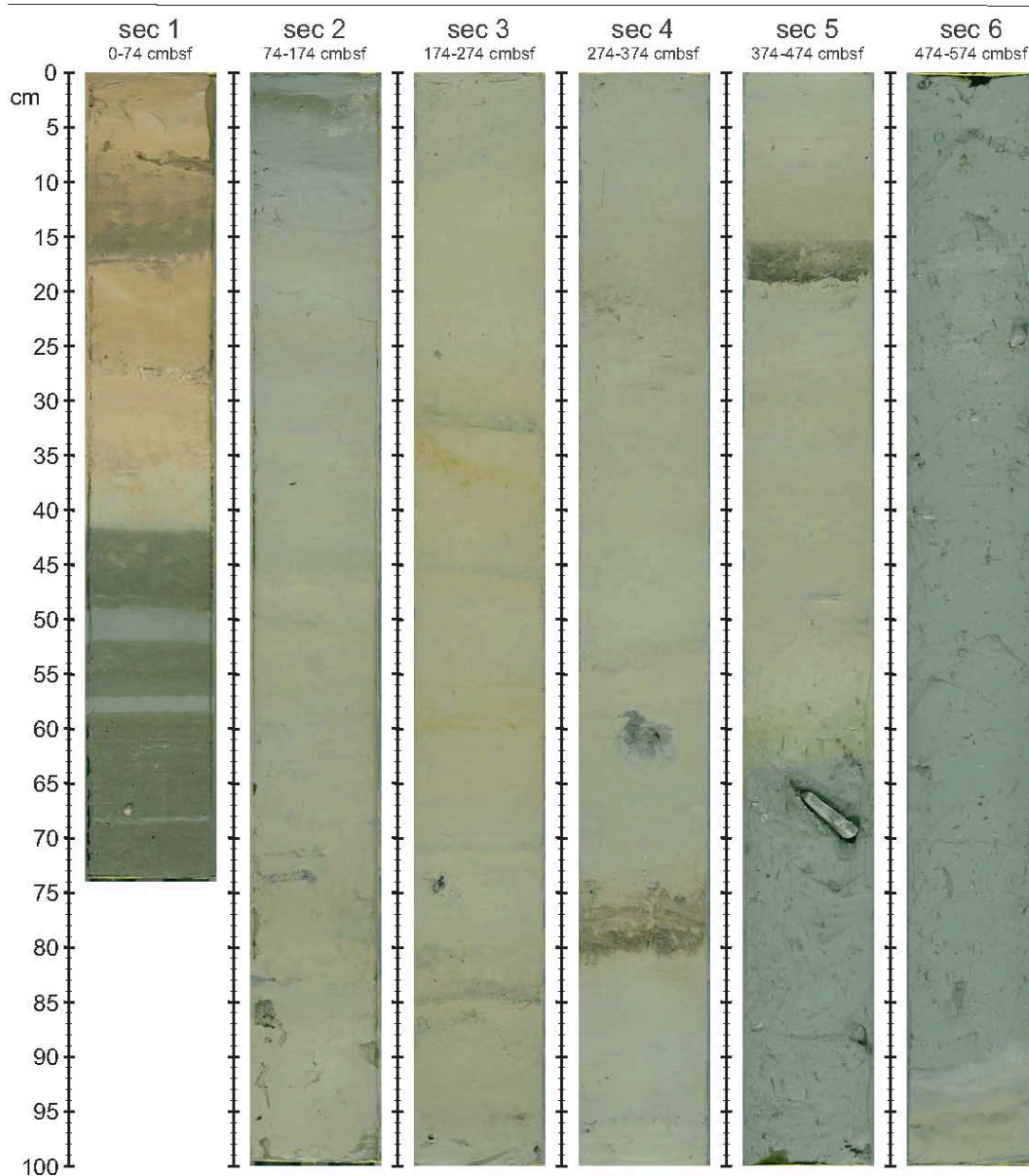


SO278

GC-32 GeoB24366-01 South of Sartori MV

Latitude: 38° 10.9078 N Longitude: 17° 36.8892 E

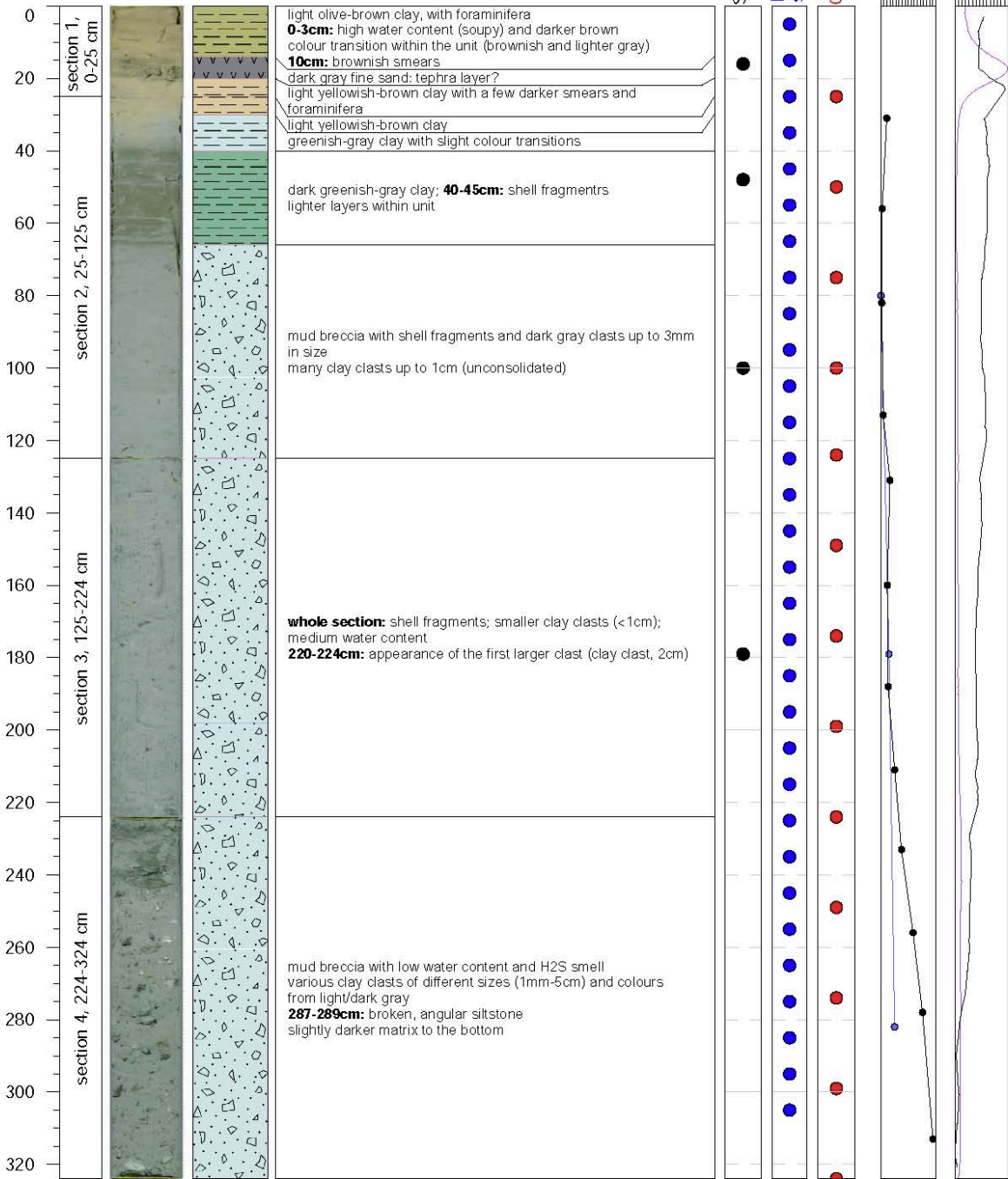
Length of core: 574 cm Water depth: 1967 m



Continuation Strater Profiles and Core Photos



SO278  
**GC-33 GeoB24370-01 Mud flow rim Sartori MV**  
 Latitude: 38° 12.3616 N Longitude: 17° 36.7491 E  
 Length of core: 324 cm Water depth: 1887 m



Comments: -

40  
 2.40  
 4.40  
 Mag. Sus

### Continuation Strater Profiles and Core Photos

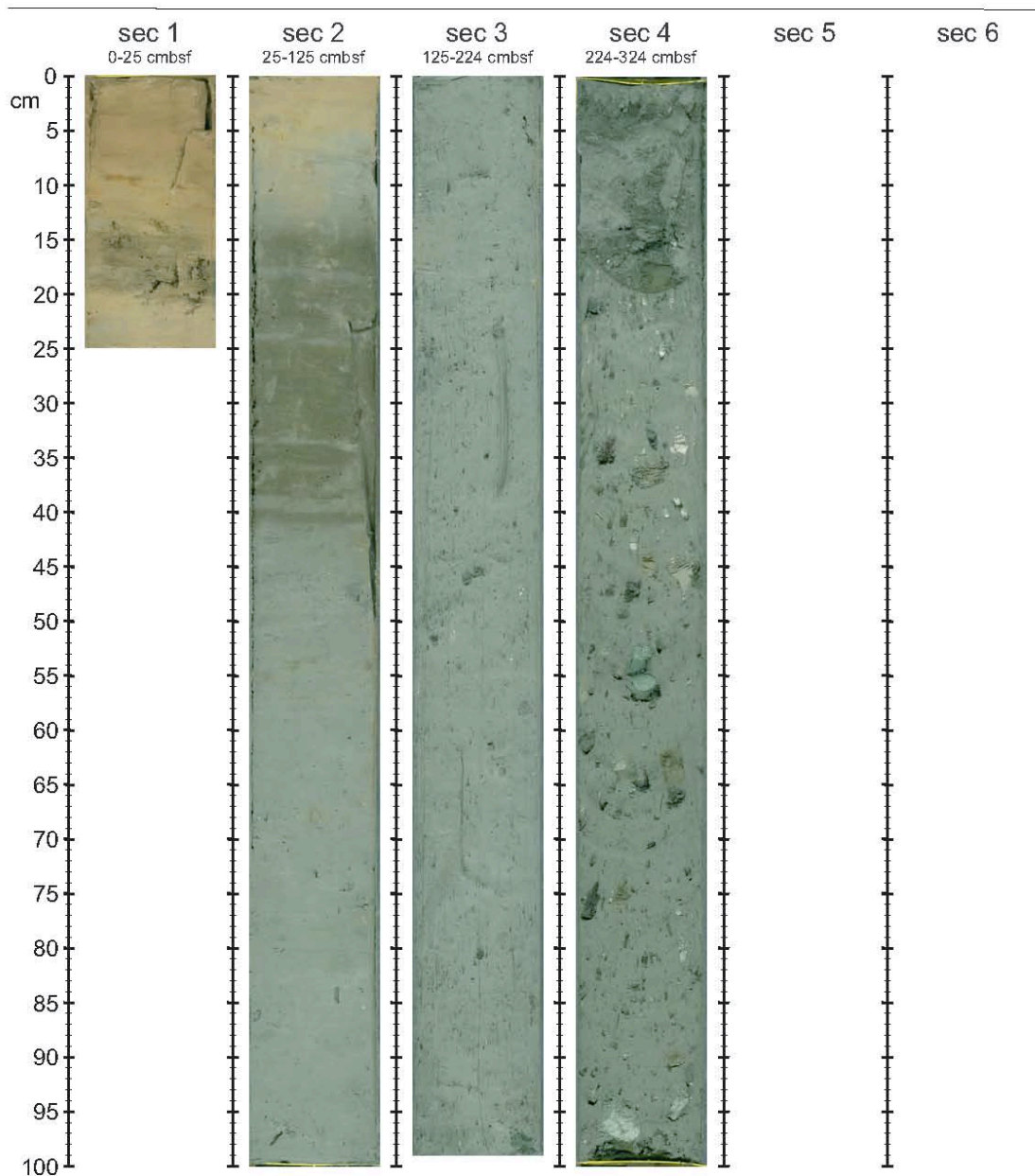


SO278

GC-33 GeoB24370-01 Mud flow rim Sartori

Latitude: 38° 12.3616 N Longitude: 17° 36.7491 E

Length of core: 324 cm Water depth: 1887 m



Continuation Strater Profiles and Core Photos



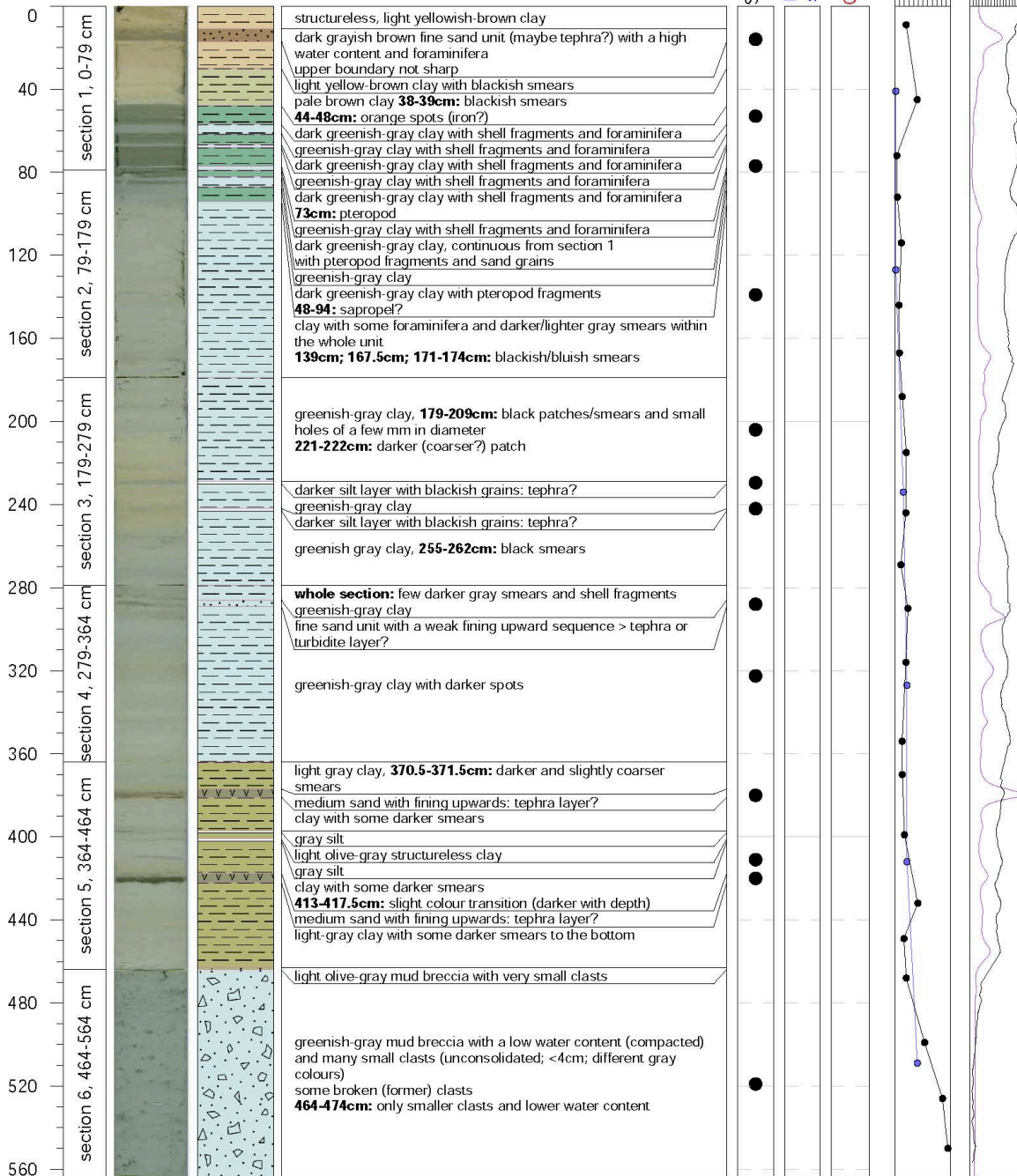
SO278

GC-35 GeoB24373-01 SW of Sartori MV

Latitude: 38° 11.3728 N Longitude: 17° 35.6644 E

Length of core: 564 cm Water depth: 1981 m

Samples



Comments: core catcher: 23 cm mud breccia, preserved undisturbed in liner



Mag. Sus

### Continuation Strater Profiles and Core Photos



SO278

GC-35 GeoB24373-01

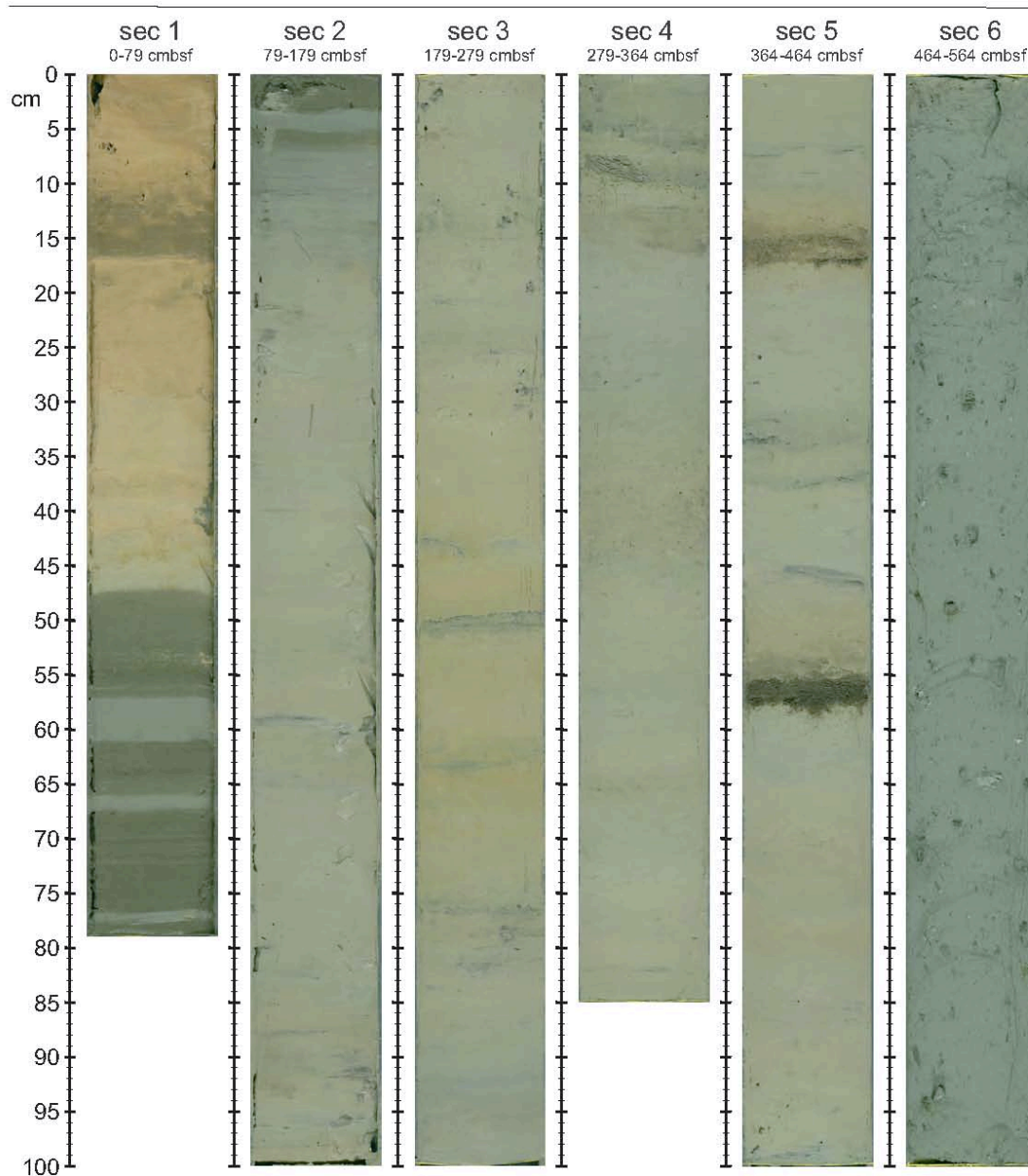
SW of Sartori MV

Latitude: 38° 11.3728 N

Longitude: 17° 35.6644 E

Length of core: 564 cm

Water depth: 1981 m



Continuation Strater Profiles and Core Photos

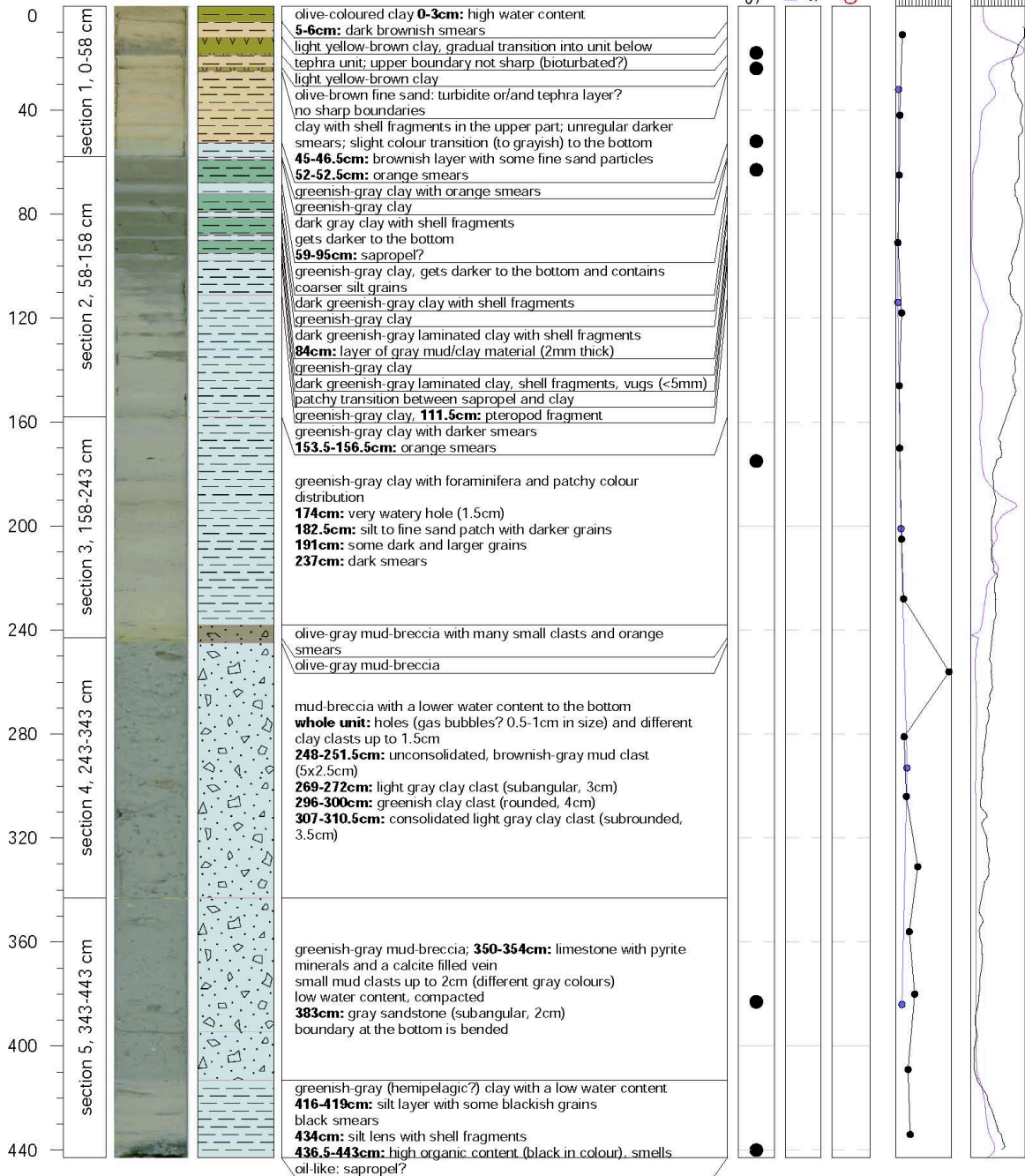


SO278

GC-36 GeoB24374-01 SW of Sartori MV

Latitude: 38° 11.6180 N Longitude: 17° 36.1995 E

Length of core: 443 cm Water depth: 1977 m



Comments: core catcher: 18 cm mud breccia, preserved undisturbed in liner

40  
240  
440  
640  
Mag. Sus

### Continuation Strater Profiles and Core Photos



SO278

GC-36 GeoB24374-01

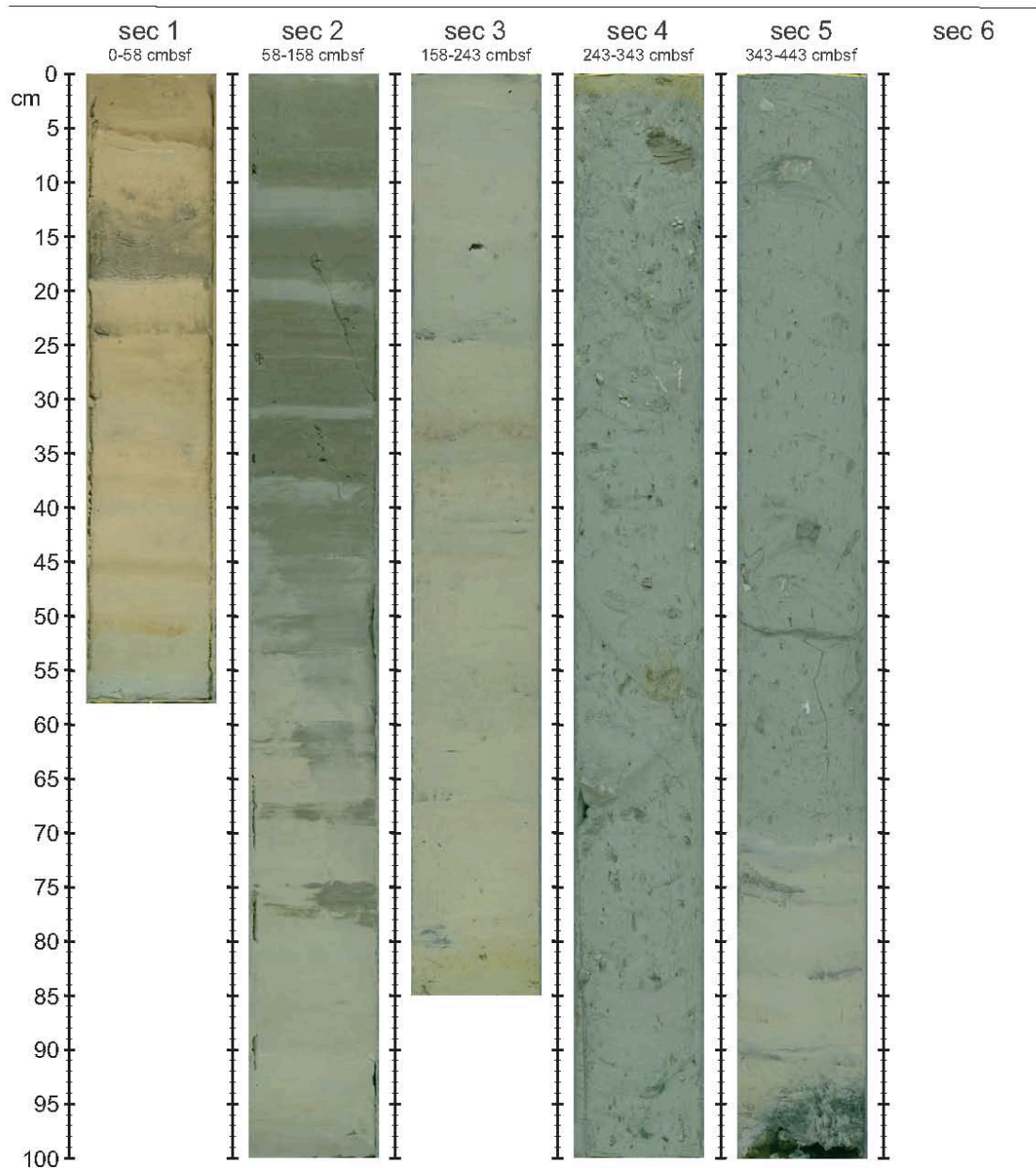
SW of Sartori MV

Latitude: 38° 11.6180 N

Longitude: 17° 36.1995 E

Length of core: 443 cm

Water depth: 1977 m



Continuation Strater Profiles and Core Photos

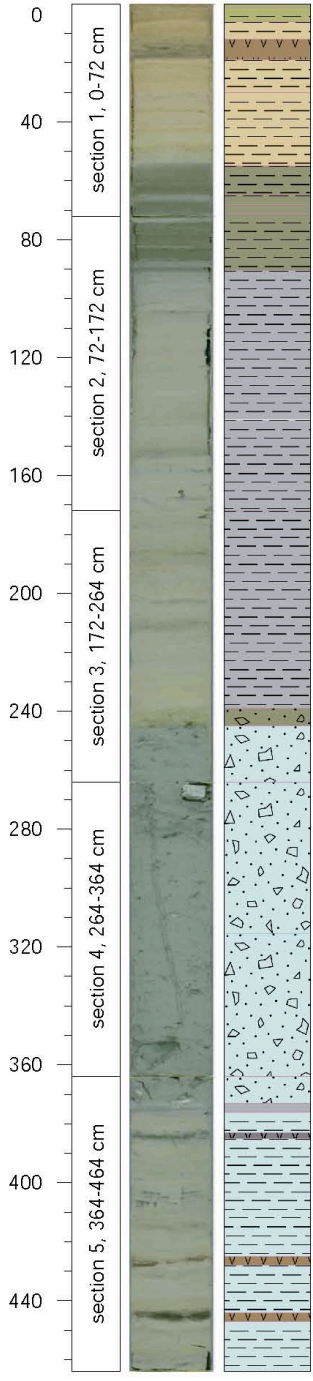
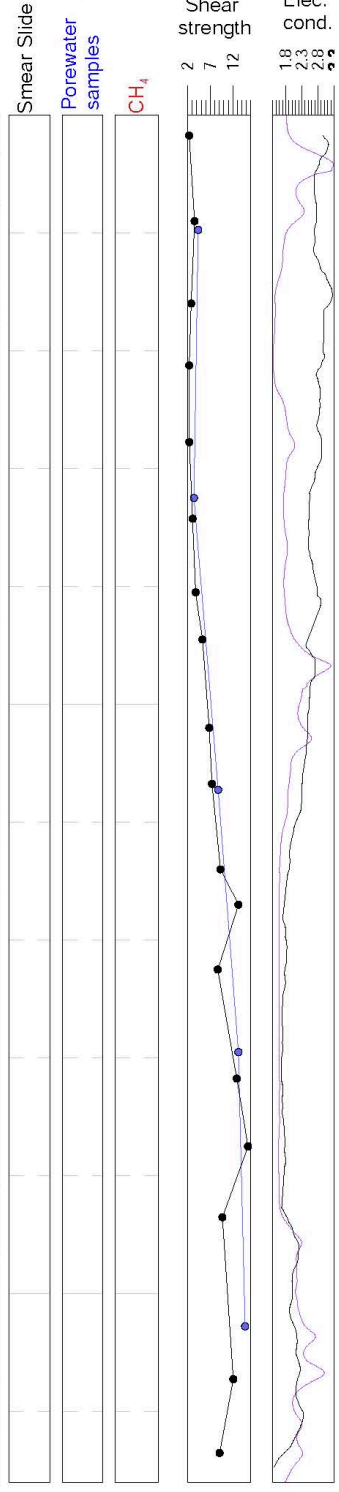


SO278

GC-37 GeoB24375-01 SW of Sartori MV

Latitude: 38° 12.3388 N Longitude: 17° 35.5201 E  
 Length of core: 464 cm Water depth: 1976 m

Samples



**whole section:** higher water content; darker gray smears/spots  
 light olive-brown clay  
 light olive-brown clay  
 light olive-brown clay, lower boundary not sharp  
 fine sand tephra layer  
 light yellowish-brown clay with shell fragments and blackish smears  
 light yellowish-brown clay  
**35.5-38.5cm & 43-45cm:** layers similar to the layer above  
**40cm:** watery patch **48-50cm:** orange smears  
 olive-gray clay with many shell fragments and weak lamination (grayish, blackish and greenish)  
 sapropel?  
 olive-gray clay  
 olive-gray clay with shell fragments and a weak lamination  
 sapropel?  
 sequence of darker and lighter olive-gray clay  
**77.5cm:** 2mm thin clay layer  
**85.5cm:** thin light gray layer (about 2mm)  
**85-90.5cm:** sapropel?  
 grey clay with lighter and darker layers and dark gray smears  
**147-151cm:** orange smears  
**165-167cm:** vug lined with gray mud and high water content

gray clay, continuous from section 2  
 water content decreases to the bottom  
**200.5-204.5cm:** black smears

mud-breccia with very small sand clasts (<0.5cm) and slight colour transition  
 no sharp boundaries visible  
 mud-breccia with light gray mud clasts (<0.5cm); low water content

greenish-gray mud-breccia, clay clasts up to 3cm  
**264-270cm:** light gray, angular silt clast with gypsum crust (4x4cm)  
**353-359cm:** angular, light gray mudstone with calcite crust and pyrite (7cm in diameter)

mud-breccia with mud clasts up to 2cm in size, many mm-sized clasts  
**366cm:** siltstone (4cm in size)  
 clay with inclined boundaries at top and bottom  
 clay with shell fragments  
 weakly laminated (cm-scale; variation in colour)  
 dark gray fine sand: tephra layer?  
 greenish-gray clay  
**403-408.5cm:** 6-8 lenses of very fine sand  
**414-416cm:** patchy silty layer (slightly darker in colour)  
 dark grayish-brown medium sand: tephra layer?  
 greenish-gray clay **432cm:** fine sand lens

very dark grayish-brown fine sand: tephra layer?  
 greenish-gray clay; more brownish/orange towards bottom  
 black smears cutted by the unit above  
**462-463cm:** fine sand lens

Comments: -



### Continuation Strater Profiles and Core Photos



SO278

GC-37 GeoB24375-01

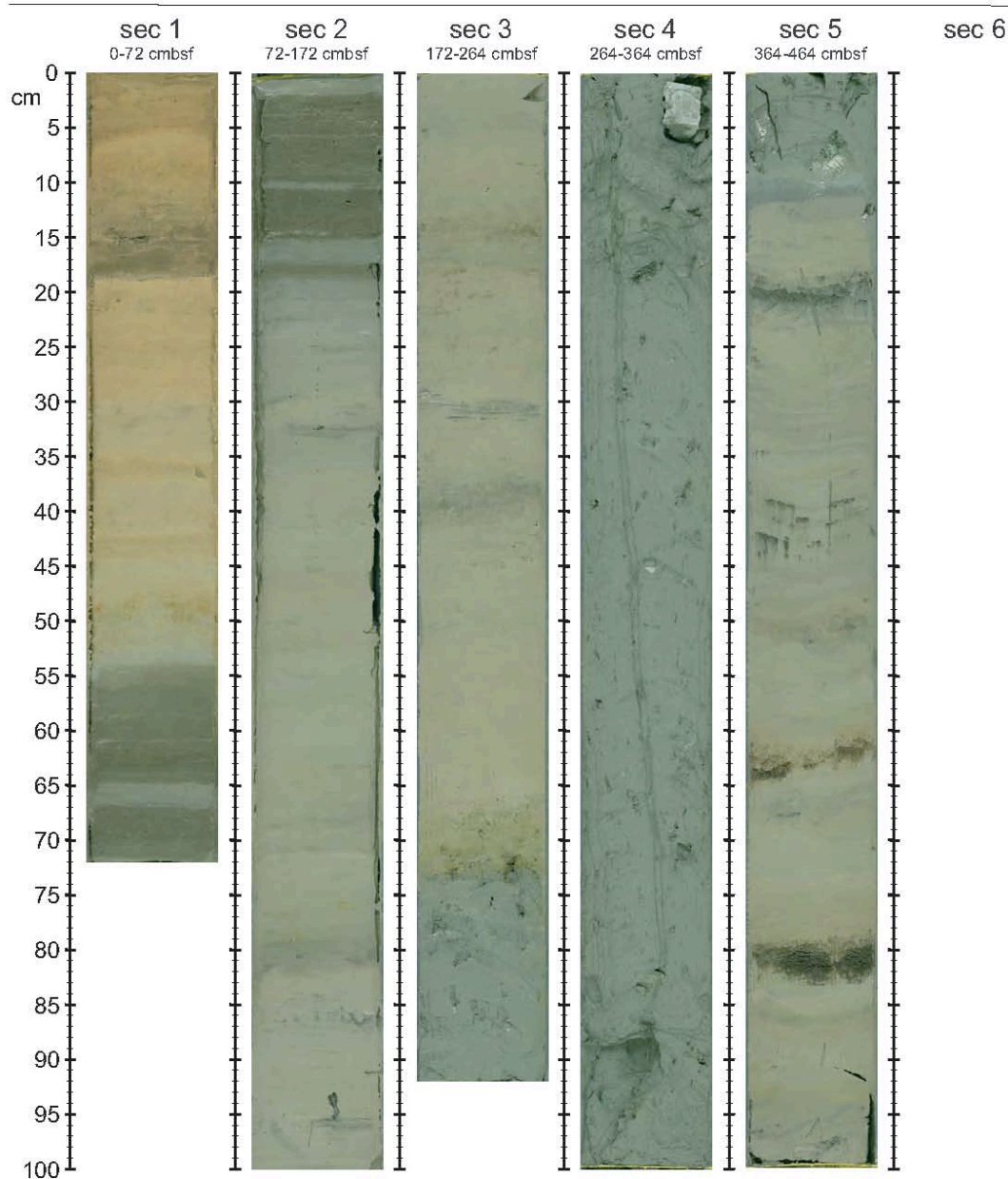
SW of Sartori MV

Latitude: 38° 12.3388 N

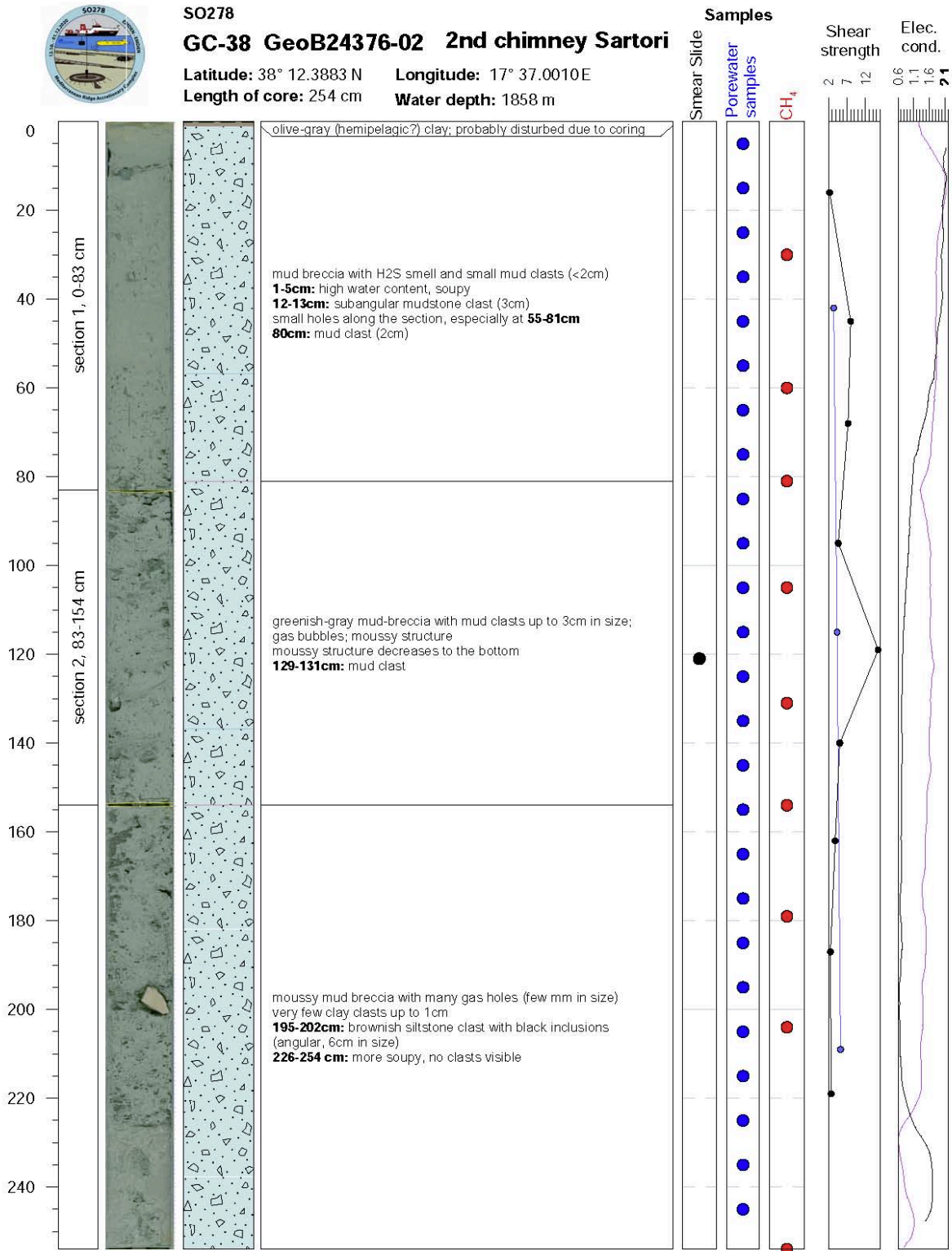
Longitude: 17° 35.5201 E

Length of core: 464 cm

Water depth: 1976 m



Continuation Strater Profiles and Core Photos



Comments: section 2 got shortened by ~27 cm, gas expansion gap (?)

100g  
 Mag. Su:

### Continuation Strater Profiles and Core Photos



SO278

GC-38 GeoB24376-02

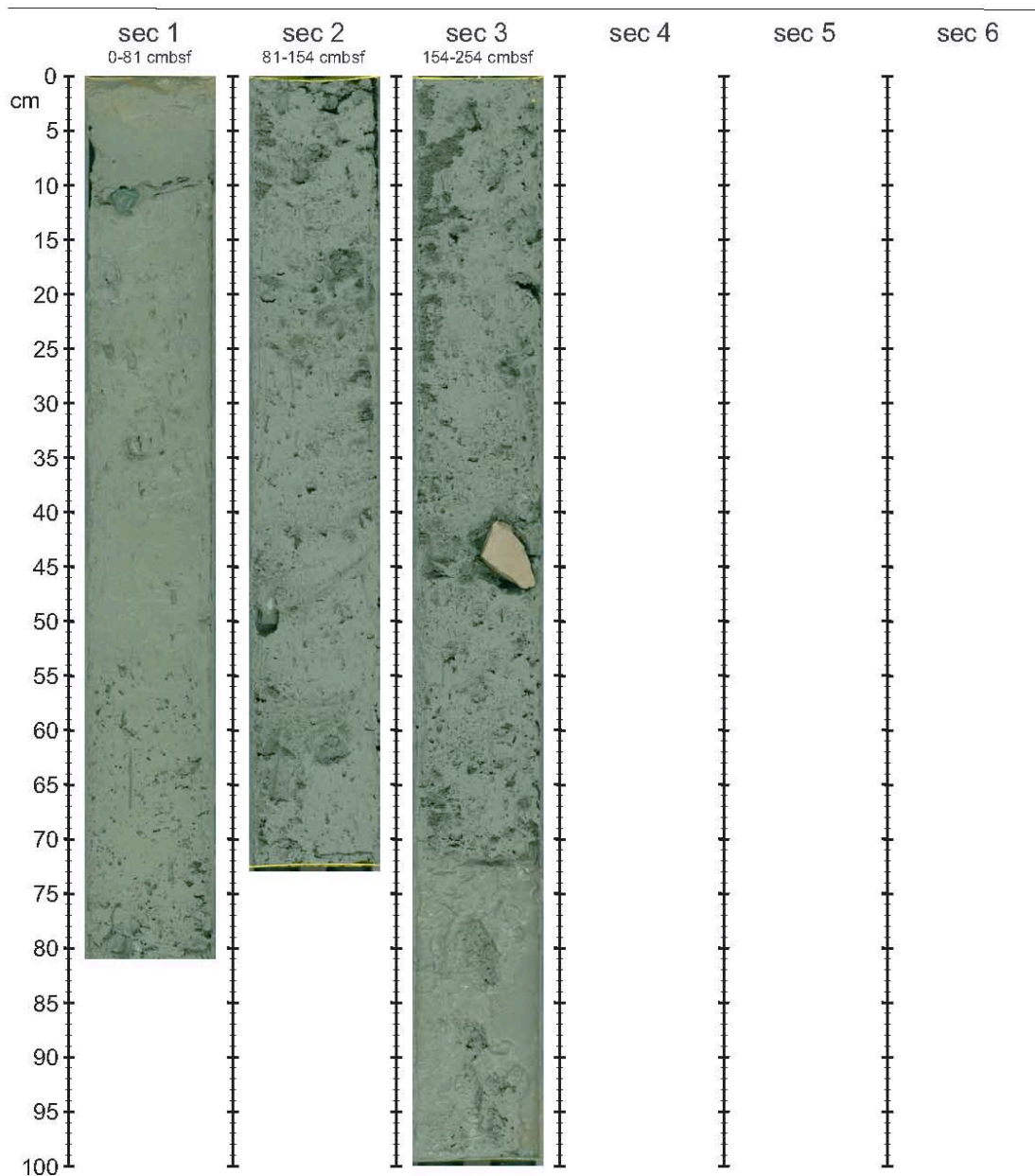
2nd chimney of Sartori

Latitude: 38° 12.3883 N

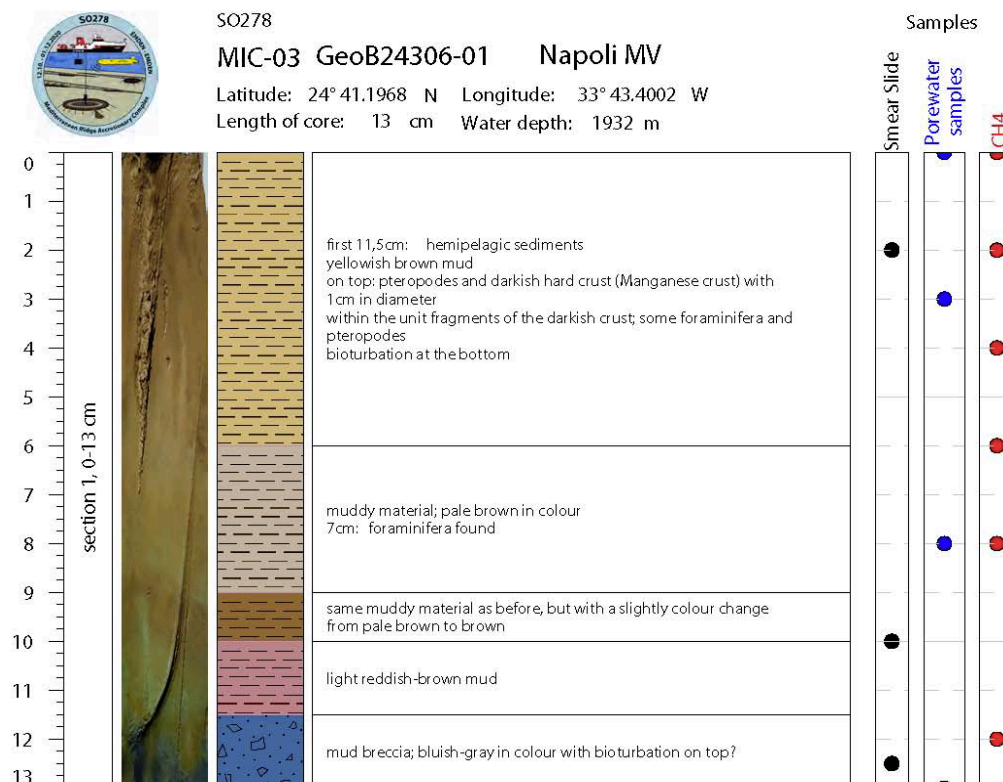
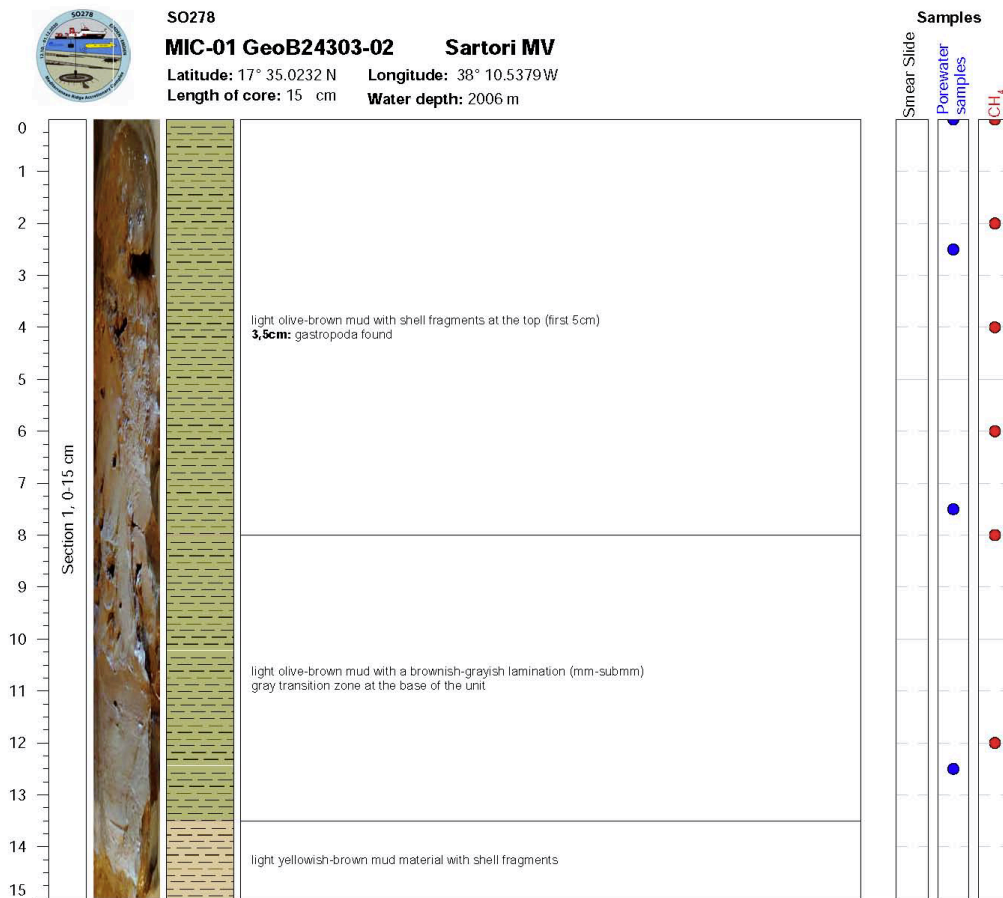
Longitude: 17° 37.0010 E

Length of core: 254 cm

Water depth: 1858 m



## 10.2 Mini Corer/Multi Corer Straters



### Continuation MIC/MUC Straters



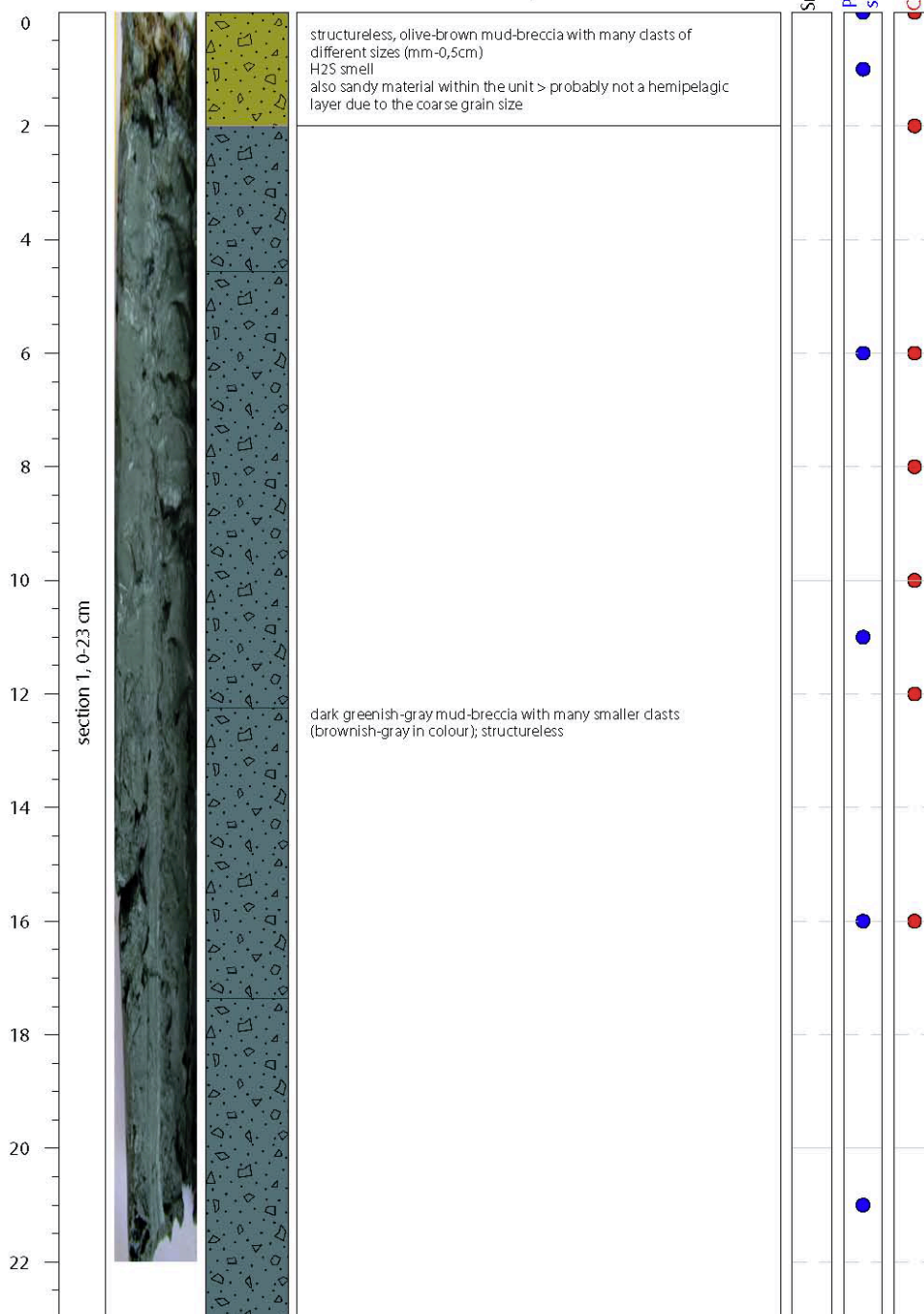
SO278

MIC-04 GeoB24311-02 Bergamo MV

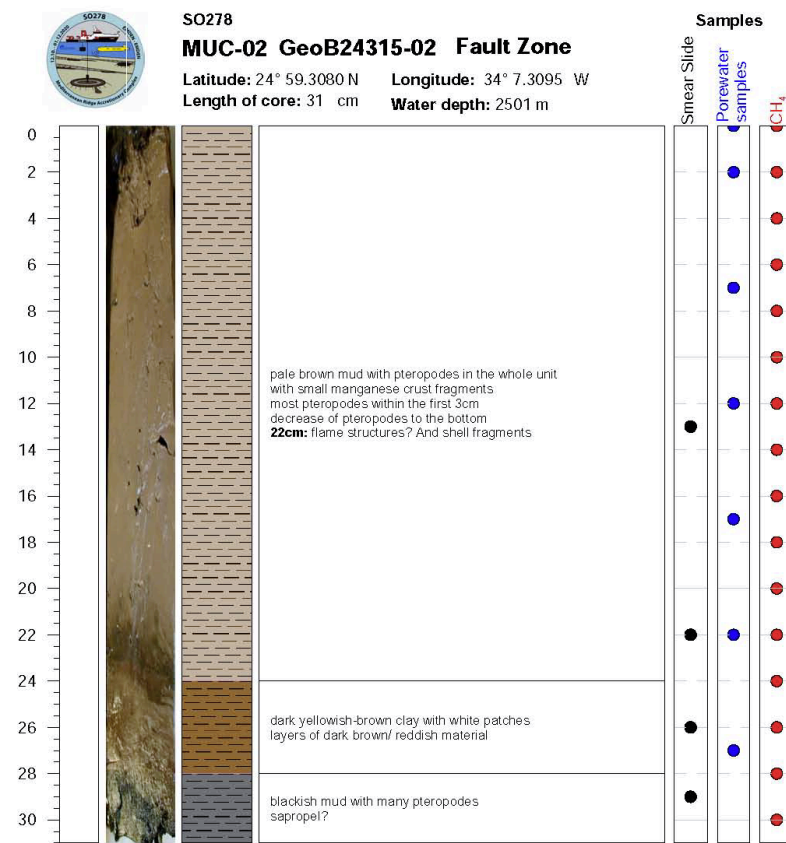
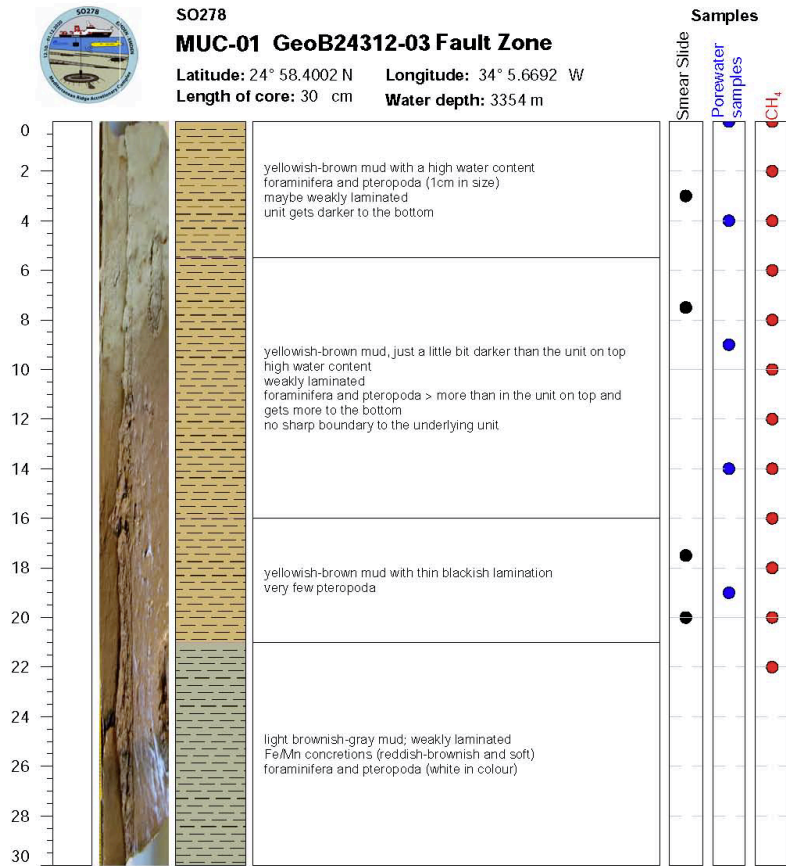
Latitude: 24° 45.0503 N Longitude: 33° 44.3282 W

Length of core: 23 cm Water depth: 1930 m

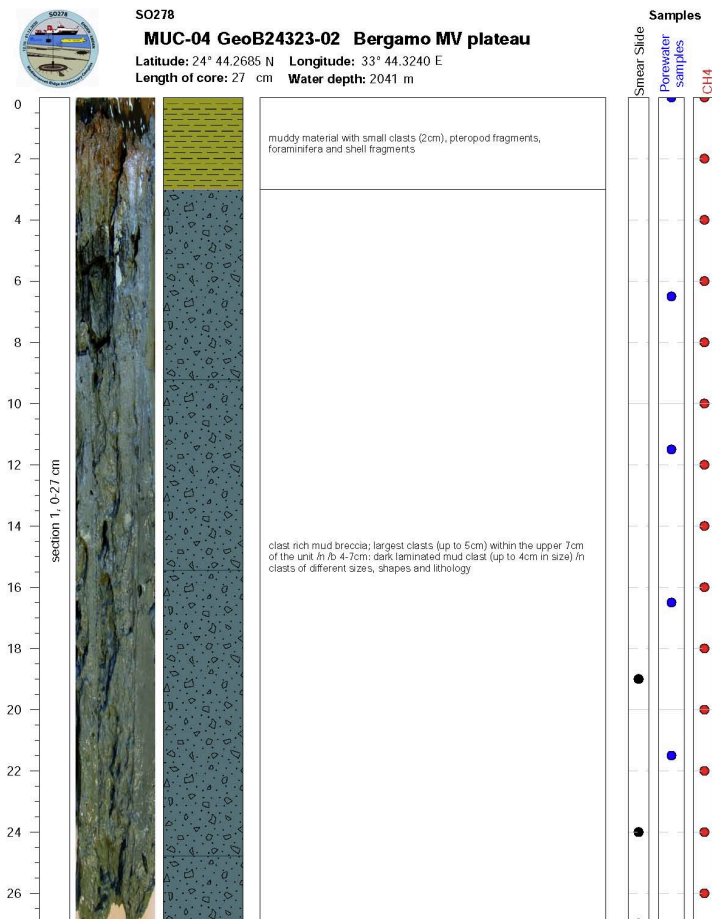
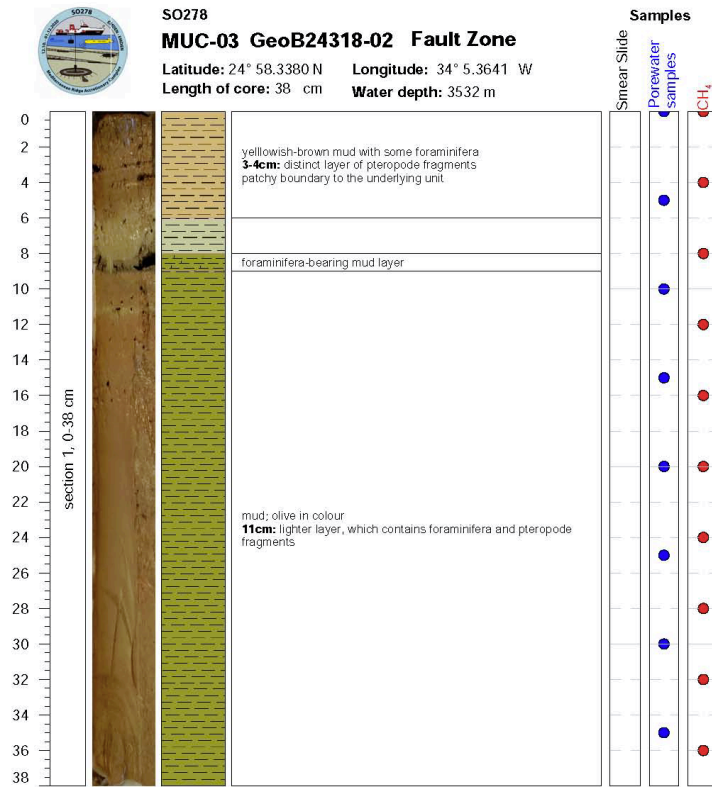
Samples



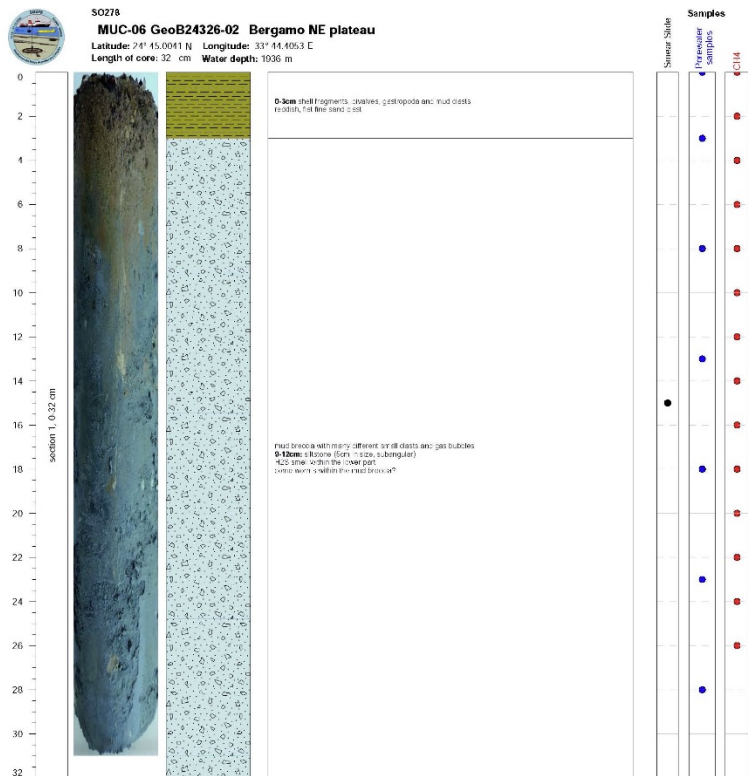
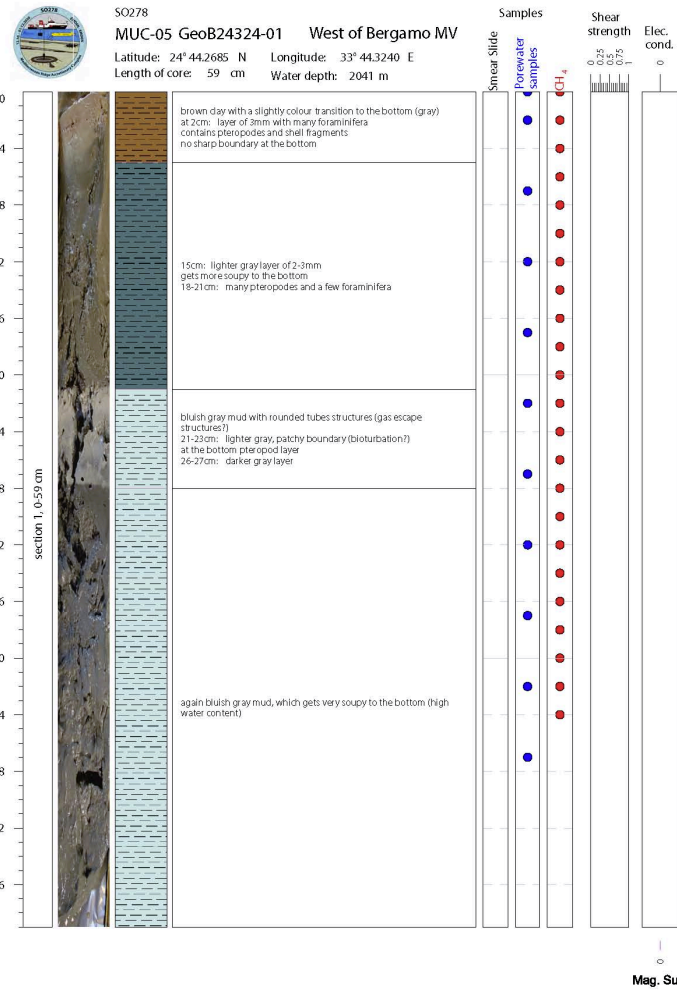
Continuation MIC/MUC Straters



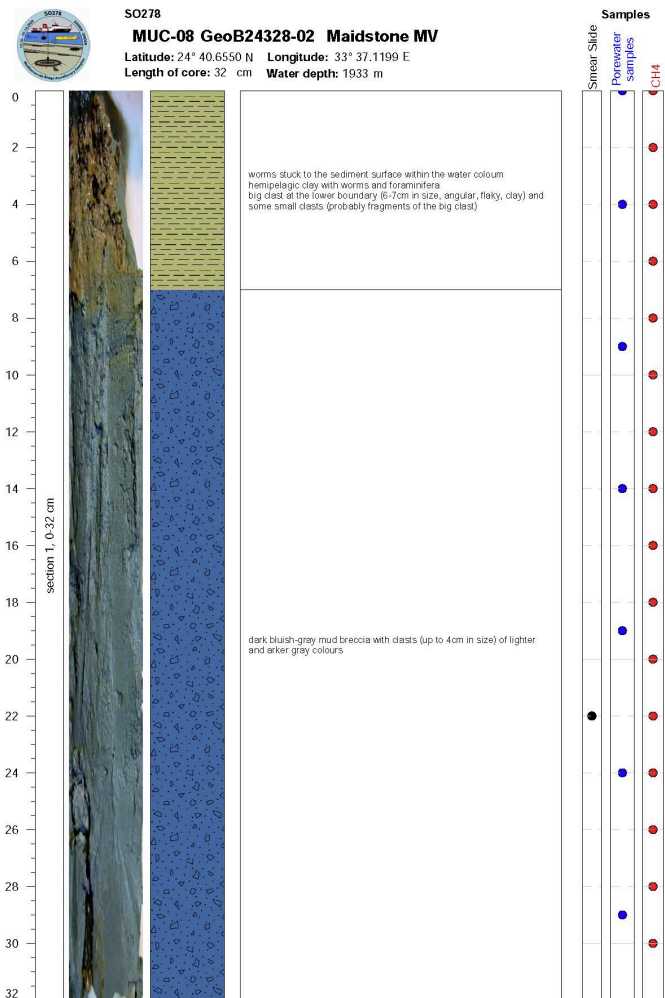
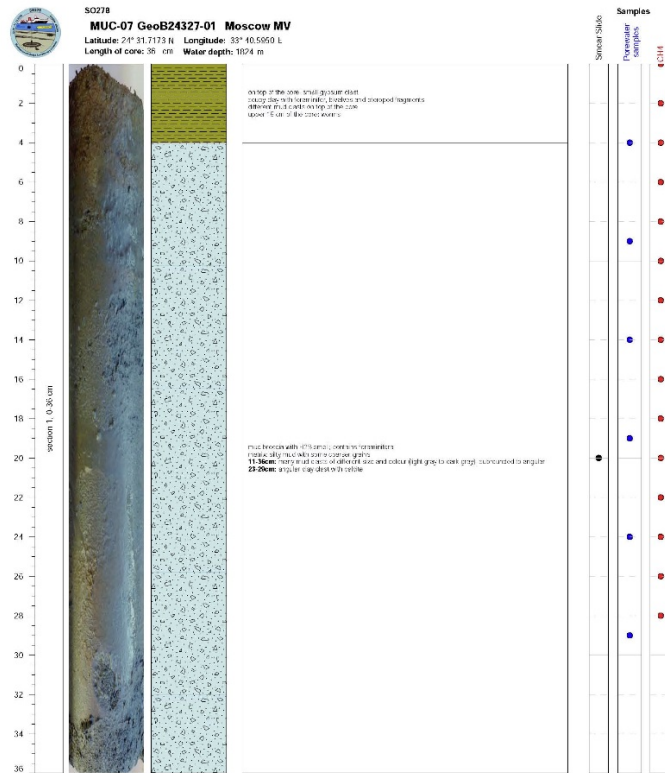
### Continuation MIC/MUC Straters



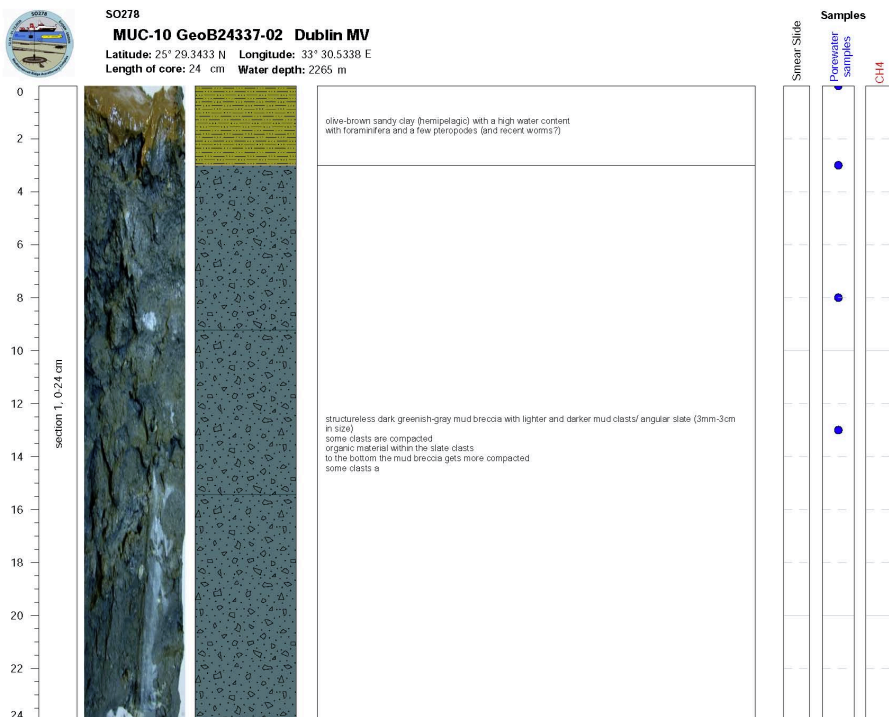
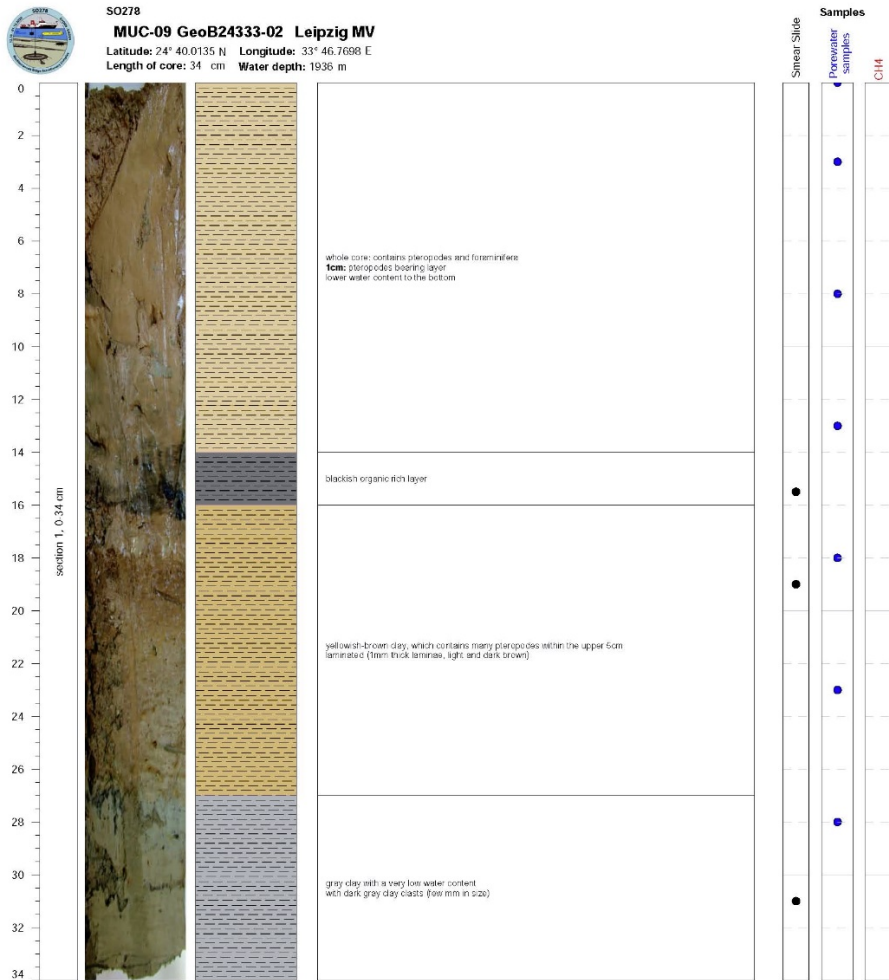
Continuation MIC/MUC Straters



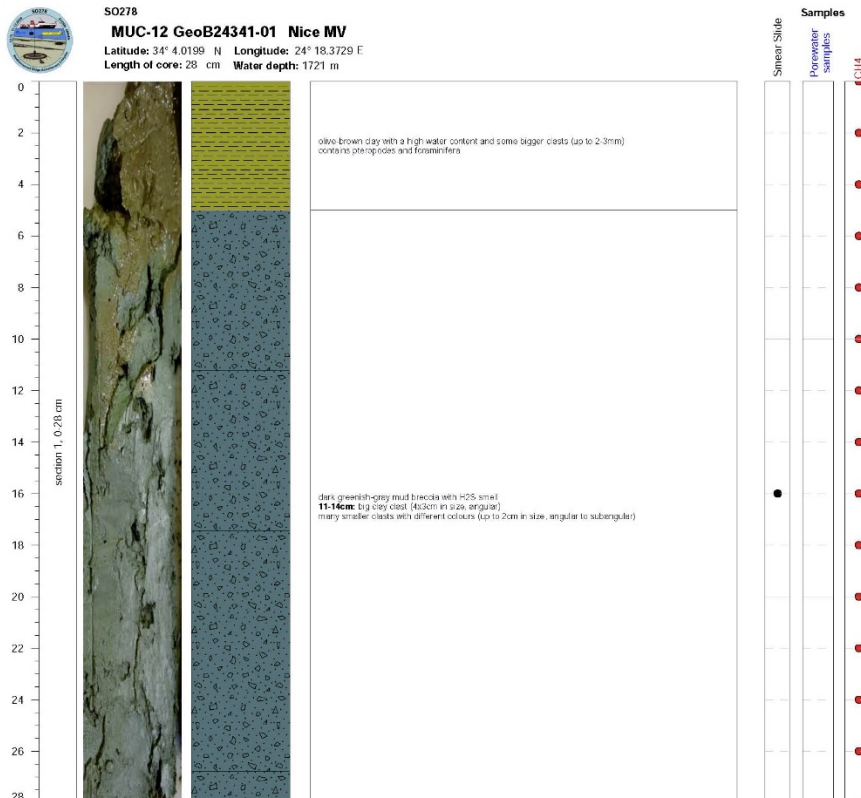
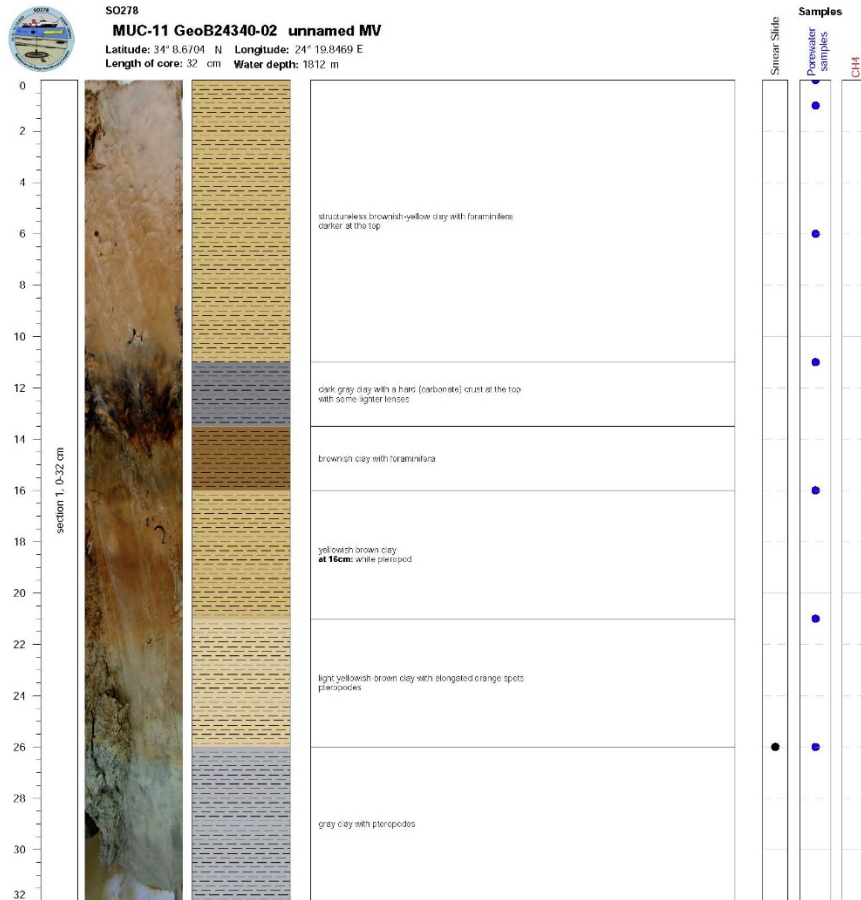
### Continuation MIC/MUC Straters



Continuation MIC/MUC Straters



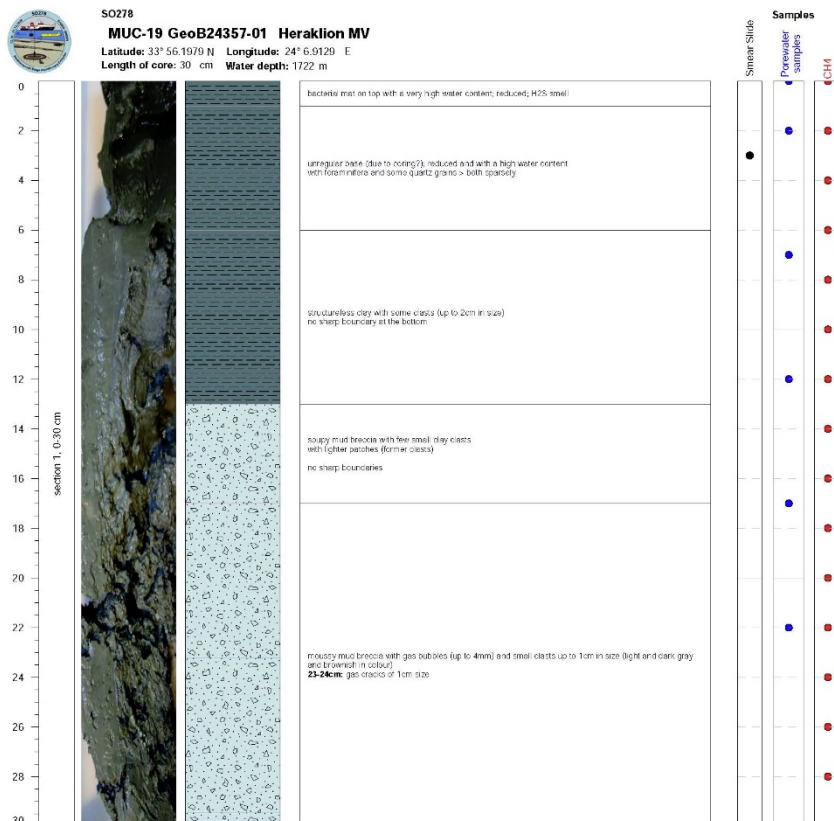
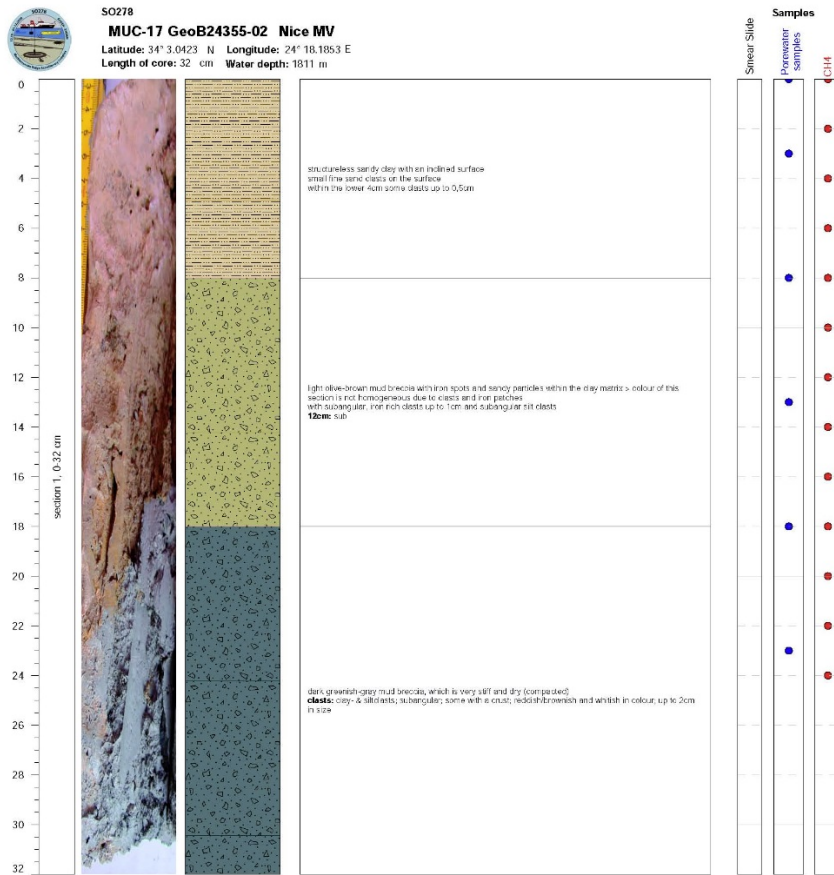
### Continuation MIC/MUC Straters



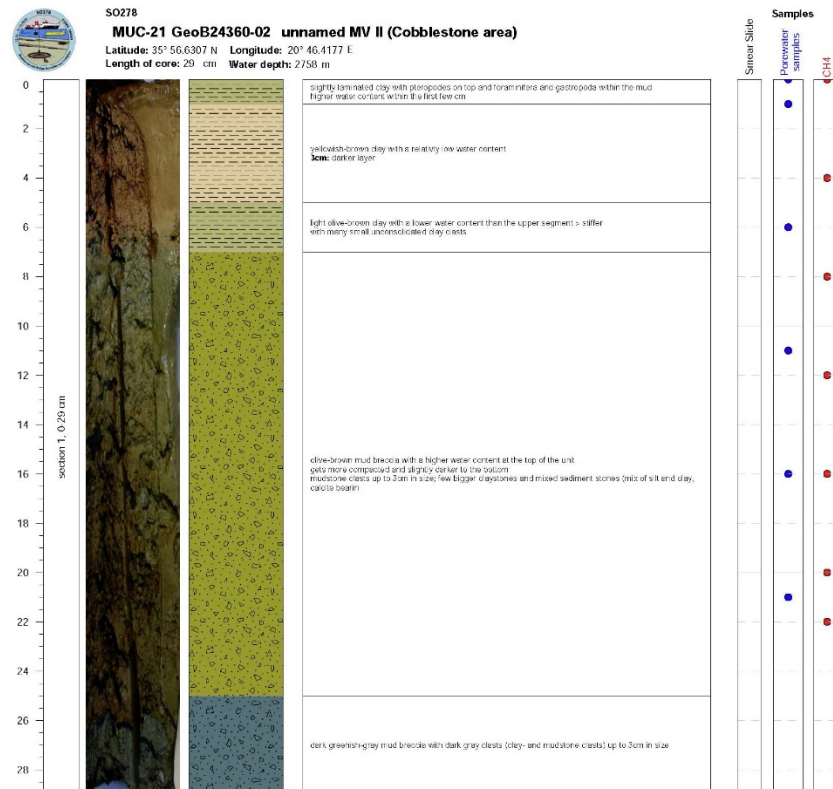
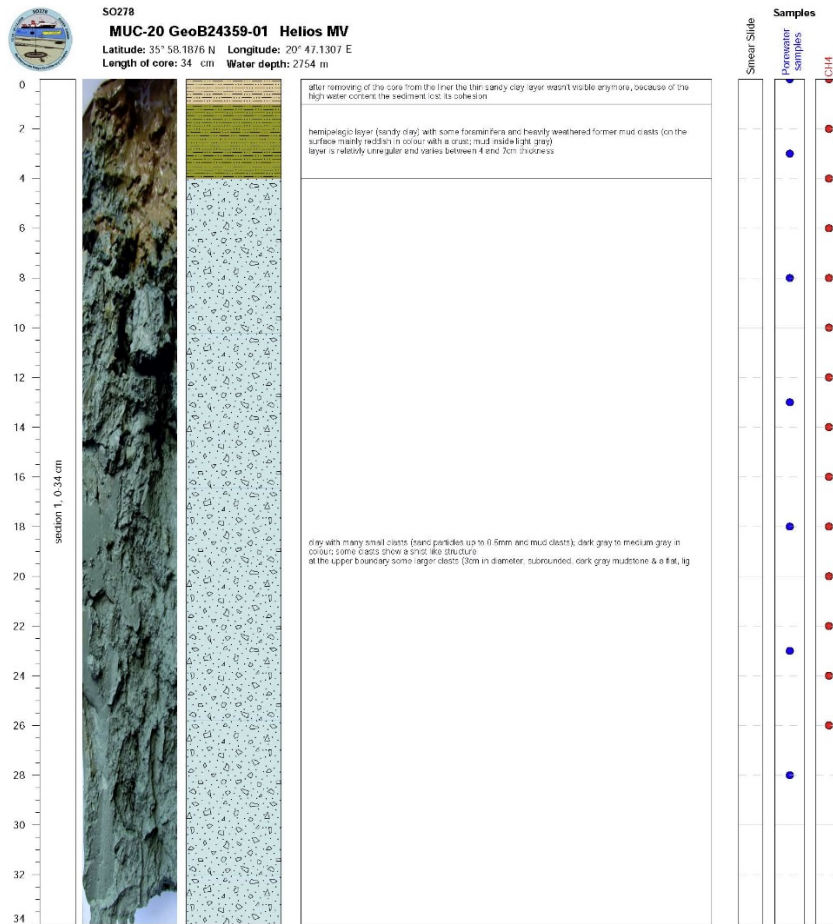




Continuation MIC/MUC Straters



### Continuation MIC/MUC Straters

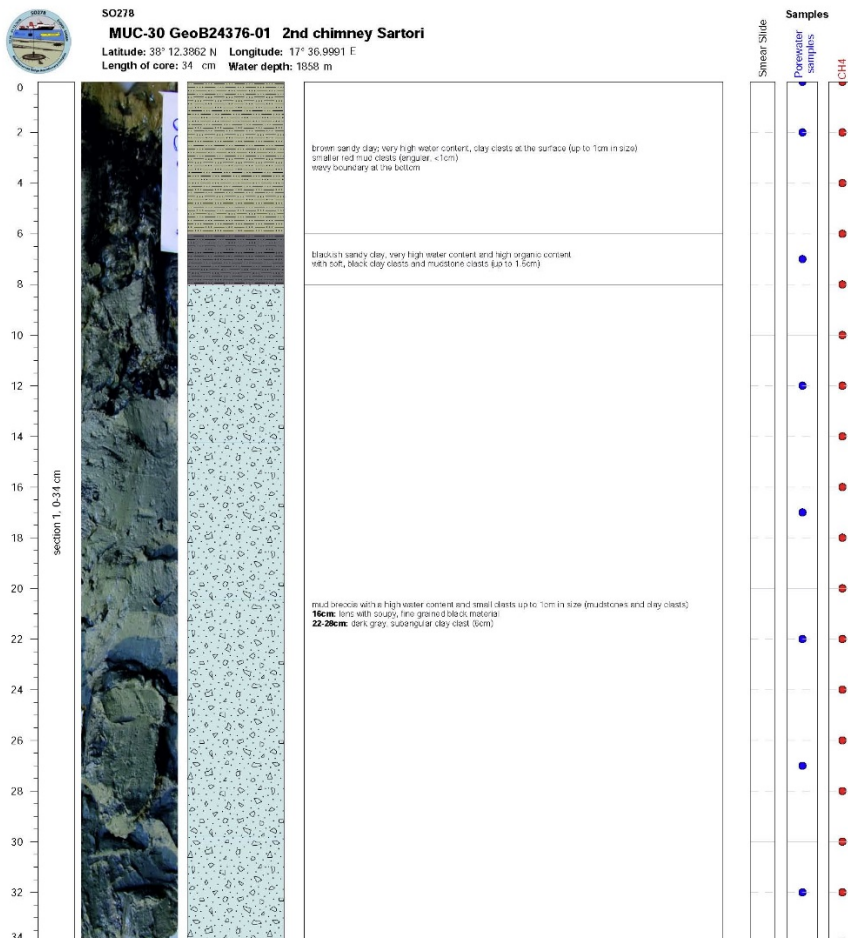
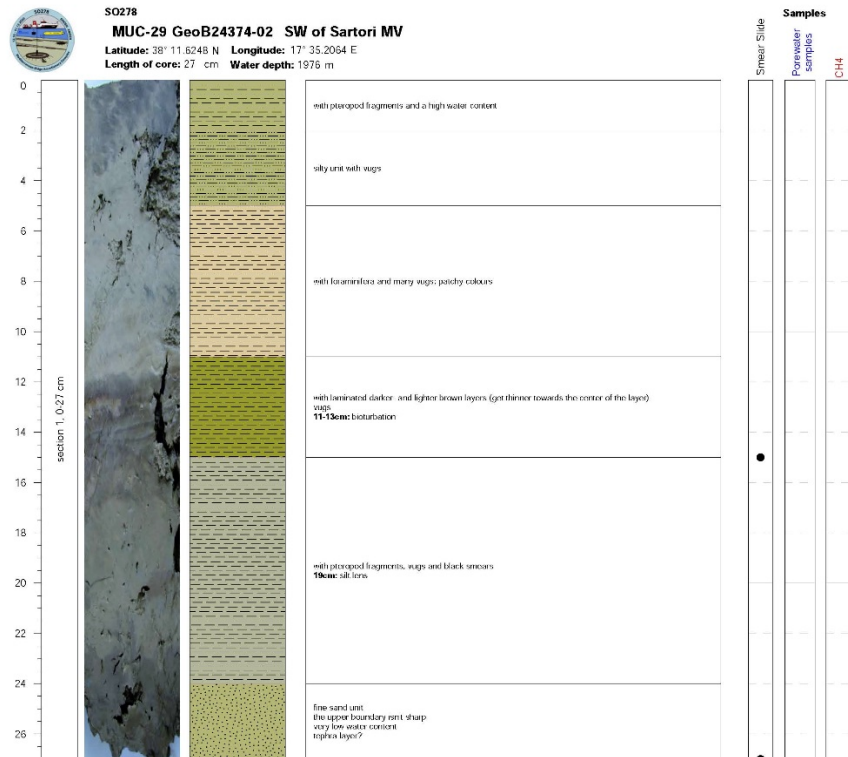




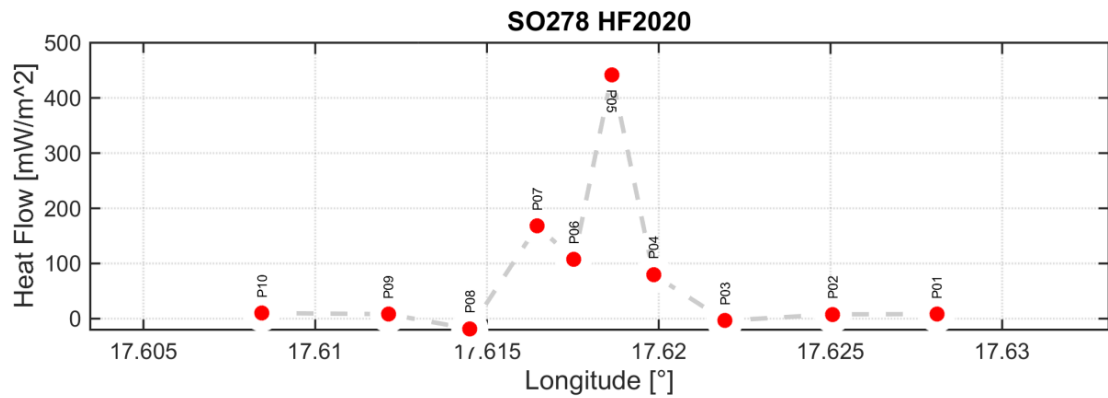




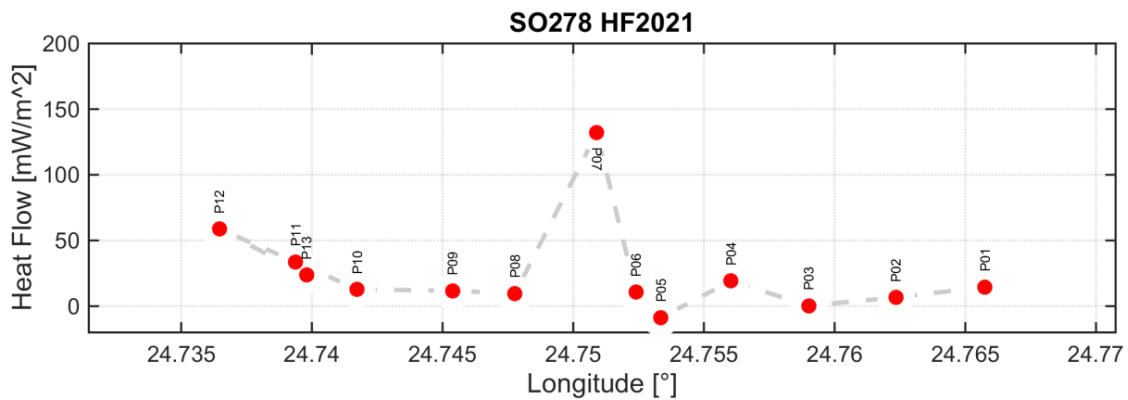
### Continuation MIC/MUC Straters



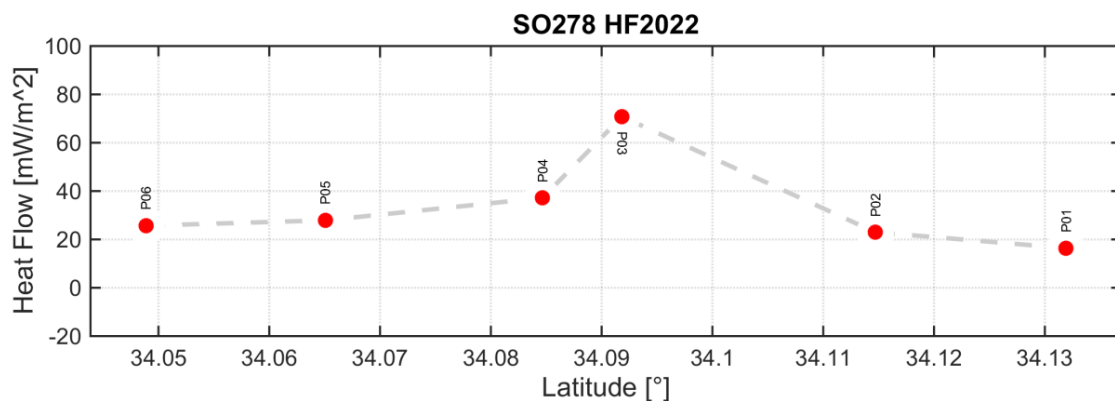
### 10.3 Heatflow Profiles



W-E heat flow profile HF20 across Sartori MV, Calabrian accretionary wedge, meeting western (P07) and eastern chimney (P05).

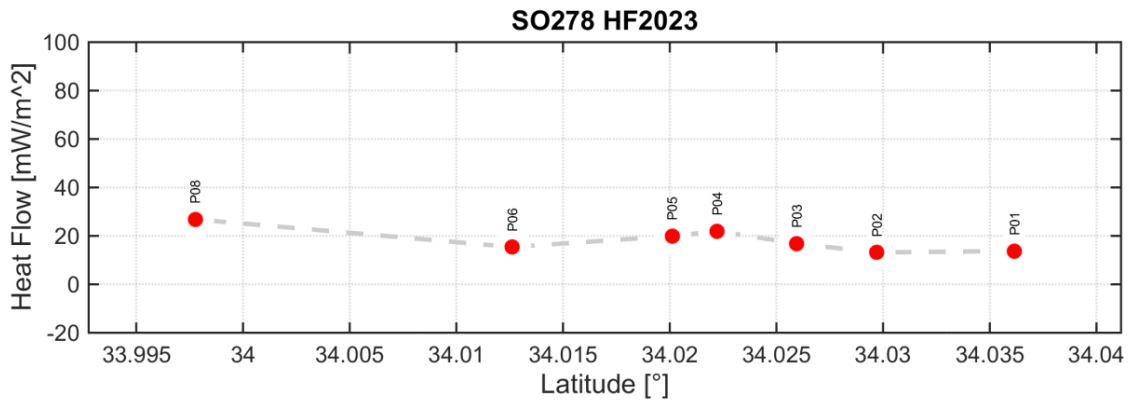


E-NW heat flow profile HF21 across Bergamo MV, Olimpi mud volcano field. P12 and P13 targeted inferred subsrosional pits.

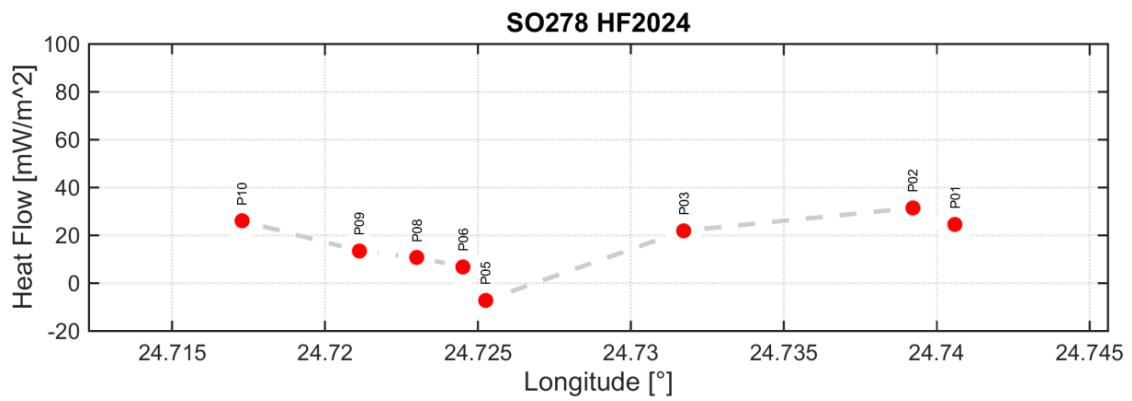


S-N heat flow profile HF22 across a presumed fault zone (P03-P04), S-Crete. Profile length is 9 km.

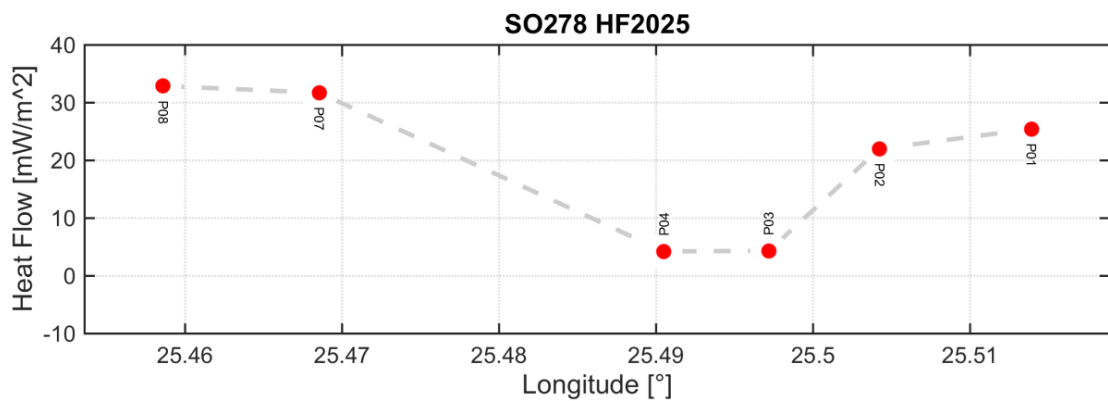
### Continuation Heatflow Profiles



S-N heat flow profile HF23 across the Inner Ridge of the Cretan Margin. P07 failed.

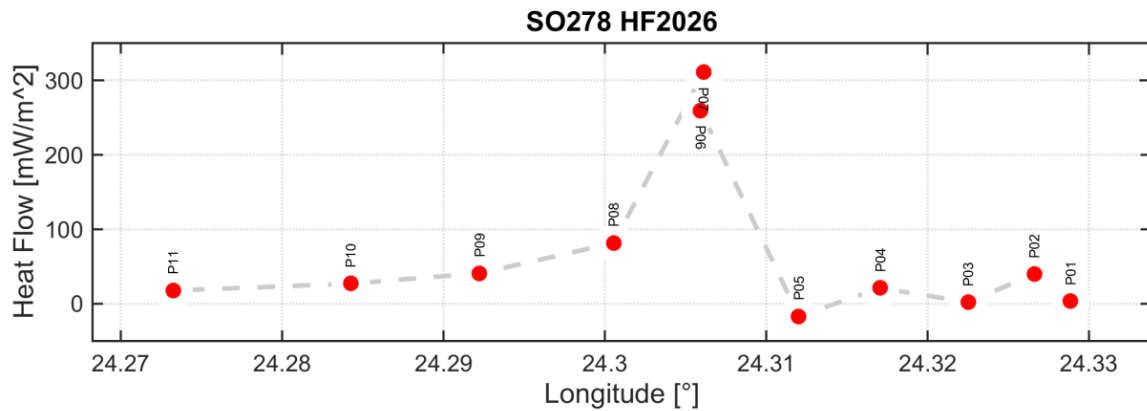


S-N profile HF24 across Monza MV, Olimpi mud volcano field. P04 and P07 failed. P05 on top of Monza MV shows signs of non-steady state processes, resulting in a negative temperature gradient.

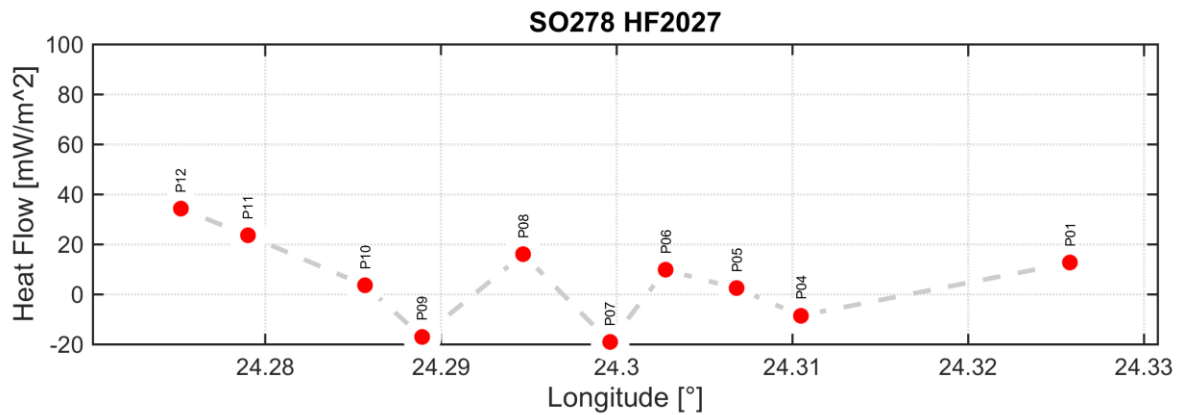


W-E heat flow profile HF25 across Dublin MV, United Nations Rise. P05 on the top and P06 on the steep flank failed.

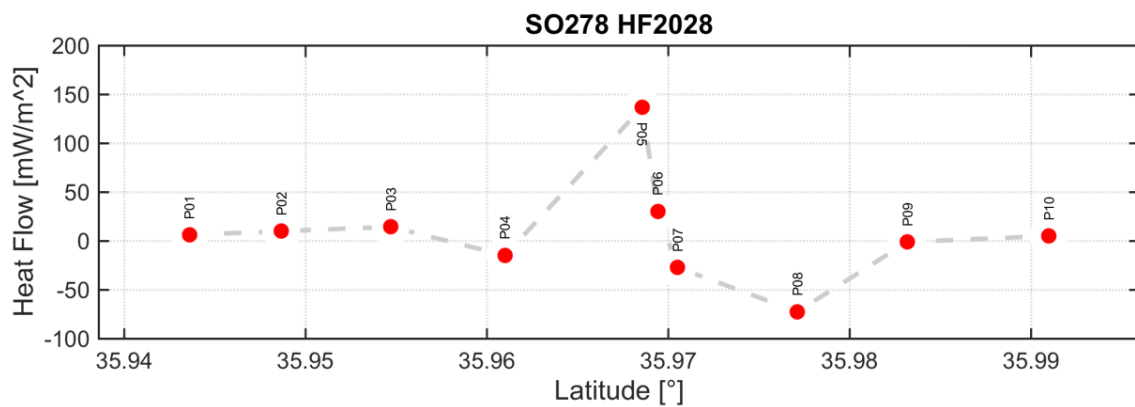
## Continuation Heatflow Profiles



NW-SE heat flow profile HF26 across Nice MV and two adjacent dome structures, West Olimpi mud volcano field. Only Nice MV (P06 and P07) shows elevated temperatures.

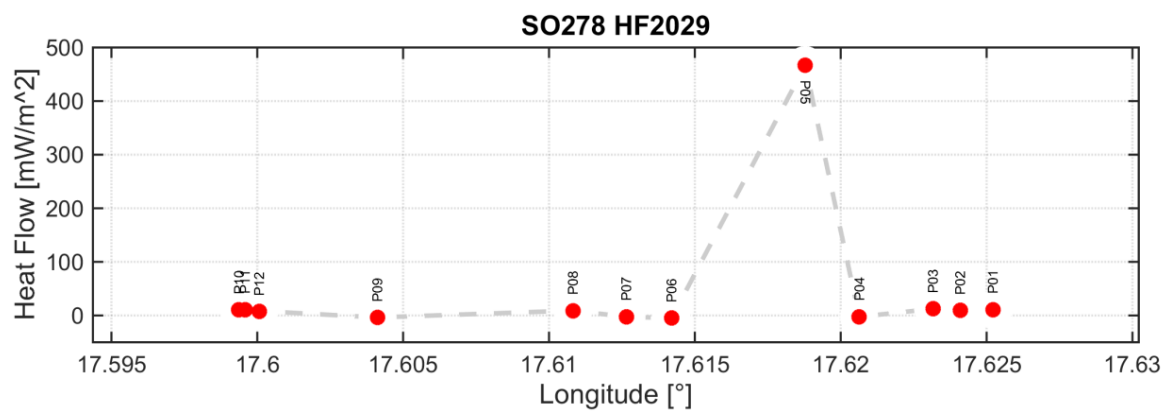


W-E heat flow profile HF27 across slump structures south of Nice MV, West Olimpi mud volcano field. P02 and P03 failed due to steep slope. Partial penetration and strong excursions within the temperature gradient occasionally result in negative temperature gradients.



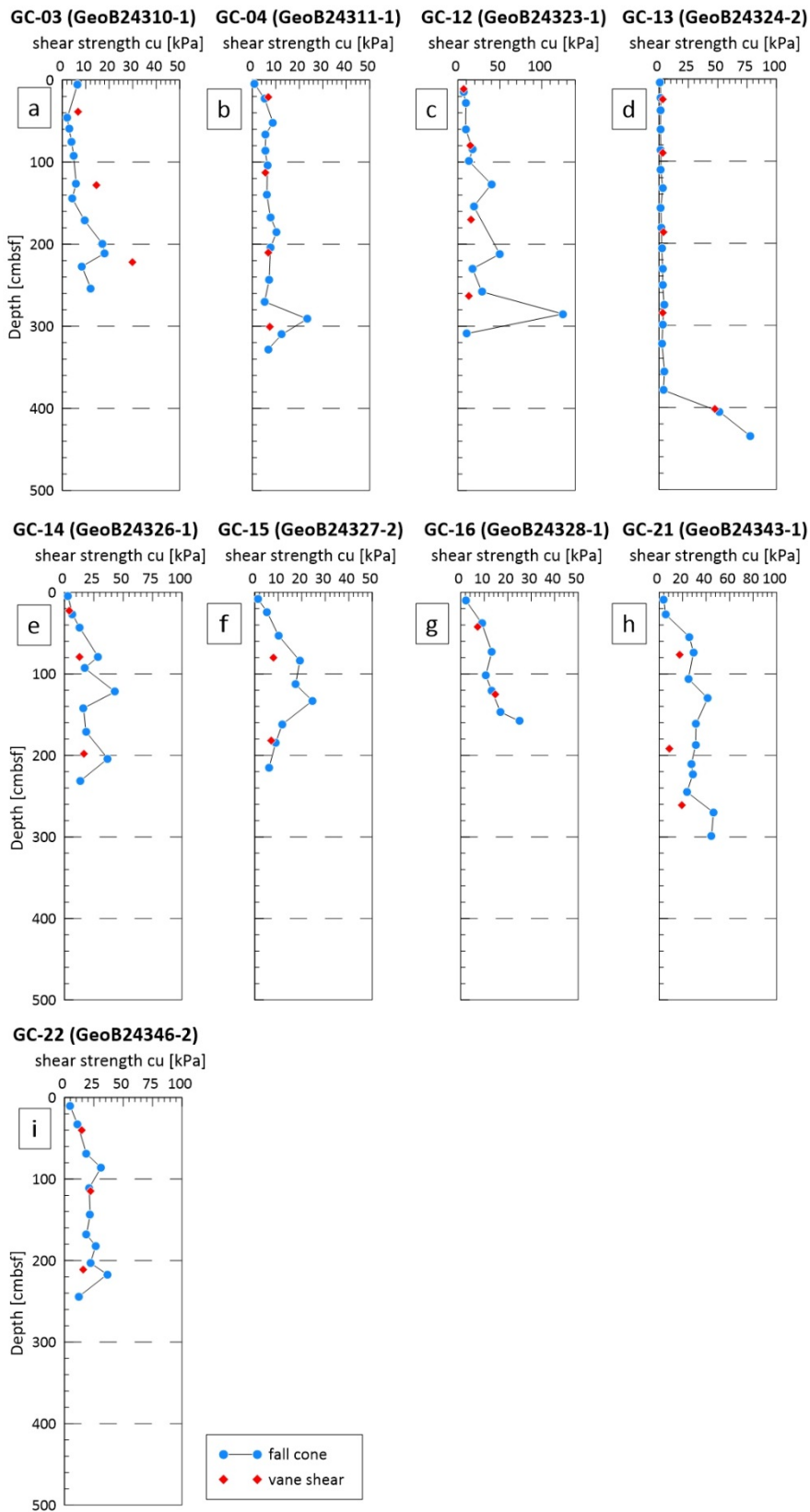
S-N heat flow profile HF28, Cobblestone area. The mud volcano in the center of the profile is suggested to be called Helios MV.

## Continuation Heatflow Profiles



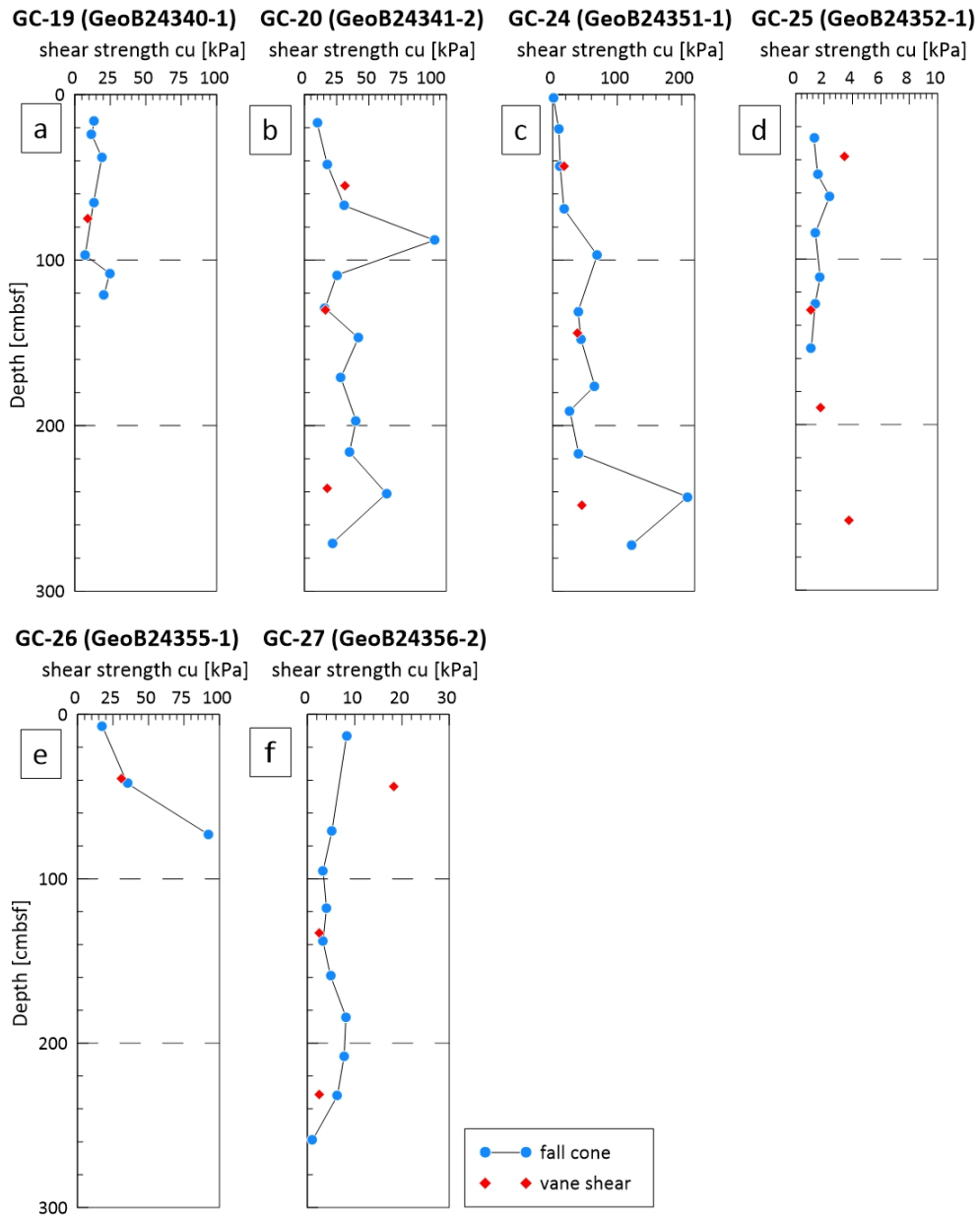
W-E heat flow profile HF29 across Sartori MV, Calabrian accretionary wedge. 470 mW/m<sup>2</sup> within the eastern chimney is a repeatable result.

### 10.4 Geotechnical Measurements



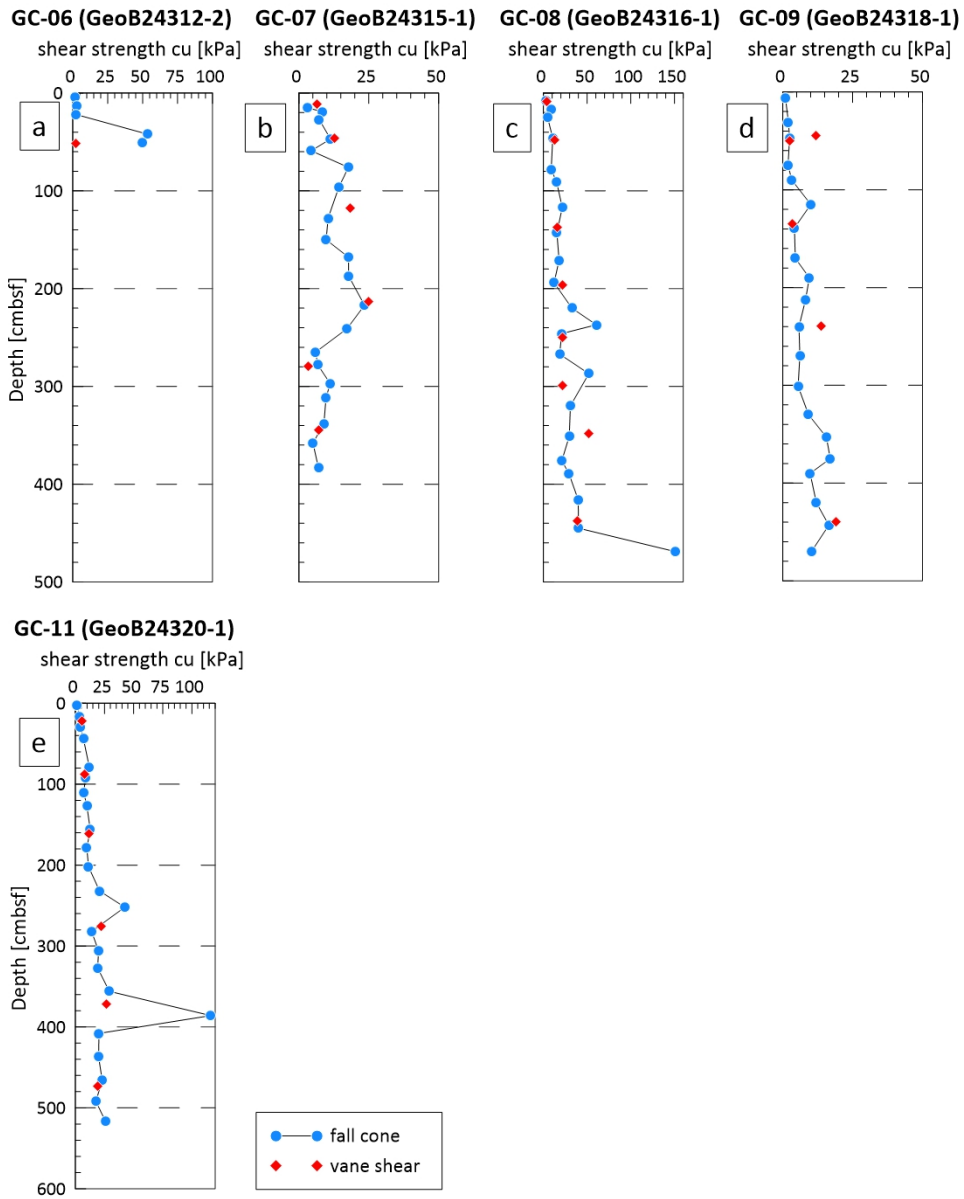
Shear strength of sediment cores from the Olimpi Field. a: Napoli MV. b: Bergamo MV. c: Bergamo MV plateau. d: west of Bergamo plateau. e: Bergamo NE plateau. f: Moscow MV. g: Maidstone MV. h: Monza MV. i: Milano MV.

### Continuation Geotechnical Measurements



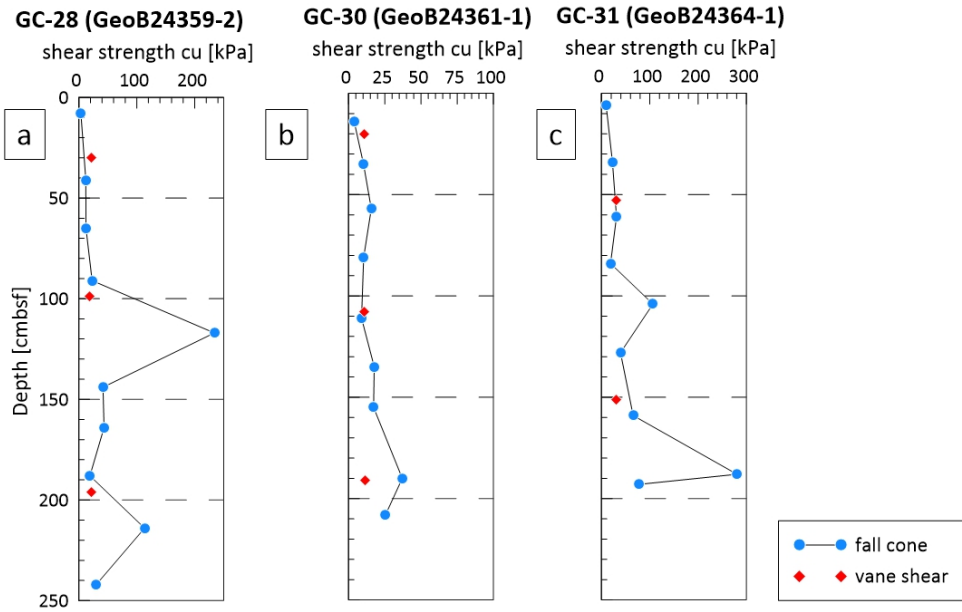
Shear strength of the sediment cores retrieved from the west Olimpi Field. a: unnamed MV. b: Nice MV. c: Gelendzhik MV. d: Heraklion MV. e: Nice MV. f: unnamed MV.

### Continuation Geotechnical Measurements

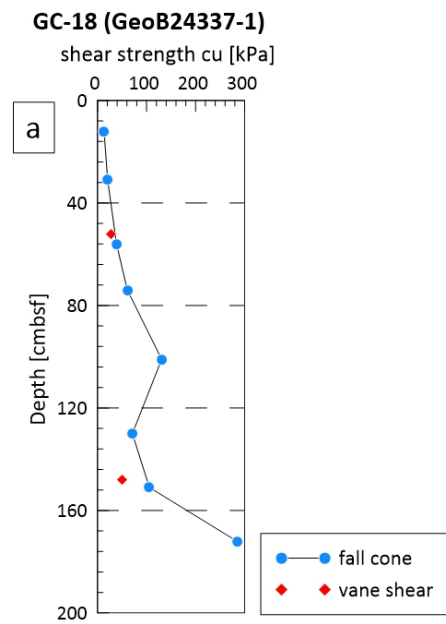


Shear strength of the sediment cores retrieved from the fault zone.

### Continuation Geotechnical Measurements

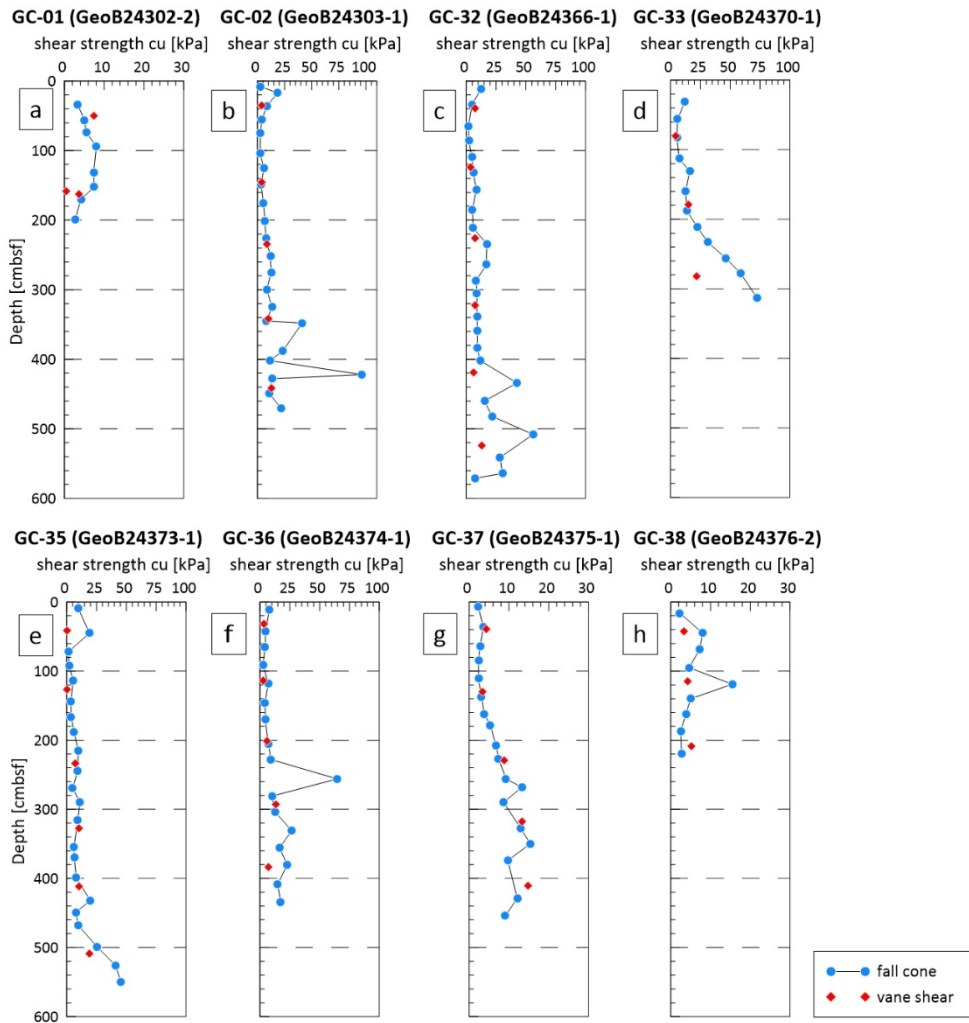


Shear strength of the sediment cores retrieved from the Cobblestone Area. a-c: Helios MV



Shear strength of the sediment core retrieved from the United Nations Rise. a: Dublin MV.

### Continuation Geotechnical Measurements



Shear strength of the sediment cores from the Calabrian Arc. a: Sartori MV. b: south of Sartori MV. c: south of Sartori MV. d: mud flow rim. e: SW of Sartori MV. f: SW of Sartori MV. g: SW of Sartori MV. h: second chimney of Sartori MV.

From report No. 289 onwards this series is published under the new title:

**Berichte aus dem MARUM und dem Fachbereich Geowissenschaften der Universität Bremen**

A complete list of all publications of this series from no. 1 to 292 (1986 – 2012) was printed at last in issue no. 292.

- No. 289 – Mohtadi, M. and cruise participants (2012).** Report and preliminary results of RV SONNE Cruise SO 223T. TransGeoBioC. Pusan – Suva, 09.09.2012 – 08.10.2012. 47 pages.
- No. 290 – Hebbeln, D., Wienberg, C. and cruise participants (2012).** Report and preliminary results of R/V Maria S. Merian cruise MSM20-4. WACOM – West-Atlantic Cold-water Corals Ecosystems: The West Side Story. Bridgetown – Freeport, 14 March – 7 April 2012. 120 pages.
- No. 291 – Sahling, H. and cruise participants (2012).** R/V Heincke Cruise Report HE-387. Gas emissions at the Svalbard continental margin. Longyearbyen – Bremerhaven, 20 August – 16 September 2012. 170 pages.
- No. 292 – Pichler, T., Häusler, S. and Tsuonis, G. (2013).** Abstracts of the 3rd International Workshop "Research in Shallow Marine and Fresh Water Systems". 134 pages.
- No. 293 – Kucera, M. and cruise participants (2013).** Cruise report of RV Sonne Cruise SO-226-3. Dip-FIP - The extent and structure of cryptic diversity in morphospecies of planktonic Foraminifera of the Indopacific Warm Pool. Wellington – Kaohsiung, 04.03.2013 – 28.03.2013. 39 pages.
- No. 294 – Wienberg, C. and cruise participants (2013).** Report and preliminary results of R/V Poseidon cruise P451-2. Practical training cruise onboard R/V Poseidon - From cruise organisation to marine geological sampling: Shipboard training for PhD students on R/V Poseidon in the Gulf of Cádiz, Spain. Portimao – Lisbon, 24 April – 1 May 2013. 65 pages.
- No. 295 – Mohtadi, M. and cruise participants (2013).** Report and preliminary results of R/V SONNE cruise SO-228, Kaohsiung-Townsville, 04.05.2013-23.06.2013, EISPAC-WESTWIND-SIODP. 107 pages.
- No. 296 – Zonneveld, K. and cruise participants (2013).** Report and preliminary results of R/V POSEIDON cruise POS448. CAPRICCIO – Calabrian and Adriatic Past River Input and Carbon Conversion In the Eastern Mediterranean. Messina – Messina, 6 – 23 March 2013. 47 pages.
- No. 297 – Kopf, A. and cruise participants (2013).** Report and preliminary results of R/V SONNE cruise SO222. MEMO: MeBo drilling and in situ Long-term Monitoring in the Nankai Trough accretionary complex, Japan. Leg A: Hong Kong, PR China, 09.06.2012 – Nagoya, Japan, 30.06.2012. Leg B: Nagoya, Japan, 04.07.2012 – Pusan, Korea, 18.07.2012. 121 pages.
- No. 298 – Fischer, G. and cruise participants (2013).** Report and preliminary results of R/V POSEIDON cruise POS445. Las Palmas – Las Palmas, 19.01.2013 – 01.02.2013. 30 pages.
- No. 299 – Hanebuth, T.J.J. and cruise participants (2013).** CORIBAR – Ice dynamics and meltwater deposits: coring in the Kveithola Trough, NW Barents Sea. Cruise MSM30. 16.07. – 15.08.2013, Tromsø (Norway) – Tromsø (Norway). 74 pages.
- No. 300 – Bohrmann, G. and cruise participants (2014).** Report and Preliminary Results of R/V POSEIDON Cruise P462, Izmir – Izmir, 28 October – 21 November, 2013. Gas Hydrate Dynamics of Mud Volcanoes in the Submarine Anaximander Mountains (Eastern Mediterranean). 51 pages.
- No. 301 – Wefer, G. and cruise participants (2014).** Report and preliminary results of R/V SONNE Cruise SO219A, Tohoku-Oki Earthquake – Japan Trench, Yokohama – Yokohama, 08.03.2012 – 06.04.2012. 83 pages.
- No. 302 – Meinecke, G. (2014).** HROV: Entwicklung und Bau eines hybriden Unterwasserfahrzeugs – Schlussbericht. 10 pages.
- No. 303 – Meinecke, G. (2014).** Inverse hydroakustische USBL-Navigation mit integrierter Kommunikation – Schlussbericht. 10 pages.
- No. 304 – Fischer, G. and cruise participants (2014).** Report and preliminary results of R/V POSEIDON cruise POS464, Las Palmas (Canary Islands) – Las Palmas (Canary Islands), 03.02.2014 – 18.02.2014. 29 pages.
- No. 305 – Heuer, V.B. and cruise participants (2014).** Report and preliminary results of R/V POSEIDON cruise POS450, DARCSEAS II – Deep seafloor Archaea in the Western Mediterranean Sea: Carbon Cycle, Life Strategies, and Role in Sedimentary Ecosystems, Barcelona (Spain) – Malaga (Spain), April 2 – 13, 2013. 42 pages.
- No. 306 – Bohrmann, G. and cruise participants (2015).** Report and preliminary results of R/V METEOR cruise M112, Dynamic of Mud Volcanoes and Seeps in the Calabrian Accretionary Prism, Ionian Sea, Catania (Italy) – Catania (Italy), November 6 – December 15, 2014. 217 pages.
- No. 307 – Fischer, G. and cruise participants (2015).** Report and preliminary results of R/V POSEIDON cruise POS481, Las Palmas (Canary Islands) – Las Palmas (Canary Islands), 15.02.2015 – 03.03.2015. 33 pages.
- No. 308 – Wefer, G. and Freudenthal, T. (2016).** MeBo200 – Entwicklung und Bau eines ferngesteuerten Bohrgerätes für Kernbohrungen am Meeresboden bis 200 m Bohrteufe, Schlussbericht. 9 pages.
- No. 309 – Sahling, H. and cruise participants (2016).** R/V POSEIDON cruise POS498, Recovery of Observatories at Athina Mud Volcano, Izmir (Turkey) – Catania (Italy), 18 April – 1 May, 2016. 63 pages.
- No. 310 – Fischer, G. and cruise participants (2016).** Report and preliminary results of R/V POSEIDON cruise POS495, Las Palmas (Canary Islands) – Las Palmas (Canary Islands), 18.02.2016 – 02.03.2016. 29 pages.
- No. 311 – Bohrmann, G. and cruise participants (2016).** Report and preliminary results of R/V POSEIDON cruise POS499, Calabrian Mud Volcanoes, Catania (Italy) – Catania (Italy), 04 May – 22 May, 2016. 76 pages.
- No. 312 – Kopf, A., Fleischmann, T. and cruise participants (2016).** Report and preliminary results of R/V POSEIDON cruise POS500, LISA, Ligurian Slope AUV mapping, gravity coring and seismic reflection, Catania (Italy) – Malaga (Spain), 25.05.2016 – 09.06.2016. 58 pages.
- No. 313 – Stegmann, S. and cruise participants (2017).** Report and preliminary results of R/V POSEIDON cruise POS472, NORGEotech, Geotechnical in situ investigation of slope stability in Norway, Trondheim (Norway) – Tromsø (Norway), 27.07.2014 – 12.08.2014. 103 pages.
- No. 314 – Bohrmann, G. and cruise participants (2017).** R/V MARIA S. MERIAN Cruise Report MSM57, Gas Hydrate Dynamics at the Continental Margin of Svalbard, Reykjavik – Longyearbyen – Reykjavik, 29 July – 07 September 2016. 204 pages.
- No. 315 – Sahling, H. and cruise participants (2017).** R/V METEOR Cruise Report M114, Natural hydrocarbon seepage in the southern Gulf of Mexico, Kingston – Kingston, 12 February – 28 March 2015. 214 pages.
- No. 316 – Mohtadi, M. and cruise participants (2017).** R/V SONNE Cruise Report SO256, TACTEAC, Temperature And Circulation History of The East Australian Current, Auckland (New Zealand) – Darwin (Australia), 17 April – 09 May 2017. 70 pages.
- No. 317 – Bohrmann, G. and cruise participants (2017).** R/V METEOR Cruise Report M134, Emissions of Free Gas from Cross-Shelf Troughs of South Georgia: Distribution, Quantification, and Sources for Methane Ebullition Sites in Sub-Antarctic Waters, Port Stanley (Falkland Islands) – Punta Arenas (Chile), 16 January – 18 February 2017. 220 pages.
- No. 318 – Strasser, M., Kopf, A. and cruise participants (2017).** Report and preliminary results of R/V SONNE cruise SO251, Extreme events Archived in the Geological Record of Japan's Subduction margins (EAGER-Japan), Leg A SO251-1, Yokohama - Yokohama, 04.10.2016 – 15.10.2016, Leg B SO251-2, Yokohama - Yokohama, 18.10.2016 – 02.11.2016. 217 pages.
- No. 319 – Iversen, M. and cruise participants (2018).** Report and preliminary results of R/V POSEIDON cruise POS508, Las Palmas (Canary Islands) – Las Palmas (Canary Islands), 22.01.2017 – 06.02.2017. 36 pages.

- No. 320 – Bohrmann, G. and cruise participants (2018).** R/V METEOR cruise report M142, Drilling Gas Hydrates in the Danube Deep-Sea Fan, Black Sea, Varna – Varna – Varna, 04 November – 22 November – 09 December 2017. 121 pages.
- No. 321 – Wefer, G. and Freudenthal, T. (2018).** MeBo-Upgrade: Neu- und Weiterentwicklungen für das Bohren am Meeresboden mit MeBo, Schlussbericht. 15 pages.
- No. 322 – Meinecke, G. (2019).** H-ROV-LARS: Entwicklung eines Aussetz- und Bergesystems mit integrierter, neuartiger Kommunikation und Ortung für das Hybrid-ROV (LARS), Schlussbericht. 19 pages.
- No. 323 – Iversen, M. and cruise participants (2020).** Report and preliminary results of R/V POSEIDON cruise POS531, Las Palmas (Canary Islands) – Mindelo (Cape Verde), 18.01.2019 – 01.02.2019. 32 pages.
- No. 324 – Hüpers, A. and cruise participants (2020).** Preliminary results of R/V METEOR cruise M149: Shipboard and Post-Cruise Analysis, Recurrence of tsunamigenic hazards from MeBo drilling records and hazard mitigation using MeBo observatories, Las Palmas (Canary Islands) – Cadiz (Spain), 24.07.2018 – 24.08.2018. 200 pages.
- No. 325 – Milucka, J. and cruise participants (2020).** Report and preliminary results of R/V POSEIDON cruise POS539, Varna (Bulgaria) - Varna (Bulgaria) November 6 - November 22, 2019. 30 pages.
- No. 326 – Bohrmann, G. and cruise participants (2021).** Fluid-rock interaction at the backstop to the Mediterranean Ridge Accretionary Complex South of Crete, R/V SONNE Cruise Report SO278, 12 October – 01 December 2020, Emden (Germany) – Emden (Germany), FRINGE. 208 pages.